UNIVERSITY OF SOUTHAMPTON

FACULTY OF PHYSICAL SCIENCES AND ENGINEERING

Optoelectronics Research Centre

ADVANCED TECHNIQUES OF CHARACTERISATION FOR HIGH POWER FIBRE LASERS AND AMPLIFIERS

DOI: 10.5258/SOTON/D1215

by

Vincenzo Scarnera

ORCID ID 0000-0001-8646-7063

Thesis for the degree of Doctor of Philosophy

April 2020

UNIVERSITY OF SOUTHAMPTON

ABSTRACT

FACULTY OF PHYSICAL SCIENCES AND ENGINEERING

Optoelectronics Research Centre

Doctor of Philosophy

ADVANCED TECHNIQUES OF CHARACTERISATION FOR

HIGH POWER FIBRE LASERS AND AMPLIFIERS

By Vincenzo Scarnera

We present advanced techniques to optimise splices between dissimilar fibres and to characterise High Power Fibre Lasers (HPFL). Developed in an industrial context of volume manufacturing and supported by academia, these techniques aim to improve HPFL efficiency and stability, understand causes of failure, increase the yield on the production line and deliver working prototypes in shorter times.

An innovative high power test-kit has been purposely built to perform advanced characterisation on HPFLs and amplifiers. The high power test-kit can concurrently record data from a multitude of sensors connected to various parts of the laser whilst conditioning the pump power in continuous wave or pulsed regime. Concurrent data logging has allowed unveiling failure's mechanisms and has given us precise clues on how to resolve instability and efficiency related problems. An innovative non-destructive technique has been invented to resolve, along the active fibre length and during high power operation, quantities such as pump absorption, atomic inversion, signal power and non-linear effects evolution.

Splicing of the various components composing the optical systems plays a very important role, especially when splicing dissimilar fibres inside the laser cavity. An S^2 (Spatial and Spectral) test-kit has been developed with the intent of optimising splices. The S^2 test-kit allowed us to measure the modal excitation of multimode fibres in presence of SM-MM splices. We have experimentally discovered, repeatedly re-produced and theoretically justified the existence of an optimal splice between SM and diffusing MM fibres. Application of the so called optimal splice has proven to lead to measurable and positive effects in terms of HPFL's performance. The splice optimisation criterion seems quite counterintuitive and contradicting some common beliefs related to fundamental mode excitation in multimode fibres.

The optimal splice discovered in this work is now adopted in the mass production cycle of lasers at SPI Lasers.

Contents

List of Figures

List of Tables

List of acronyms

FWM	Four wave mixing
AF	Active fibre
BDF	Beam delivery fibres
BPM	Beam Propagation method
BVP	Boundary value problem
CC	Coupling Configuration
CMS	Cladding mode stripper
CW	Continuous wave
DCF	Dual clad fibbers
DM	Dual mode
EA	Effective Area
FFT	Fast Fourier transform
FM	Fundamental mode
FMC	Fundamental mode cavity
FPY	Fist pass yield
FS	Fusion splicer
HOMC	High order mode cavity
HPC	High power combiner
HPFL	High power fibre laser
HR	High reflector
IOR	Index of refraction
LM	Local Mode
LMA	Large mode area
LMB	Longitudinal mode beating
MAFWM	Mode Assisted Four Wave Mixing
MCVD	Modified chemical vapour deposition
MFD	Mode field diameter
MM	Multimode
MMF	Multimode fibre
MOPA	Master Oscillator Power Amplifier
MOPA	Master oscillator power amplifier
MPI	Multi path interference

MR	Molar Refractivity
MS	Mode stripper
NA	Numerical Aperture
OC	Output coupler
PM	Power meter
PSU	Power supply unit
RL	Radiation loss
SBS	Stimulated Brillouin scattering
SD	Selective doping
SIMS	Secondary Emission Mass Spectroscopy
SM	Single mode
SMF	Single mode fibre
SRS	Stimulated Raman scattering
TMC	Transversal mode competition
TMI	Transversal mode instability
USP	Unique selling point

Declaration of Authorship

I, Vincenzo Scarnera, declare that the thesis entitled *"Advanced technique of characterisation for high power fibre lasers and amplifiers"* and the works presented in it are my own and have been generated by me as the result of my own original research.

1. This work was done wholly or mainly while in candidature for a research degree at this University;
2. Where any part of this thesis has previously been submitted for a degree or any other qualification at this University or any other institution, this has been clearly stated;
3. Where I have consulted the published work of others, this is always clearly attributed;
4. Where I have quoted from the work of others, the source is always given. With the exception of such quotations, this thesis is entirely my own work;
5. I have acknowledged all main sources of help;
6. Where the thesis is based on work done by myself jointly with others, I have made clear exactly what was done by others and what I have contributed myself;
7. Parts of this work have been published as:

- *V. Scarnera, F. Ghiringhelli, A. Malinowski, C. A. Codemard, M. K. Durkin, and M. N. Zervas, "Modal instabilities in high power fiber laser oscillators," Optics Express 27, 4386-4403 (2019).*

- *V. Scarnera, F. Ghiringhelli, M. K. Durkin, C. A. Codemard and M. N. Zervas, "Transient modal instabilities in high power fibre lasers," 2017 Conference on Lasers and Electro-Optics Europe & European Quantum Electronics Conference (CLEO/Europe-EQEC), Munich, 2017, pp. 1-1.*

Signed: .....
Date: 23/02/2020

Acknowledgment

I thank SPI Lasers for having given me the opportunity of pursuing this degree at the Optoelectronic Research Centre. I will never forget the day of my Job interview, more than ten years ago. It was immediate chemistry! Doctor Steve Norman greeted me in perfect Italian and offered me an espresso... how to refuse such an offer? Subsequently Professor Michalis Zervas interviewed me and I realised we had things in common: we liked fibres and lasers!

Michalis, I want to thank you for suggesting me to pursue a doctoral degree and above all thanks for having set the best example, at 360 degrees, in every occasion. I hope I am now somehow the “laser man” you wanted me to become.

I would like to thank all the people I have met at the ORC and of course Doctor Christophe Codemard, my PhD co-supervisor. I would like to thank Christophe for the bibliographic references and technical tips he provided me during these years. I wish to thank Doctor James Gates and Professor Johan Nilsson for the useful discussion had during my intermediary viva, before submitting the final version of my thesis.

I very thankful to Doctor Mike Durkin, my manager at SPI Lasers. Mike, with your help I have immediately recognised when the conclusion about some measurements were wrong. A special thanks goes to Doctor Malcolm Varnham: thanks for spurring me to complete this piece of work. Thanks also to all the other colleagues of SPI Lasers for the useful technical conversations, code and samples.

I wish to thank Doctor Peristera Andreaku, Doctor Thomas Esterle and Doctor Alex Boyland, my precious friends and colleagues; thanks for the superhuman support you gave me in the last period. Thanks for the wonderful days we spend together! Absolutely the best…

It has been a privilege knowing with you all.

Dedico questo lavoro a mio figlio Francesco, all'amore della mia vita Joanna e alla mia famiglia. Dedico questo lavoro a †Niccolò Scarnera, mio padre. Padre, la tua tenacità', integrità' ed onesta' illumineranno sempre la mie strade.

I dedicate this work to my son Francesco, to the love of my life Joanna and to my family. I particularly dedicate this work to †Niccolò Scarnera, my Father. Dad, your tenacity, integrity and honesty will always illuminate my ways.

1 Introduction

In the introduction of this thesis, we review some key concepts related to the technology and physics of HPFLs, namely optical fibre modes, pumping schemes, doping schemes and non-linear effects. The salient applications of HPFLs will follow. Finally, we will describe what motivates our efforts trying to place our work in the complex work of HPFLs design and power scaling.

1.1 The topic area

1.1.1 Optical fibre modes

Any electromagnetic field propagating into an optical fibre can be expressed as a weighted sum of modes. Fibre modes are the eigen-solutions of the Maxwell's wave equation, resolved with opportune boundary conditions in the optical fibre. Generally speaking, we resolve the Helmholtz scalar equation, obtained by separation of the spatial and temporal variables from the Maxwell's wave equation [1]. The electric field of a mode of order γ is represented as:

$$\widetilde{E_\gamma}(x,y,z,t) = E_\gamma(x,y)e^{-i(\omega t-\beta_\gamma z)} \qquad (1.1)$$

Modes depict a transversal distribution of field $E_\gamma(x,y)$ propagating unchanged along the fibre axis (z), with angular frequency $\omega = 2\pi f$ and propagation constants β_γ. The number of guided modes is finite. From a ray optics point of view, modes are the resultant power distribution of rays trapped into the optical fibre. Trapping of the rays is due to the total internal reflection occurring at the interface between the core and the cladding. For this to happen, the index of refraction of the core n_1 must be bigger than that of the cladding n_2. It can be shown that each mode corresponds to a set of rays forming a predefined angle θ_γ with the axis fibre.

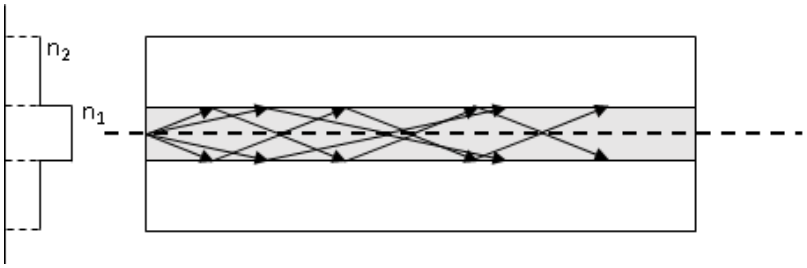

Figure 1. Mechanism of total internal reflection in step optical fibres.

In this view of reflecting rays resides the significance of the effective index of refraction $\mathrm{n}_\gamma^{\mathrm{eff}}$ for a mode. Given the core index of refraction of the core n_c, the propagation constant β_γ for a mode is expressed as:

$$\beta_\gamma = \frac{2\pi}{\lambda}\,\mathrm{n_c}\cos(\theta_\gamma) = \frac{2\pi}{\lambda}\,\mathrm{n}_\gamma^{\mathrm{eff}} \tag{1.2}$$

This defines $\mathrm{n}_\gamma^{\mathrm{eff}} = \mathrm{n_c}\cos(\theta_\gamma)$. The phase velocity of the mode is therefore:

$$\mathrm{v}_\gamma^{\mathrm{p}} = \frac{\omega}{\beta} = \frac{c}{\mathrm{n}_\gamma^{\mathrm{eff}}} \tag{1.3}$$

The higher the order of the mode γ, the higher the inclination of its rays θ_γ. Given a step index fibre, the number of modes guided can be inferred by consulting the normalised dispersion chart.

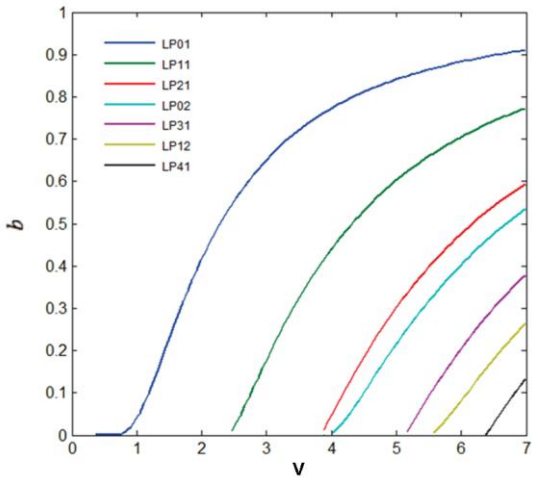

Figure 2. Normalised dispersion curve for a step index optical fibre. Taken from [1]

Figure 2 depicts the so called dispersion curve of a step index fiber. Although in this work we will not use only step index fiber, the consideration made on figure 2, taken from [1] still apply. In figure 2, the x axis is represented by the normalised frequency V, defined as

$$V = \frac{2\pi}{\lambda} r \sqrt{n_1^2 - n_2^2} \qquad (1.4)$$

The quantity $\sqrt{n_1^2 - n_2^2}$ is defined as Numerical Aperture (NA). NA is related to the critical total reflection angle at the interface between core and cladding; this ultimately limits the number of modes guided by the fibre. NA also represents the maximum inclination an incoming ray can have when entering the fibre, to be subsequently guided therein. In (1.4) r is the core radius and λ is the wavelength. In Figure 2, the y-axis, called 'b', is a normalised version of β defined as:

$$b = \frac{n_{eff}^2 - n_2^2}{n_1^2 - n_2^2} \qquad (1.5)$$

When the 'b' parameter for a mode is high, it simple means that n_γ^{eff} is close to n_1 ; in this case the mode propagates for most of the time in the core of the fibre and it is well guided. Viceversa, if 'b' approaches zero, it means that $\mathrm{n}_{\mathrm{eff}}^{\gamma}$ is close to n_2 ; in this case the mode propagates most predominantly outside the core. Finally, if 'b 'equals zero (i.e. the curve does not exist), it just means that mode is no longer guided; its rays are too oblique to undergo total internal reflection, and mode leaks its energy outside the core. From Figure 2, it can be seen that the number of supported modes depends on the value of V. If V is smaller than 2.4048, fibre guides only one mode (SMF) as there is only one curve. It can be shown that bending the fibres perturbs the field distribution of the modes and shifts their 'b' parameter toward zero [2]. Therefore, bending a fibre can be a way to filter out modes.

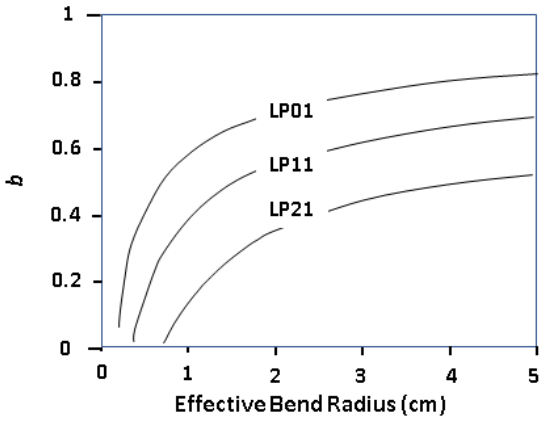

Figure 3. Normalised propagation constant 'b' versus bend radius for a multimode fibre. [inspired by 2]

From Figure 3 it can be seen that the fundamental mode (LP01, in blue) is the most resilient to bends as its 'b' parameter curve is above the other modes (LP11s, LP21s) and that the first modes to be leaked out upon progressive bending will certainly be those with higher order. In this work we will use Active Fibres (AF) with V numbers at least equal to 6, so guiding at least 6 modes or more. The maximum Δn of our fibres is in the order of $2x10^{-3}$. If Δn is small (Δn ~ 10^{-3}), the so called linearly polarised (LP) solutions can be calculated[3]. In this approximation, the polarization of the field lays on the transversal x, y plane of the fibre and does not have any component along the fibre axis z. The appearance of the intensity of the LP modes $|E_Y(x,y)|^2$ is shown in Figure 4. In the LP nomenclature (LP_{lp}), the 'l' number is the azimuthal number and the 'p' number is the radial number. The azimuthal number is the number of axis the modes has around its circumference, whilst the radial number is the number of zeros the mode has along its radius.

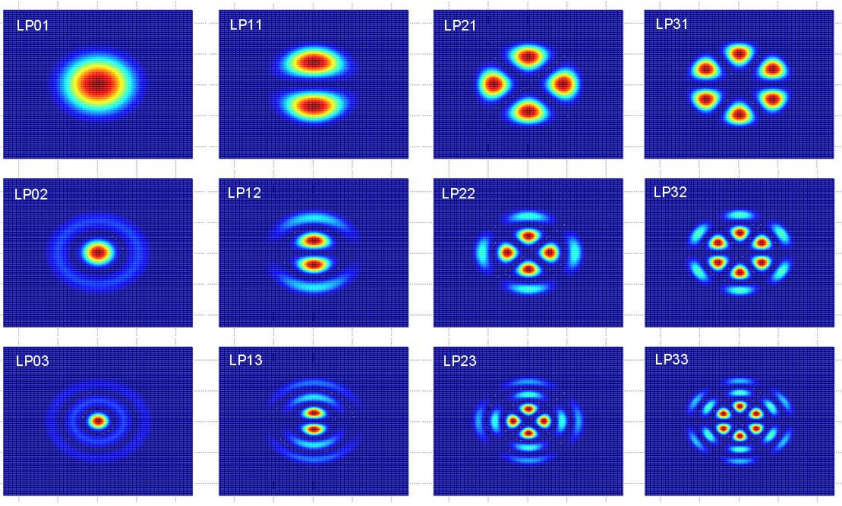

Figure 4. LP modes shape (Intensity) calculated for a generic multimode step index fibre.

1.1.2 Pumping schemes.

In the 1988 E. Snitzer developed a "cladding pump" pumping scheme able to inject efficiently pump light efficiently into fibre lasers [4]. In cladding pumping schemes (Figure 5), low-brightness pump light is launched into a large NA and large size cladding. The so launched pump light propagates into the MM cladding and gets progressively absorbed by interacting with the inner active core. The light generated in the core is guided by a much smaller size and lower NA structure; as a result, the cladding-pumped amplifier or laser output is much brighter and intense than the diodes that pump it. Fibre structured in such way are described in Figure 5 are referred as Double Clad fibers (DCF).

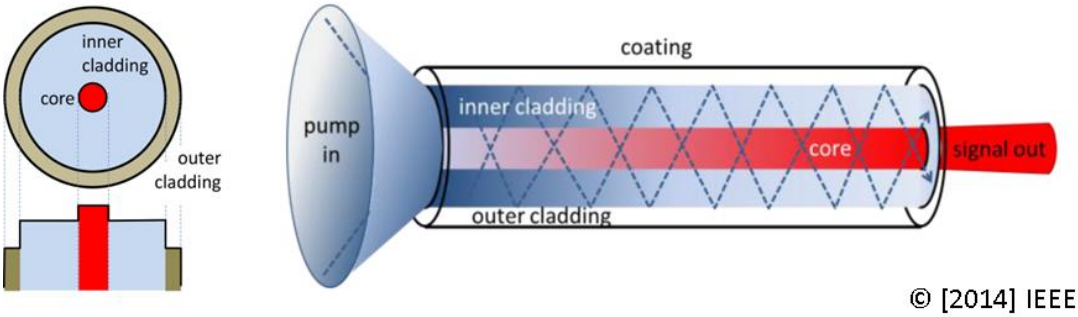

Figure 5. Cladding pumping scheme [taken from 5]

The technique currently used at SPI Lasers to pump the core it somewhat similar to the cladding pump scheme, but here the pump cladding is actually separated from the core (blue fibre in Figure 6). This technique is either called Distributed Side Coupled Cladding-Pump (DSCCP) or Grudinin-Turner Wave GTW [6-8].

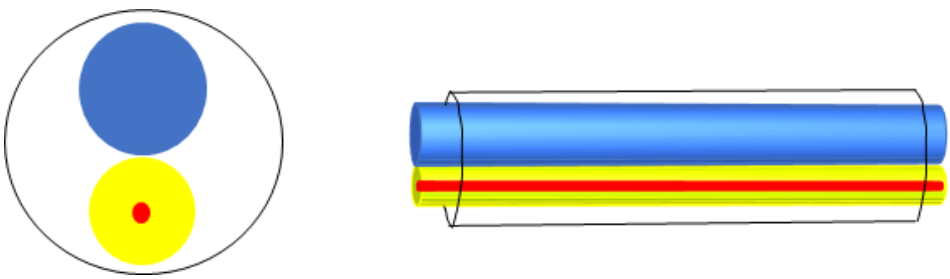

Figure 6. GTW Fibre. Left: GTW Frontal view. Right: Side view.

In GTW technology (Figure 6) , the Pump fibre (in blue) and the Signal fibre (in yellow) are held together by mean of a low index polymeric coating (white part encircling fibers). In GTW technology there could be more than one pump fibre (Figure 7). In some variants of both DC and GTW pumping schemes, fibres claddings can be multifaceted (i.e. AF of Figure 7) or the core can be not located in the exact centre of the fibre; this proves to improve pump absorption [5, 9], that otherwise tends to saturate after a certain fibre length [10].

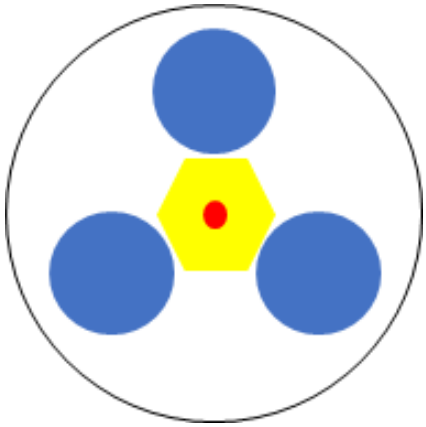

Figure 7. GTW Active fiver with three pump fibres (blue) and octagonal core fibres (yellow) [inspired by 11]

DC and GTW based AF have different ways to be embedded in the laser (see section 1.2.). It can be noticed from now that in DC fibres, one single splice must accommodate for both pump and signal fibres whilst in GTW fibers there are two different kind of splices: one optimised for the pump fibre(s) and one optimised for the signal fibre.

1.1.3 Doping scheme.

In this thesis, we consider CW HPFLs based on Ytterbium as the active dopant for the fibre core. The Yb ions embedded in the silica host have their 4f orbital partially filled that, under the effect of the electric field of the host become split (the Stark effect removes the energy level degeneracy of the states associated with the 4f orbitals). The energy levels of interest of the Yb in silica are depicted in Figure 8 [12]. The states of the ground state manifold $^2F_{7/2}$ are labelled *a,b,c,d* and states of the excited state manifold $^2F_{5/2}$, are labelled

e,f,g. The optical transitions between the individual states of the ground and excited state manifolds are used for lasing. In reality, the energy transitions and respective absorption and emission lines are not discrete because of homogeneous and inhomogeneous broadening in the glass host [13].

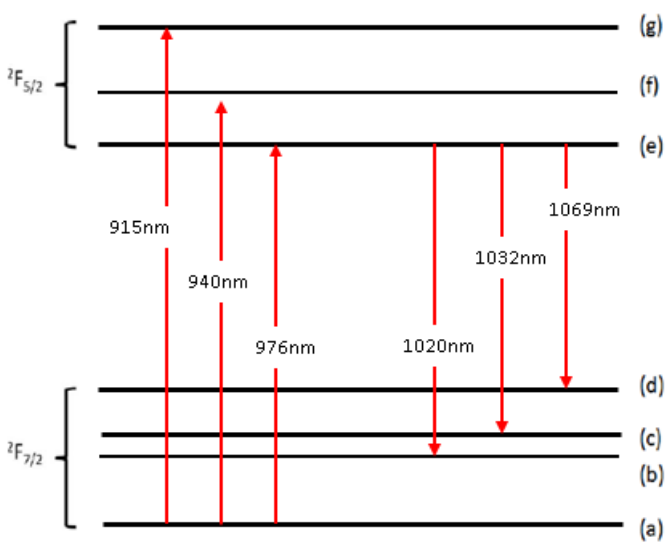

Figure 8. Energy level diagram for Yb ion in silica [as reported in 8]

Typical co-dopants used in AF are alumina and phosphorous. Absorption and emission cross sections are dependent on the host glass [14]. Figure 9 shows the typical emission and absorption cross-sections in aluminosilicate and phosphosilicate fibres [5]. The sharp peak at 975 nm in both the absorption and emission spectra is due to transitions between both lowest levels in the ground state and excited state manifolds, labelled *a* and *e* in Figure 8. The lifetime of this energy level is circa 0.85 ms. The emission peak around 1030 nm is due to transitions from state *e* to the higher states of the ground state *b*, *c* and *d*. In turn these three states decay to the ground state *a* by fast non-radiative transitions. With these transitions, it is possible to have gain at from around 1 μm to 1.2 μm. Pumping at 975nm is a common pumping configuration used with Yb-doped fibre lasers. A broad peak in the absorption spectrum can be also found at around 915 nm with transitions from the ground state *a* to the excited state manifold levels *f* and *g*. In the case of phosphosilicate fibres, the absorption region around 915nm is quite flat and for this reason, it can be preferred in case pump diodes' wavelength is not stabilised. No matter which pumping scheme is used, the signal wavelength must always be longer than the pump wavelength as in the amplification process, pump photons are converted into signal photons of lower energy. This energy difference, known as the *quantum defect*, is acquired

by the phonons of the host and hence converted into heat. Since the refractive index of silica is sensitive to temperature, the heating caused by the quantum effect leads to thermal nonlinear effects. As we will see, in the non-linear effects section, this effect can have a deep impact on the performance of the amplifiers, leading to Transversal Mode Instability.

Compared to other rare-earth dopants, Yb has a relatively small quantum defect and is therefore well suited for high power fibre amplifiers.

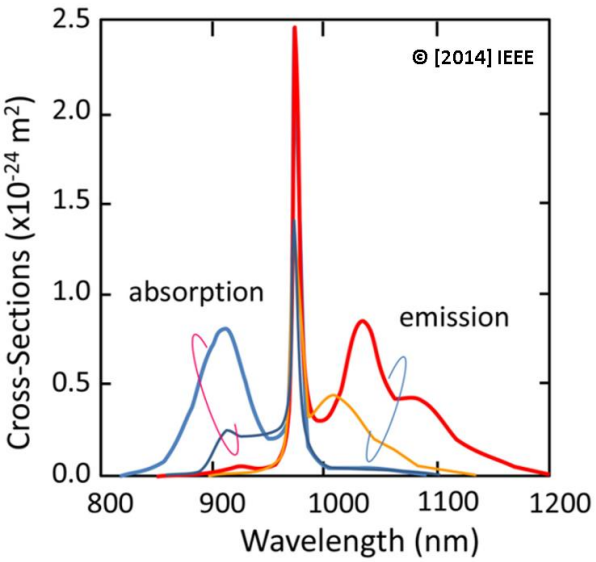

Figure 9. Typical emission and absorption cross-sections in aluminosilicate (thicker lines) and phosphosilicate (thinner lines) fibres (the arrow shows the peak emission and absorption for both type of fibres)[taken from 15]

Aluminosilicate and phosphosilicate hosts were developed to mitigate a light-induced optical loss, affecting HPFLs, known as photo-darkening (PD). The physical origins of PD are still under dispute [16-18]. However, the occurrence of photo-darkening depends on the materials composing the fibre core [19]. The Yb3+ concentration and co-dopants such as aluminium [20, 21], phosphorous [22] or cerium [23] can reduce significantly or even eliminate PD. In this work, we will utilise phosphosilicate fibres.

1.1.4 Non-linear effects in HPFLs

Optical fibre technology allows the achievement of unprecedented beam qualities, thanks to the small core area used and of efficient heat dissipation, thanks to fibre length. However, long fibre length and reduced area size constitute at the same time the main

performance limitation of HPFLs architecture; this is due to the presence of non-linear effects. In this section, we will discuss, with some detail, the non-linear effects that we will encounter in the course of this work, namely: Stimulated Raman Scattering (SRS), Transversal Mode Instability (TMI) and Modal Assisted four Wave Mixing (MAFWM).

The SRS and the Stimulated Brillouin Scattering (SBS) both originated from scattering processes. In these processes, incident beam and glass host exchange energy by means of inelastic scattering. The most likely process is that where the radiation energy is transferred to the glass host in the form of vibration modes. This results in the excitation of phonons and the release of lower energy photons (Stokes process). Host vibrations can also disappear by transferring their energy to the incoming light; creating a photon with higher energy (anti-Stokes process). However, anti-stokes processes are thermodynamically less favoured.

For the SRS, we have excitation of optical phonons, whose vibration modes tend to oscillate symmetrically around a centre of mass without creating any wave, so without transporting acoustic energy. The re-emitted energy reduced- photons have a spectral shift of about 13 THz. From a quantum mechanics point of view, SRS emission can be associated with the existence of a virtual quantum level of energy. This level has a gain and it is accountable for stimulated emission; at its shifted wavelength. If the medium is pumped hard enough, due to stimulated emission, the SRS energy level will produce an increasing number of photons at the shifted wavelength. This process will be at the expense of the pump, which in this case is the incoming light. The SRS threshold $P_o^{cr}$is defined by calculating in which situation the incident light power becomes equal to the generated forward propagating SRS power[24].

$$P_o^{cr} = 16\,\frac{A_{eff}}{g_r L_{eff}} \qquad (1.6)$$

Where g_r is the Raman gain at the peak, P_o^{cr} is the critical incident power, A_{eff} is the effective area of the fibre and L_{eff} is the effective length of the fibre. A_{eff} and L_{eff} both influence the HPFLs design. In order to increase the critical incident power, that is the critical power inside a fibre laser, the only solutions are either to increase A_{eff}, working

with bigger cores or to decrease L_{eff} , working with shorter fibres. SRS power in a laser cavity must be minimised. In fact, the presence of any spurious reflection at the SRS wavelength could make SRS photons reach threshold and lase. Presence of an SRS cavity, coexisting with the primary cavity would be detrimental, as laser output stability would be affected negatively. This will be shown in the last chapter of this thesis.

In SBS, the vibrations of the host oscillate asymmetrically around their centre of mass and can collectively create acoustic waves propagating along the fibre axis. These acoustic waves are kept alive by the coherence of the incoming light; it can be proved that the photons produced by SBS only propagate backward. Acoustic waves can be so strong to damage the optical fibre [5]. SBS is not a major limitation for the laser of this work as this SBS becomes dominant over SRS only if the radiation is coherent, with a bandwidth BW < 0.1 GHz. As we will see the bandwidth of our lasers are in the order of the 10 nm or even more.

Transverse mode instability (TMI) is a recently observed nonlinearity [25] proving to be a major power-scaling limitation in high-power fibre lasers and amplifiers [26-28]. TMI provokes a sudden output beam break-up and beam-quality degradation above a certain output power threshold. TMI is widely attributed to a refractive index (RI) grating formation due to transverse mode beating and coupling between the fundamental mode (FM) and high order modes (HOM) [28-35].

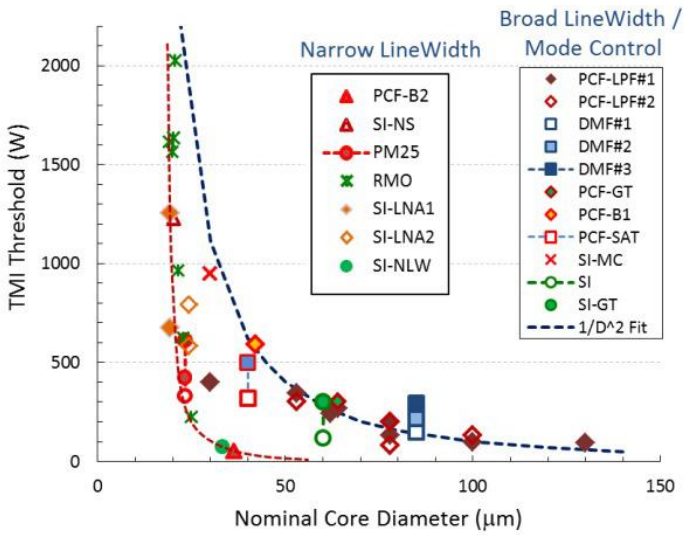

Figure 10. Empirically characterised TMI threshold in various works [taken from 36]

Empirically, as shown in Figure 10, TMI threshold decreases with core diameter and it is more severe in case of coherent signals [36]. In a recent work, a stability analysis in the presence of thermal and inversion-related effects has been performed, showing that the amplification process of the FM in multimode fibres is fundamentally unstable above a signal power threshold [27, 36]. The derived TMI power threshold formula of [27, 36] is:

$$P_{TMI} = \frac{kU_{11}^2(U_{11}^2 - U_{01}^2)}{2\pi\ n_{eff}\ \frac{\eta_{heat}}{\eta_{laser}}\ \frac{dn}{dT}} \left(\frac{\lambda_0}{d_0}\right)^2 L \qquad (1.7)$$

Where U11 and U01 are the transverse wavenumbers of the perturbation (LP11 mode) and fundamental LP01 mode (FM), respectively, κ is the silica thermal conductivity; (dn/dT) is the thermo-optic coefficient and n_{eff} is the FM effective index. λ_0 is the signal wavelength and d_0 is the core diameter. η_{heat} is the quantum defect and η_{laser} is the slope efficiency. For $P \geq P_{TMI}$ the amplification process becomes unstable, leading to TMI. Another non-linear effect thought to be a limitation for HPFLs is Thermal Lensing (TL). The formula for the TL threshold in [37] is comparable with that derived for the TMI in [38], however TMI threshold is systematically lower [39], revealing to be the real limitation in HPFL power scaling. Furthermore, TL threshold is defined as the power for which, due to thermo-optic effect, the effective area of the fundamental mode become 80% of when the fibre is at room temperature, without proving that this is the real cause of instability. For these reasons, the concept of TL as a limiting effect in HPFLs power scaling is now out of use. The TMI threshold fits well the data reported in the literature and provides useful information about HPFLs design. First of all: small cores and long fibres both increase the TMI threshold. This conflicts with the need of working with big cores and short fibres to avoid SRS. Secondly, if the quantum defect η_{heat} approaches zero, the TMI threshold diverges: this can only be practically obtained in tandem pumping configurations [40, 41].

Another non-linear process occurring in HPFLs and MOPAs is the Modal Assisted Four Wave Mixing (MAFWM). The process of FWM is a direct consequence of the polarizability of silica[24]. More specifically, the amorphous silica host has a centrosymmetric potential, null second order susceptibility, but a small third order susceptibility. The third order susceptibility ($\chi^{(3)}$) is mathematically represented by a 4th rank tensor (81 operator elements) that depends on both time and space.

$$\vec{P}_{NL} = \varepsilon_0 \chi^{(3)} \vdots \vec{E}\vec{E}\vec{E} \qquad (1.8)$$

Under the approximation of localised nature of the interaction and instantaneous wave-matter interaction, and far away from resonances, third order susceptibility tensor in silica reduces to a scalar number. The non-linear polarizability $P_{NL}(\omega)$ response to a field $E(r,t) = Ee^{i(\omega t - \beta z)}$, will be

$$P_{NL} = \varepsilon_0 \frac{1}{3} \chi^3_{1111} E^3 e^{i3(\omega t - \beta z)} \qquad (1.9)$$

The non-linear polarizability P_{NL} oscillates at 3ω and has propagation constant 3β. Without loss of generality, we can imagine a single transversal mode field composed by a subset of 4 wavelengths.

$$E(r,t) = E_1 e^{i(\omega_1 t - \beta_1 z)} + E_1 e^{i(\omega_2 t - \beta_2 z)} + E_1 e^{i(\omega_3 t - \beta_3 z)} + E_1 e^{i(\omega_4 t - \beta_4 z)} + \text{c.c.} \qquad (1.10)$$

Here $\beta_x = \beta(\omega_x)$, depends on wavelength, but the transversal mode is one and common to all four wavelengths; this is the case of a SM fibre. As result, the non-linear polarizability associated with this incoming field will be a very complicated cube of a quadrinomial, including numerous terms. Particularly, there will be a term of this type:

$$P_{NL}(\omega_4) = \frac{3\varepsilon_0}{4} \chi^3_{1111} |E_4|^2 E_4 + 2(|E_1|^2 + |E_2|^2 + |E_3|^2) E_4 + 2E_1 E_2 E_3 e^{i\theta_+} + 2E_1 E_2 E_3^* e^{i\theta_-} \qquad (1.11)$$

With

$$\theta_+ = (\beta_1 + \beta_2 + \beta_3 - \beta_4)z - (\omega_1 + \omega_2 + \omega_3 - \omega_4)t \qquad (1.12)$$

And

$$\theta_- = (\beta_1 + \beta_2 - \beta_3 - \beta_4)z - (\omega_1 + \omega_2 - \omega_3 - \omega_4)t \qquad (1.13)$$

It can be demonstrated that if θ_+ or θ_- are null, then the non-linear interaction between waves will produce a field oscillating at $\omega_4 = \omega_1 + \omega_2 + \omega_3$. This condition is called the phase matching condition. In this condition, the new produced wave has the same speed, frequency and propagation constant of the polarizability that produces it. For SM fibres, phase matching condition is achievable only in θ_- and in the case degenerate case where $\omega_1 = \omega_2$. In that case, two photons of the main peak annihilate, producing two other photons (stokes and anti-stokes peaks). In case of MM fibres, the spectral component of the field in equation (1.10) may well be associated to different transversal modes. In that case phase matching can be possible achieved in many other ways in both θ_+ and θ_- [42], we refer to this mechanism as Modal Assisted Four Wave Mixing (MAFWM).

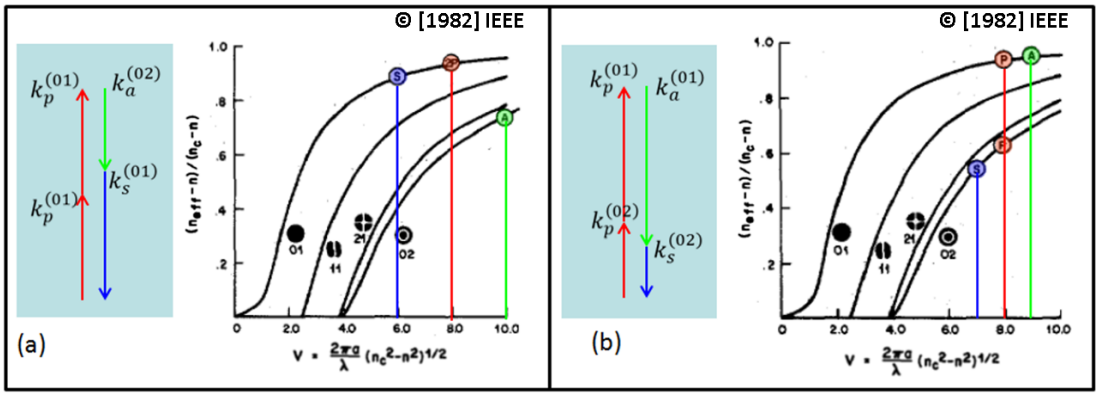

Figure 11. MAFWM as reported in [taken from 42]

In Figure 11(left) two pump photons at the same wavelength and both guided by the LP01 produce two photons at different wavelength guided by different transversal modes; LP01 and LP02. In Figure 8 (right), two pump photons at the same wavelength one guided by LP01 and one by LP02, produce two photons at different wavelengths and guided by different transversal modes. In [43] it was shown how that the broadening produced by the MAFWM can be bigger than that provoked by SRS. This effect clearly impacts on the design of HPFLs, as if the core is not properly designed, the advantage of having reduced the SRS by adopting a MM fibre, could be degraded by the occurrence of massive broadening due to MAFWM, occurrence HOM coupling and possibly TMI.

1.1.5 Applications

Laser technology can process many materials, such as plastics, metals and wood and allows processing of dissimilar materials (for instance, welding of different metals). Increasing of the average power of such tools allows performing the above-mentioned applications at higher speeds. During the last twenty-five years, gas lasers such as CO_2 lasers utilised in the steel industry, have been progressively substituted with more efficient solid state Yb fibre lasers[44]. Several advantages distinguish fibre lasers from CO_2 lasers; these include more compactness, zero maintenance, higher wall plug efficiency and higher brightness [5, 45]. The applications of HPFLs are numerous: 2D cutting, welding, additive manufacturing, precise machining, paint and rust removal and marking to name a few [46-49]. In cutting, the high brightness and optimised beam profile of HPFLs produce neat borders; most of the time these borders do not need any further processing. Commercial kW class HPFLs can cut metal sheet of thickness up to 25mm. The variety of metals that can be cut is quite vast: copper, brass and aluminium to name a few. Some materials have very high reflectivity (e.g. copper) and can destabilise HPFLs due to back reflections. To prevent such drawbacks, intelligent light probes, hardware logic and fine optical engineering have been developed; in this way laser manufacturers can add further value to the build systems, ensuring laser stability in any reflectivity condition. Other advanced features implemented are the measurement of the piercing time and the embedded measurement of the distance from the work piece [50]. The presence of these features differentiates the laser market; these features are often defined as Unique Selling Points (USP). The following

picture illustrates the performances of kW seeds and incoherently combined multi kW systems in terms of cutting at various powers.

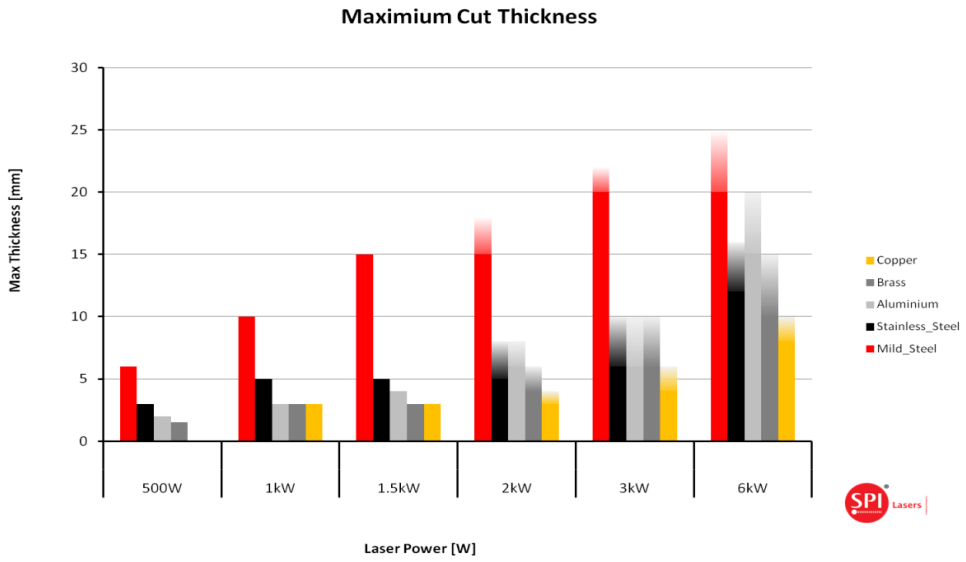

Figure 12. Cutting thickness for various metals at different power levels [Courtesy of SPI Lasers]. Above 2kW, laser beams are here obtained combining incoherently multiple seeds.

In Figure 12, it is possible to spot that, higher power allows cutting higher thickness. At any power, materials with higher/lower reflectivity (i.e. copper/steel), result in smaller/bigger cutting thickness. On top of that, at high power and with thick metal sheets, cut quality starts to degrade. This is partly due to the excessive quantity of melt involved in the process (this disturbs the light-material interaction) and partly because very high powers in commercial lasers is achieved combining incoherently several lasers (combining lasers incoherently worsens beam quality). As per the welding, HPFLs have net advantages compared to other techniques. Advantages include versatility and speed. Versatility is given by the long reaching action of the beam; light delivery can be far from the work piece (e.g. remote welding). One of the most important advantages compared to classic welding techniques is the reduced amount of thermal distortion. In fact, given the small beam size and the high intensity of the interaction, the heat laid on the work piece is quite low and the altered part is very confined. This is very important in presence of dissimilar material in electronic devices, where the thermal contraction of the weld part should not affect the surrounding dissimilar parts. On the other hand, welding can be intentionally made between dissimilar materials[51]. Generally speaking , welding does not require the same beam size and quality needed for cutting, however, also single mode lasers can be adopted to weld by utilising the so-called wobble welding [52, 53]. HPFL are also the favourite choice to implement additive manufacturing [54, 55]. This is substantially due to the

stability of the laser and in the granularity with which power can be delivered on the various powders (stainless steel, titanium, gold etc). Clearly, also in this case fine engineering is required to ensure protection from back reflections, fine beam positioning at high speed and great positioning reproducibility. The capability of switching the beam profile instantly, during any of the processes above listed, is of pivotal importance and it is gaining increasingly more interest [56]. Several laser manufacturers are including the possibility of beam morphing as added capability; this makes all the process faster as switching beam property (e.g. size and shape) would ideally allow the user to carry on working without changing the delivery optics, hence saving time and increasing productivity. To contextualise better the role of HPFLs we report a chart from [1], showing the applications of various HPFLs as function of their beam quality, expressed with the beam parameter product (BPP = $\omega_0\theta_0$) and power (Figure 13.)

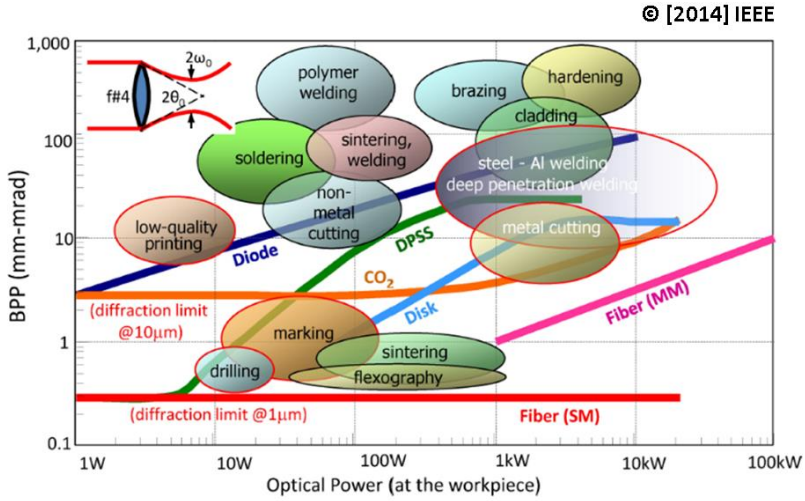

Figure 13. Summary of lasers applications [taken from 1]

In Figure 13, the various applications occupy a certain range in the BPP and power domain. The applications shown are substantially based on thermal processes (heating, melting and vaporization) and based on lasers operating predominantly in CW or relatively long pulse mode. Another class of lasers that have become increasingly used in the industry are the so call ultra-fast lasers. The high peak power of femtosecond lasers, for instance, allows the 3D printing inside transparent materials by mean of nonlinear processed (e.g. multiphoton absorption).

1.2 The motivation

In the arena of CW Yb HPFLs, average power has increased from 10W in the 1995 to 100kW in the year 2014[1]. The Electro Optical efficiency, which is prerogative of HPFLs, is very important from energy consumption and pollution prospective, the stability factor is important to obtain repeatable results on the work piece. Good efficiency and stability need to be achieved together. Non-linear effects must be kept under control to avoid unreliable behaviour of the laser: for instance, it is not easy to make arbitrarily long delivery fibres, conserve beam quality, have kilo-Watt level powers and not incur in non-linear effects. The design of a SM HPFL is an arduous task as many technological and fundamental limitations, very interrelated between them, need to be resolved before realising arbitrarily powerful and stable systems. Without claiming to be exhaustive, the following image attempts to describe the correlations between fundamental limitations and the design parameter of a SM HPFL. In Figure 14, the design parameters of a HPFL (in lower case) are surrounded from top and bottom by physical limitations / unwanted effects (In Upper Case). The origin of all issues in SM HPFLs power scaling is at the top of the chart, in Italic fonts.

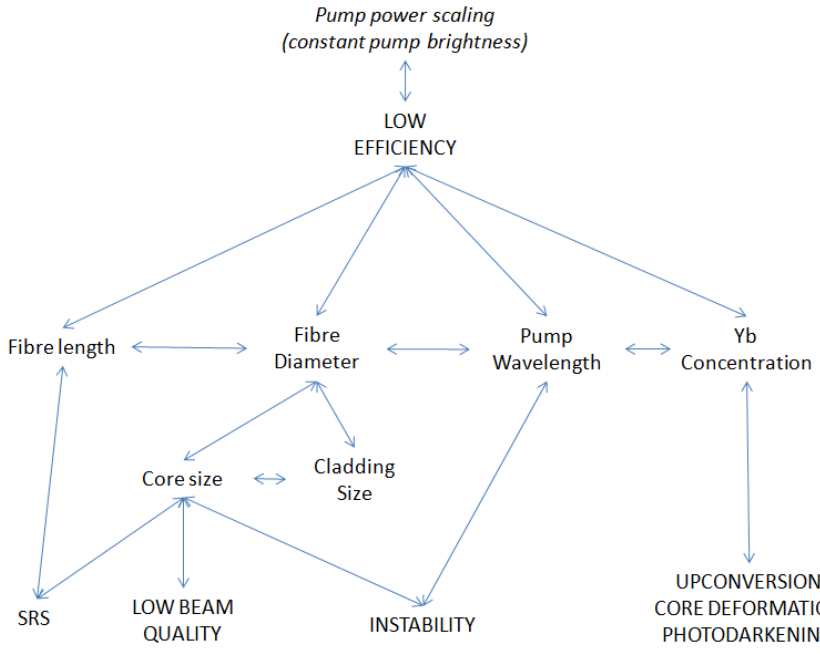

Figure 14. Correlation between fundamental limitation and design parameter in the design of HPFLs.

Achieving increasingly higher output power from a low moded oscillator implies achieving increasingly higher brightness. However big, the brightness enhancement factor

of a laser is a finite number; therefore, the laser's output brightness will always be directly correlated with the pump brightness. Diodes' technology and their brightness have evolved during the past two decades, increasing from 20mW/um^2/ste in the year 2008 to 200mW/um^2/ste in the year 2018[27, 37]. Nonetheless, at any defined technologic era for the diodes, brightness can be considered as a fundamental limit in HPFLs brightness scaling. The entry "Pump power scaling, with constant brightness", in Italic font, is placed on the top of this chart to represent the fundamental limit in SM HPFLs power scaling. In commercial HPFLs, pump power scaling is achieved by combining incoherently the power of several diodes thought High Power Combiners (HPC). Due to brightness conservation, when combining diodes, the bigger the number of pump diodes, the bigger the fibre size at the output of the HPC. The HPC output fibre is then spliced to the size matching pump cladding of the AF.

For the AF there are two main technologies, namely GTW [6] and double clad fibres (DC) [57]. In both technologies, the relative size of the pump cladding and core diameter affects the pump absorption. When scaling up the pump power, not only we have to increase the HPC fibre size, but also the matching AF pump cladding attached to it. If the other design parameter of the AF are not opportunely adapted, scaling up the pump power without increasing the brightness, results immediately in low absorption and therefore low efficiency. For this reason, the low efficiency label in Figure 14 is annexed in the fundamental limitations. To recover absorption and efficiency we can substantially alter the AF length, the core size, the pump wavelength and the Yb concentration. The AF's length cannot be arbitrarily long, as eventually SRS lasing will occur in the cavity; this would in turn destabilise the laser. Increasing the core size will intrinsically deteriorate the beam quality and expose the laser to Transversal Mode Instability (TMI)[33]. Likewise, increasing Yb concentration above certain values becomes unpractical due to the arising of PD[20], broken cores and irregular IOR [58]. Broken cores imply lack of rotational symmetry for the fibre's IOR with consequent loss of power and stability (this aspect will be clarified later). Choosing a pump wavelength resonant with the sharp Yb absorption (e.g. at 975nm) increases greatly the pump absorption, however, the wavelength must be stabilised at any pump power and external temperatures to prevent sudden variation of the absorption and therefore efficiency. Utilising wavelengths increasingly close to 975nm has proven to create problems of stability [59, 60]. According to [37], the maximum power extractable by a broadband fibre laser (SRS dominates over SBS) is of 36kW. The theoretical limit in [15] is obtained by increasing the core area to capture more pump light and increasing the fibre

length to preserve a 20dB of pump absorption. A balance of SRS and TL dictates such limit. Subsequently, power scalability has been reduced to 27kW acknowledging that TMI is the real effect related to instability, rather than TI [16]. Further scalability can be accomplished by removing the limit assumed at the very beginning of this chapter, which is the limit on the brightness. In Tandem Pumping (TP) configurations [41, 61], Yb fibre lasers (wavelength ~ 1060nm) are used to pump Yb laser. In TP, the lack of spectral absorption at 1060nm is entirely compensated by the high brightens of the laser source used as pump, allowing the usage of little cores and longer AF, yet achieving enough absorption. Overall tandem pumped HPFLs are less prone to SRS and have also intrinsically lower quantum defect (more quantum efficiency). The low quantum defect of TP increases the TMI threshold [36] and allows, at least theoretically to increase the theoretical power scaling limit up to 52kW.

Most HPFLs adopt DCF [62-64] with pump combiners placed outside the cavity (Figure 15). In these configurations, pump light reaches the active medium passing across the gratings. The output combiner has a dedicated fibre to bring the signal's light out of the system [65-67]. The AFs and the passive fibres of such systems are usually few moded, but matched. The typical AFs used for these configurations are similar or coinciding with the commercially available "Nufern LMA matched" series (with typical NA =0.06, and cores ranging from 20 μm to 30 μm) [68]. A common approach, to reduce modality in presence of big effective areas, proven to mitigate TMI is to coil the fibres appropriately; in such way High Order Modes (HOM) are filtered [69, 70].

Figure 15. HPFLs with DCF and combiners placed outside the gratings[taken from 5] .

Conversely, other lasers manufacturers such as IPG and SPI Lasers use GTW technology [71]. In GTW, pump light is injected from the side of the active medium and light exits the oscillator without having to pass through the combiner (Figure 16).

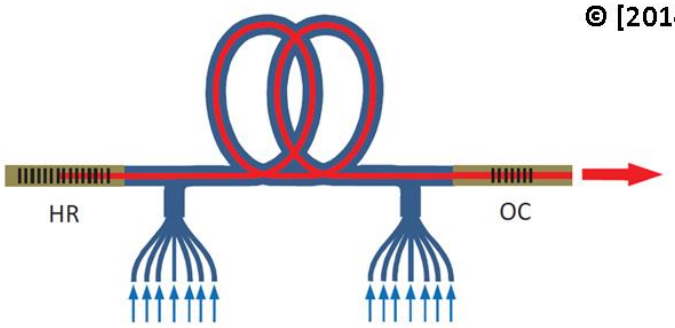

Figure 16. HPFLs with GTW fibres. In this case gratings are placed outside the cavity [taken from 5].

SPI use few modes active cores as well, but modality is filtered by splicing the MM active medium to SM fibres [72], rather than by coiling the fibres. In GTW with SM used fibre as modal filters, SM output is intrinsically guaranteed. In DCF schemes the output is not necessarily SM as coiling can filter HOMs, but at the same time can also re-couple them[73], with potential degradation of the output beam quality. GTW technology allows more flexibility when it comes to splicing as the pump and the signal splices can be optimised separately. The pump combining scheme is simpler in GTW than in DCF as GTW does not require a dedicated pass-through fibre for the signal in the HPC. GTW scheme is also convenient as pump light does not pass through the gratings, like in the DCF scheme, exposing the gratings to less thermal strain. From a theoretical study, it has been concluded that DCF and GTW schemes can achieve the same laser efficiency [8]. SPI lasers produce and use active LMA fibres as AF [74]. Splicing SM fibres to active MM fibre is not a trivial task when the target of the splice is that of minimising the HOM excitation in the MM fibre. As it will also be clarified later, HOM excitation in HPFLs leads to instability and reduces the efficiency of the laser [75, 76], therefore splicing reliability and optimisation proves to be crucial for the high volume production HPFLs. To deliver high power, the output of several oscillators is combined incoherently. This 'n' combination of multiple lasers, on top of degrading the beam quality, leads to the requirement of multiplying, accordingly to 'n', all components of the single lasers (pump combiners, fibres, gratings, etc). If only a single oscillator could deliver all the required power, this would result in a massive manufacturing saving; this makes the realisation of increasing higher powers out of a single oscillator of our interest.

Various R&D groups and leading manufacturers around the world have for years kept breaking records in terms of power extracted from single oscillators, MOPAs, combined lasers, finding out new ways of mitigating unwanted effects such as SBS, SRS and TMI. We can distinguish two types of oscillators, namely: narrow bandwidth and large bandwidth. Narrow bandwidth lasers find application in coherent beam combination [77, 78] and non-linear frequency generation [79] and have as a main limitation their low SBS threshold. Coherent combination has the potential of adding up the power of several lasers and keeps the beam quality as high as that of a single laser. Power scaling of narrow bandwidth systems embraces several mitigation techniques including, modulation of the seed, adoption of two tones for the amplifier and inducing strains in the AF, have all been demonstrated to work [80-82]. Broad band fibre lasers are used in various applications where there is no requirement of coherence and polarisation such as cutting and welding. In Figure 17, we can see the evolution of high power systems from the 1993 to the year 2014, including incoherently combined systems (MM), single mode diode pumped oscillator (SM – DP), single mode MOPAs tandem pumped MOPA (SM-TP) and coherently combined systems (CBC).

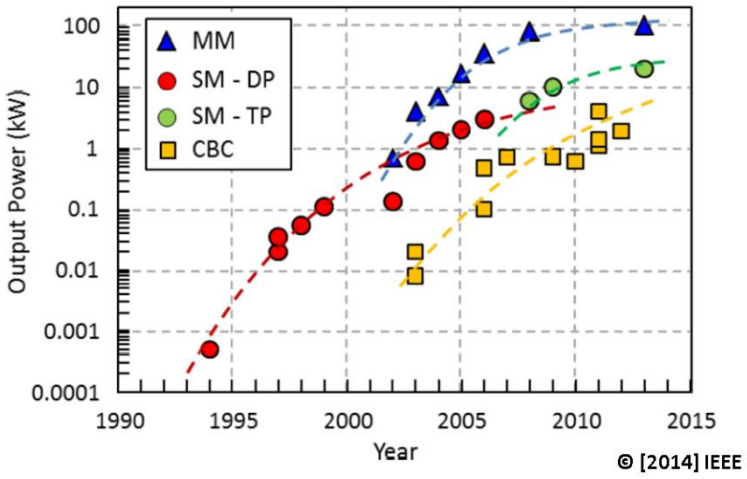

Figure 17. Power scaling of high power fibre lasers[taken from 5]

Currently, the maximum power for SM-DP lasers is in the order of 5kW, reported by FUJIKURA [83], further power scaling up 20kW has been obtained by IPG adopting tandem pumping [83, 84]. On the other hand, if a pure beam quality is not necessary, MM incoherent combining can provide an easy way to scale the power; IPG already reported 100kW in 2014 [85]. In SPI, the author of this thesis has personally experienced an increase

of power from 250W in the year 2011 to 2.4kW in the year 2018 (with 10 meters of SM delivery fibre), out a SM oscillator and an increase of power from 500W to 3500W (with 7 meters of SM delivery fibre) in the case of SM MOPA. From a construction point of view, HPFLs consist of several optical components such as high power laser diodes, high power combiners, AF, gratings, mode-strippers, and delivery fibres. Correspondently the choice and design of the construction parameters is vast and includes pump wavelength, pump brightness, pump combining architecture, index of refraction profiles, doping concentrations, fibre lengths, fibre concentricity, gratings' peak wavelength and strength, appropriate coiling and routing of the fibres and up-tapered zones for the beam delivery section. The motivation behind this work is to discover methodologies to deploy high power HPFLs on a vast scale; this involves the reliable achievement of top performances, at an industrial level; therefore, with a very high First Pass Yield (FPY). Specifically, we will focus our attention on the methodology of splice optimisation between dissimilar fibres. Understanding SM-MM splicing inside the laser cavity is of paramount importance in achieving high optical / optical efficiency, stability and good first pass yield during the fabrication process.

1.3 Layout of the thesis

In chapter 1 we reviewed the topic of HPFLs and their applications. In the review, we emphasise the parts of this vast topic that most overlap with this work. In chapter 2 we revisit the splice concept as it was conceived in the telecom industry and anticipate the need of thinking about splices in a more exhaustive way. In chapter 2, we introduce the tools developed to study and optimise splices and the tools developed to verify the splices' repercussion on the laser's performance, during high power operation. In chapter 3 we describe the advances we made in the splicing technology. We introduce the fibres used in the thesis and we explain with a simple model how dopants' diffusion and Index Of Refraction (IOR) alteration works. After introducing some immediate application of the S^2, we present a less immediate application of the S^2: its usage in splice optimisation. S^2 usage for splice optimisation is *per se* a novelty. The remaining part of chapter 3 is focused on splice optimisation and can be divided in two sections: the empirical and the theoretical. The two sections are very interrelated since measured phenomena on the sample produced (in paragraph 3.3), are subsequently analysed theoretically (in paragraph 3.4).

We derive a principle to have pure SM excitation in a MM fibre that, besides constituting novelty, has the basis to nullify the claims of a patent. In chapter 4, we present an innovation in terms of HPFLs characterisation: the vertical probing technique. With the technique, we demonstrate the ability of measuring, in real time and along the laser length, quantities such as: absorbed pump power, inversion, signal power and non-linear effects. The technique is non-destructive and never reported before. In chapter 5 we characterise the HPFLs' functioning. We initially describe the generic structure of an SPI HPFLs and we give details about the testing methodology adopted with the developed high power test-kit. Three classes of lasers are presented by means of the testing of three typical lasers, one representative for each class. Testing of the first laser will highlight the problems encountered with the old technology, adopted prior to 2017. Thanks to the usage of the high power test-kit, we determined that the cardinal problem affecting the old technology was the presence of a parasitic HOM cavity, cause of TMI. The study of this laser constituted the basis for the conference paper presented at CLEO 2017 and for a journal publication in Jan 2019. In the second laser, we show how the concept developed for splicing in chapter 2, are related to laser performance and are used to maximise optical to optical efficiency. The testing of the third laser, built by adopting all the understandings gathered in this thesis, results in the most efficiency CW HPFLs developed at SPI. The output power of the third laser is limited by SRS, rather than by TMI. In the conclusions of the thesis, we retrace the advances made in this work and propose future works in both the field of splice optimisation and HPFLs testing. At the end of the conclusions chapter, we make a list of the concepts, tools and volume manufacturing methodologies developed in this thesis and constituting nowadays core technology at SPI Lasers.

2 Background and tools developed.

Splicing technology development started at the beginning of the 80s for SM fibres, with the advent of optical communications [86]. Nowadays splicing technology is evolving to assist the development of high-power systems where usage of MM Large Mode Area (LMA) fibres has become increasingly popular. Vendors such as Fujikura, Furukawa, 3SAE are developing systems that help with the technological advance of multi-core structures, high power combiners and tapers[87].

2.1 Review of prior art

One of the most comprehensive works for fibre splicing can be found in the book written by Yablon in 2005[88]. In the book, fibre splicing technology is described in terms of fibre preparation (e.g. cleaving and stripping), mechanisms associated with the fusion (e.g. heat transport and dopant diffusion), optics of the splice (e.g. splice loss, reflection) and stress related effects. The optical behaviour of the splice is described extensively for SM-SM splice and briefly for SM-MM splices. As in many other papers written in the period of the telecom boom and after [70, 89-91], the figure of merit for splices refers to the Fundamental Mode (FM). Loss between fibres is calculated, in proximity of the splicing point, as a local overlap integral between the FMs of the two fibres.

$$IL(dB) = -10Log\left|\iint_{\Omega} \psi_1 * \psi_2 \, d\Omega\right|^2 \qquad (2.1.1)$$

Here, in formula (2.1.1), $\psi_{1,2}$ are the normalised fields associated with the FMs of the two spliced fibres and the integration domain Ω is the transversal section of the fibres. This formula was quite appropriate for the times as most of the fibres were SM, based on few dopants and not prone to diffusion upon arc discharge. In the absence of dopants diffusion during the splice a formula describing the sole contact's point was sufficient, even in case of SM-MM modes[90]. As we will see in Chapter 3, dopants diffusion make a splice behave like a taper, so the simple formula (2.1.1) no longer applies. On the other hand, however,

the behaviour of tapered areas and bifurcation of optical paths in planar waveguide was described theoretically since 1975 [92]. In the field of planar waveguide, in [93] a very handy recursive formula was derived allowing the calculation of the power of each mode as they propagate in the taper, in this work we have revisited this theory and applied it to optical fibres. Other ways of calculating modal evolution in tapers are based on coupled equations [42]. Various models and approximations have been attempted to describe fibre optics based tapers with the aim of calculating a close formula and establish in which condition the taper does not induce a loss on the fundamental mode [94, 95] . Many of these papers insist on the fact that, if the taper's transition is not too abrupt, there is negligible loss for the FM (e.g. negligible coupling toward the HOMs). A taper that does not couple HOM is usually referred as an adiabatic taper [42, 89]. To reduce the modality of our HPFLs, we make use of SM fibres and diffusing LMA fibres, spliced together, to form a SM-MM joint. We announce that the formula (2.1.1) is not able to describe SM-MM splices in presence of dopant diffusion, as it does not take into consideration the tapered nature of such splices.

To the author's knowledge, the first attempt to describe the mechanism of field propagation in a SM-MM diffused region can be found in the work of [96]. In [96], Luo simulated the diffusion of a MM fibre in a SM-MM joint, demonstrating, not only that a precise level of diffusion leads to optimal splicing, but also that that light de-phasing plays an important role in the optimisation splicing process as well. The results of simulation work in [96] are the closest we have found in the literature to the results we present in this work. Differently from [96], our work is both theoretical and empirical and reveals some general principles in the design of a SM-MM splices.

Image processing for HOM excitation has in the past been used for the characterisation of tapers. For instance, already in the year 1999 [97], to validate the mode coupling theory in tapers, a down tapered area was progressively cut back with its outgoing field imaged on a CCD camera. Imaging obtained at any taper length was then fitted to reconstruct the modal content evolution across the taper length and to validate mode coupling theory. Modal reconstruction in [97] and in other papers of that period [98] were based on *a priori* knowledge of the modal shape and fitting was made using incoherent superimposition of modes. It is easy to imagine how, these sort of fittings, especially if modes involved are numerous and phase is used, can lead to ambiguous, non-univocal fittings. Subsequently, in the year 2008, the S^2 measurement was proposed and demonstrated [99, 100]. The S^2 measurement is based on both spatial and spectral

measurements. The advantage of the S^2 theory is that it allows modal reconstruction in terms of image and power, without having any *a priori* information about the modal shape or supposed presence. After few years from its initial development the S^2 technique was improved in the sense that the acquisition speed became one order of magnitude faster (thanks to the usage of CCD cameras) and much easier to set up [101]. S^2 can be used to detect localised scattering, but also distributed scattering [102] and micro-bending [103]. In this work, we have developed our own fast S^2 measurement kit (hardware and software) and used it to develop our HPFLs splicing technology. The speed of the S^2 measurement makes the characterisation time compatible with the splice duration allowing us to use the S^2 whilst materially conducting the splicing process. As per the state of the art, it is worth mentioning that Convolutional Neural Networks (CNN) have been trained to recognise the modal content of beams. With these ultimate techniques based on artificial intelligence (AI) modal content and shapes can be evaluated in presence of 10 eigenmodes at the speed of hundreds of Hertz [104]. However, also in the CNN based techniques, modal shape must be known *a priori* as part of the CNN training. In general, therefore, CNN must be trained for each different fibre under test. The S^2, as it will be detailed shown in the (paragraph 2.2.2) can reconstruct the modal shape and power without any information about the fibre, making this technique the most suitable for this work as it is capable to process seamlessly any kind of fibre.

2.2 Test-kit and techniques adopted and developed.

2.2.1 IFA-100

This instrument is developed by Interfibre Analysis and it is capable of measuring the IOR of fibres via transversal interferometry [105-108]. The IOR measurements can be 1D or 2D.

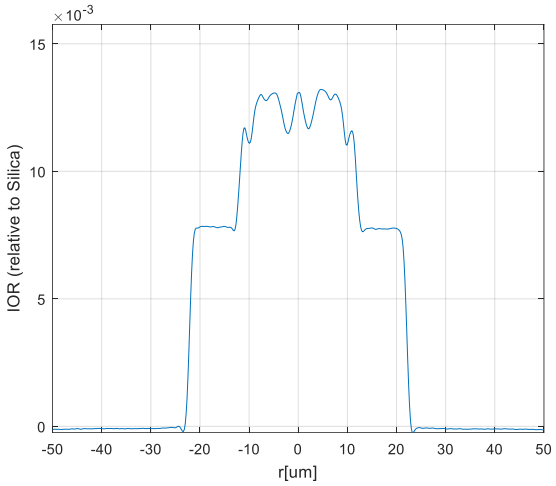

Figure 18. IFA: 1D measurement of a typical SPI LMA fibre

Since cores are never exactly centrosymmetric (intended as rotational symmetry), the 1D IOR measurements can vary with the position of the fibre at the moment of the acquisition. A 1D measurement, excluding fibre positioning, takes about one minute.

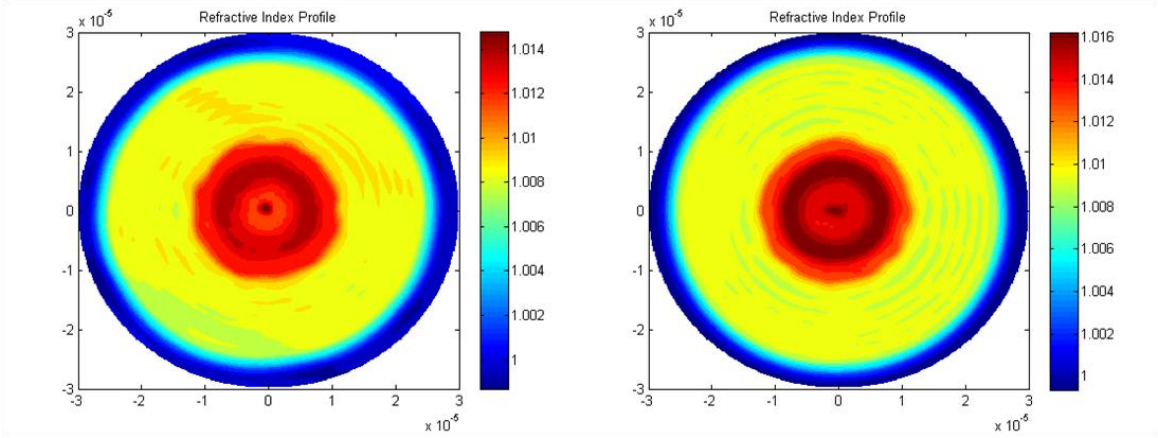

Figure 19. IFA: 2D measurement of typical SPI LMA fibres. X, Y axis in meters, IOR in the colour scale is relative to silica.

The 2D IOR measurements reveal the core's symmetry of the fibre. For instance in Figure 19, on the left we have a low centrosymmetric fibre and on the right we have a high centrosymmetric fibre. As it will be clearer later, LMA AF having poor centrosymmetry will result in poor fundamental mode excitation when spliced to SM pigtails.

2.2.2 S^2 Technique and test-kit description

The S^2 is a measurement technique that allows evaluating the modal contents of the field propagating in FMF. We use this technique to characterise the power and the shape of each mode coupled at the SM-MM splice. We briefly report here the theory of the measurement; this is important to understand how S^2 software is implemented.

2.2.2.1 S^2 Theory of measurement

The original paper presenting the S^2 technique dates back in the year 2008[100]; S^2 theory is here quickly presented. Parallel polarisation for the modes is assumed. Let us consider the fundamental mode LP01 propagating in a FMF fibre. At the end of the fibre we will have

$$\widetilde{E_{01}}(x,y,\omega) = E_{01}(x,y)e^{-i\omega t} \qquad (2.2.2.1)$$

At the end of the fibre any higher mode 'b' can be expressed as

$$\widetilde{E_b}(x,y,\omega) = \alpha_b(x,y)\widetilde{E_{01}}(x,y,\omega)e^{-i\omega\tau_b} \qquad (2.2.2.2)$$

Where $\alpha_b(x,y)$ is a mask transforming, point by point, the LP01 transversal distribution into the HOM transversal distribution and τ_b is the delay of the HOM respect to the LP01.

The intensity resulting from the beating of LP01 and any HOM is:

$$I(x,y,\omega) = < |E_{01} + E_b|^2 > = I_{01}(x,y,\omega)[1 + {\alpha_b}^2(x,y) + 2\alpha(x,y)\,cos(\omega\tau_b)] \qquad (2.2.2.3)$$

Where $I_{01}(x,y,\omega) = < |E_{01}|^2 >$.

The Fourier transform of the beating's intensity is equal to

$$\mathrm{F}(x,y,\tau) = \left(1 + {\alpha_b}^2(x,y)\right)F_{01}(x,y,\tau) + \alpha_b(x,y)[F_{01}(x,y,\tau-\tau_b) + F_{01}(x,y,\tau+\tau_b)] \qquad (2.2.2.4)$$

We then define a function f as

$$f(x,y,\tau) = \frac{F(x,y,,\tau)}{F(x,y,0)} \qquad (2.2.2.5)$$

When calculated in$= \tau_b$, $\mathrm{F}_{01}(x,y,2\tau_b) \approx 0$ and the mask $\alpha_b(x,y)$can be easily extracted from (2.2.2.4) as

$$\alpha_b(x,y) \approx \frac{1-\sqrt{1-4f^2(x,y)}}{2f(x,y)} \qquad (2.2.2.6)$$

Under the hypothesis that most of the light is in carried by the LP01,

$$I_{01}(x,y) \cong \int_{\Omega} I(x,y,\omega)\, d\omega = F(x,y,0) \qquad (2.2.2.7)$$

and knowledge of $\alpha_b(x,y)$ permits reconstructing an approximate image of the HOM.

$$I_b(x,y) = |\alpha_b(x,y)|^2 F(x,y,0) \qquad (2.2.2.8)$$

Under the same hypothesis, the relative power of the HOM with respect to the total can also be evaluated.

$$MPI_b = \frac{P_b}{P_{TOT}} = \frac{\iint |\alpha_b(x,y)\sqrt{F(x,y,0)}\,|^2 dxdy}{\iint I_{TOT}(x,y)dxdy} \qquad (2.2.2.9)$$

The power of one mode over the total is in the literature referred as MPI (multi path interference). Another very important piece of information is the shape of the Zero Picoseconds ("0 ps") Image, $I_{01}(x,y)$, as described in equation (2.2.2.7). Clearly, if the HOM content is minimal, the shape of the "0 ps" image resembles closely that of the LP01 mode. The shape of the LP01, as it will be clear later, depends on the IOR rotational symmetry and plays an important role in characterising AF suitability for HPFLs.

2.2.2.2 *Implementation of the S^2 techniques*

Figure 20 shows the implementation's arrangement of the S^2 in its first demonstration. The technique's setup consisted of a broadband ASE source igniting light into the FMF under test. The output of the FMF test was imaged with a near field system, creating a beam waist. At the beam waist, the beam was probed by an SMF moving along the transversal dimensions (x, y) by means of a 2D motorised stage. The other end of the SMF was connected to an OSA. For each position (x, y) within the beam waist, the spectrum of the probed part of the field was measured. Space and spectra of the field were in this way measured, hence the name S^2. After the acquisition of the data, the algorithm presented in 2.2.2 was applied on every trace of the OSA and from these; modal excitations and modal shapes were evaluated.

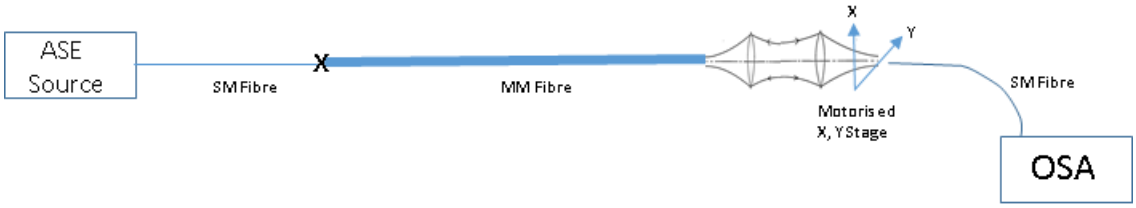

Figure 20 First implementation of the S^2 technique.

Drawbacks of this first implementation were certainly due to the slowness of the measurement, the laborious initial process of alignment of the SMF within the beam waist and the possible misalignment due to vibrations occurring during the time-consuming measurement. Indicatively, the typical time for a modern OSA to perform a sweep across 20nm of bandwidth with low sensitivity is about 2 seconds. To acquire 625 sweeps across the beam waist, saying a mere resolution of 25 X 25 equivalent pixels, the whole acquisition process would take as long as 20 minutes. Since 2008, other implementations of the S^2 technique have been demonstrated. New techniques adopt a narrow band tuneable laser as source and a beam profiler acquiring the whole beam waist image at once [109]. The setup developed entirely by the author of this work and used during the course of this PhD, including hardware assemblage and software coding, is shown in Figure 21,Figure 22 and Figure 25.

Figure 21. S^2 scheme as implemented in the work carried out in this thesis.

In the setup used in this thesis, the TLS used as source is a Newport velocity TLB-6722, with line width of 200pm, scanning range from 1045nm-1085nm and maximum output power of 25mW. The output of the tuneable laser is delivered by a standard SM fibre with a core diameter of 10µm and cladding diameter of 125µm. The SMF fibre of the TLS is spliced to a SMF of interest; quite often, this latter SMF is the same type used in the Bragg gratings of our high power laser. The SMF of interest is then spliced to the MMF, this MMF will normally be the AF of our laser. At the SMF-MMF splice, generally, more than one mode will couple into the MMF. The multimode output of the fibre is then imaged on a CCD camera by a couple of planes-convex lenses having a combined magnification of 200. A neutral density filter is used to attenuate the laser light, whilst the oblique/ stray visible light coming from the external environment is spatially filtered by the presence of a tube surrounding the imaging system. The CCD Camera is Thorlabs BSC106 having a dynamic range of 12 bit/pixel and a resolution of x*y pixels equal to 1360*1000. The source code managing both acquisition and processing of the data has been written by the author of this work in C# language, using the AForge.net framework [110] and implementing parallel processing to shorten the processing time. The user interface of the software is shown Figure 22. The measurement process is managed by the S^2 software and is divided in two parts. In the acquisition part, the laser's wavelength is scanned over a user defined span of wavelength S[nm] (e.g. from 1065nm to 1085nm) using a set of N equally spaced wavelengths (user can select N = 128, 256 or in general 2^N). During the scan, for each of the n wavelength set by the laser λ_n, a snapshot of the beam profile $I(x, y, \lambda_n)$ is recorded. In the subsequent processing part, the algorithm presented in 2.2.2.1 is applied to each of the pixel of $I(x, y, \lambda_n)$.

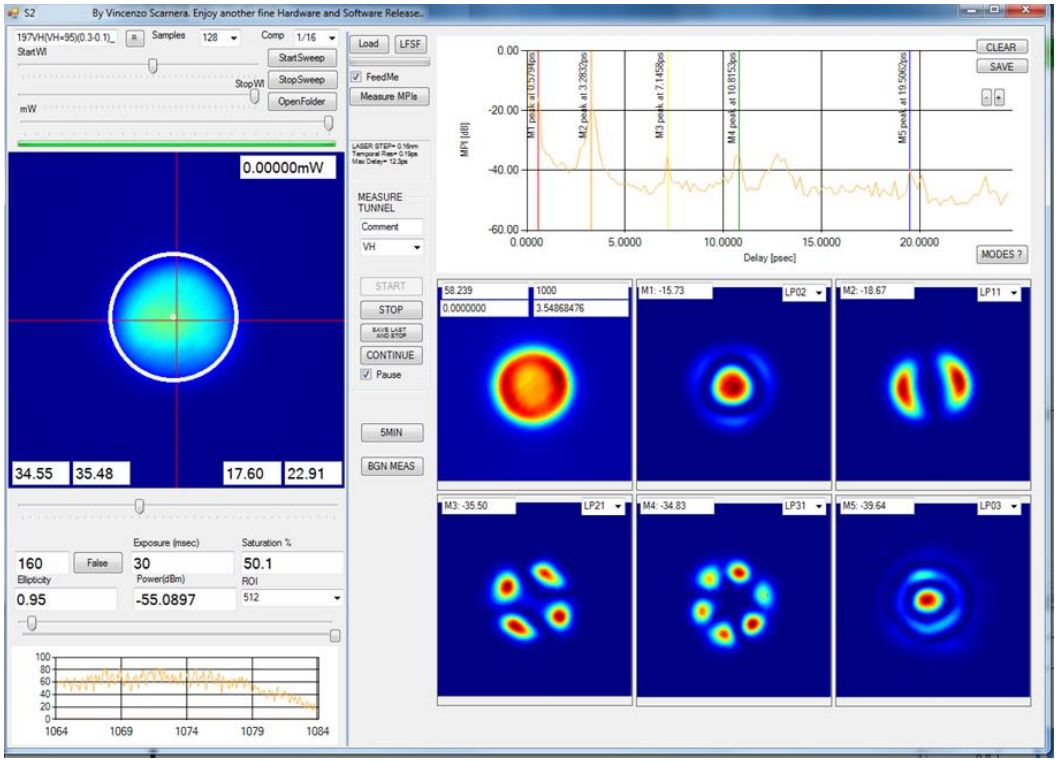

Figure 22. S² Software user interface. Acquisition part on the left hand-side, processing part on the right hand-side.

Particularly, the 3D array $I(x, y, \lambda_n)$ is processed via FFT, pixel by pixel along λ_n, producing therefore $F(x, y, \tau_n)$. From $F(x, y, \tau_n)$, the MPI is calculated for each τ_n, producing an interferogram like that shown in Figure 23.

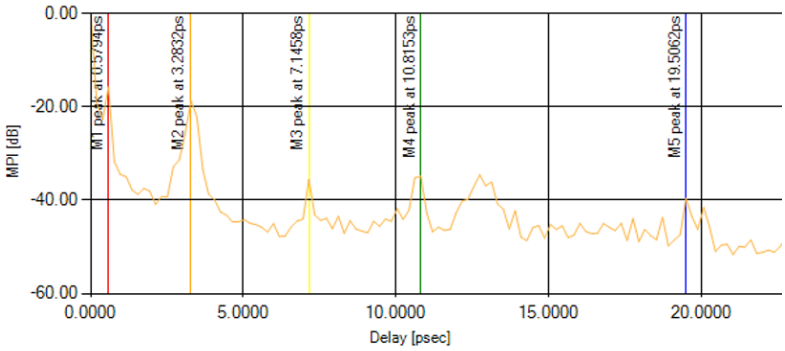

Figure 23. S² Software. MPI interferogram produced after the acquisition scan with five markers added by the user.

The interferogram presents peaks in correspondence of the differential delay of the HOM propagating into the MM fibre (delay with respect to the fundamental mode). The user of the software can select these peaks clicking on the interferogram, by adding markers. In

correspondence of these peaks, the approximation in formula (2.2.2.6) is valid, the mask $\alpha_b(x, y)$ can be calculated and the image of the mode can be reconstructed. Each peak can be visually associated to a mode since the correspondent reconstructed image is visually attributable to a mode.

For instance, the interferogram shown in Figure 23 has five peaks located at differential delays equal to 0.57, 3.28, 7.14, 10.81 and 19.5 ps. The images of the modes reconstructed in correspondence of these peaks are shown in Figure 24.

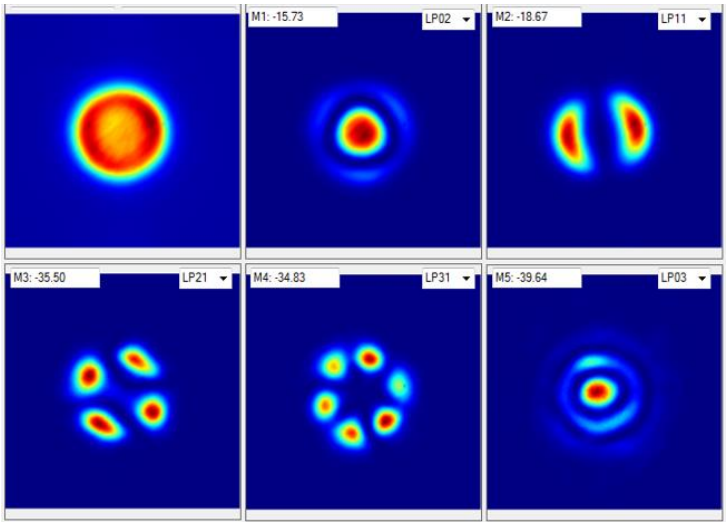

Figure 24. S² Software. Image of the modes reconstructed.

In Figure 24, the top left image is obtained by averaging the N recorded snapshots and it is equivalent to the $F(x, y, 0)$ mentioned in equation (2.2.2.7). $F(x, y, 0)$ is used as approximate image for the LP01 mode. The other five images of Figure 24 are those reconstructed for the LP02, LP11, LP21, LP31 and LP03, with calculated MPIs equal to -15.73, -18.67, -35.5, -34.84 and -39.64 dB respectively. The data of this chapter shows the modal contents measurement of 2 meters GTW MM AF (V = 6, 13µm of core diameter), spliced with an intentional offset of 3um to SM Fibre (10µm core diameter).

Here will follow some further useful details about the measurement. Data acquisition time is equal to the number of selected wavelengths N, times the acquisition time of each snapshot T_S.

$$\mathrm{T_S} = \mathrm{T_L} + \mathrm{T_{EXP}}(\mathrm{P_\lambda}) + \mathrm{T_{DS}} \qquad (2.2.2.10)$$

T_L represents the time taken by the TLS to sweep from one wavelength to the next, T_{EXP} is the exposure time of the camera, P_λ is the power reaching the camera and T_{DS} is the time necessary to save a snapshot in the computer's memory. T_L depends on the sweeping speed of the TLS and on the distance between wavelengths, in most of the case this term is ~50ms. T_{EXP} must be long enough so that, the charge accumulated in each pixel is well above the noise. For this reason, the weaker P_λ, the longer the exposure time. When measuring the modal contents of long Yb^{3+} doped fibre P_λ can be very weak due to the dopant absorption and T_{EXP} can be in the order of the second. With the AFs used in this work, when the fibre length is in the order of the meter, T_{EXP} ~ 50ms is suitable. T_{DS} depends from the computer's performance and the programming paradigm used. In this work, we have used a modern computer and written code leveraging on multithreading and multi-processor capability made available by C# and the Microsoft.Net framework v4.5 [111].

In our setup, with the latest developed version of the S^2 software, T_{DS} ranges in the order of 150ms when using the maximum resolution of the camera (1.3 Mega Pixel/snapshot). For a typical acquisition of 256 snapshots, when using one meter long FMF (active), the total time needed is about 256*(50+150+50ms) = 60 seconds. Once all snapshot have been stored, the interferogram is calculate by performing, as many FFTs as the pixel used for the acquisition (1.3 Mega FFTs in case of full CCD area, normally we use one quarter of it). For each pixel, FFT length is N, as the number of wavelengths selected in the user interface. A fast FFT routine is provided by the open source AForge framework [110] in a form of an external assembly to be imported in the C# compiler. The time to calculate the interferogram depends on both number of pixels and number of wavelengths. The processing time for the interferogram, is typically around 1 second in most of the measurements presented in this work. Once the user has selected the peaks on the interferogram, the time to reconstruct the high order mode shape is in the order of 1 second. Compared to the original implementation of the S^2, the implementation used in this works is much faster since acquisition takes about a minute and post processing is made straight after.

In [109] the usage of a polariser before the camera is adopted, however, even if here it is not reported, no difference was found by introducing it. This is because the fibre considered in this work do not introduce much polarisation dispersion given their short length and little birefringence.

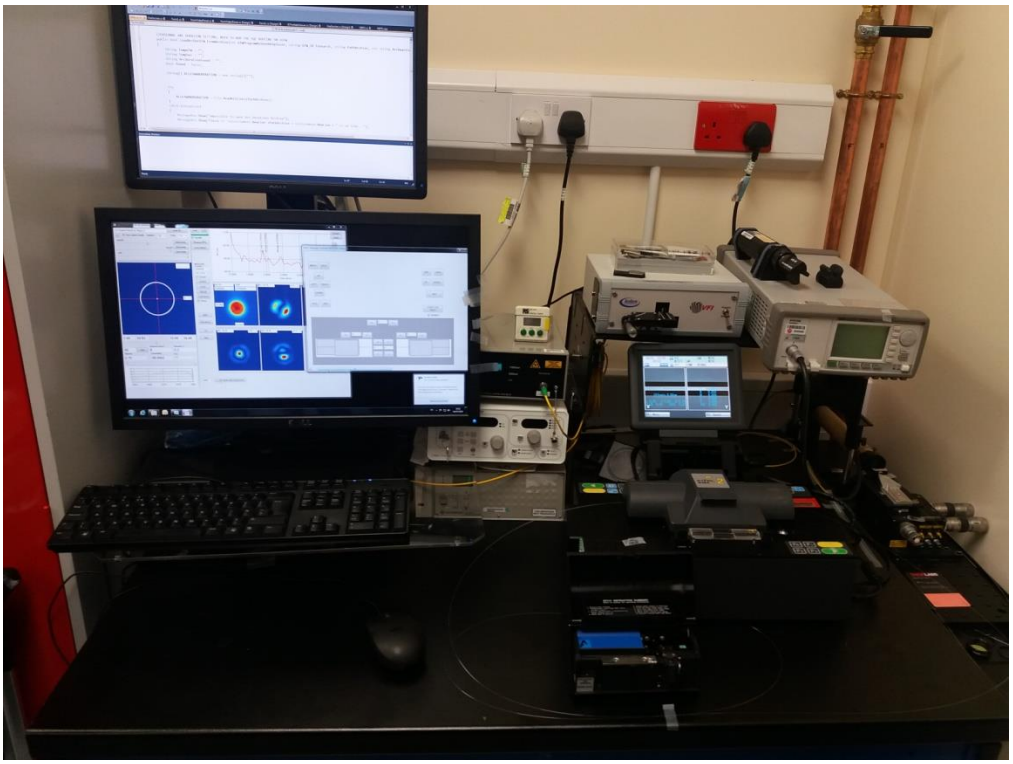

Figure 25. S^2 Test kit picture. Both hardware and software developed by the author of this thesis.

2.2.3 HPFLs characterisation test-kit

A brand new, empty, laboratory was made available by SPI for the testing of HPFLs and MOPAs. In this new laboratory, the author of this thesis has built from scratch the advanced high power test-kit. Apart from the pump blocks assemblage (Figure 28), the remaining parts composing this test-kit have been sourced, arranged, connected and programmed by the author of this thesis. The high power test-kit, used to characterise HPFLs and MOPAs, includes:

- Two cold-plates: one for the seed fibre and one for the amplifier fibre
- Two pump blocks: one for the seed and one for the amplifier (more details will follow)
- Two waveform generators to drive seed and amplifier pump blocks (Agilent 3352).
- Two chillers (Thermo flexi 2500W and 7500W)
- An optical spectrum analyser (Yokogawa AQ6370)
- A thermal image camera (TIM by Micro Epsilon)
- Acquisition board capable of measuring various temperatures (National instruments 6620)
- A 4GHz oscilloscope (Lecroy Waverunner 640Zi)
- 4 InGaAs Photodiodes (Thorlabs - DET 10N)
- 10kW CW DC electrical power supply (TDK lambda GEN 50A-200A)
- 1.5kW CW DC power supply (TDK lambda GEN 100V-15A)
- 2X 5kW optical power meter (OPHIR 5kW series)
- An optical table surmounted by a custom made enclosure.
- A translation motorised stage to perform vertical probing.

The two pump blocks include several Lumentum ST fibre coupled lasers (Figure 26, 140W, 106um fibre, 0.22NA, 950nm) via multimode combiners (Figure 27). The maximum available pump power for the seed part is ~1700W (12 ST, 850W per combiner), whilst that for the amplifier counterpart is 3400W (24 ST, 1700W per combiner). With an output fibre of 250µm of diameter, the maximum pump brightness available is ~0.1 W/ μm^2/sr.

Figure 26. Lumentum ST (140W, 106µm fibre, 0.1NA)

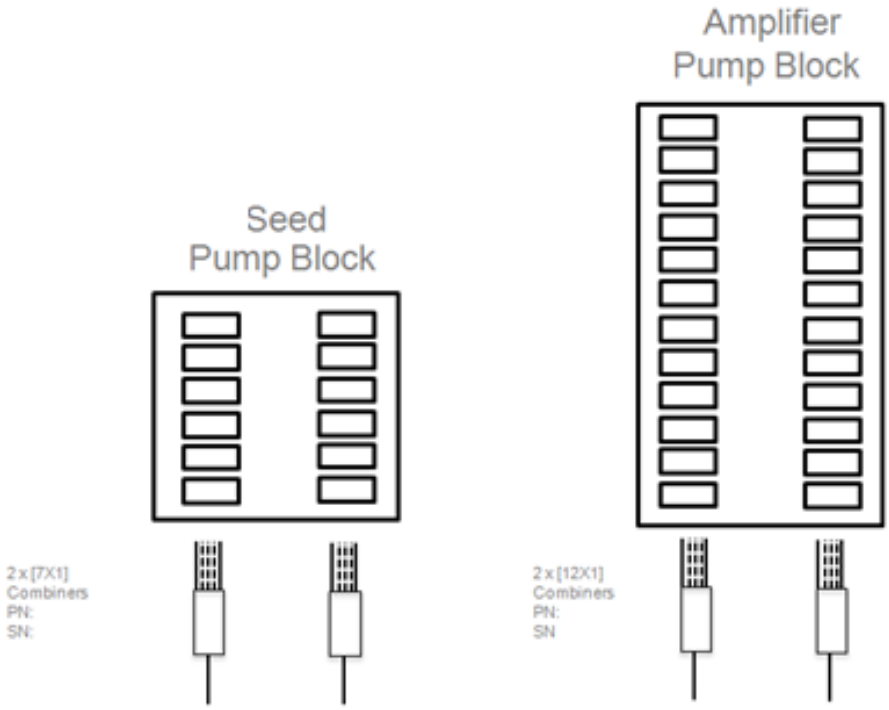

Figure 27 Optical Layer of the MOPA pumping architecture and pump combining.

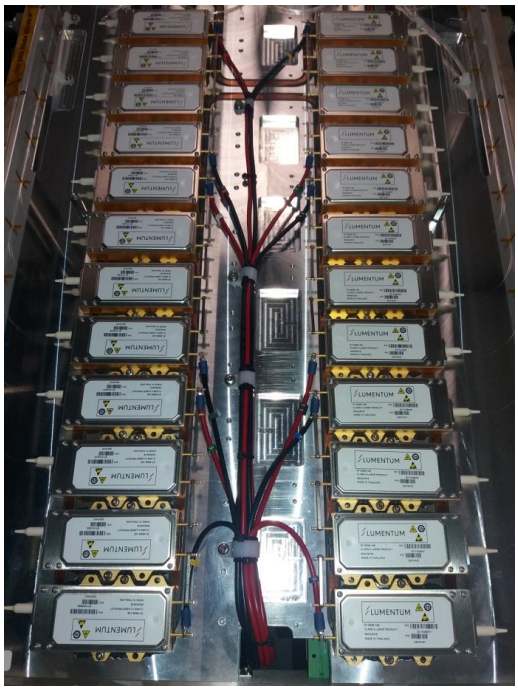

Figure 28. 24 Lumentum ST on heat sink. Pump blocks like that in this picture are routinely build at SPI Lasers.

Electrically, the pump blocks are connected in parallel to a single 10kW PSU (Figure 29). Dedicated driver boards modulate the current flowing through the diodes, with demand signal provided by the waveform generators. An exception is made for 4 simmer diodes connected to the seed: these simmer diodes are excited in CW current without modulation (Only ON/OFF), by a separate 1.5kW PSU. Simmer diodes must be always on when amplifier is powered up ("anti-Q- switching" turn on protection). This expedient is put place to prevent catastrophic failure due to amplifier Q-switching: this would happen if the amplifier were pumped without any seeding light at its input. The Seed/Simmer pump block has been customised to manage the simmer pumps (shortened bus bar and connection of 4 Lumentum ST to the 1.5kW power supply) and to implement the "anti-q-switching" protection circuitry (electronics developed by the author, but not reported here). The pump layer is cooled with a 7500W chiller, managing both pump blocks at the same time. A pump block characterisation will be shown in section 5.7.1.

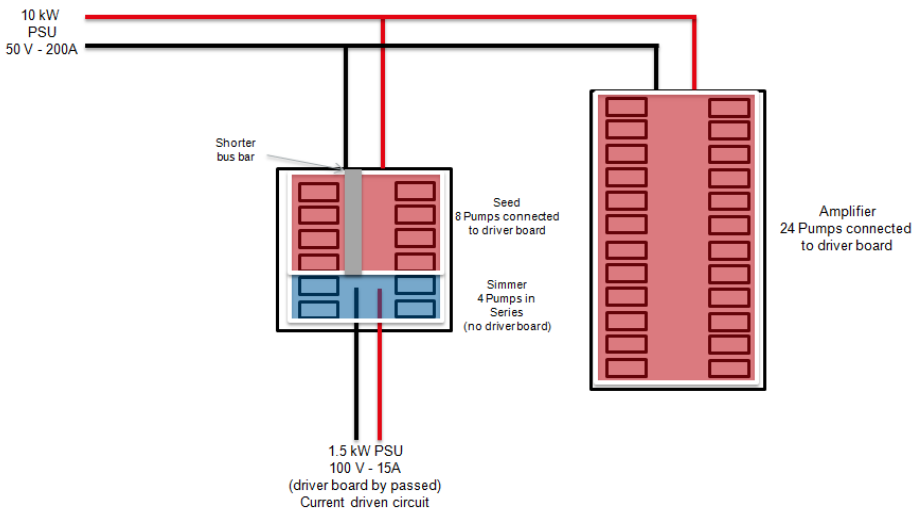

Figure 29. Electrical Layer. On the left Seed/Simmer Pump block, on the right Amplifier pump block. Simmer/Seed pump block customised during this work (not SPI standard).

A dedicated 2500W air cooled chiller is used to cool the optical fibres; this includes seed heat sink and the amplifier heat sink.

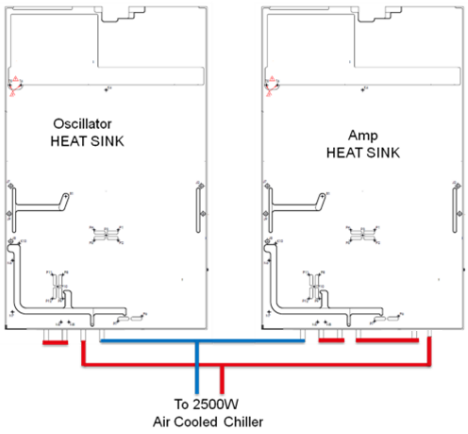

Figure 30 Active fibres cooling scheme.

Up to four photodiodes are connected to the oscilloscope; more details on the position of the photodiodes will be provided when describing the optical architecture and the associated experiment for the HPFLs/ MOPAs . Their position and intended use of all the probes will be explained later, in the relevant experiments (chapters 4, and 5). The entire instrumentation has been connected with various ports (GPIB, RS232, USB and Ethernet) to a PC running windows 7. Code managing asynchronously all instruments has been written by the author of this thesis in Visual C# using various programming paradigm (sequential, parallel, functional and event driven) and leveraging on the multithread, multiprocessor

capabilities made available by the microprocessor (Intel Core i5) and by the .net framework (version 4.5).

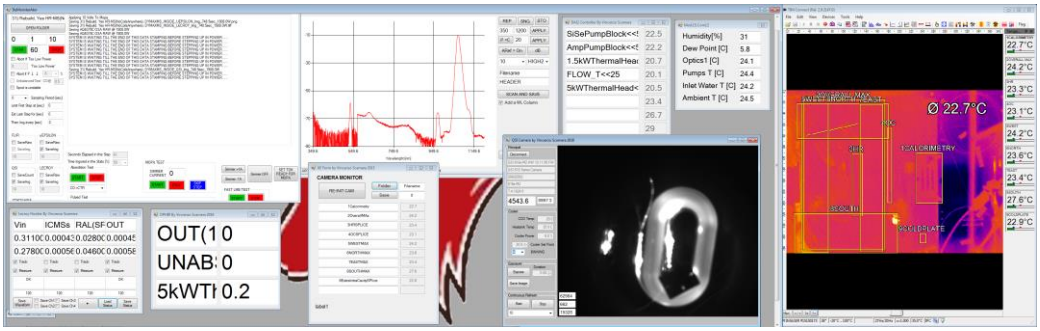

Figure 31. High Power Testkit Software screenshot

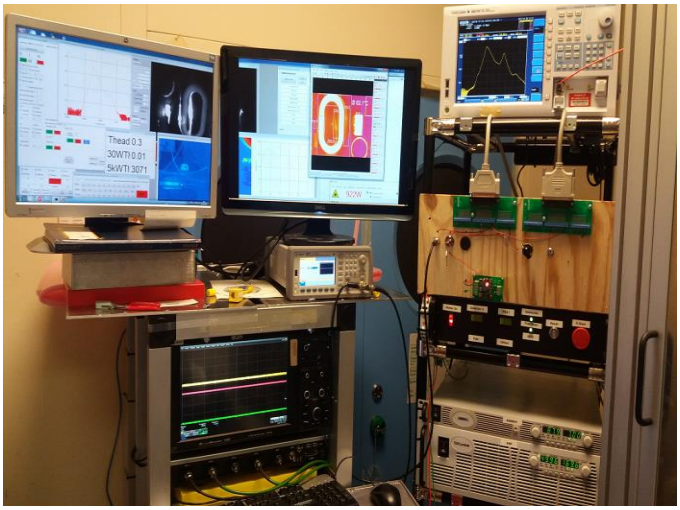

Figure 32. High power test kit console and instruments

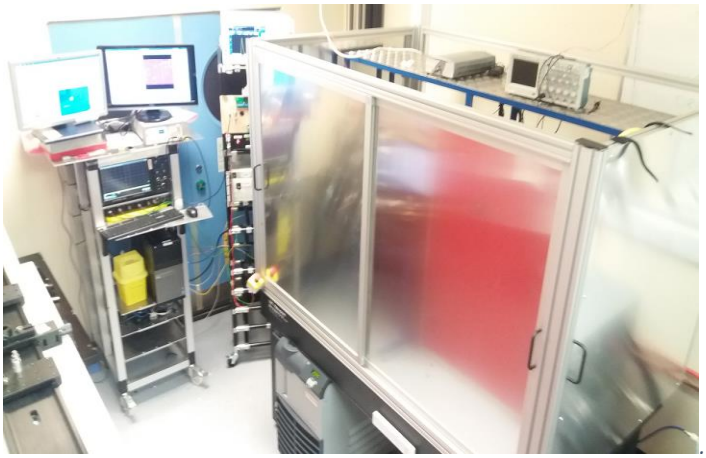

Figure 33. High power test kit enclosure.

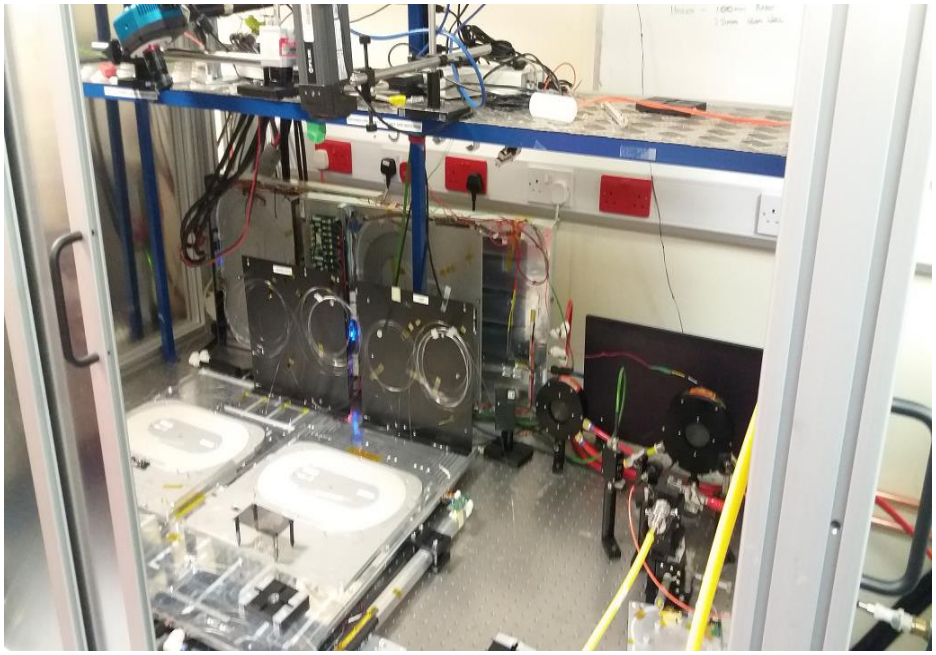

Figure 34 High power test kit. Photo from inside the enclosure, when testing a MOPA.

2.3 Conclusions

We have recalled the easy formula used in the telecoms to evaluate splice loss in SM-SM joints anticipating that this formula is no longer suitable to describe SM-MM joins. In the HPFLs arena and in this work, SM-MM splices in the presence of dopants diffusion, play an important role for the achievement of good efficiencies and controlled fabrication processes. Image processing is of cardinal importance for the achievements of optimised SM-MM splices; we have therefore reviewed the most common techniques adopted to evaluate the modal content at the output of a MM fibre. Amongst the techniques, the S^2 measurement is the most suitable for our work as it is flexible (does not need *a priori* information about the beam shape) and relatively fast (imagine and modal content is measured in about 60 seconds). The hardware and the software of an S^2 test kit has been developed during the course of this PhD by the author of this work. In order to test the effect of the optimised SM-MM splices at high- power, a high power test-kit (hardware and software), was developed during the course of this PhD by the author of this work. The high power test-kit can test both oscillators and MOPAs, in CW and pulsed regime, and allows the concurrent probing of data from a vast number of detectors. The test-kit features a novel characterisation method that includes a motorised stage, a collecting fibre and a monochromator (described in detail in chapter 4).

3 Fibre Splice development

3.1 Introduction

In this chapter, we present the fibres used and the splicing technique adopted to join them. The splicing process is explained first from a phenomenological point of view and then from a theoretical point of view.

3.1.1 Fibres used

In this paragraph, we will describe the splicing technique adopted for the construction of our HPFLs and MOPAs. Particularly, our attention focuses on the optimisation of Single Mode Fibres (SM) to Few Mode Fibre (FMF) splices. Bimodal passive Fibres (BMF) are also used. Generally speaking, in our laser and amplifiers, SMF and BMF are gratings fibres or fibres interconnecting active parts, whilst FMF are those pertaining to active media. Figure 35, Figure 36 and Figure 37 exemplify the guiding properties of the typical fibres used in the construction of our laser sources in terms of Index of refraction (IOR). Here, IORs are expressed as an offset with respect to silica IOR (n_{si} = 1.445 @ 950 nm). IORs are measured via IFA-100 refractive index profiler.

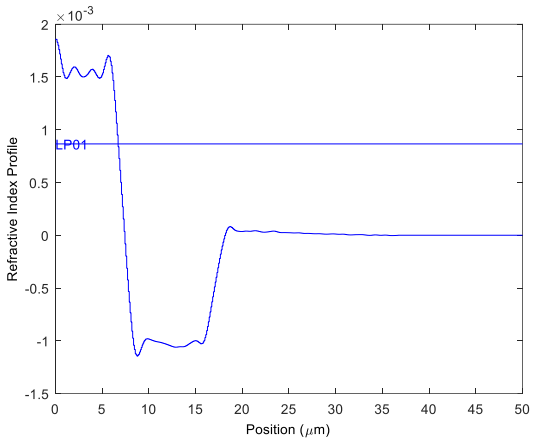

Figure 35. SMF (passive): measured IOR and calculated effective IOR for the guided mode.

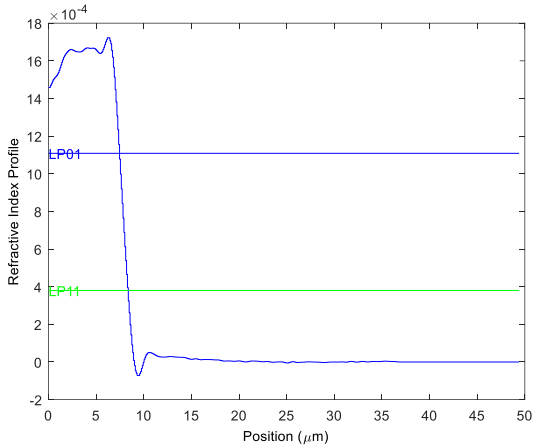

Figure 36. BMF (passive): measured IOR and calculated effective IOR for the two guided modes.

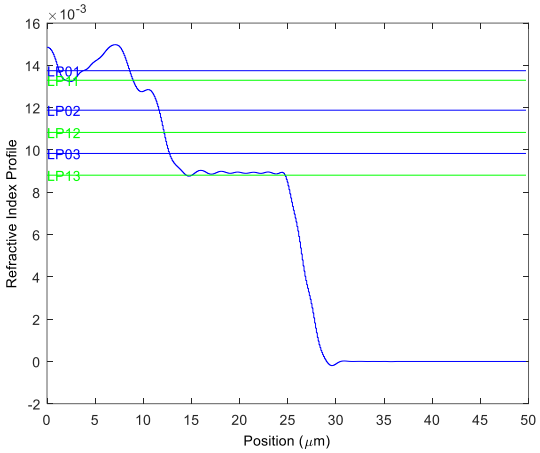

Figure 37. FMF (active): measured IOR and calculated effective IOR for the guided modes.

In Figure 37, the core of the AF, whose radius is about 12µm, is surrounded by a pedestal having diameter of about 27µm. We will try to explain the presence of such pedestal in SPI AFs by invoking the need of achieving enough pump absorption. To achieve enough pump absorption (about 20dB) and reasonably short fibre (length < 25 meters), Yb in the AF must be above a certain level of concentration; in our case this is in the order of 2.5 x 10^{26} ions/m^3. With these Yb concentrations, given the big Molar Refractivity (MR) of the Yb, the index of refraction of the core of the fibre becomes very high compared to the cladding. Referring to Figure 37, working without a pedestal would mean having a V number equal circa to 15. In these conditions, far too many core modes would be guided, making the fibre unsuitable for HPFLs applications. By inserting the pedestal, the V number of the core

becomes circa 8, reduces the number of guided modes and makes the fibre more suitable for the construction of SM HPFLs. As it will be clear in chapter 4, for the correct functioning of our laser, it is of pivotal importance to maintain the field propagating in the FMF concentrated in the LP01 mode, without coupling of the HOM. SMF and FMF fibres used are very dissimilar and, if spliced without any criteria, HOM coupling in the FMF fibre is expected.

To avoid big losses and keep the propagation mainly on the LP01 mode, the guidance property of the fibres needs to be altered in proximity of the splice. The most common strategy to achieve single mode excitation in the MM fibre is to match the effective areas of the fundamental modes in proximity of the splice and to create a taper as adiabatic as possible in the MM fibre. In this thesis, we will use a novel approach. The novel approach treats the SMF-FMF splice as an optical a coupler where neither effective area matching nor adiabatic tapering is required in order to minimise splice loss and maintain single mode propagation. To invent and to explain the principle of this splicing technique, we developed a fast S^2 measurement test kit and we adapted some theories of beam propagation in tapers, complementing them with the aid of fine index of refraction measurements resolved across the splice.

3.1.2 Diffusion of dopants in optical fibres during splicing

The effect we utilise to modify the guiding properties of the fibres in proximity of the splice relies on the diffusion of dopants. Fick's laws govern diffusion of elements dispersed in another and are widely adopted to describe dopants diffusion in silica [112-114].

The first law of Fick (3.1.2.1) shows how an element having higher concentration in a point, tends to migrate toward points having smaller concentration.

$$\vec{J}(\vec{r},t) = -D(\vec{r},t)\,\boldsymbol{\nabla C}(\vec{r},t) \qquad (3.1.2.1)$$

In (3.1.2.1) the local flux $\vec{J}$ [#/(m^2*s)] represents the number of elements per area per second migrating in a certain direction, $\boldsymbol{C}$ represents the local concentration [#/m^3] and D

is defined as diffusivity [m^2/sec]. D is defined for a certain species diffusing in a certain solution. The three-listed quantities are space and time dependent, with migration of dopants ending when J = 0; this happened either when $\boldsymbol{\nabla C}$ = 0 or when D = 0. From a temperature point of view, diffusion coefficients follow the Arrhenius equation.

$$\mathrm{D} = \mathrm{D_0}\exp\left(-\frac{\mathrm{E_a}}{\mathrm{RT}}\right) \qquad (3.1.2.2)$$

In (3.1.2.2) D_0 [m^2/sec] is the maximum diffusivity coefficient (when T = ∞), E_a [J/mole] is the activation energy, R = 8.3145 J/(mol*K) is the ideal gas constant, and T[K] is the temperature. Both D_0 and E_a are characteristic of a dopant in a particular solution. Values of this coefficients for some dopants used in silica fibres can be found in [114-118]. However, the effect of having more dopants diffusing at the same time and for the particular composition of our glass has never been reported. Equation (3.1.2.2) highlights that diffusion of dopants can take place during the arc discharge as the diffusivity of the dopants increases with temperature.

The second law of Fick (3.1.2.3), which corresponds with the diffusion equation, shows how concentration of dopants evolves in the space and time:

$$\frac{\partial \mathrm{C}}{\partial \mathrm{t}} = \boldsymbol{\nabla}(\mathbf{D}\boldsymbol{\nabla}\mathbf{C}) \qquad (3.1.2.3)$$

If we assume the fibre's temperature is constant in both space and time during arc discharge [88], D will also be constant in space and time. In this case, the second law of Fick simplifies to

$$\frac{\partial \mathrm{C}}{\partial \mathrm{t}} = \mathbf{D}\boldsymbol{\nabla}^{\mathbf{2}}\mathbf{C} \qquad (3.1.2.4)$$

Ignoring azimuthal and longitudinal diffusion and rewriting the equation above in cylindrical coordinate, we obtain:

$$\frac{\partial \mathrm{C}}{\partial \mathrm{t}} = \mathrm{D}\frac{\partial \mathrm{C}}{\partial \mathrm{r}}\left(\mathrm{r}\frac{\mathrm{dC}}{\mathrm{dr}}\right) \qquad (3.1.2.5)$$

The partial differential equation (3.1.2.5) is resolvable via variable's separation technique and by using a summation of Bessel functions. Given an initial concentration C(r, t=0), a core radius R, the evolution of the concentration is:

$$C(r, t > 0) = \sum_{m=1}^{\infty} C_m e^{-\Lambda_m D t} J_0(\Lambda_m r) \qquad (3.1.2.6)$$

Where Λ_m are such that $J_0(\Lambda_m R) = 0$ and C_m are defined as follow:

$$C_m = \frac{\int_0^R r\, J_0(\Lambda_m r) C(r, 0) dr}{\left[\frac{R}{\sqrt{2}} J_1(\Lambda_m R)\right]^2} \qquad (3.1.2.7)$$

Equations (3.1.2.6) provide some important information about the diffusion process. In (3.1.2.6) the temporal part $e^{-\Lambda_m D t}$ has for exponent the product $\Lambda_m * D * t$, highlighting that elements with low diffusivity (D small) will require longer arc durations to diffuse (t big). The spatial part is a sum of $J_0(\Lambda_m r)$ functions. In this sum, the fast varying parts of the profile are represented by terms having big Λ_m. Since Λ_m is also part of the temporal part, one can see that fast varying part of the profile (e.g. sharp edges) will fade away faster during the arc discharge. Dopants of our AF and relevant characteristics for the diffusion and change of index are listed in Table 1.

Element	dn/d(mol%)	E_0 [J/mole]	D_0 [m^2/sec]
P_2O_5	0.00100	415905	0.000066
GeO_2	0.00150	310000	0.0000024
Yb_2O_3	0.00540	454110	0.0030
$AlPO_4$	-0.00008	423570	0.0030

Table 1. Constituents of the AF with molar refractivity, Activation energy E_0 and leading coefficients D_0 [114-118].

The index of refraction variations, also called molar refractivity dn/d(mol%) with respect to the SiO_2(in mol%), the Activation energies E_0 and the leading coefficients D_0 in Table 1, extracted from [114-118] mostly pertain the diffusion of single elements in silica (apart

from reference 114). The diffusion values in the presence of more dopants diffusing at the same time, like in the case of our FMF, are unknown. However, in very first approximation, supposing that the values of Table 1 still holds, and by using formulas (3.1.2.6) (3.1.2.7), we can model the change of index of refraction of the FMF after undergoing the arcs discharge of the Fusion Splicer (FS).

The initial distribution of each 'i' dopant $C_i(r, t=0)$, has been measured via Secondary Ion Mass Spectrometry (SIMS). Theses distributions, not measured by the author of this work, are omitted as constituting confidential intellectual property of SPI Lasers. $AlPO_4$ is used to increase Yb solubility. This element is ignored in the modelling of the diffusion as its molar refractivity is very small and therefore it does not play a big role in the change of the index of refraction upon diffusion.

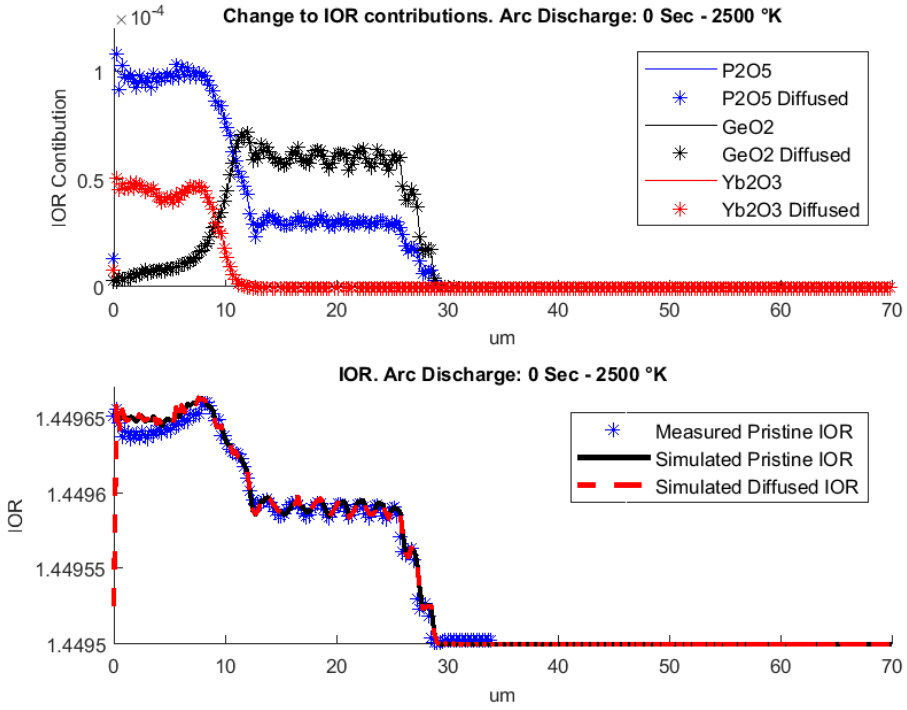

Figure 38. FMF data with no arch discharge (0 Sec).

Figure 38 shows the results obtained with no arc discharge (0 Seconds); this is just a basic reconstruction of the IOR, starting from the SIMS measurement. On the figure at top, for each dopant, we have the IOR contributions (derived from SIM measurement and molar refractivities) and the IOR contributions upon arc discharge (no change in this case, since arc duration is zero seconds). At the bottom we have the IOR measured via IFA, the

simulated pristine IOR (this is merely obtained by summing the individual IOR contributions to the IOR of SiO_2 = 1.4495), and the simulated diffused index of refraction upon no discharge. From Figure 38 top and bottom, we can see that the effect of 0 seconds discharge does not result in any appreciable difference between the pristine and diffused arrangement. This simply means that the numerical decomposition in C_m of (3.1.2.7) and the subsequent reconstruction of C(r, t=0) via (3.1.2.6) has worked fine. In these simulations, the maximum 'm' used equals 50. Still in Figure 38, at bottom, we can notice that there is a discrepancy between measured IOR and reconstructed IOR. The discrepancy could for instance be due to lack of rotational symmetry of the preform. Lack of rotational symmetry makes both measurements of IFA and SIM dependent on the axis of investigation, hence the discrepancy. Lack of rotational symmetry also affects the beam shape in the AF and the laser's performance; this aspect will be clarified later in section 5.6. Another effect that could explain the discrepancy between measured IO and simulated IOR in the centre of the fibre is the so-called Lamaire effect, where molar refractivity has a more complicated behaviour according to the relative molar content of aluminium and phosphorous [119]. These more complicated effects are here omitted because the purpose of this simulation is solely to show how diffusion alters the IOR in proximity of the splice, rather than fitting any subsequent IOR measurement in presence of diffusion.

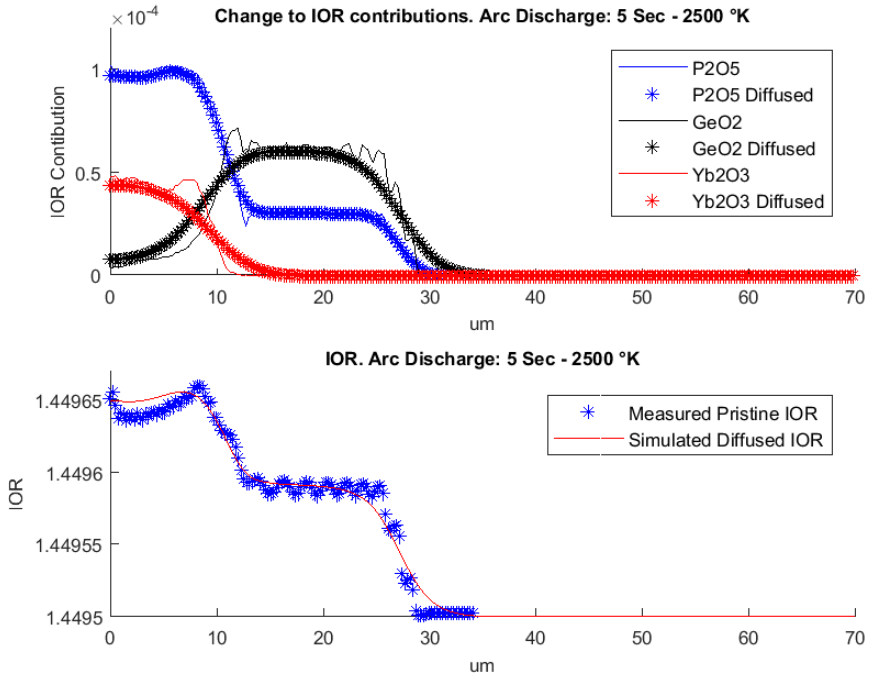

Figure 39. FMF data with 5 Sec arc discharge at T = 2500 °K

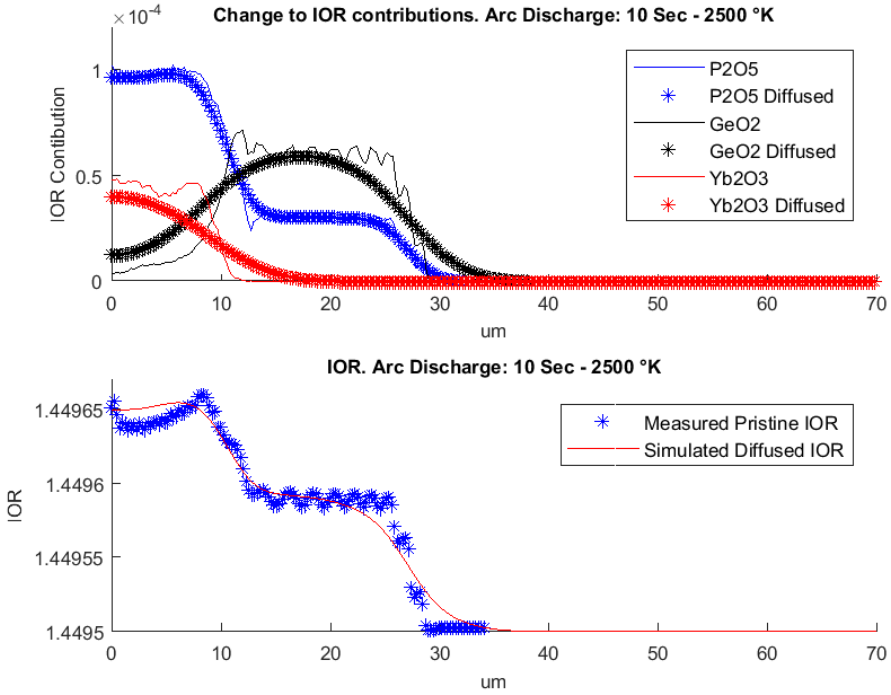

Figure 40. FMF data with 10Sec arc discharge at T = 2500 °K

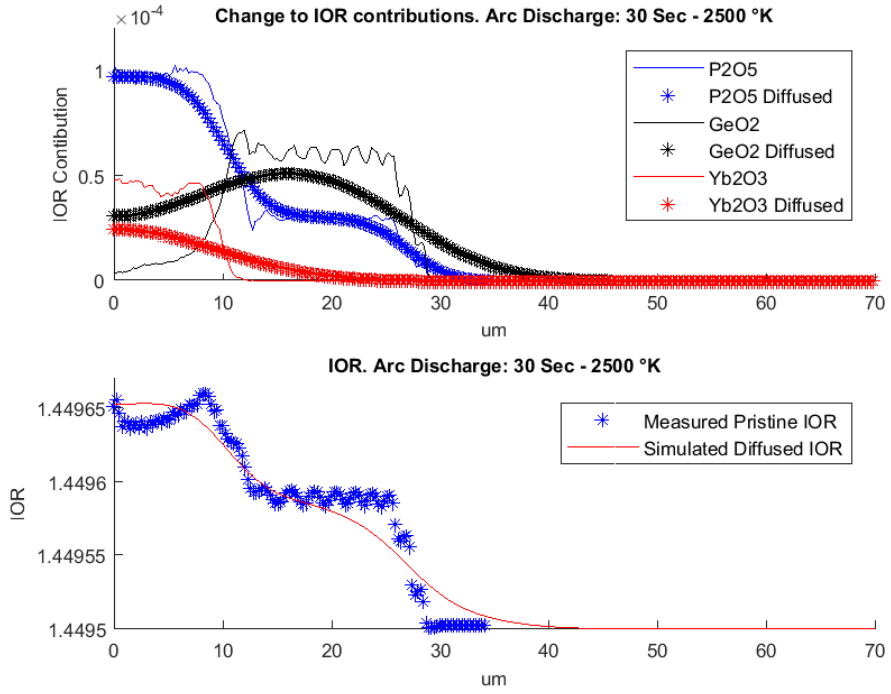

Figure 41. FMF data with 30Sec arc discharge at T = 2500 °K

Figure 39 presents the diffusion results obtained with a 5 seconds arc discharge at T = 2500 K. Meaning of the legend is as explained for Figure 38. As predicted by the theory, the immediate effect of the diffusion is the smothering of the sharp edges. Figure 40 and Figure 41 show the diffusion results obtained respectively with 10 and 30 seconds of arc discharge at 2500°K. Increasing the diffusion time, makes the edge of the IOR become progressively less sharp. In addition, the GeO_2 diffuses toward the centre of the perform raising the index of refraction in the centre of the fibre. It is easy to imagine how these effects alters the guiding property of the fibre in correspondence of the splice; this is a wanted effect as we use it to match fibres having very different un-diffused effective areas.

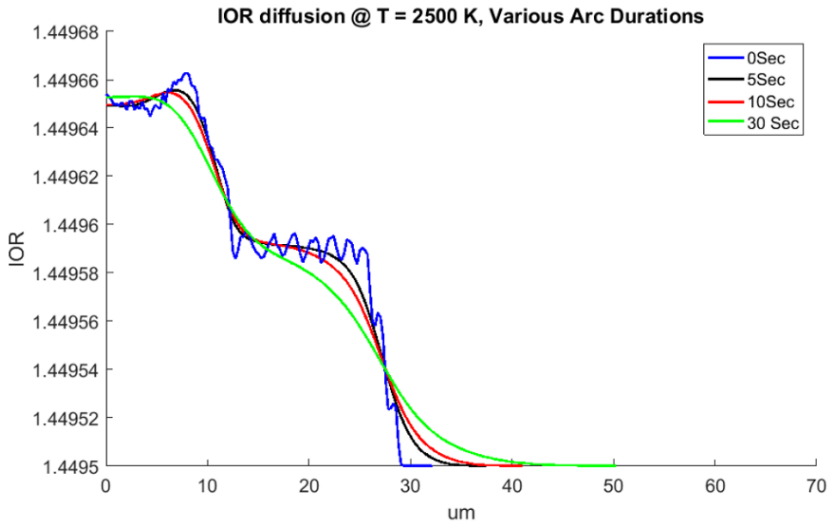

Figure 42. Simulation: Diffused IOR obtained with different arc durations.

Figure 42 groups the results obtained from the simulation at increasing arc durations. Before concluding, we observe that any hypothetical targeted IOR shape, achieved with a specific combination of arc temperature T_1 and arc duration t_1, could also be achieved with higher T and shorter t (or vice versa lower T and longer t). In fact, recalling equation (3.1.2.6), we acknowledge that the argument of the exponential includes the product $D(T) * t$, where D is a increasing function of T. Without pretence of fitting the diffusion's data shown later (e.g. in paragraph 3.4.4), the results in Figure 42 visualise quite well what append to the IOR of the AF, upon arc discharge, in correspondence of the splice.

The approximations of this diffusion model are:

- Temperature could not be exactly uniform along the radius.
- Diffusivity takes place also longitudinally (eg along the fibre's axis).
- Diffusivity of some dopants depends also on concentration.
- Effective diffusion of dopants diffusing simultaneously in our FMF is unknown.
- In reconstructing the IOR, Lamaire effect due to the simultaneous presence of Aluminium and Phosphorous is ignored

Source code of the model has been written by the author of this thesis in Matlab using object-oriented paradigm with implementation of classes representing the various dopants.

3.2 Applications of S^2 the measurement

3.2.1 Critical bending radius characterisation

One immediate application of the S^2 is to characterise effect of bends in Dual Mode Fibers (DMF). The usage of DMF in is widely adopted in HPFLs. Several manufacturers, such as NLight, Coherent and Fujikura, utilise 20/400µm, 0.065 NA fibres as active medium spliced to matched passive fibre. The V number of these systems is about 3.8, so these fibres are dual moded. The advantage of DMF is to have effective areas of the LP01 bigger than of purely SMF. Bigger effective areas result in easier splices between FMF AF, due to better area matching, and in less pronounced SRS, due to reduced intensity of power. However, as it will be clear in the construction of the lasers, presence of HOM is unwanted. HOM presence cause beam degradation, exacerbation of non-linear effects and cavity instability. The LP11's guidance can be suppressed by mean of bends having opportune bending radius, however tight bends can provoke losses also in the LP01. The S^2 technique allows determining the correct bending ratio that suppresses the LP11 mode and does not introduce substantial loss in the LP01. In the experiment described in Figure 43, the SMF of the S^2 kit (SM-HI1060) has been spliced to a 3 meter long DMF, like that presented in Figure 36. To achieve substantial LP11 excitation, the splice was intentionally made with core misalignment of 2.5µm. A single coil having progressively smaller diameter has been applied at 1.5 meters from the splice. For each diameter, both S^2 and total transmitted power have been measured. Referring to Figure 43, with the unbend fibre, we obtain -

14.1dB of excitation for the LP11 a certain total transmitted power; we will set this latter power to 0dB. One can easily see that both total power and LP11 power will drop with decreasing coiling diameters. However, at any given bending diameter, LP11 will have relatively lost more power than the LP01. Quantitatively, already at 9 cm of bending diameter, whilst the total power will have decreased of only -0.2dB, the LP11 will have lost -3.9dB (going from -14.1dB to -18dB).

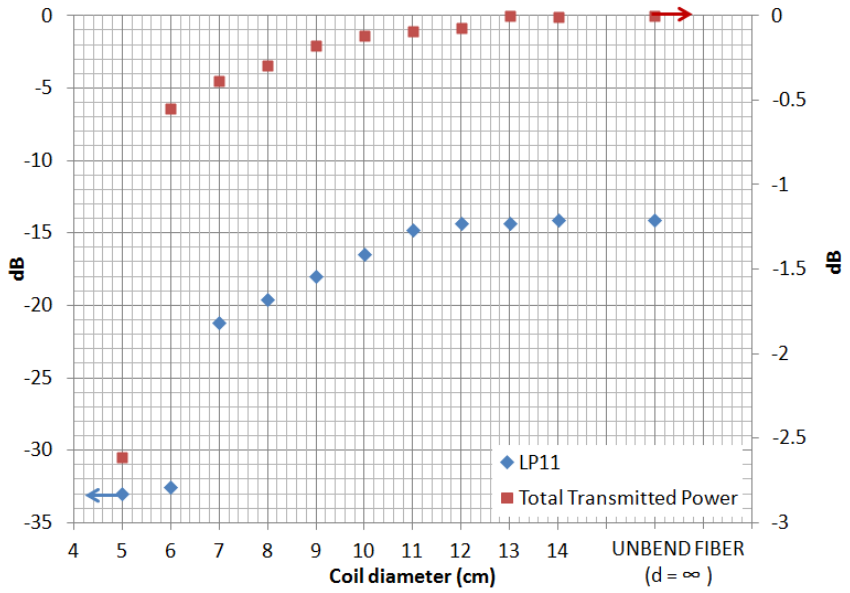

Figure 43. S^2 and output power measured at different bending radius for a typical bimodal fibre used in our laser.

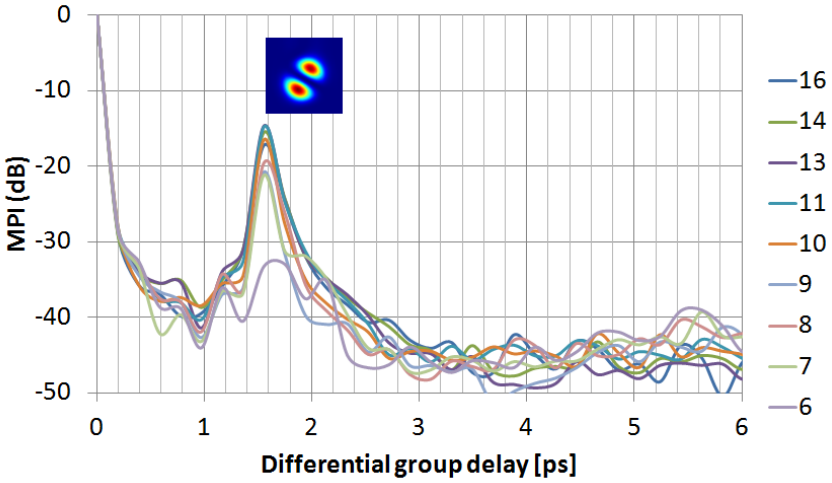

Figure 44. S^2 interferogram for the various coil diameter of Figure 43. Coils diameter in the legend in cm

In this manner, the S^2 technique can be utilised to establish the right bending radio at which losses on the total power are acceptably low and filtering of the LP11 is sufficiency high. Clearly, it is expected that, for fibre supporting more modes, or in general having modes with effective indexes close together, selective filtering of only one mode via bending becomes prohibitive; this is because above a certain bending radius every guided mode will start losing power in an equalised way. The mechanism of LP01 leakage outside the core could also be indirect: a preliminary LP01-LP11 coupling could be followed by a LP11 leakage.

3.2.2 S^2 measurement as an indicator of beam quality in beam delivery optics

Beam Delivery Fibres (BDF) are utilised to lead the light form the light source to the work piece. Arbitrary long BDF would be very useful, however due to SRS, BDF must be limited in length. Since SRS threshold is proportional to the ratio between fibre's area and fibre's length [24], an approach to increase BDF lengths without incurring in SRS, is to increase the fibre's area. However, increasing the area makes the BDF multimodal, exposing, in general, the delivery system to a deterioration of the beam quality. Beam quality factor M^2 expresses how divergent is a beam compared to a diffraction limited beam [120]. Following the M^2 definition, SM fibres results in M^2 =1. Generally speaking M^2 close to 1 can also be achieved with MMF; this providing the light propagating into the MMF is mostly concentrated in the LP01 mode [121].

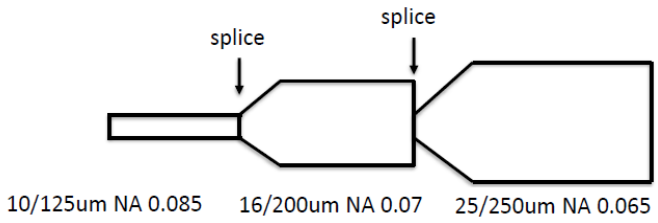

Figure 45. BDO up-taper chain made of three fibres with respective core/cladding dimension and NAs.

Figure 45 represents a chain of components tapered and spliced together in order to obtain single mode excitation in the multimode BDF (25/250µm). The SMF, output of a laser cavity (10/125µm), is spliced to a tapered DMF (16/200µm). In turn, DMF is spliced to a tapered (25/250µm) MMF. The LP11 guided by the DMF is partly suppressed by means of coils as

explained in 3.2.1. The number of modes excited in the 25/200µm DMF depends on its modal overlap with the launching mode of the 16/200µm, on the presence of kinks in the splice (caused for instance by bad cleave angles) and from the type of taper transition. Three samples of the chain sketched in Figure 45 have been produced by using a tapering machine (TMS by Northlab), a cleaver from Fujikura and a ring of fire (ROF) fusion splicer (S184PM by Fitel/Furukawa). Figure 46 , Figure 47 and Figure 48 show the result obtained in terms of S^2 with these three samples, numerated accordingly. In the three charts of the three samples, modal shape is shown in correspondence of the peaks. It can be noticed that samples 1 and 2 have much higher HOM contents than sample 3. Consequently, also the zero seconds delay image, is less round in sample 1 and 2 than in sample 3. Succeeding in having a good excitation in the BDF depends on the quality of the tools, on the setting of the tools and on the dexterity of the operator. For the construction of these three samples, machine settings of both splicer and tapering machine were the same. However, during the construction of the samples, before the splicing, the measured cleave angles at the 16/200 - 25/200 interface were 0.5-0.5 and 0.5-0.6 degrees for samples 1, 2 and only 0.1-0.1 degrees for sample 3. As intuition suggests, and empirical data support, when splicing SMF to MMF, bad cleaves do result in excitation of LP_{lp} modes having $l \neq 0$.

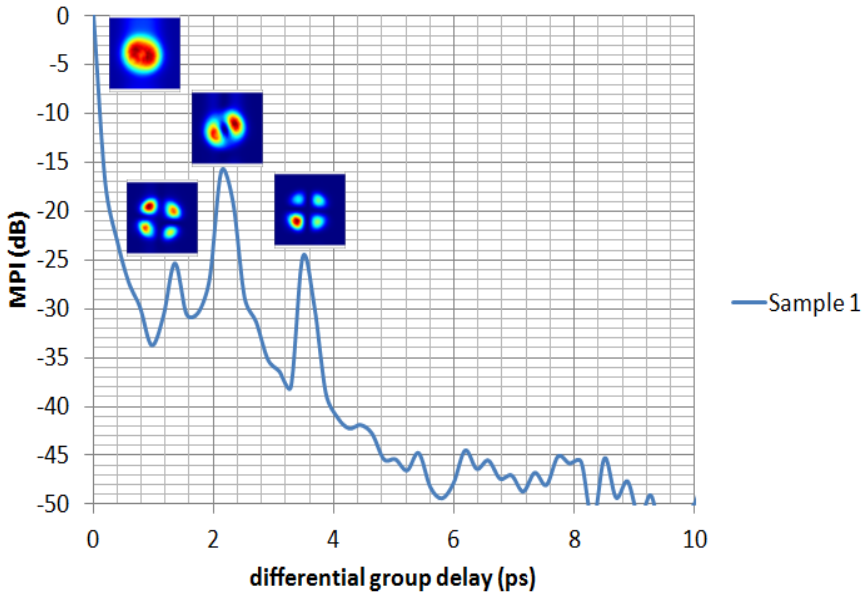

Figure 46: BDF Tapering/Splicing Sample 1 (cleave angles 0.5-0.5 deg).

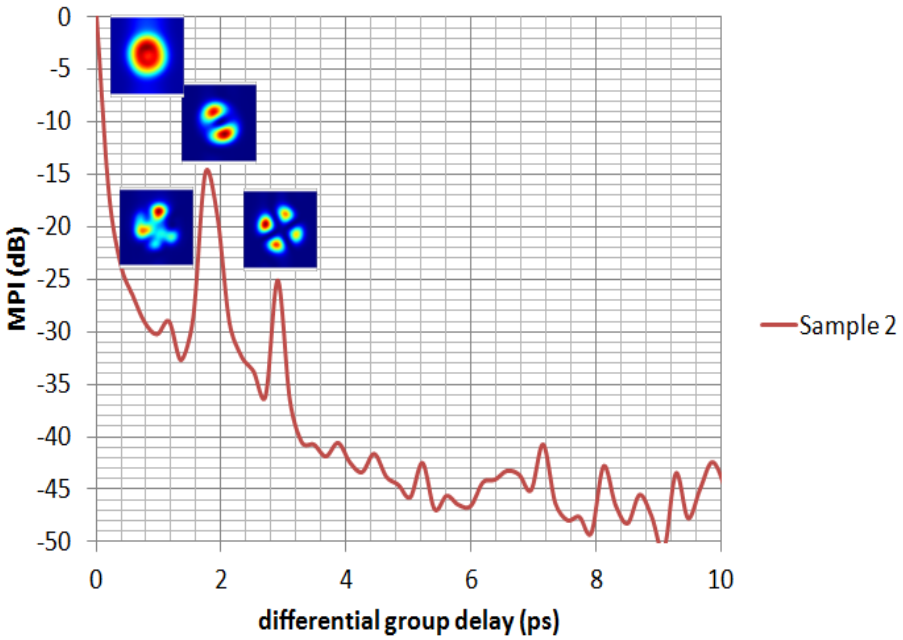

Figure 47: BDF Tapering/Splicing Sample 2 (cleave angles 0.5-0.6 deg).

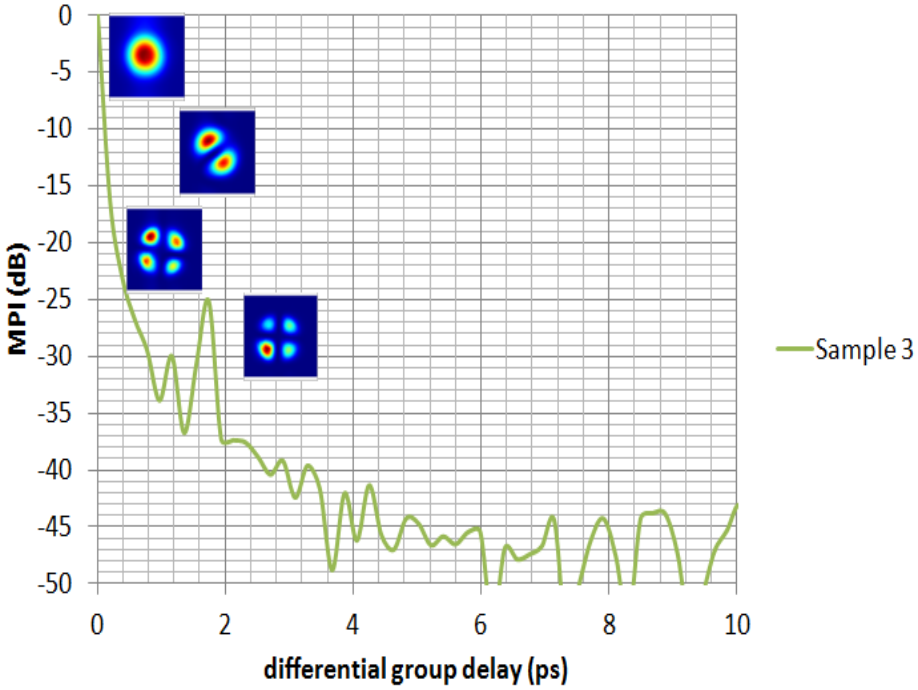

Figure 48: BDF Tapering/Splicing Sample 3 (cleave angles 0.1-0.1 deg).

*The up-tapered structures of this paragraph have been materially tapered and spliced by Dr. Yuthat Cho SPI Lasers.

3.3 Splicing optimisation

The acquisition speed and the on line-processing capability of the developed setup, as explained in 2.2.2.2, permits the usage of S^2 for splicing optimisation; almost in real time. S^2 technique has proven to be very useful in optimising splices between dissimilar fibres, particularly SMF to FMF. The S^2 has therefore been complemented with a fusion splicer as shown in Figure 49.

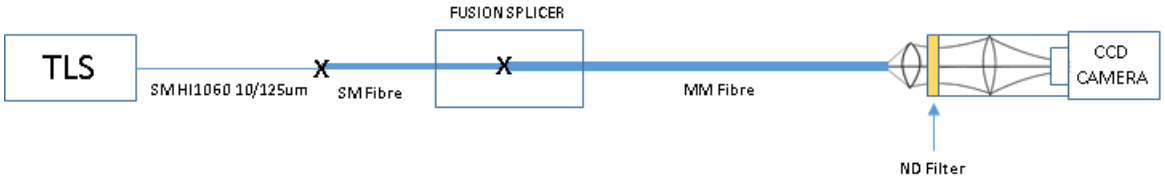

Figure 49. Splice optimisation setup utilising S^2 measurement.

Targets for splicing, when formulating splicing receipt for similar or dissimilar fibres, vary greatly. A target for instance could be minimising the splice loss between similar SMF. When splicing dissimilar fibres (e.g. SMF to MMF) another target could be maximising the modal excitation of HOMs, or conversely minimising it. We anticipate that, minimising the HOMs excitation at the splice between SMF and FMF is of great importance in the development of our HPFLs and MOPAs. To achieve a particular target, fibres preparation before splicing and arc fusion splicer settings have to be chosen accordingly. The amount of parameters that can be set on a modern splicer is quite vast; arc duration, arc power, overlap between fibres, prefuse duration and power, stuffing speed, position of the electrodes, sweep speed, tension post arc, to name a very few compared to all the available settings. However, in very abstract terms, a splicing procedure can be subdivided in consecutive phases. The S^2 is adopted to track the evolution of the modal excitation, in between these phases. In section 3.3 and its subparts, we will focus on empirical evidences, drawing intuitive conclusions. A more rigorous explanation of the measurement will be presented in 3.4, where a theoretical model will be presented to describe the propagation of the field across the splice.

3.3.1 Effect of the arc duration

At the splicing point, we substantially alter the guiding property of the fibres. As explained in 3.1.2, thanks to diffusion of dopants, different amount of heat provided to the

fibre result in different variation of the index of refraction. We expect therefore that, at the splice between a SM-FMF, the FMF modal excitation will depend upon arc discharge duration. In the following experiment, we use a ring of fire fusion splicer, FITEL-S184PM. This splicer utilises three electrodes generating an arc discharge that encircles uniformly the fibres. Plasma discharge is not in contact with the fibres, but around the fibre. Splicer can be finely calibrated to ensure heat symmetry of the arc discharge surrounding the fibre [122, 123]. The modal excitation between the same SM-FMF couple has been measured repeating the splice six times, keeping the arc power constant, but using six different arc durations. IOR profiles of the fibre used, will be provided in great detail in section 3.4. Figure 50 shows the MPI interferogram obtained with the six arc durations. Practically, re-splicing, involved stripping and re-cleaving, resulting in a fibre shortening of 15 cm minimum each time. In Figure 50 the differential group delay has been normalised to the exact fibre length at the moment of the six splices (hence x axis unit is ps/m). Without length normalisation, peaks comparison would have been uneasy; peaks would have not been overlapped, but shifted according the fibre length at the moment of the splice. Figure 51 and Figure 52 extract the MPI peaks value of the MPI interferogram and plot them against the arc duration for LP11 and LP02 respectively. Whilst no evident correlation is found between arc duration and LP11 excitation, the LP02 excitation has a minimum at an arc duration equal to 7 seconds.

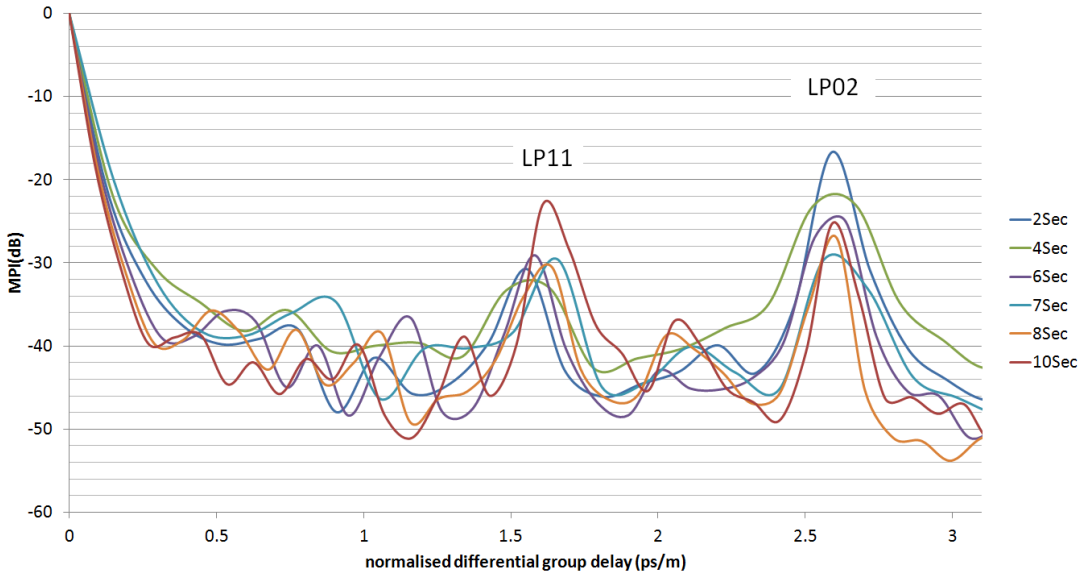

Figure 50. MPI interferogram vs arc duration

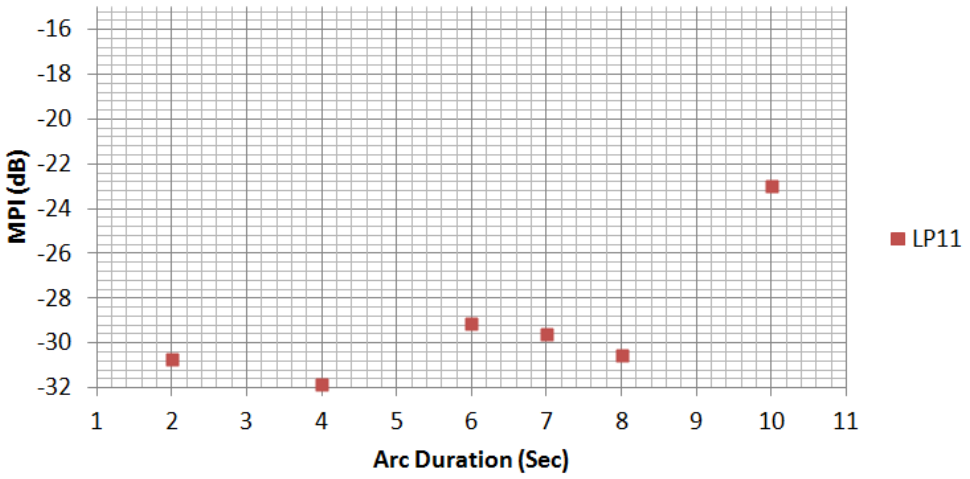

Figure 51. LP11 excitation versus arc duration

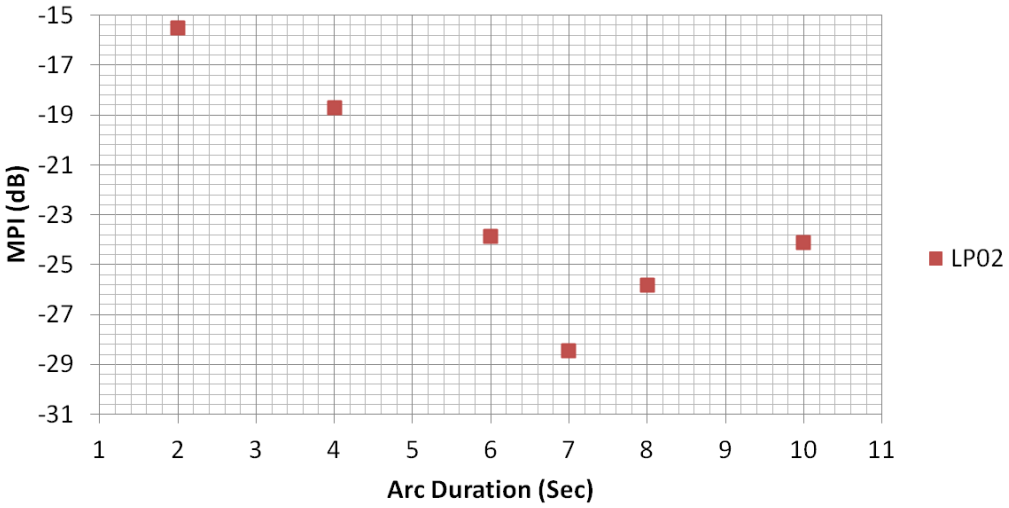

Figure 52. LP02 excitation versus arc duration

S^2 measurement cannot provide absolute values for the LP01 power, but just the relative power of the HOMs respect to the LP01. However, since the excited modes this FMF are just three (namely LP01, LP11 and LP02), and that the LP11 does not seem to depend on arc duration, conservation of energy suggests that having found a minimum for the LP02 should correspond to a maximum for the LP01. This would be rigorously true if we did not excite radiation modes. A more immediate evidence of the presence of this minimum has been measured with a second method; this does not require re-stripping and re-cleaving of the fibre. Always utilising FITEL-S184PM and the same SMF-FMF couple of the experiment

above, we use an initial arc of 4 seconds, joining the fibres, and then a series of shorter re-arcs lasting one second each. Between each re-arc, the modal excitation is measured.

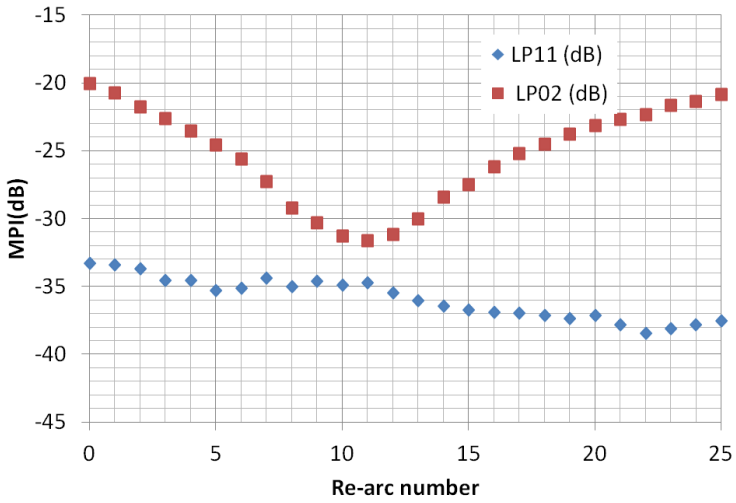

Figure 53. MPI values obtained by re-arching.

Figure 53 shows the results obtained with the re-arcing method. Equally, also with this method, the LP02 has a minimum in correspondence of a certain amount of heat provided to the fibres. LP11 does not seem to vary as much as the LP02 upon re-arcing, this would rather suggest that LP11 excitation has been imprinted at moment of the first splice, and therefore it can be argued that LP11 excitation depends on cleave angles, relative core-clad concentricity/positioning of the fibres and arc discharge symmetry. In Figure 53, the point at 0 is that obtained after the initial arc, that joining the fibres. The minimum of the LP02 occurs at re-arc number eleven: the minimum has been reached after a four second initial arc, plus another eleven arcs lasting one second each. If one sums the nominal arc durations as such, then conclusion would be that the necessary arc duration to optimise the splice is fifteen seconds (four plus eleven). This would disagree with the seven second obtained without re-arcing (results of Figure 52). This apparent disagreement is just the result of the thermal inertia of the glass and the electrical turn on time of the electrodes. Because of this, the one second re-arcs have an effective contribution of 0.3 seconds each. For instance, starting with initial arc duration of 3 seconds requires about 14 re-arcs to reach the minimum, staring with 5 seconds initial arc, would requires 7 re-arcs and so on.

In the next experiment we used a FUJIKURA FSM-100M fusion splicer. This splicer has only two electrodes. Six splices have been performed on the same SMF-FMF couple. For each of the six splices we used the same initial arc discharge. After joining the fibres by mean of the same initial main arc, each splice has undergone a series of re-arcs lasting all one second, but having six different currents (Figure 54). Currents of the re-arc are expressed in the units of the splicer's vendor (Bit) and are relative to the current used for the main arcs (common to all splices and equal to 254 Bits).

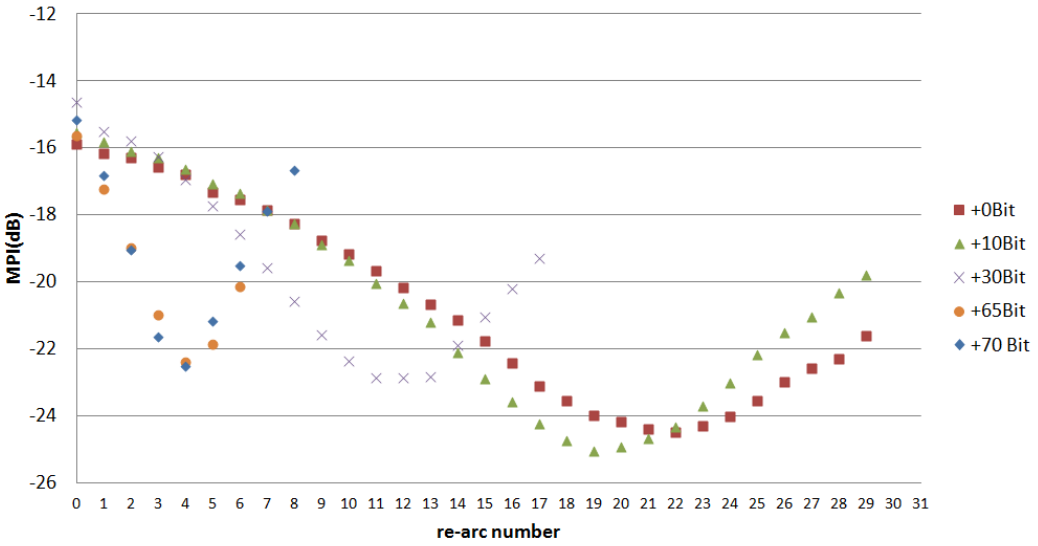

Figure 54. LP02 obtained with re-arcs having different currents.

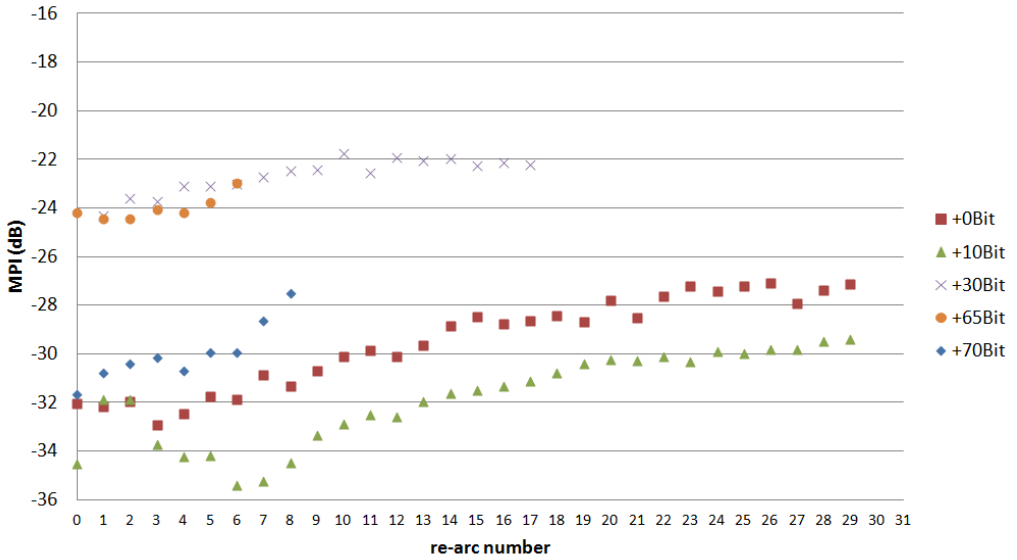

Figure 55. LP11 obtained with re-arcs having different currents.

As evident from Figure 54, regardless of the re-arc current, a minimum for the LP02 can always be found in all six cases. Furthermore, the number of arcs required to find the minimum diminishes when the arc current (and temperature) increases. This proves unequivocally that there is a constant amount of heat (energy) to be provided to the fibre to minimise the LP02 excitation. This was forecast in the concluding remarks of paragraph 3.1.2, when talking about different temperatures and arc durations couples leading to the same diffused IOR profile for the fibre. In Figure 55, upon re-arcing, the LP11 does not undergo a variation as big as that of the LP02. LP11 has the tendency of going up with re-arc number. It is easy to imagine that with only two electrodes; the arc discharge is intrinsically more unstable and that this system cannot guarantee circular heat symmetry around the fibre. This makes the LP11 excitation worse and worse upon re-arcing, perhaps heating the fibre only on one side, creating a increasingly stronger phase plate. This increase of the LP11 does not happen when re-arcing with the three electrodes FITEL-S184PM (Figure 53). Aspects of the splicing capability for the two above-mentioned FS will be clarified in a later section.

3.3.2 Effect of fibres concentricity and cleave angles

As highlighted in the previous section, arc duration choice does not seem to affect predictably the LP11 contents coupled at the SMF-FMF splice. LP11 mode is non centrosymmetric mode. If the splice were geometrically ideal, LP11 could never be excited by the centrosymmetric LP01 coming from the SMF. For this reason, we must find the causes of LP11 excitation in the lack of symmetry of the splice. Lack of symmetry can be due to: bad claves resulting into deformation and residual stress at the splice, bad core-cladding concentricity of the fibres, and asymmetrical diffusion of dopants at the splice point (both transversal and longitudinal) .The latter point will be discussed in 3.3.4 when discussing about arch discharge symmetry and fusion splicers' quality. In the experiment of this chapter, two SMFs having different core cladding concentricities have been re-spliced to the same piece of FMF ten times each, for a total of twenty splices. From another independent measurement made by the fibre department area (by mean of an Optical Fibre Analysis System - PK2500 by Photokinetics), it was known that SM fibres core clad centricities were 0.14µm for SMF1, 0.58µm for SMF2. FMF's core clad concentricity was 0.11µm.

For each splice, cleave angles and modal excitation has been recorded. The splicing receipt for this experiment, adopts an optimised arc duration that minimise the LP02 excitation (as explained in 3.3.1). The FITEL splicer aligns fibres using cladding alignment by mean of image processing. The arc of the particular receipt used in the experiment is not exactly located in the middle of the fibres, but 50µm onto the FMF (Figure 56). This is purely for historical reasons, as this particular splice recipe has been adopted by SPI for several years.

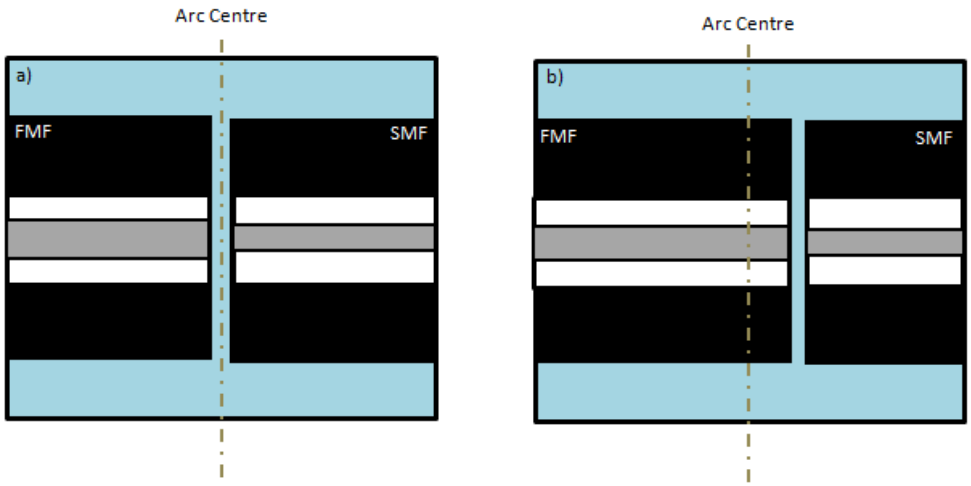

Figure 56. a) Arc discharge located in the middle of the fibre.b) Arc discharge located 50µm on the FMF (as used in the experiments of this chapter)

The result of splicing ten times SMF1 is shown in Figure 57.

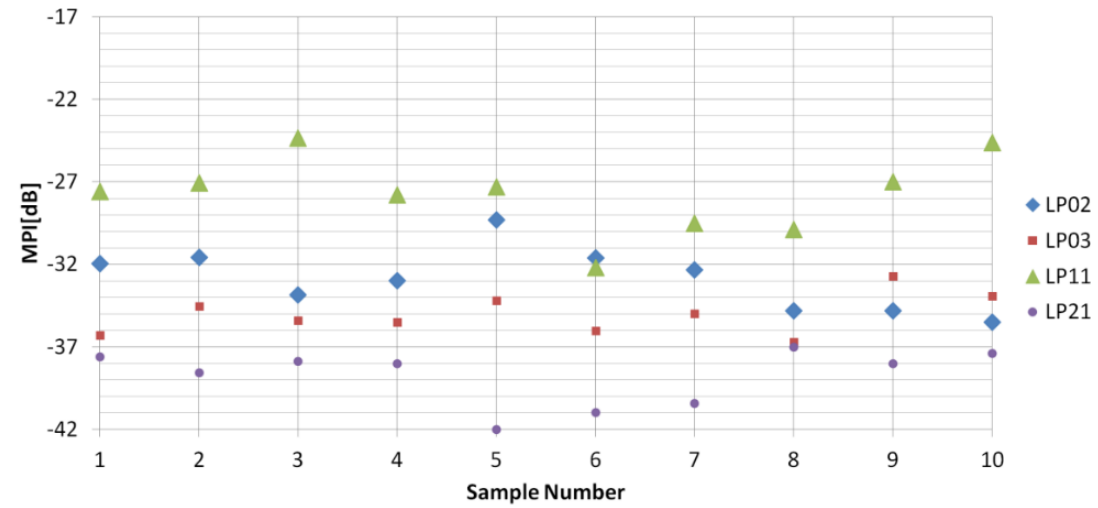

Figure 57.SMF1-FMF splice. Modal Excitation over 10 splices.

From the splice data of Figure 57, the following table has been produced.

	LP02	LP03	LP11	LP21
Average MPI over 10 splices[dB]	-32.5	-34.9	-27.2	-38.5
Relative Power of HOMs (Total Power = 1)	0.00056	0.00032	0.001914	0.000141
Tot Relative Power HOM	0.002946			
Power Left To LP01 % (Overestimated)	99.71			
Loss LP01 %	>0.29			

Table 2. SMF1-FMF splicing. Average modal excitation and LP01 loss estimation.

S^2 technique does not measure directly LP01 excitation. However, if we invoke energy conservation and recall the existence of radiation modes coupled at the splice, we can (under) estimate the loss of the LP01 mode. In this view, for SMF1, LP01 loss is certainly bigger that 0.29%. The result of splicing ten times SMF2 as shown in Figure 58.

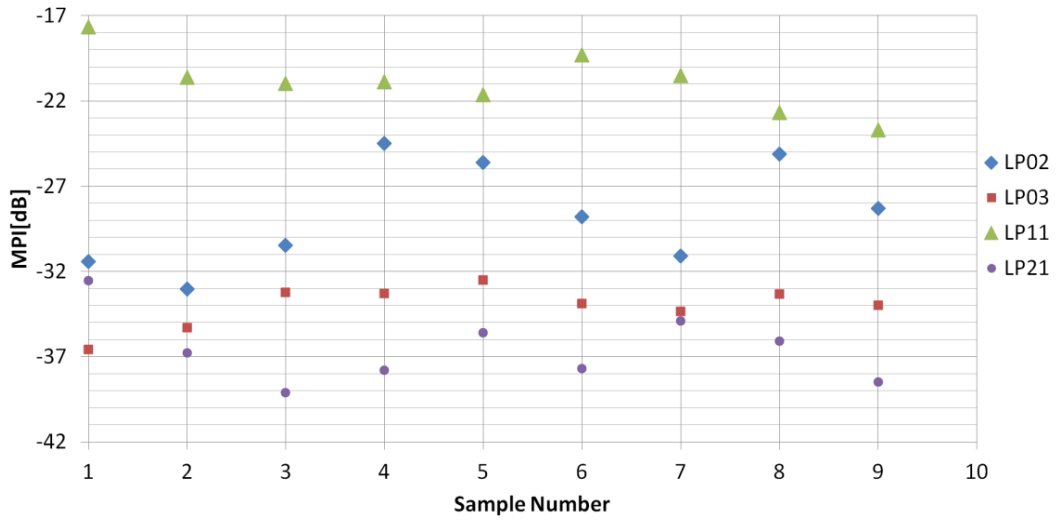

Figure 58. SMF2-FMF splice. Modal Excitation over 10 splices.

From splice data of Figure 58, the following table has been produced.

	LP02	LP03	LP11	LP21
Average MPI over 10 splices[dB]	-27.8	-33.9	-20.6	-36.1
Relative Power of HOMs (Total Power = 1)	0.00167	0.00040	0.00878	0.00024
Tot Relative Power HOM	0.011108			
Power Left to LP01 % (Overestimated)	98.89			
Loss LP01 %	>1.1			

Table 3. SMF2-FMF splicing. Average modal excitation and LP01 loss estimation.

For SMF2 we estimated LP01 loss to be bigger that 1.1%.

Comparing the performances of the two SMFs we can clearly see that the modal excitation of the LP11 is essentially bigger for the less symmetrical SMF2 (worse core clad concentricity). As result, the expected loss for the LP01 is worse for the SMF2 than with SMF1.

Average LP02 excitation also differs between the two fibres. This is due to the fact that SMF2 splices were performed one day after those of SMF1. Due to inattention, the second day splicer power was not re-calibrated, so the amount of energy provided to the two fibres was not exactly the same. As explained in 3.3.1, a little drift in the arc power makes the splicing process no longer optimised for LP02 minimisation. After the splicing for the SMF2, splicer was re-calibrated and its heat was 8% lower compared to the first day; this variation of heat is compatible with the variation of LP02 observed between the two fibres. Nevertheless, even if splicer was still calibrated and we had scored in average -32.5dB also for the LP02 of SMF2, calculation would have led to a loss for the LP01 of 1% (not much different from 1.1%). This is because, from linear loss point of view, the main difference between fibres is due to the LP11 ranging between -20.6dB and -27.2dB, rather than the LP02 ranging between –27.8 and –32.5dB.

In the remaining part of this chapter we will focus our attention to the correlation between cleave angles and modal excitation. Here we refer to the cleave angles the fibres had before being spliced together (as measured by the splicer) and modal excitation resulting from that splice. The result for SMF1 (good concentricity fibre) will be presented first (Figure 59, Figure 60). We will use the squared Pearson coefficient (R^2) as an estimator of the linear correlation between cleave angles and modal excitation.

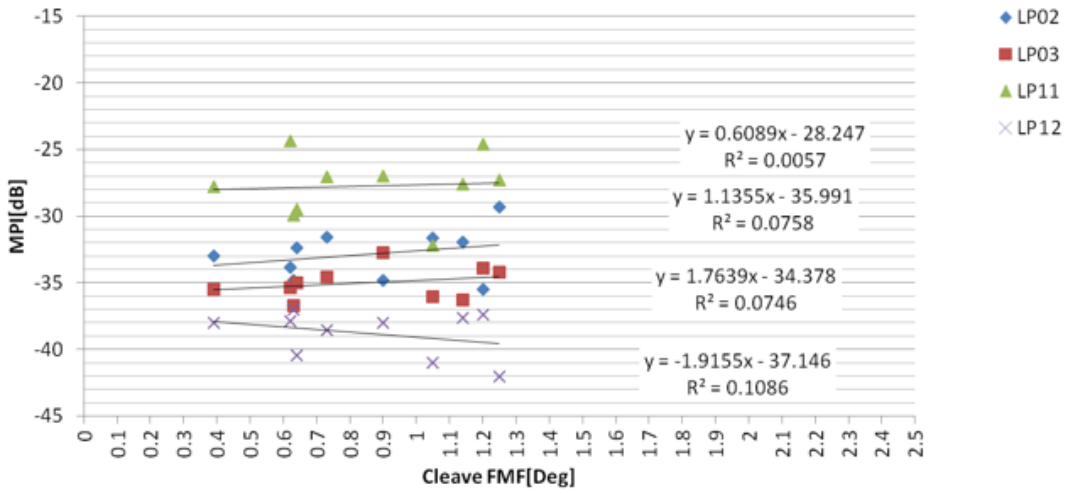

*Figure 59. SMF1-FMF splicing. Correlation between **F**MF cleaves and modal excitation.*

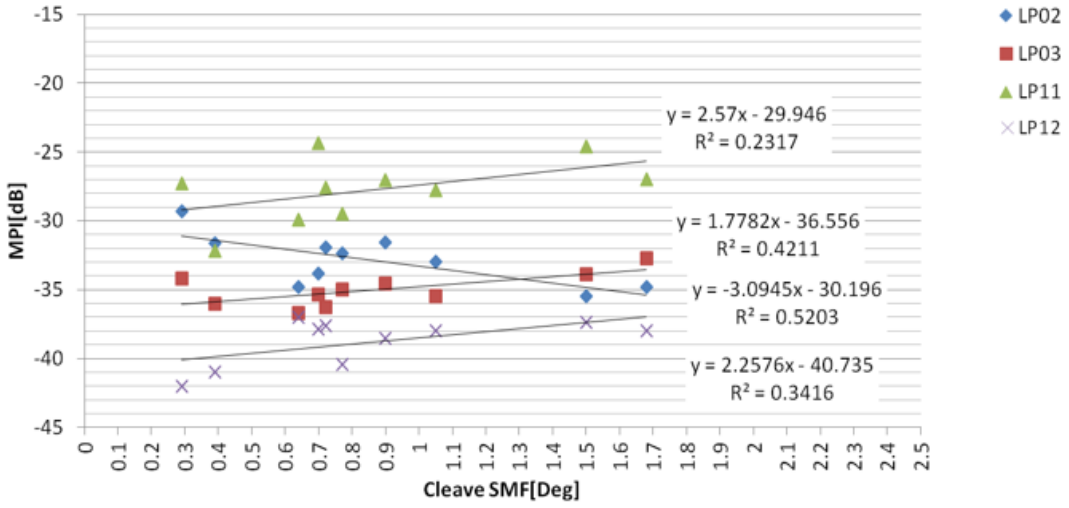

*Figure 60. SMF1-FMF splicing. Correlation between **S**MF cleaves and modal excitation.*

Figure 59,Figure 60 show the correlation between cleave angles (had by the fibres before the splice) and modal excitation achieved upon splicing; this for both SMF and FMF cleave

angles respectively. Apparently SMF angles (Figure 60) correlate better then FMF angles (Figure 59) with modal excitations (R^2 coefficients much bigger for the SMF cleave angles). To explain this, we need to remember that the arc is longitudinally shifted 50µm over the FMF (Figure 56). This makes SMF colder than FMF during the arc discharge. After fibres consolidate, SMF (colder during splice) will retain more the angles it had before melting than the FMF (hotter during splice). For this reason, LP11 MPI correlates more with the SMF cleave angles than with the FMF cleave angles. We can certainly conclude that, in case of good fibre centricity (like in SMF1), the bigger the cleave angle the bigger the LP11 excitation.

The result for SMF2 (bad core cladding concentricity fibre) will follow.

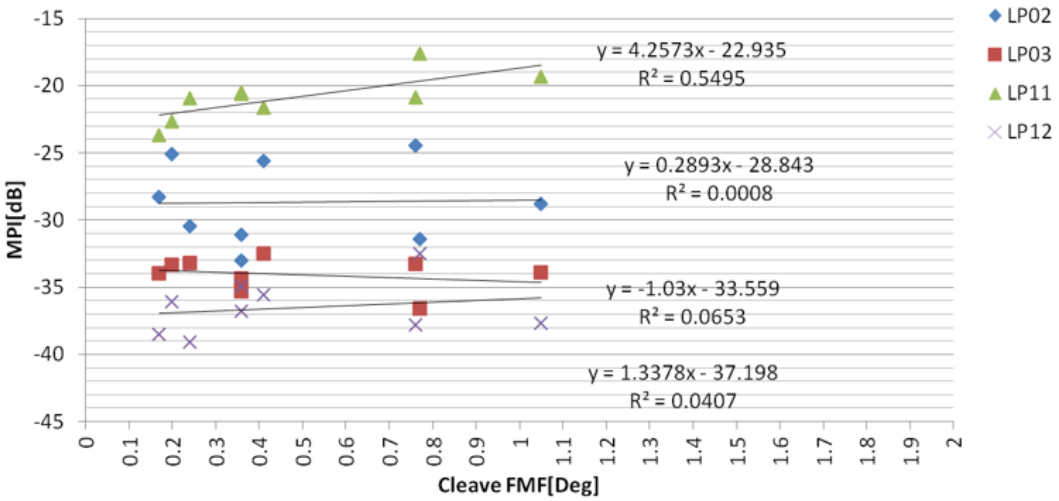

*Figure 61. SMF2-FMF splicing. Correlation between **F**MF cleaves and modal excitation.*

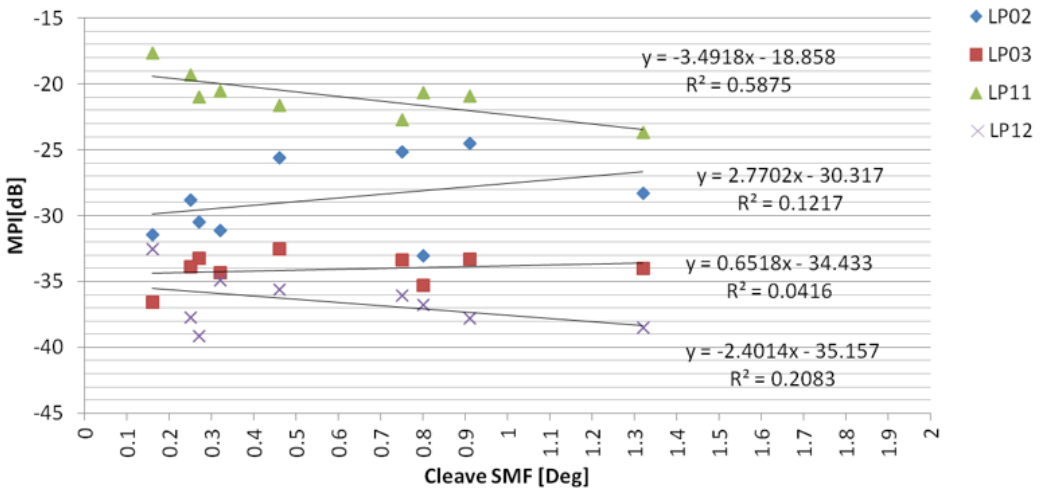

*Figure 62. SMF2-FMF splicing. Correlation between **S**MF cleaves and modal excitation*

For SMF2 also, SMF cleaves correlate better than FMF cleaves with modal excitations. For SMF2, it would seem like that the bigger the cleave angles, the smaller the LP11 excitation. However, for SMF2 (bad core clad concentricity), the symmetry is already deterministically broken because of the two fibres have different centres for their cores. In addition, cleave angles also have effects on symmetry. For SMF2, we have therefore two separate effects breaking the symmetry; for this reason, 10 splices are too few to be statistically meaningful. However, paradoxically, one could extrapolate that, in presence of bad core-cladding concentricity, an acute cleave angle can result in a smaller LP11 excitation, correcting therefore the effect of lack of concentricity (sample with 1.3 Deg in Figure 62 has the smallest LP11 excitation of the set).

3.3.3 Effect of transversal sweeping arc discharge.

Modern fusion splicers implement several functionalities. The Fujikura FSM-100M, allows keeping the arc discharge turned on whilst both fibres are monolithically shifted under the arc discharge (sweeping arc). In the following experiment, SMF and FMF are first joined together and then subjected to sweeping arcs. We programmed the splicer so that, for each sweeping arc, the fibres move only in one sense and do not go back at the end of the sweep. For every sweep performed, the perturbed IOR of the FMF will becomes increasingly longer. Without getting into the details of the splicing program settings, we just mention that arc current of the sweeps was comparable to that of the first joining splice and that each transversal sweep increases the perturbed length of 50µm. After the first joining arc, and in-between each arc sweep, the modal excitation at the output of the FMF was measured.

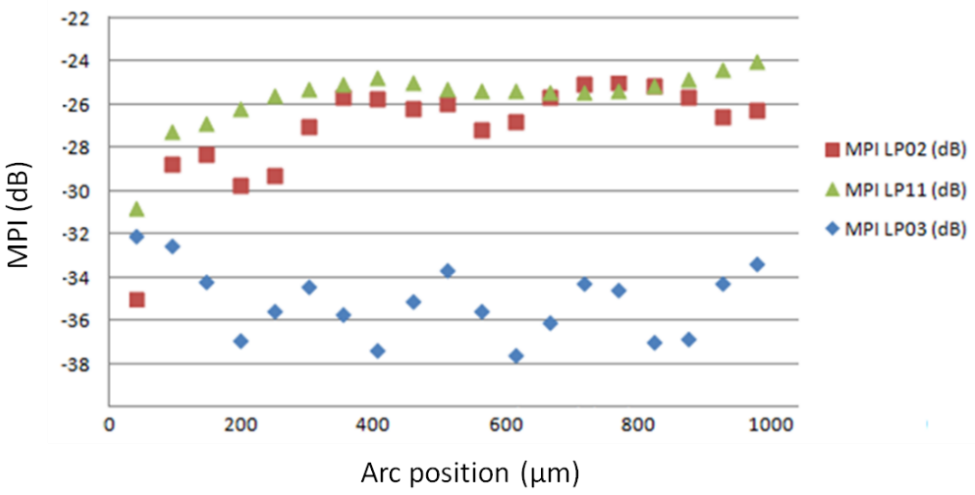

Figure 63. Effect of transversal sweeping. Arc position is relative to joining point of the two fibres (0 µm).

In Figure 63, the modal excitation of the LP02, LP11 and LP03 has been tracked against the arc position reached on the FMF. The modal excitation is periodical with the length of the perturbed area (e.g. position reached by the arc onto the FMF) and each mode has a different periodicity. We can see that the LP03 has the fastest periodicity, followed by LP02 and then LP11. From Figure 37, we see that the effective IOR difference between LP01 and the HOMS is bigger for the LP03, followed by LP02 and then LP11. This suggests that modes are beating in the perturbed area and that the beating length depends on the effective IOR of the modes, relative to the LP01. This empirical observation will be clarified in the theoretical explanation, dealing with the propagation of the field in the splice/perturbed area.

3.3.4 Qualification of fusion splicers for large area fibres splicing

Usage of increasingly bigger fibres has become ubiquitous in HPFL and MOPAs [124-127]. Bigger cores are required to minimise non-linear effects. Consequently, larger claddings are required to minimise micro-bending loss in presence of bigger cores and low NA [128, 129]. FMF used in this work have core diameters size of about 24µm and cladding diameter size of 200 µm respectively (Figure 37); passive fibres for the pump power transport have claddings up to 250µm. Normal fusion splicers developed for common telecommunication fibres (e.g. 6µm core, 125µm cladding), are not adequate to splice our fibres. SPI Lasers moved from telecom industry to the HPFL arena in the year 2004, so no old telecom splicers were available and have been tested on the fibres of this work.

Nonetheless, we have measured differences between splicers intentionally manufactured to splice large diameter fibres. We expect that good heat symmetry, provided by the splicers, will result in a more symmetrical diffusion of the dopants in the fibre; hence a more symmetrical index of refraction in proximity of the splice. In the next experiment, the same FMF has been spliced two times with discharges of similar energies, to the same SMF: once with a two electrodes FUJIKURA FSM-100M splicer and once with a Ring Of Fire (ROF) - three electrodes FITEL-S184PM. For both splices, the 2D index of refraction of the FMF has been measured 50µm away from the splice via IFA-100 Refractive Index Profiler.

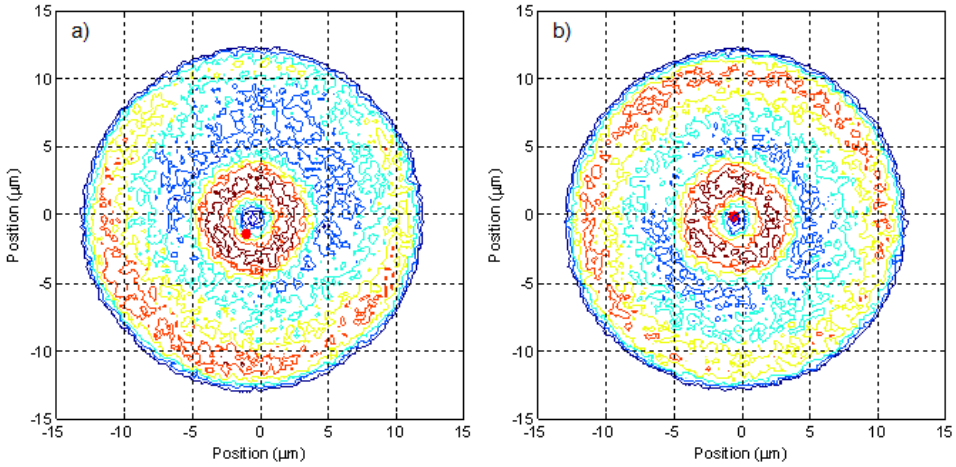

Figure 64. 2D IOR measurement on the core of the FMF fibre 50 µm away from the splice. a) two electrodes splicer b) ROF splicer. For the max/min IOR of the figures refer to core of the Figure 34.

Figure 64 shows the 2D index of refraction profiles obtained with the two splicers, the figure also shows the centre of mass of the two figures (red dot). The index of refraction obtained with the ROF splicer is more symmetrical than obtained with the two electrodes splicer. Please refer to Figure 65 for the following discussion. In the two electrodes configuration, the accelerated plasma produced by the discharge hits the fibre and surrounds the fibre only from one side resulting in an asymmetric supply of heat. The splicer provides two tools corroborate the above statement:

1) A “hot image” of the fibre is recorded by an internal camera during the arc discharge.
2) The nominal offset between fibre axis and electrodes common axis, can be varied. This nominal offset is called VH parameter (Vertical Height).

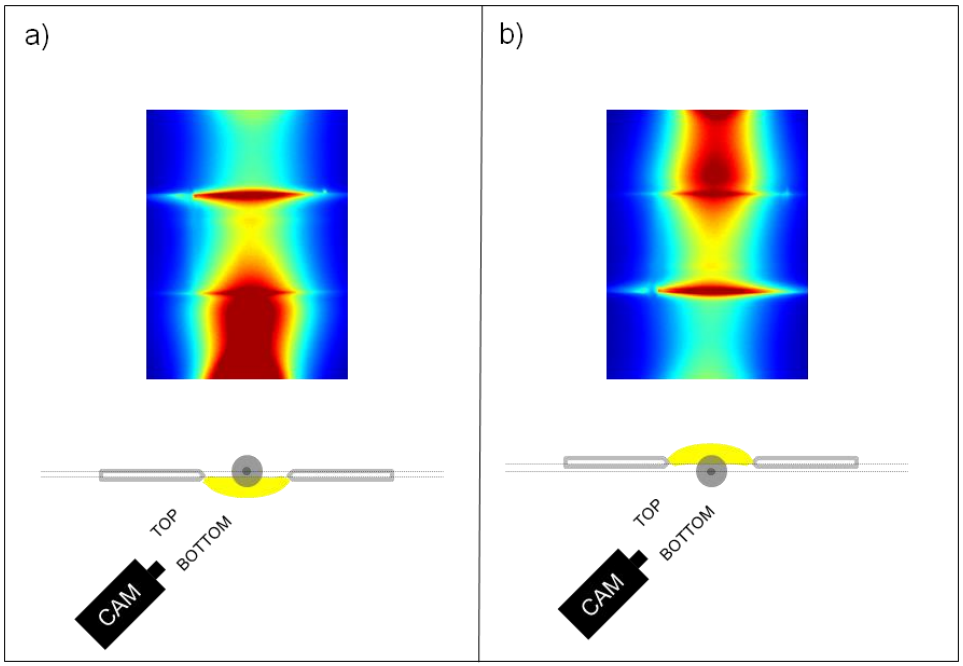

Figure 65. Two electrodes splicer configuration with "hot image" during the discharge a) VH<0 and b) VH> 0.

In Figure 65 a, the fibre is above the electrodes' axis, for this reason the "hot image" is colder on the top and hotter on the bottom. Conversely in Figure 65 b, the fibre is below the electrodes axis; in this case the "hot image" is hotter on the top and colder on the bottom(VH>0). Dubious about the alignment of the electrodes, the author of this work developed a software to measure the VH parameter correctness. Subsequently this software has been adopted by SPI for the routinely calibration of all FUJIKURA two electrodes splicers. In the "V-Height calibration" software, a number of discharges is tested for each VH position to test. After each discharge, an image processing routine establishes if the fibre was hot up or hot down.

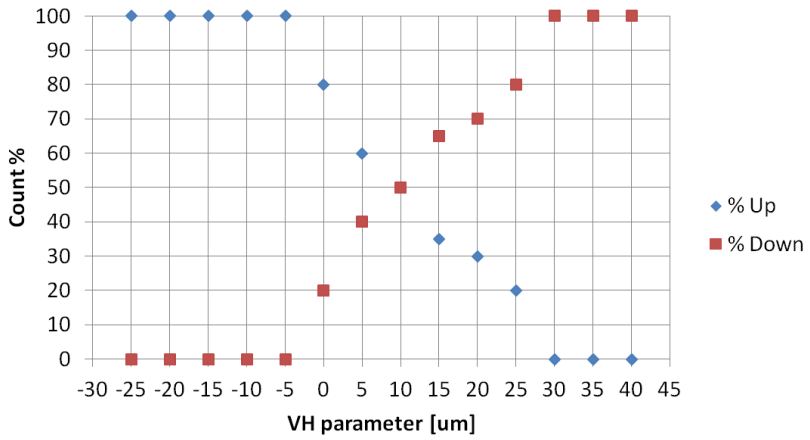

Figure 66. V-Height software. Optimum VH parameter equal to 10 (fibre and electrodes' axis physically aligned)

In Figure 66, 10 arc discharges have been tested for VH positions ranging from -25µm to 40µm. For low values of the VH, the fibre was “hot up” 10 times out of 10 (100% Up, 0% Down). Conversely, for high values of VH, fibre was “hot up” 0 times out of 10 (0% Up, 100% Down). At VH = 10, the fibre resulted to be 5 times “hot up“ and 5 times “hot down”.

After dealing with the R&D of FUJIKURA, we found out that the VH parameter can drift with time. This is due to the usage of several stacked motorise stages driven without encoders. This just means that the optimum VH parameter can be different from zero when fibre and electrodes are perfectly aligned, in this case fibre and electrodes’ axis were physically aligned for VH =10. However, even at VH =10, hot images were either of kind a) or of kind b); this highlighted the intrinsic limitation of the two electrodes splicer. Even with perfect alignment, the plasma particles will pass either from one side or from the other of the fibre, resulting in an asymmetric supply of heat.

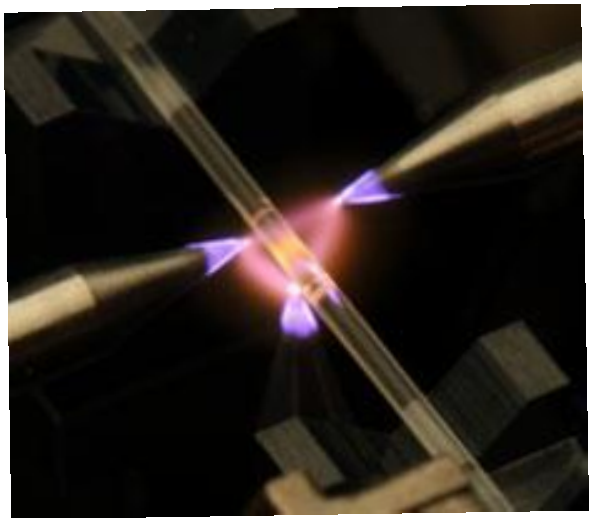

Figure 67. Three electrodes splicer configuration (ring of fire technology[122]

In the ROF technology, the three electrodes are circularly excited with a three-phase current creating a triangular arc discharge. Differently from the two-electrodes technology, here the created plasma is not accelerated toward the fibre, but surrounds it uniformly. In the ring of fire technology, the heat is provided to the fibre solely by the radiation of the recombining plasma. The vendor of the ROF splicer states that because of lack of plasma collision, ROF technology provides a better uniformity of the supplied heat, resulting in a more circular index of refraction in proximity of the splice[122]. This statement has been in some way empirically verified (Figure 64). As pointed out in 3.3.2, lack of symmetry at the SMF-FMF point of contact, couples the LP11 mode and reduces the power available for the

coupling of the LP01 mode. When re-arcing with two electrodes, the LP11 grows with the heat provided to the fibre /with the number of arcs (e.g. Figure 55). In other words, the two electrodes technology limitation is exacerbated when using longer arcs. Conversely, with the ROF, it has been repeatedly observed that the LP11 coupling does not change much upon re-arcing.

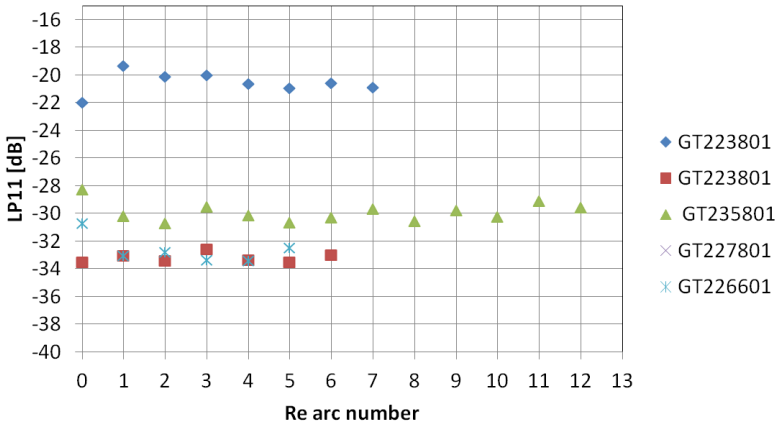

Figure 68. LP11's MPI obtained on several FMF part numbers upon re-arcs with the ROF splicer.

In Figure 68, five different FMFs have been spliced with ROF to the same SMF. After an initial joining arc of 4 seconds, the fibres have been re-arced with arcs of one second duration each. At the end of the first main arc, and in between re-arcs, the LP11 excitation has been measured. With the ROF technology, the LP11 does not vary much with the re-arc and conserve the initial value it had after the first joining arc. This value of LP11 excitation, explained in 3.3.2, depends on fibre concentricity and angles of cleaves. In other words, with the ROF technology, re-arcing or usage of longer arcs does not degrade the LP11 coupling and therefore is a better candidate to splice HPFLs and MOPAs.

3.4 Field propagation across tapered areas

In this part of the thesis, we develop a theoretical framework able to explain most of the empirical evidences highlighted in section 3.3. We will resolve the Maxwell equation in a fibre whose guiding property vary along the length. Physical tapers with varying core size or zone with altered index of refraction such as in presence of diffusion splices will both be called, for simplicity, tapers. This theory will then be applied to samples of splices of which we have measured modal excitation (via S^2) and refractive index in various points along the spliced region (via IFA).

3.4.1 Theory

To calculate the field propagation in a waveguide whose guiding property are not constant along its length, we use the concept of local modes [92, 93]. Let us assume the IOR of the fibre to be centrosymmetric, but varying along z (e.g. IOR = IOR(r, z)). Local modes in a point z* are those the fibre would support if IOR(r, z) = IOR(r, z*) $\forall z$. Like normal fibre modes, also local modes are characterised by field distribution and effective index of refraction.

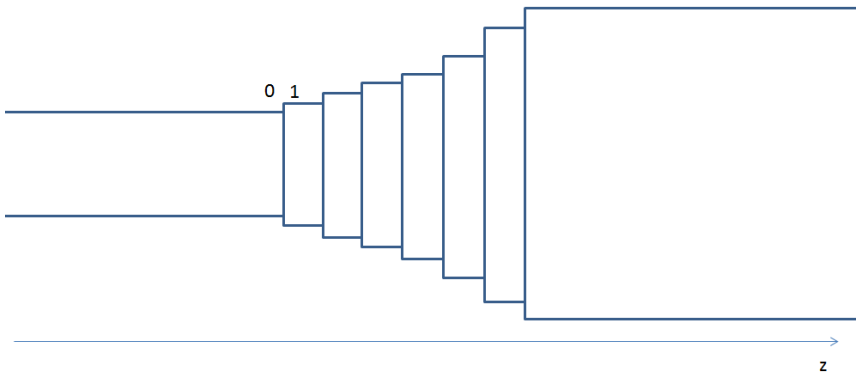

Figure 69. Fibre with guiding property varying along the z

Referring to Figure 69, we can think to divide the tapered zone in layers; within these layers, index of refraction will be assumed constant. At the left and right of the interfaces between layers, we have two fields, respectively denoted with E_0, E_1. We will assume field linearly polarised, therefore the notation of the theory is scalar.

Continuity of transversal components of H and E, is imposed at every interface

$$E_0=E_1 \text{ and } H_0=H_1 \qquad (3.4.1.1)$$

At each interface, decomposing the field in local modes, (3.4.1.1) becomes

$$\sum_i E_{i0} = \sum_i E_{i1} + \mathrm{o}(E_0) \qquad (3.4.1.2)$$

$$\sum_i H_{i0} = \sum_i H_{i1} + \mathrm{o}(H_0) \qquad (3.4.1.3)$$

Here, $\mathrm{o}(E_0)$ and $\mathrm{o}(H_0)$ have been added to remind the reader about the presence of radiation modes. Radiation modes are lossy, they capture the part of the incoming field distribution that cannot be coupled into any of the modes of the subsequent part of fibre. Without the claim of being exhaustive, we cite a simple example. For instance, if we splice two dissimilar SM fibres, having very different LP01s, we will have that these modes will not overlap well and we will get a lossy splice. The lost power is captured by radiation modes, these modes leak the light in the cladding of the fibre. If transitions across interfaces are not too abrupt, we can imagine that the energy transported by the modes of the '0' zone will be entirely captured by the modes of zone '1'. In the case of smooth transitions, radiation modes can be ignored. Ignoring radiation modes is the approximation we will make in the development of the theory, but we will recall the approximation's repercussion in the application of the algorithm that calculate the propagating field. Despite this approximation, we will see that our model can explain most of the useful measurements of this thesis.

Applying $\iint..\times H_{j1}^* dxdy$ to (3.4.1.2) and $\iint..\times E_{j1}^* dxdy$ to (3.4.1.3), we get

$$\iint \sum_i E_{i0} \times H_{j1}^* dxdy = \iint \sum_i E_{i1} \times H_{j1}^* dxdy \qquad (3.4.1.4)$$

$$\iint \sum_i H_{i0} \times E_{j1}^* \, dxdy \; = \iint \sum_i H_{i1} \times E_{j1}^* \, dxdy \qquad (3.4.1.5)$$

Due to orthogonality between local modes belonging to the same layer, right terms of (3.4.1.4) and (3.4.1.5) reduces to one sole integral, yielding:

$$\sum_i \iint E_{i1} \times H_{j1}^* dxdy = \iint E_{j1} \times H_{j1}^* dxdy \qquad (3.4.1.6)$$

$$\sum_i \iint H_{i1} \times E_{j1}^* dxdy = \iint H_{j1} \times E_{j1}^* dxdy \qquad (3.4.1.7)$$

Adding together the two sides of (3.4.1.6) and (3.4.1.7) we get:

$$\sum_i \iint E_{i0} \times H_{j1}^* dxdy + \sum_i \iint H_{i0} \times E_{j1}^* dxdy = \iint E_{j1} \times H_{j1}^* dxdy + \iint H_{j1} \times E_{j1}^* dxdy \qquad (3.4.1.8)$$

For transversal waves and for guided modes $H = E\frac{n_{eff}}{c\,u_0} = Ec\varepsilon_0 n_{eff}$, allowing us to rewrite (3.4.1.8) as

$$\iint E_{j1} \times H_{j1}^* dxdy + \iint H_{j1} \times E_{j1}^* dxdy = \frac{2n_{j1}}{c\,u_0} \iint E_{j1} \times E_{j1}^* dxdy \qquad (3.4.1.9)$$

Let us represent local modes with phasorial notation such that

$$\widetilde{E_\gamma}(x,y,z) = \alpha_\gamma E_\gamma(x,y) e^{-i\beta_\gamma z} \qquad (3.4.1.10)$$

With α_γ being a complex number and $E_\gamma(x,y)$a real function and by imposing

$$\iint E_\gamma(x,y) * {E_\gamma}^*(x,y)\, dxdy = 1 \qquad (3.4.1.11)$$

The power of the field is calculable as

$$P_\gamma = \frac{1}{2} c\varepsilon_0 n_\gamma \iint \widetilde{E_\gamma}(x,y) * \widetilde{E_\gamma}^*(x,y)\ dxdy = \frac{1}{2} c\varepsilon_0 n_\gamma \alpha_\gamma \alpha_\gamma^* \qquad (3.4.1.12)$$

With the phasorial representation right part of (3.4.1.9) becomes

$$\frac{2n_{j1}}{c\,u_0} \iint \widetilde{E_{j1}} \times \widetilde{E_{j1}^*} dxdy = \frac{2n_{j1}}{c\,u_0} \alpha_{j1}\alpha_{j1}^* = \frac{2n_{j1}}{c\,u_0} \alpha_{j1}\alpha_{j1}^* \frac{c}{c} = \frac{2cn_{j1}}{c^2\,u_0} \alpha_{j1}\alpha_{j1}^* = 2c\varepsilon_0 n_{j1}\alpha_{j1}\alpha_{j1}^* \qquad (3.4.1.13)$$

With the phasorial representation left part of (3.4.1.8) becomes

$$\sum_i \iint \widetilde{E_{i0}} \times \widetilde{H_{j1}^*} dxdy + \sum_i \iint \widetilde{H_{i0}} \times \widetilde{E_{j1}^*} dxdy = \sum_i \frac{n_{j1}}{c\,u_0} \iint \widetilde{E_{i0}} \times \widetilde{E_{j1}^*} dxdy + \sum_i \frac{n_{io}}{c\,u_0} \iint \widetilde{E_{i0}} \times \widetilde{E_{j1}^*} dxdy \qquad (3.4.1.14)$$

$$=$$

$$\sum_i \left(\frac{n_{io}}{c\,u_0} + \frac{n_{j1}}{c\,u_0}\right) \iint \widetilde{E_{i0}} \times \widetilde{E_{j1}^*} dxdy = \sum_i \left(\frac{n_{io}}{c\,u_0} + \frac{n_{j1}}{c\,u_0}\right) a_{i0}\alpha_{j1}^* e^{-i(\beta_{i0}-\beta_{j1})Z} \iint E_{i0} \times E_{j1}^* dxdy$$

Joining left and right part of (3.4.1.8) and (3.4.1.9) plus few trivial manipulation, we obtain

$$\sum_i \left(\frac{n_{io}}{c\,u_0}+\frac{n_{j1}}{c\,u_0}\right) a_{i0}\alpha_{j1}^{*} e^{-i(\beta_{i0}-\beta_{j1})Z} \iint E_{i0}\times E_{j1}\,dxdy = 2c\varepsilon_0 n_{j1}\alpha_{j1}\alpha_{j1}^{*}$$

$$\sum_i \left(\, c\,\varepsilon_0 n_{io} + c\,\varepsilon_0 n_{j1}\right) a_{i0} e^{-i(\beta_{i0}-\beta_{j1})Z} \iint E_{i0}\times E_{j1}\,dxdy = 2c\varepsilon_0 n_{j1}\alpha_{j1}$$

$$\sum_i \frac{\left(n_{io}+n_{j1}\right)}{2n_{j1}} a_{i0} e^{-i(\beta_{i0}-\beta_{j1})Z} \iint E_{i0}\times E_{j1}\,dxdy = \alpha_{j1} \qquad (3.4.1.15)$$

The final expression derived in (3.4.1.15) allows calculating amplitudes α_{j1} in a stepwise/iterative way. The power evolution of each mode P_γ can be tracked by applying the following passages. Let us define A_γ such as:

$$A_\gamma = \sqrt{\frac{1}{2}c\varepsilon_0 n_\gamma}\,\alpha_\gamma, \text{ so that} \qquad (3.4.1.16)$$

$$P_\gamma = A_\gamma * A_\gamma^{*} \text{ and } \angle A_\gamma = \angle\,\alpha_\gamma \text{ and } \angle E_\gamma = \angle\,\alpha_\gamma * e^{-i\beta_\gamma Z}$$

Let us multiply both side of (3.4.1.15) by $\sqrt{\frac{1}{2}c\varepsilon_0 n_{i0}}$

$$\sum_i \frac{\left(n_{io}+n_{j1}\right)}{2n_{j1}} \sqrt{\frac{1}{2}c\varepsilon_0 n_{i0}}\, a_{i0} e^{-i(\beta_{i0}-\beta_{j1})Z} \iint E_{i0}\times E_{j1}\,dxdy = \sqrt{\frac{1}{2}c\varepsilon_0 n_{i0}}\,\alpha_{j1} \qquad (3.4.1.17)$$

Obtaining

$$\sum_i \frac{\left(n_{io}+n_{j1}\right)}{2n_{j1}} A_{i0} e^{-i(\beta_{i0}-\beta_{j1})Z} \iint E_{i0}\times E_{j1}\,dxdy = \sqrt{\frac{1}{2}c\varepsilon_0 n_{i0}}\,\alpha_{j1} \qquad (3.4.1.18)$$

Multiplying the expression above for $\sqrt{n_{j1}}$ we finally obtain

$$\sum_i \frac{(n_{io} + n_{j1})}{2\sqrt{n_{i0} n_{j1}}} A_{i0} e^{-i(\beta_{i0} - \beta_{j1})Z} \iint E_{i0} \times E_{j1}\, dxdy = A_{j1} \qquad (3.4.1.19)$$

Equation (3.4.1.19) shows that, if local modes are known along every section of the tapered structure, we can calculate the local mode power evolution iteratively (in a stepwise manner). It is important to notice that the amplitude of a mode in the zone 1, A_{j1}, depends on the integral overlap between this mode and all the incoming modes of zone 0. From equation (3.4.1.19), it is also clear that, within the limits of this 1-D model, that assumes all local modes have the same axis along z, modes having different symmetry (e.g. LP01 vs LP11) will never couple power as the term $\iint E_{i0} \times E_{j1}\, dxdy$ will be null.

Single Interface, Simple case:

Let us take the case of a multimode straight fibre and let us virtually divide it two zones (0,1). Local modes of both zones will be the same. The integral overlaps across layers $\iint E_{i0} \times E_{j1}\, dxdy$ will be equal to one or zero when coupling respectively the same or different modes across the virtual interface. The terms $\frac{(n_{io}+n_{j1})}{2\sqrt{n_{i0} n_{j1}}} e^{-i(\beta_{i0} - \beta_{j1})Z}$ will be equal to one anytime overlap integral is also one. This simply says that in a straight multimode fibre, modes do not exchange power ($A_{i0} = A_{j1} when\ i = j$) and evolve with their own phases across the fibre.

Single Interface, Medium case:

Let us suppose we have a joint between two dissimilar multimode fibres, hence having different modes, but fibres are perfectly concentric and share the same centre. Across the joint, the integral overlaps $\iint E_{i0} \times E_{j1}\, dxdy$ will be null between modes having different rotational symmetry (e.g. between LP01 and LP11), but it will be not null and in general not unitary between modes with the same symmetry (e.g. between LP01 and LP02 or between LP01 and LP01). The terms $\frac{(n_{io}+n_{j1})}{2\sqrt{n_{i0} n_{j1}}} e^{-i(\beta_{i0} - \beta_{j1})Z}$ will not be be identically one, and these terms represent the optical impedance mismatch. Practicallly, when fibres are reasonably concentric and well aligned (same centre), only modes with the same rotational symmetry will exchange power. Namely, for every LP_{lp} couple of modes across the interface, only modes having the same 'l' will exchange power across the joint.

Single Interface, Complete case:

Let us suppose we have a joint between two dissimilar multimode fibres, and fibres are not perfectly concentric or do not share the same centre. In this case, the integral overlaps across the joint $\iint E_{i0} \times E_{j1}\, dxdy$ will be never null. This is because even modes having different symmetry (e.g. LP01 and LP11) will have their centre offset and therefore will not be orthogonal; hence exchanging power. This cannot be modelled by this 1D algorithm.

Multiple interface, Taper case and our working hypnosis:

A tapered zone is represented as a series of joint between dissimilar layers. In general, all the three cases above presented can happen at any of the layers. In diffusion splicing, if arc discharge is not centrosymmetric, the interfaces composing the taper will not have the same centre (i.e. taper is not straight) and there will be coupling between all the modes. When adopting three electrodes splicer, arc discharge is more centrosymmetric, taper is straighter, layers have the same centre and modes having different symmetry do not exchange much power. This is also been highlighted in 3.3 as we did not observe much power evolution of the LP11 upon discharging. As we will see in the next chapter, since the implementation of our algorithm relies on 1-D IOR measurements, we cannot measure offsets between interfaces. We will assume the taper reasonably straight. In this view, our model will be represented as a stack of layers falling within the "Medium case" as described above. The LP11 excitation at the beginning of the taper will be assumed (guessed in the third step of the algorithm described in 3.4.2) and we will be able to track only the power exchange between LP01 and LP02 and between LP11 and itself. This will be for most of the times a good approximation and our working hypothesis, given that:

A) The FMF we will analyse only strongly guides LP01, LP02 and LP11

B) Empirical evidence suggests LP11 is not exchanging a big amount of power with the LP01 and the LP02 (paragraphs of 3.3).

3.4.2 Algorithm implementation

Algorithm calculating field evolution across zones with varying guiding characteristics can be divided in four main stages.

1) Given a tapered zone or a spliced region, multiple 1D - IOR(r, z) are measured at different z along the interested region via IFA.

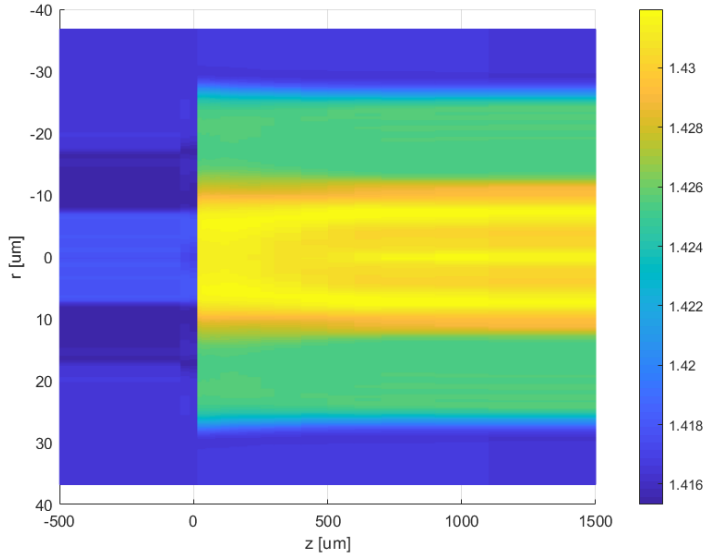

Figure 70. IOR measurement across a passive SMF (left) to an active FMF fibre (right) splice.

The IOR measurements in Figure 70 have been measured on a sample of diffusion splice between a SMF and a FMF (IORs like those presented Figure 35 and Figure 37 respectively). IORs in Figure 70 are those of the sample obtained with arc discharge of 8 seconds, presented in section 3.3.1 (Figure 50). The Z-axis, orthogonal to the page, is the index of refraction of the fibre. The Y-axis, is the fibres radius. In the X-axis, the 0µm point represents the contact point between the dissimilar fibres. IOR(r,z) has been measured at 20 discrete points, these are z = -500, -50-, -15, 15, 30, 60, 80,100, 133,166, 200, 250, 300, 400, 500, 600, 700, 900, 1100, 1500µm. In between these points, IOR(r,z) is assumed to be constant. In Figure 70, the effect of the dopants diffusion in the AF, as presented in 3.1.2, can be spotted up to +500µm away from the contact point. A SMF->FMF splice represent therefore a tapered region in the sense that guiding property evolve along the z direction. An arbitrary number of discrete IOR(r,z) slices can be measured via IFA, however IFA resolution along z is 20µm circa. Measurement takes 3 minutes for each IOR slice. As it will be clearer later, zones where IOR(r,z) changes fast with z (e.g. close to the splice on

the AF) must have a reasonably high spatial sampling rate, whilst zones where IOR does not change much with z (e.g. far away from the splice) can be under-sampled. Virtual IOR measurements can be fabricated and slotted in between IOR couples as an average in the following way

$$IOR(r,\bar{z}) = \frac{1}{2}[IOR(r,z_n) + IOR(r,z_{n+1})] \qquad (3.4.2.1)$$

With $\bar{z} = (z_n + z_{n+1})/2$.

The number of virtual IOR can be increased arbitrarily, fitting an increasing number of virtual measurements between each couple of real measurement. Adding virtual IORs increases the number of points and makes transitions across interfaces smoother. This, as it will be shown later, increases the algorithm accuracy by reducing the artificial radiation modes losses produced by the discretization process and reduces measurements' time. Given the spatial longitudinal resolution of the IFA, the closest measurement one can get is at 20µm away from the splicing point. Around z =0, two further virtual index of refraction $IOR(r,0^{\pm})$ can be fabricated. $IOR(r,0^{\pm})$ are obtained by linear regression of the two neighbouring $IORs$, from the two relative fibres. $IOR(r,0^{\pm})$ are fabricated at z = $\pm$1pm. Data like that show in Figure 70, with or without extra virtual IOR, can be provided to the algorithm.

2) For each IOR(r, z) provided, and therefore for each z, local modes are calculated* with the method presented in [130]. In the algorithm, local modes $'\gamma'$ are characterised by:

   a. Z position
   b. Normalised real fields $E_\gamma(r,z)$ such that

$$\int_0^{2\pi}\int_0^{+\infty} E_\gamma(r,z) * E_\gamma(r,z)\, r dr = 1 \qquad (3.4.2.2)$$

   c. Effective indexes of refraction $\beta_\gamma(z)$
   d. Amplitudes and phases of $\widetilde{A_\gamma}(z)$. These are yet not known at this stage.

*The part of the code calculating the modal shape and effective index of refraction from the IOR measurement (step 2) was implemented in Matlab by Dr. Fabio Ghiringhelli @SPILasers.

3) A boundary condition (power and phase) is assigned to the power of all local modes of the first '0' interface; defining therefore $\tilde{A}_{i0} \forall i$ at z=-500µm. Additionally, since the model is not capable of reproducing coupling between modes having dissimilar symmetry a guess excitation for LP1x modes can be injected at the first point after the splice (at z =0µm).

4) The $\widetilde{A_{j1}}$ for each subsequent z are calculated applying recursively (3.4.1.19), here expressed in cylindrical coordinates

$$\sum_i \frac{(n_{io} + n_{j1})}{2\sqrt{n_{i0} n_{j1}}} A_{i0} e^{-i(\beta_{i0} - \beta_{j1})Z} \int_0^{+\infty} E_{i0}(r,z) * E_{j1}(r,z)\, r dr = A_{j1} \qquad (3.4.2.3)$$

At any stage of the propagation, for every z, power and phase of each local mode 'j' can be tracked by evaluating respectively $|A_{j1}|^2$ and $\angle|A_{j1}$.

The presented propagation algorithm has been implemented in Matlab by the author of this thesis. From a programming point of view, local modes are implemented as class in the context of oriented objected paradigm. Complex amplitudes A_{j1}, those of a succeeding zone ('1'), are returned by a propagator function. The propagator function accepts, as argument, two pointers to local modes of zones ('0' and '1') plus an array of complex amplitudes A_{i0} representing the incoming modes. The so returned A_{j1}, will be used as new A_{i0} and fed again the propagator function to generate the subsequent A_{j1}. The procedure is iterated until the last IOR data provided is reached.

3.4.3 Algorithm benchmarking

In this paragraph, we will show the typical results of the application of the above presented algorithm. Particularly, the splice sample utilised to introduce the algorithm is that obtained with an 8 seconds long arc discharge, presented in section 3.3.1 (Figure 50).

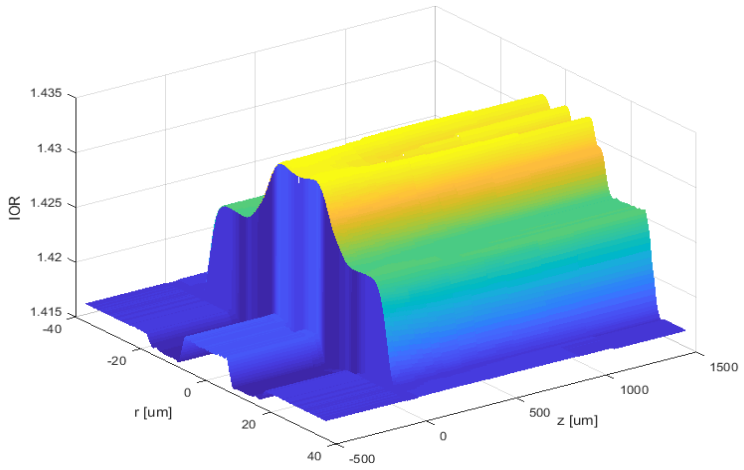

Figure 71. 3D rendering of the IOR measurement.

A detailed description of the local modes calculated in the various zones of the taper above will follow. Figure 72 shows a subset of the measured IORs and correspond effective IORs.

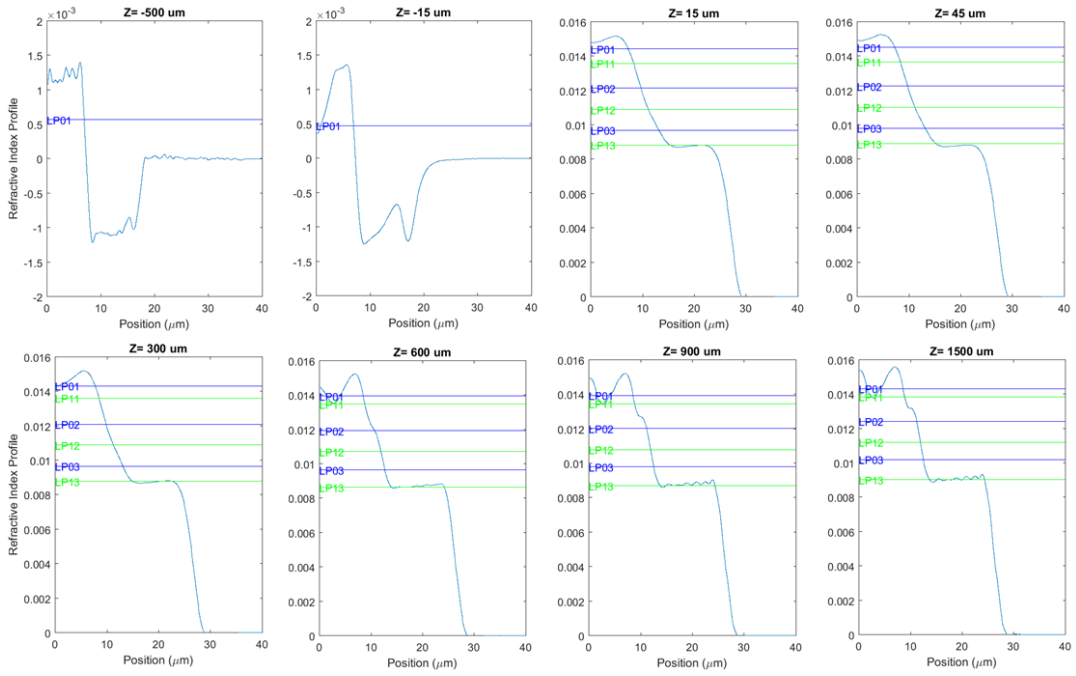

Figure 72. IOR and effective indexes of the some of the data shown in Figure 71

As one can see, far away from the splicing point (z= 0), the features of the IOR are sharp; these features become progressively smoother close to the splicing point. This is substantially due to the temperature of the arc discharge being hotter for z= 0. Both SMF and FMF fibre diffuse, but the effect is more visible on the active FMF. FMF is designed to diffuse in order to become matched upon splicing to the SMF. As already observed, diffusion takes place up to +500µm away from the splicing point. FMF guides very weekly HOMs such as LP03, LP13; these will leak away almost immediately when the AF is bent. As shown in paragraphs 2.2.2 and 3.3, modes such as LP12, LP03, LP13 have very low values of excitation, and unless excitation is intentionally provoked with a bad splice (offset, big cleaves or arc unbalanced), these are hardly measurable. Figure 73 and Figure 74 show the calculated intensity shape for the LP0x and LP1x respectively (x = 1, 2). In Figure 73 and Figure 74, field intensities are normalised like in formula (3.4.2.2).

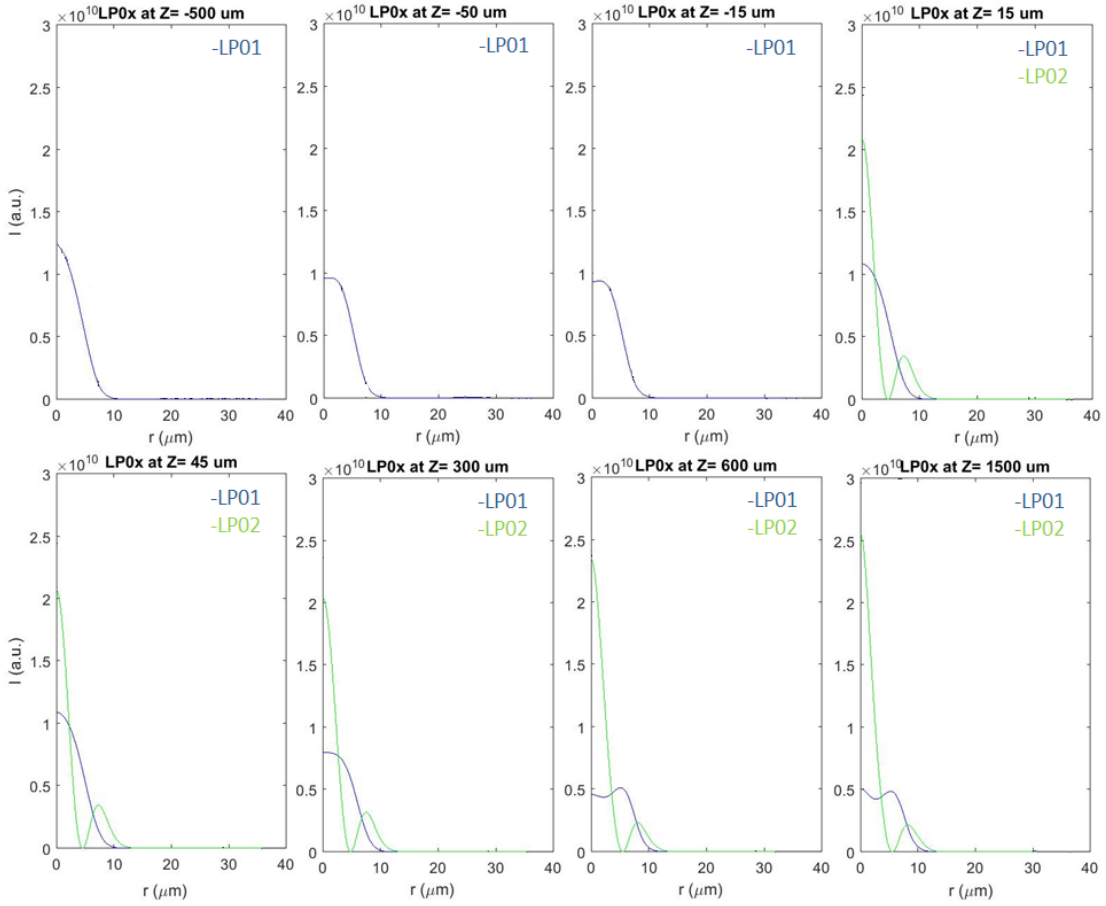

Figure 73. LP01 and LP02 intensity of the some of the data shown in Figure 71.

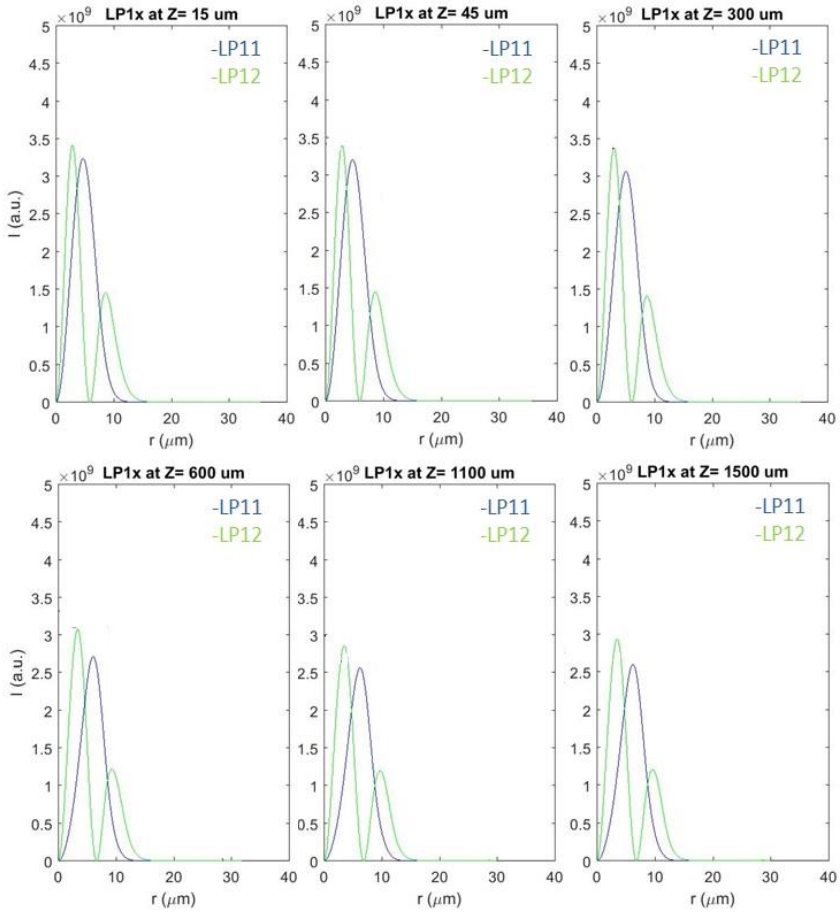

Figure 74. LP11 and LP12 intensity of the some of the data shown in Figure 71

Far away from the splice, on the un-diffused/ pristine FMF, the LP01 shape is very different from a Gaussian and it resembles the shape of the IOR. However, because of the diffusion occurred in proximity of the splice, the LP01 shape becomes round like a Gaussian, matching the field coming from the SMF. A useful quantity we can track along the taper is the Effective Area (EA) of the LP01 mode. Given a mode with intensity I(r, z), effective area is defined as:

$$A_{eff}(z) = \frac{\left[\int_0^{2\pi}\int_0^{+\infty} I(r,z) r dr\right]^2}{\int_0^{2\pi}\int_0^{+\infty} |I(r,z)|^2 r dr} \qquad (3.4.3.1)$$

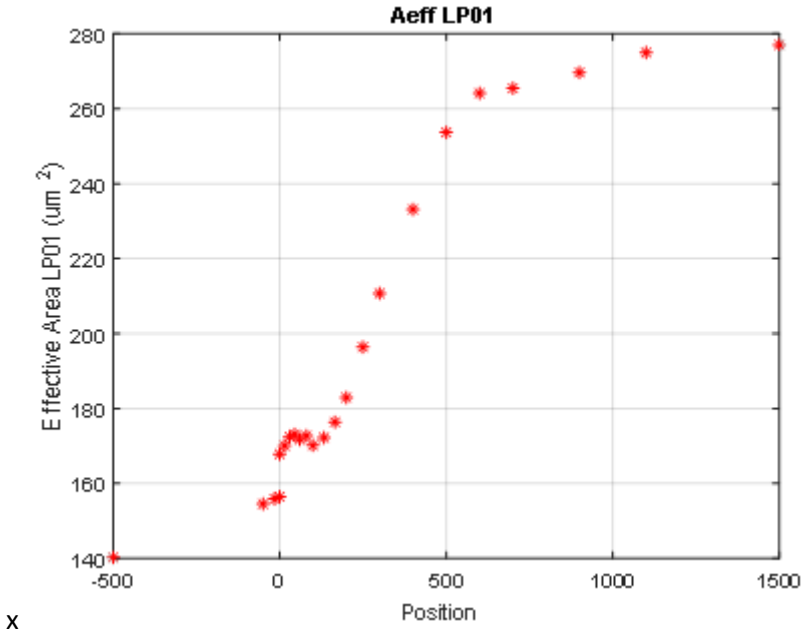

Figure 75. Effective area of the LP01 mode along the splice.

As shown in Figure 75, far away from the splicing point, SMF and FMF have very different EAs for the LP01 mode, measuring respectively 140µm^2 and 280µm^2. Thanks to the diffusion taking place during the splicing, the EAs of the LP01 mode is somewhat matched at the splicing point. At the splicing point, the EAs of the LP01 of the FMF and SMF measure respectively about 175 µm^2 and 155 µm^2. Given the result of the simulation presented in paragraph 3.1.2, we can easily image that if we had used longer arc duration, we could have better matched the LP01 effective areas of the two fibres. Being the arc temperature longitudinally symmetric around z=0, one can understand how FMF diffuses much more that the SMF. The value of the EA is flat from z = 0 to z~120µm. As it will be clear subsequently, this flat zone can be very useful to optimise the splice. So far, we have just analysed the data to provide to the recursive algorithm explained in 3.4.1. To calculate the amount of power carried by each mode whilst propagating into the tapered area, we can now apply the recursive algorithm.

To start using the recursive algorithm, we need to set the boundary conditions. We will do so by imposing that the SMF carries only one mode, namely we will set $|A_{LP01}|^2_{z=-500um} = 1$. All the other amplitudes at z=-500µm are equal to zero. For the sake of the exposure, we will initially show the results obtained from the raw data, without any virtual IORs. The effect of slotting in virtual IORs will be discussed later. As discussed in the theoretical section 3.4.1, right after formula (3.4.1.19), we also need to guess the modal excitation of the LP1x modes at the first point after the splice (z = +15µm), on the FMF side. Since we have that LP11 does not vary much upon re-arching with ROF splicer (empirical section 3.3.1), and we know that LP11 should not exchange power with LP01 and LP02 (theory), we will assume that LP11 power at the beginning of the taper should be the same as measured at the end of the FMF fibre with the S^2. We will therefore estimate that LP11 power is -30dB under the LP01, as shown for this sample in section 3.3.1. For the LP12 and LP13 at the beginning of the splice, we will assume their power to be <-50dB under the LP01. This is primarily justified by the fact that S^2 test kit's noise floor is -50dB and we never measure LP12 and LP03 with the S^2.

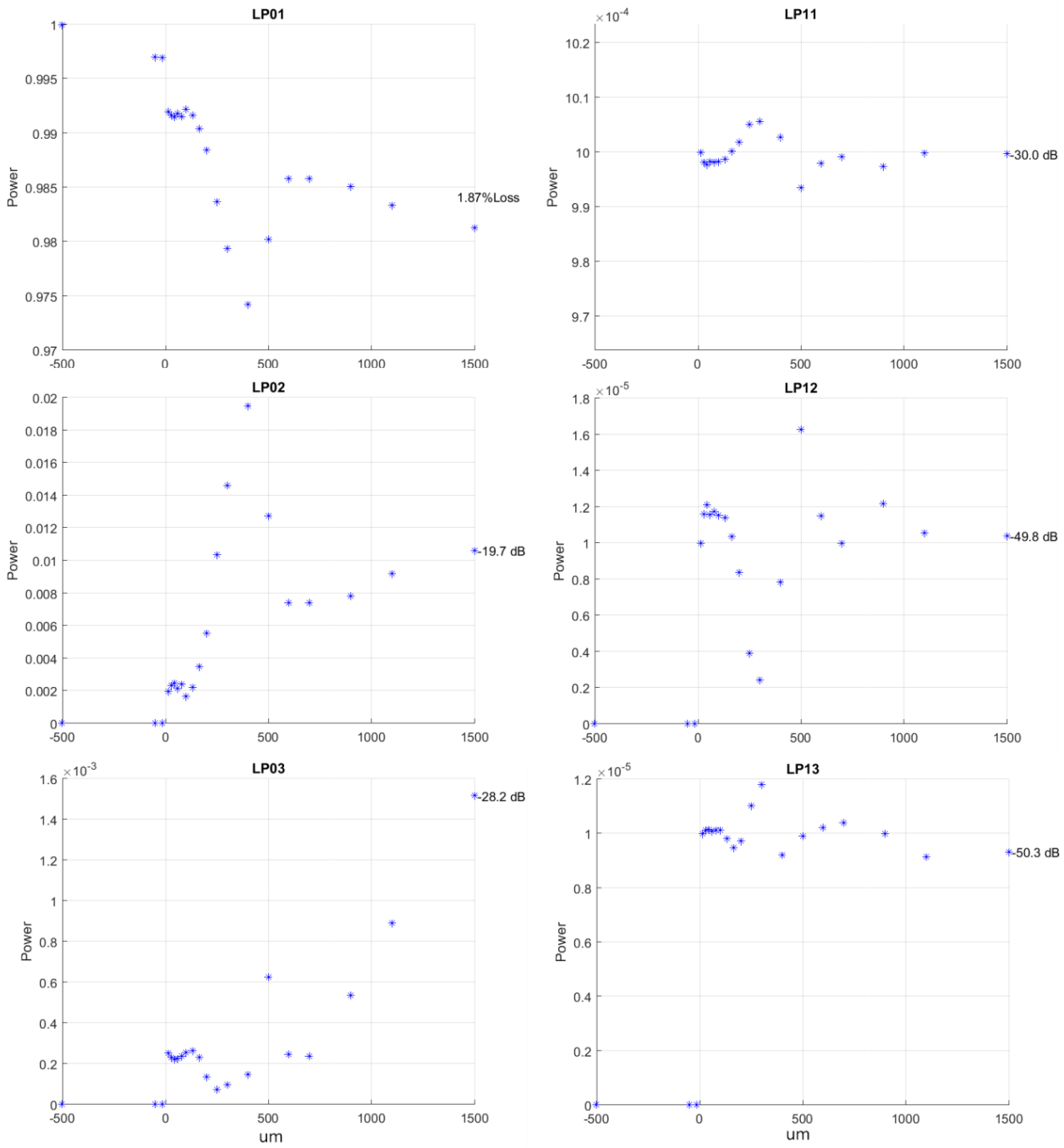

Figure 76. Propagation through the splice. Sample obtained with 8 seconds arc discharge, simulation without any virtual IOR.

Figure 76 shows the power evolution (that is $|A_i(z)|^2$) of the calculate modes along the splice. For all modes in the charts, a label indicates the power in dB at the end of the FMF fibre, apart from for the LP01 where the loss is indicated in percentage. Along the splice, LP01 and LP02 exchange the most visible amount of power. The power exchange is big up to 500µm, after that the power of the two modes settles as effectively the guiding property of the fibre become more constant away from the splicing point. LP03 has a somehow an

uncorrelated behaviour or at least, its excitation is some 10 dB inferior respect to the LP02 all along the taper. As hoped, we can effectively notice that LP11 value varies little around 30dB, so our guess when defining the boundary condition was right. Even if LP12 and LP13 do exchange power with LP11, their evolution is such that, at the end of the FMF, they conserve their assumed initial value at the beginning of the splice (certainly less than <50dB). In Figure 78, we show the effect of adding virtual IOR at the interface $z = 0^{\pm}$ and in between real IOR measurements along z. The amount of virtual IORs slotted between real measured IORSs is 2, 4, 8 and 16. In Figure 78, referring to the LP01 chart, it easy to notice that, the effect of adding the two virtual IOR at $z = 0^{\pm}$, reduces the loss of 0.37% (from 1.87% to 1.5%). Slotting in a progressively bigger number of virtual IORs, makes the LP01 loss decrease rapidly, saturating at 0.87%. Adding further virtual IORs above 4 times the real number of measurements, does not make LP01 loss decrease appreciably. Similar considerations apply to all the other modes: the power evolution shape saturates when increasing the number of virtual IOR. In Figure 77, the loss of the LP01 and the MPI of the LP02 at the end of the splice is plotted against the average sampling period (abruptly calculated as length of the splice divided by the number of IORs).

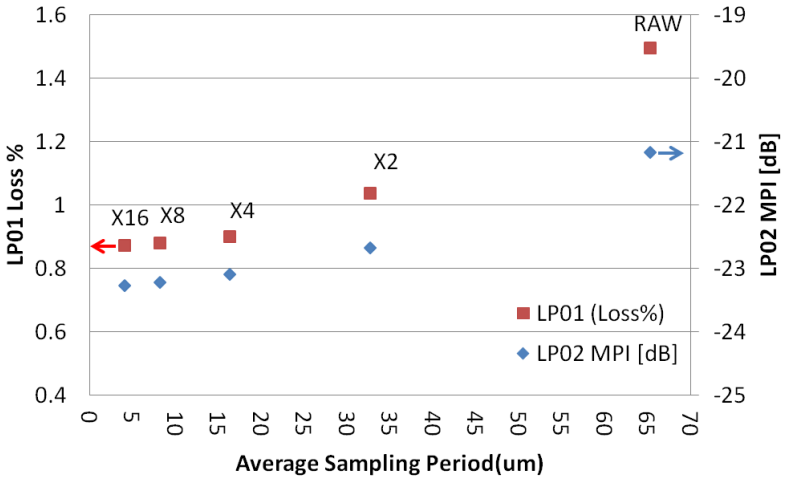

Figure 77. Propagation into splice. Power at the end of the taper vs. sampling frequency. Labels indicate the number of Virtual IOR slotted in between real IOR measurements.

From the figure above it easy to spot how, above x4 Virtual IORs, the numbers provided by the algorithm saturates. The spatial resolution of the IFA along z is 20µm; therefore, by using X4 level of virtual IORs, we do match the resolution of the machine; this would somehow save a quarter of the time in case we wanted to obtain same amount of real, time consuming, IOR measurements.

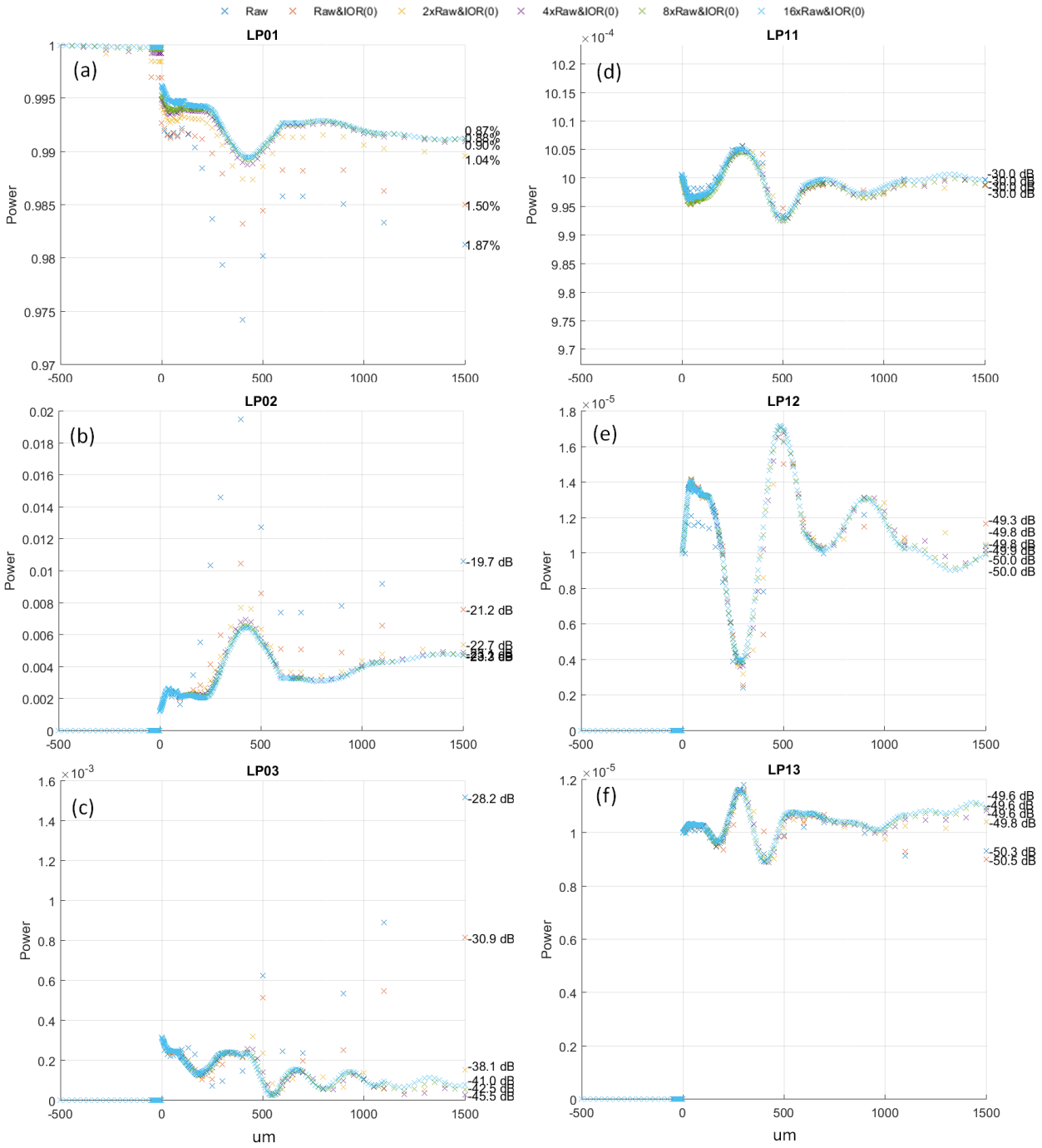

Figure 78. Propagation into splice, legend at the top of all charts. Sample obtained at with 8 second arc discharge, simulation without any virtual IOR [Raw], with virtual IORs around z=0 [Raw&IOR(0)] and with x2,x4,x8 and x16 virtual IORs slotted between real measurements.

The LP02 excitation measured with the S^2 for this sample was -25.5dB (Figure 52), the best value we can estimate with the theory applied to the IFA sample measurement is -23.3dB. We notice that there is a mismatch of 2dB circa between the two approaches. Whilst deriving the theory, in formula (3.4.1.2), we neglected the radiation modes. Furthermore, we are also using a limited number of modes in the calculation. Since we are using a

limited number of modes (6, i.e. LP01, LP02, LP03, LP11, LP11, LP12, and LP13) and also a limited number of IORs along z, it is reasonable to suggest that our algorithm introduces fictitious radiation losses. To evaluate such fictitious radiation loss, we can add up all the power calculated for all the modes at the end of the taper and see whether they add up to unity or not. A quantity to evaluate such fabricated radiation loss, is defined as follows:

$$RL = \left(1 - \sum_{i}^{n} A_i^2(L)\right) * 100 \qquad (3.4.3.2)$$

In Figure 79, the so defined radiation loss, is plotted against the spatial sampling period. The points in red are those obtained with the above-mentioned 6 modes. The radiation loss decreases with the number of samples utilised. Furthermore, the introduced radiation loss can be further reduced by adding more modes (blue point, obtained by adding other four modes, namely: LP04, LP05, LP14 and LP05). However, adding further four modes does not change the MPI of the LP02. The mismatch of 2dB between S^2 and this algorithm based on IFA measurement is still 2dB.

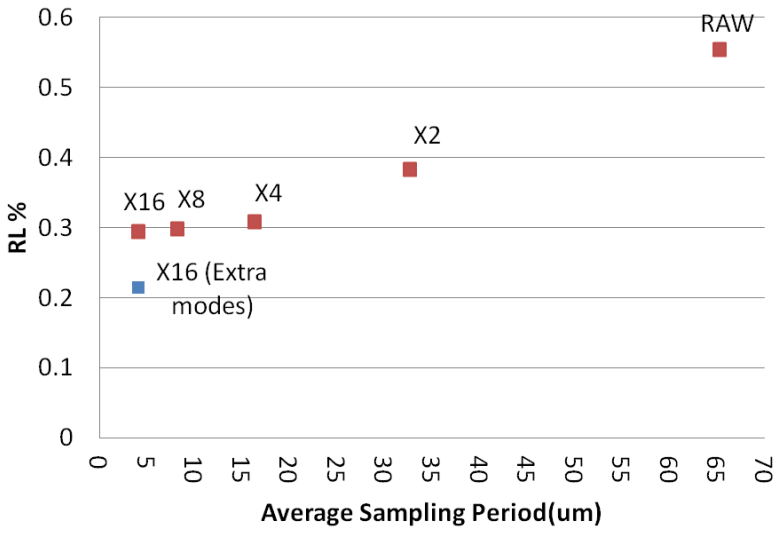

Figure 79. Fictitious radiation loss. In red the radiation loss obtained with different sampling rates and with 6 modes. In blue the radiation loss obtained with 10 modes.

To conclude this long paragraph, we would like to highlight the following aspects:

- LP01, LP02 and LP11 are those carrying most of the power.
- LP01 and LP02 are those exchanging most of the power along the taper.
- LP1x modes do exchange much power between them. LP11 power does not vary much along the taper (almost constant at -30dB) and LP12 and LP13 have very little power.
- Modes with different symmetry should not exchange power if taper is reasonably straight. Equally, the approach illustrated, is incapable to evaluate coupling between modes having different symmetry as they propagate in along splice. This might explain the discrepancy of 2dB with the S^2 measurement in terms of MPI.
- Adding few virtual IORS increase the accuracy of the model. Using X4 level of virtual IOR is accurate enough and makes calculation reasonably quick (30 seconds).

3.4.4 Theory applied on IFA samples

The samples of splice measured in section 3.3.1, with arc durations equal to 2, 4, 6, 7, 8, and 10 seconds, have been characterised with the IFA at discrete z length, like in the example of the previous chapter. In this paragraph will utilise the propagation algorithm on these samples. We will use a virtual IOR oversampling equal to four. We will calculate the results only for the modes carrying most of the power: LP01, LP02 and LP11.

Figure 80. Propagation into splice of LP01 and LP02. Results for samples spliced with different arc duration.

The results of Figure 80 show two main things. First of all, LP01 and LP02 are, for each sample at any point across the splice in anti-phase, this certainly includes the points at the end of the splice. Therefore, as intuition suggested in paragraph 3.3.1, finding the arc duration that minimise the LP02 (by S^2) does indeed correspond to maximising the LP01 excitation. Secondly, the arc duration that minimise the LP02, is that found at 7 seconds;

matching what empirically measured (Figure 52). The next chart compares the LP02 MPIs calculated with this algorithm and that measured with the S^2 for any arc duration.

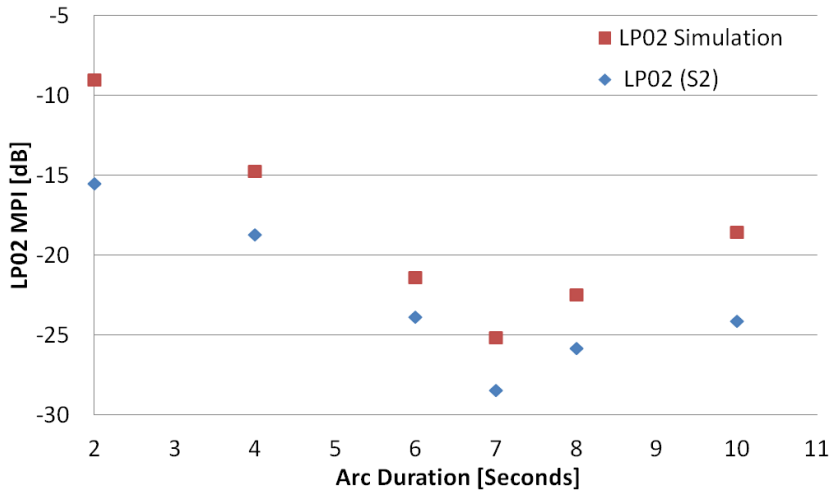

Figure 81. LP02 MPI calculated vs LP02 MPI Measured with S^2 at various arc durations.

In Figure 81, it is possible to notice that, apart from an offset of 2dB, the algorithm results nicely fits the real measurement obtained with the S^2 , forecasting that the best splice is that of the sample spliced with 7 seconds arc duration.

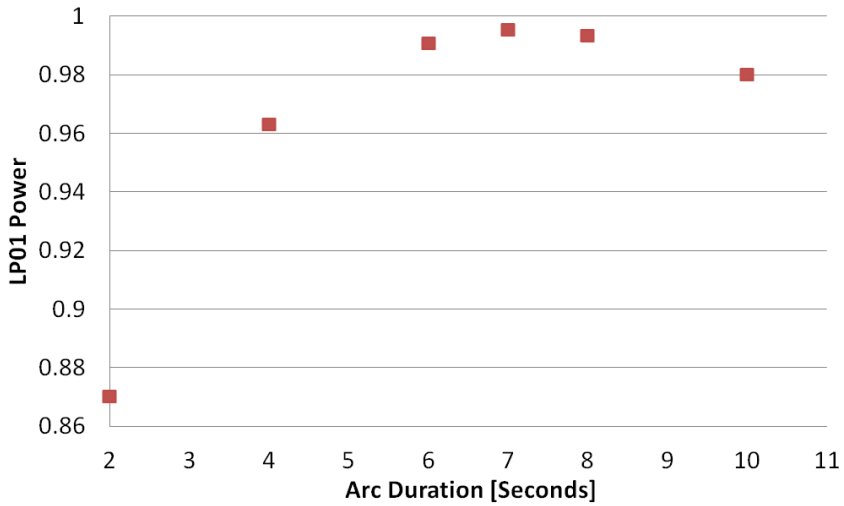

Figure 82. LP01 transmissions obtained with various arc durations.

In Figure 82 one can easily see that the maximum for the LP01 is obtained with the arc duration of 7 seconds. Therefore, with this technique, we are capable of optimising the splice between SM and FMF, ensuring the highest LP01 excitation. For completeness, we

report also the modal excitation calculated for the LP11. For the same reason explained in the previous chapter, we will assume the LP11 power at the beginning of the taper (first point after the splice) to be equal to that at the end of the taper, as measured with the S^2 (Figure 51). Within the approximation of this model, LP11 does not exchange energy with LP01 and LP02; its value varies little along the taper.

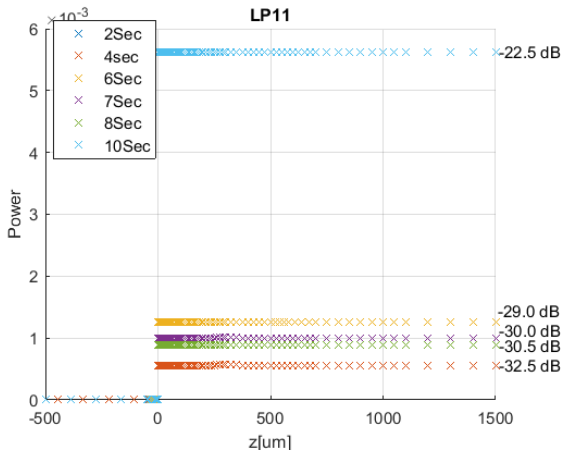

Figure 83. LP11 excitation obtained with various arc durations. The initial value of the LP11 after the splice has been guessed by using the same value measured with S^2.

Finally, to conclude this chapter, in Figure 84 the effective area of the LP01 mode is plotted for any sample along the taper length. The arc duration that better matches the LP01 areas between fibres at the splicing point, is 10 seconds. However, the sample that optimises the splice is obtained with 7 seconds arc discharge, resulting in a 20 μm^2 area mismatch between fibres at the splicing point.

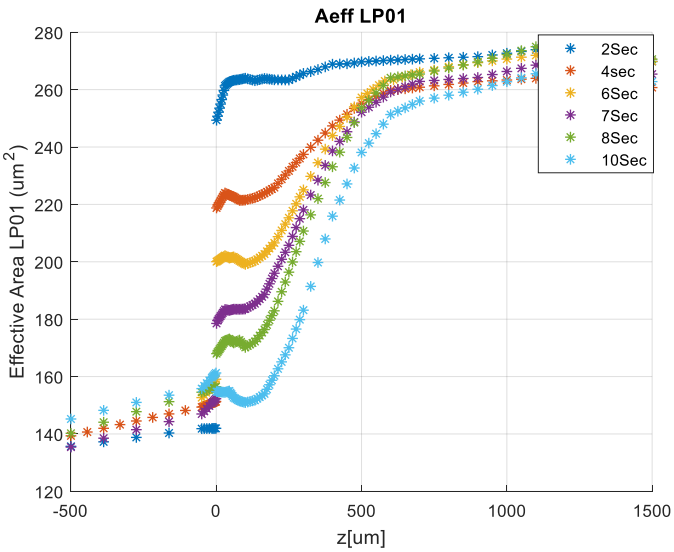

Figure 84. Effective areas of LP01 mode evolution across the splice for the various arc durations.

It seems counter intuitive that a splice with an area mismatch at the point of contact can result in the best splice. This also contradicts the foundation of some important patent pertaining the way of exciting the FM in a MM fibre [131, 132]. The other common modes to achieve SM excitation in MM fibre normally require long taper lengths and matched area at the point of contact [121], here we achieve this by a mismatched splice at the point of contact and a very short taper (less than half mm). In the last two paragraphs of this chapter, we will explain how an area mismatched splice optimises the splice between the SMF and the FMF.

3.4.5 Theoretical explanation of the splice optimisation

In this part, we will explain some fundamental property of the splice, leading us to the understanding of our SM-MM splice optimisation. We will use the word splice or taper interchangeably. We will keep using the samples obtained with 2, 4, 6, 7, 8, 10 seconds of arc duration, presented in section 3.3.1.

3.4.5.1 Response of the sole tapered region

It is extremely interesting to study the electromagnetic response of the sole diffused area of the FMF, isolating it from the SM fibre (only for z>0). To do so we use a probing input field defined as:

$$\tilde{E}^I = \begin{bmatrix} \tilde{E}^I_{LP01} \\ \tilde{E}^I_{LP02} \end{bmatrix} = \begin{bmatrix} A^I_{LP01} \\ A^I_{LP02} e^{i\Delta\vartheta} \end{bmatrix} = \begin{bmatrix} (1-l) \\ \sqrt{1-(1-l)^2}\ e^{i\Delta\vartheta} \end{bmatrix} \qquad (3.4.5.1)$$

Input field has the following property: has intensity equal to one $\left|\tilde{E}^I_{LP01}\right|^2 + \left|\tilde{E}^I_{LP02}\right|^2 = 1$ and it is completely described by l and $\Delta\vartheta$. The l value describes the purity of the field: the smaller l the more 'single mode' is the field (LP01 big, LP02 small), the bigger l the less pure is the field (LP01 small, LP02 big). The term $e^{i\Delta\vartheta}$ accounts for the differential phase between the LP01 and the LP02 modes. This input field is used as a boundary condition at the beginning of the tapered area (at the first point on the FMF). To begin, we will set $l = \Delta\vartheta = 0$, therefore using a pure SM excitation as input probing field.

From Figure 85 we can see that, even if the input is purely SM, the tapered region produces intrinsically LP02 excitation, resulting in an output field endowed with less modal purity than at input. Comparing Figure 84 and Figure 85, we immediately realise that power exchange between modes takes place where the effective area has big slopes along z. Above z>1000 µm, there is no further power exchange as effective area does not change anymore. The 'flat' part after 1000µm does not play a particular role, as power exchange will no longer take place thereafter. Likewise, up to 200 µm circa there is no power exchange between modes, modes only accumulate differential phase shift; we anticipate that this initial zone plays a role in the splice optimisation process.

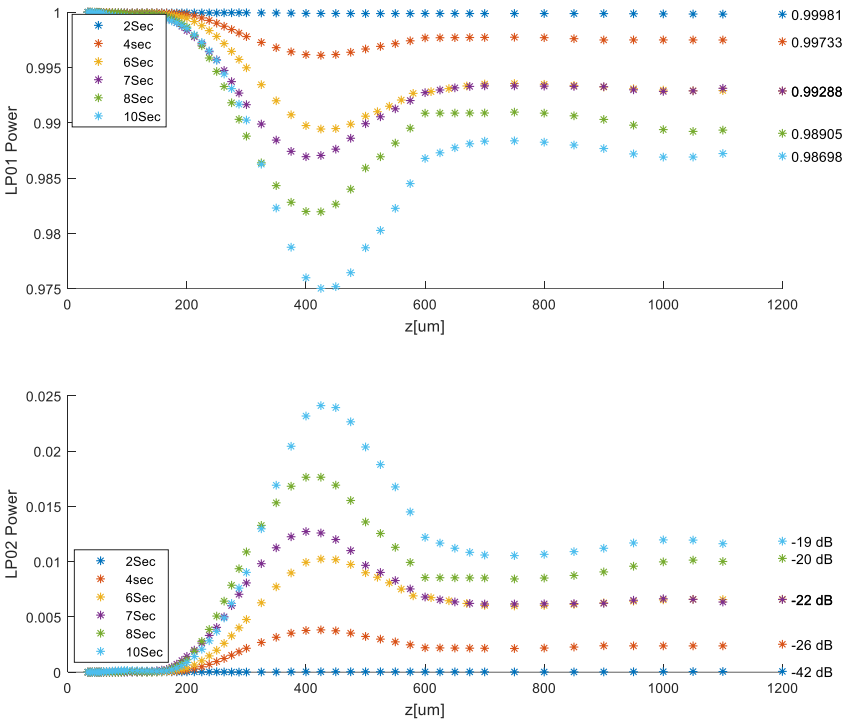

Figure 85. LP01 and LP02 excitation with purely SM excitation at the beginning of the tapered zone.

From Figure 85 we also realise that, the longer the arc duration, the bigger the effective area variation along the taper and the higher the amount of LP02 produced by the taper. As we have done for the input field, we can quantify the lack of purity introduced by the taper, by evaluating the l parameter in the output field, at the end of the taper. For consistency with (3.4.5.1), l_{out} must be defined as:

$$l_{out} = 1 - \sqrt{\left|A^{O}_{LP01}\right|^2} \qquad (3.4.5.2)$$

Where $\left|A^{O}_{LP01}\right|^2$ is the last value of Figure 85 (TOP), as reported in the labels. We can evaluate the output response of the taper, to any input field. To do so, we scan l and $\Delta\vartheta$ (e.g. $l \in [0,1], \Delta\vartheta \in [-\pi, +\pi]$, to form a discrete grid), generating probing input fields as defined in equation (3.4.5.1). In the following explanatory example, we will use the IOR data of the 4 seconds sample. For each l and $\Delta\vartheta$ pair in the grid, we calculate the LP01 and LP02 powers at the output of the taper.

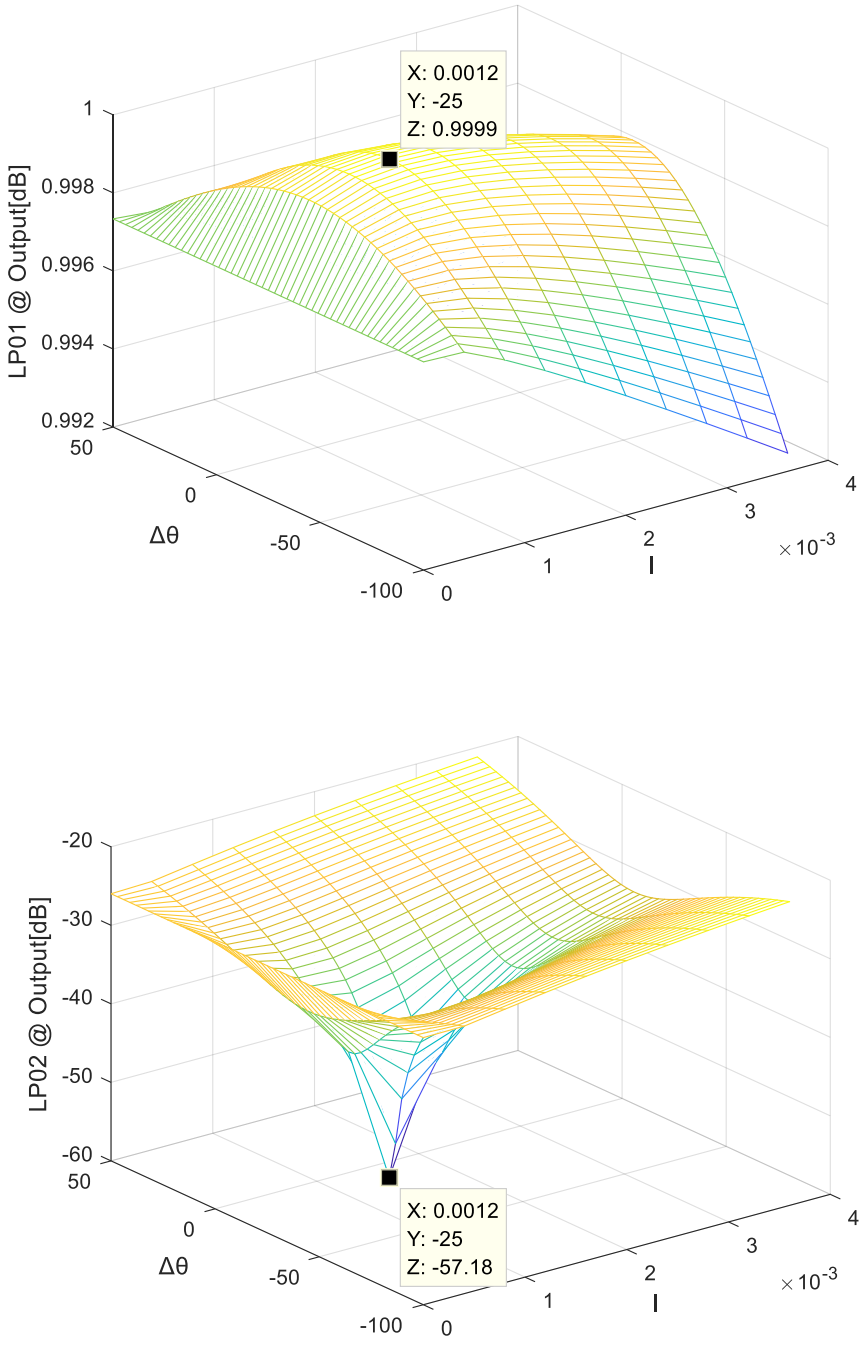

Figure 86. Sample obtained with 4 seconds arc discharge. LP01 (Top) and LP02 (Bottom) powers at the splice's output obtained with different input field parameters (l and $\Delta\vartheta$)

Figure 86 shows the value of LP01 and LP02 at the output of the taper in correspondence of the input field parameters. It is easy to observe, that for an input field characterised by $l^* = 0.0012$ and $\Delta\vartheta^* = -25\text{deg}$, the LP01 excitation at the end of the taper is maximum (0.9999) and the LP02 excitation at the end of the taper is minimum (-57.18dB).

Basically, with the right input, even sample with 4 second arc discharge can result in a pure SM excitation at the end of the splice. We can make the parameters' grid tighter and find more accurate values for l^* $\Delta\vartheta^*$ and correspondently improved output purity (Figure 86 vs Figure 87)

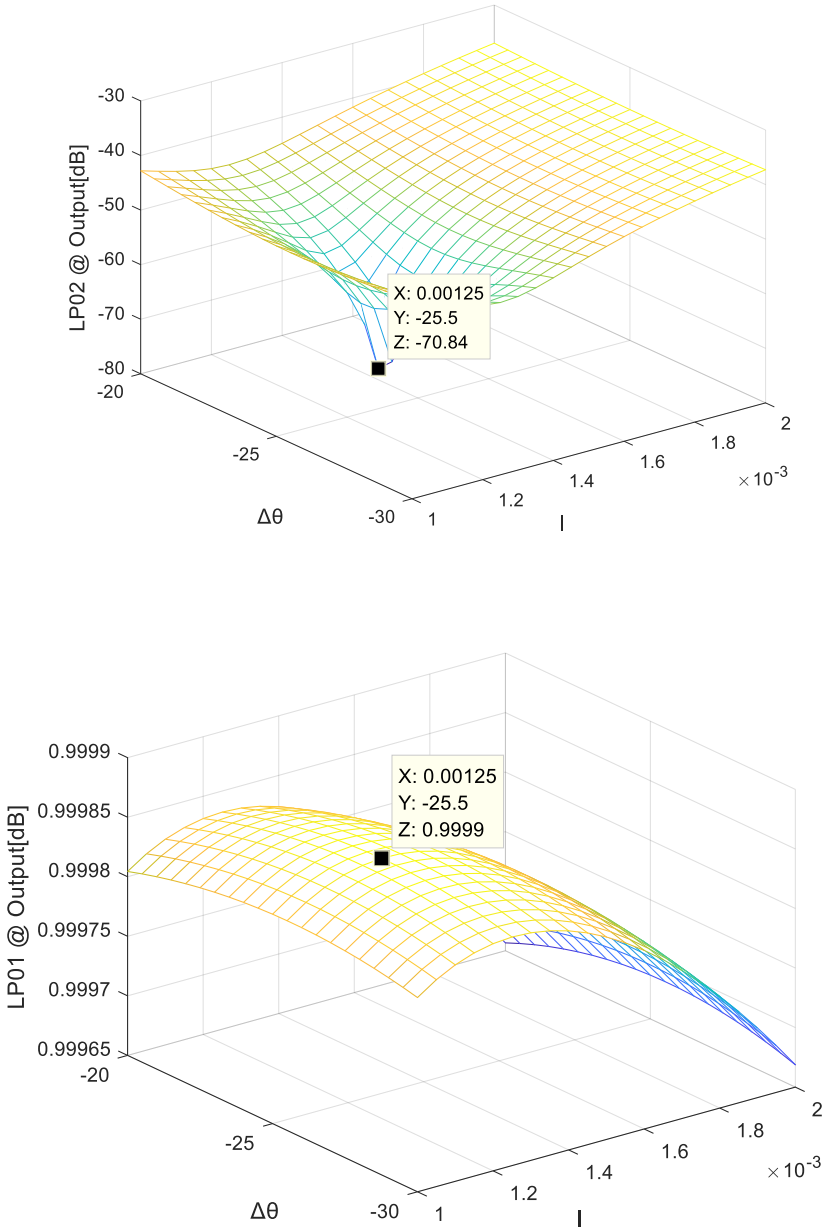

Figure 87. LP01 (Top) and LP02 (Bottom) power at the output of the taper obtained with different input field (grid here is tighter than in Figure 86)

Rather than using this time consuming 'brute force' scanning method, we can find the optimum input field in the most precise way by using some linear algebra. We can think at the splice as a black box, represented by matrix $S \in \mathbb{C}^{2x2}$. We can then probe the splice with two orthogonal input fields:

$$\tilde{E}_1 = \begin{bmatrix}1\\0\end{bmatrix}, \quad \tilde{E}_2 = \begin{bmatrix}0\\1\end{bmatrix} \tag{3.4.5.3}$$

Here $\tilde{E}_1 = \begin{bmatrix}1\\0\end{bmatrix}$ means that he input contains only the LP01 mode and $\tilde{E}_2 = \begin{bmatrix}0\\1\end{bmatrix}$ means that he input contains only the LP02 mode. The result of the two multiplications yield: $S * \tilde{E}_1 = \begin{bmatrix}S_{11}\\S_{21}\end{bmatrix}$ and$S * \tilde{E}_2 = \begin{bmatrix}S_{12}\\S_{22}\end{bmatrix}$, allowing us to reconstruct S. We can therefore calculate which input field $\tilde{E}_I^*$ would result in a pure SM output excitation $\tilde{E}^O = \begin{bmatrix}1\\0\end{bmatrix}$ with the following procedure:

$$S * \tilde{E}_I^* = \begin{bmatrix}1\\0\end{bmatrix} => \tilde{E}_I^* = S^{-1}\begin{bmatrix}1\\0\end{bmatrix} \tag{3.4.5.4}$$

Using (3.4.5.4), we obtain the most numerically accurate $\tilde{E}_I^*$. This is characterised by $l^* = 0.0012619$ and $\Delta\vartheta^* = -25.6706$ deg. We will refer to $\tilde{E}_I^*$, l^* and $\Delta\vartheta^*$, as optimised input or optimised input parameter. Application $\tilde{E}_I^*$, yields the following evolution for the LP01 and LP02 (Figure 88).

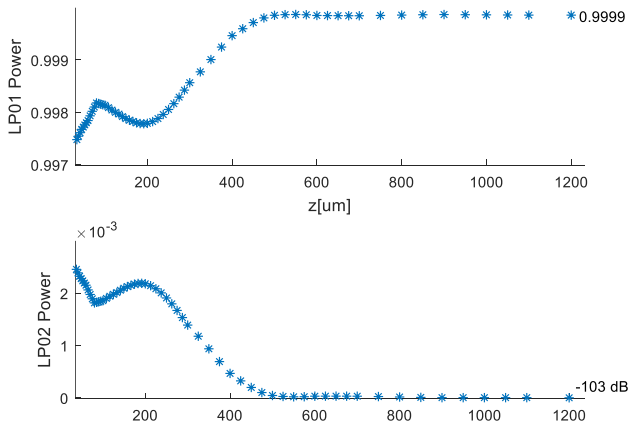

Figure 88. LP01 and LP02 evolution in correspondence of optimised input field.

With the optimised input field $\tilde{E}_I^*$, we obtain pure SM excitation at the output (LP02 = -103dB and LP01 = 0.9999). Modal excitation is again relatively constant up to 200µm, but, in the region where the effective area has a big slope, modes couple constructively in such way that, LP01 at the output is bigger than LP01 at the input; whilst LP02 completely vanishes away. It is interesting to notice that, in order to optimise the output purity (no LP02), we need to provide some LP02 at the input (or equivalently some loss to the LP01).

We are now ready to enunciate one fundamental statement, result of this study:

"In order to nullify the amount of LP02 created by the taper (and maximise the LP01 purity at output), the same amount of LP02 must be provided at the input (hence with some loss on the LP01 at input)"

To prove this statement systematically, we can evaluate both: l_{out} in presence of $\tilde{E}_I = \begin{bmatrix}1\\0\end{bmatrix}$ (as defined in (3.4.5.2)) and l^* obtained from the inverse matrix (like shown in (3.4.5.4) for all samples obtained at the various arc duration (Figure 89).

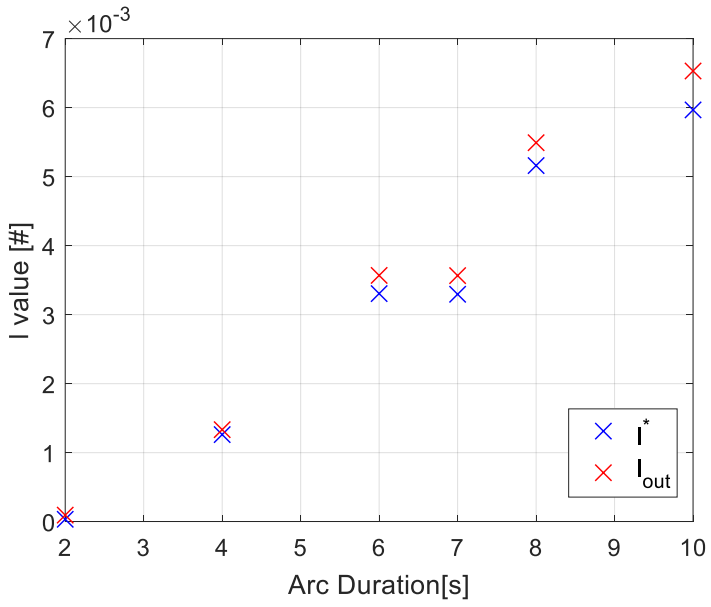

Figure 89. l_{out} and l^* for all arc durations.

In Figure 89 there is a good agreement between l_{out} and l^* for all arc duration, proving empirically the fundamental statement above. Small discrepancies are essentially deemed to be due to numerical error. The numerical correspondence of l_{out} and l^* can be also

proven mathematically. To do so we need to reconstruct the inverse matrix associated with the taper and recognise that this matrix is unitary. Let S be the matrix representing the taper when propagating from input to output (Forward).

$$S = \begin{vmatrix} S_{11} & S_{12} \\ S_{21} & S_{22} \end{vmatrix} \qquad (3.4.5.5)$$

We can represent schematically the S matrix with 4 arrows indicating how its coefficients couple the fields from input to output.

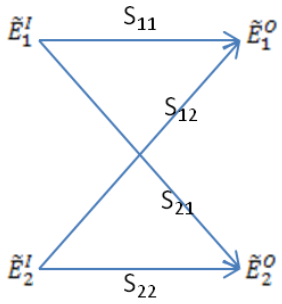

Figure 90. Forward propagation.

In Figure 90, $\tilde{E}_1^I$ and $\tilde{E}_2^I$ are the input fields (e.g. LP01 and LP02) and $\tilde{E}_1^O$ and $\tilde{E}_2^O$ are the output fields (e.g. LP01 and LP02).

When propagating backward, due to propagation's reciprocity, the scheme for S^{-1} is:

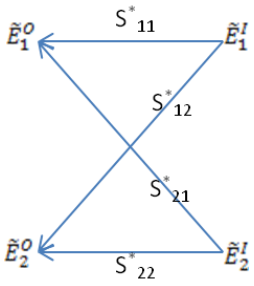

Figure 91. Backward propagation

In Figure 91 we find again all coefficients of Figure 90, but in their complex conjugate version. This simply indicates that the coupling does not change with the sense of propagation, but just the introduced phases are reversed. It follows that the inverse matrix of S, associated to the backward propagation must be:

$$S^{-1} = \begin{vmatrix} S_{11}^* & S_{21}^* \\ S_{12}^* & S_{22}^* \end{vmatrix} \qquad (3.4.5.6)$$

S is therefore unitary ($S^{-1} = S^{\dagger}$), with $S^{\dagger}$ being the adjoined operator of S.

The output field in presence of a purely single mode input is:

$$\tilde{E}^0 = \begin{vmatrix} S_{11} & S_{12} \\ S_{21} & S_{22} \end{vmatrix} * \begin{bmatrix} 1 \\ 0 \end{bmatrix} = \begin{bmatrix} S_{11} \\ S_{21} \end{bmatrix} \qquad (3.4.5.7)$$

From equation (3.4.5.7), l_{out} can be calculated as:

$$l_{out} = 1 - \sqrt{|S_{11}|^2} \qquad (3.4.5.8)$$

Using the inverse matrix, the input field that results in pure LP01 excitation at the output is:

$$\tilde{E}^I = \begin{vmatrix} S_{11}^* & S_{21}^* \\ S_{12}^* & S_{22}^* \end{vmatrix} * \begin{bmatrix} 1 \\ 0 \end{bmatrix} = \begin{bmatrix} S_{11}^* \\ S_{12}^* \end{bmatrix} \qquad (3.4.5.9)$$

From equation (3.4.5.8), l^* can be calculated as:

$$l^* = 1 - \sqrt{|S_{11}^*|^2} = 1 - \sqrt{|S_{11}|^2} = l_{out} \quad \square \qquad (3.4.5.10)$$

This proves mathematically the fundamental statement enunciated in this paragraph.

3.4.5.2 Response of the whole splice

We are in the condition of explaining, theoretically, how splice optimisation via arc duration works. In essence, optimisation techniques via arc duration scan both l and $\Delta\vartheta$ parameters as in Figure 86, presenting different field configurations at the beginning of the up-tapered region (at around z = 180µm).

Consulting Figure 80, Figure 84 and Figure 85, we can roughly divide the splice region in two sub regions, namely: the flat region (from z>0 to about 180µm) and the tapered region (from 180µm to 1000µm). After 1000µm modes propagate without exchanging energy, so this third region is of little interest.

Flat region (from z>0um to about 180um):

Modes do not exchange energy and their power is dictated by the excitation acquired at z=0. At z= 0, modal excitation (l parameter), depends substantially by the area mismatch between the SMF and the MMF. The parameter l imprinted in the vicinity of z = 0, will be constant up to about z =180µm. From the data of the splice simulation of Figure 80 and the effective areas of Figure 84, one can see that, the higher the area mismatch at z =0, the higher the LP02 modal excitation (bigger loss for LP01). For this reason, the arc duration affects the l parameter at the beginning of the tapered region. The differential phase($\Delta\vartheta$ parameter), increases from 0µm to 180µm, with

$$\Delta\vartheta = \frac{2\pi}{\lambda}(n_{01} - n_{02})z \qquad (3.4.5.11)$$

The value of $\Delta\vartheta$ at z = 180µm, briefly called $\Delta\vartheta$, is important because this is the value of modal de-phasing that will be presented at the beginning of the tapered region. Also $\Delta\vartheta$ will depend on arc duration, in fact, the effective index of refraction n_{01} and n_{02} and their difference depends on arc duration.

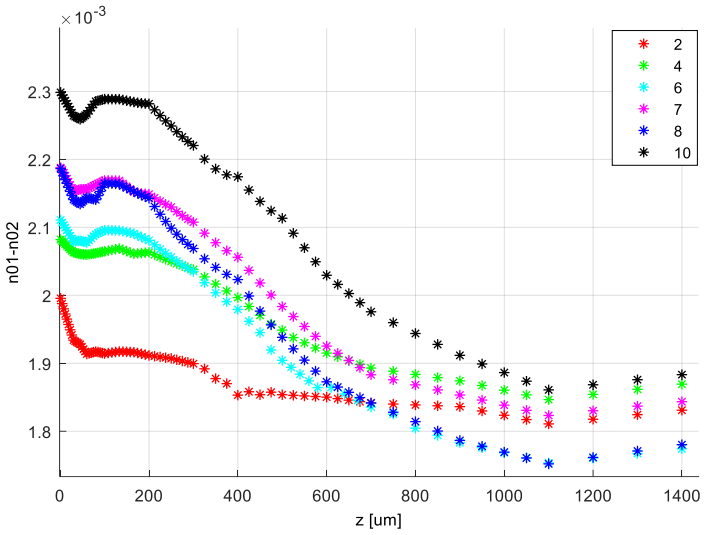

Figure 92. Index of refraction difference $n_{01} - n_{02}$ along the splice. Arc duration in the legend is in seconds.

We can therefore calculate and tabulate and store the value of both l and of $\Delta\vartheta$ at 180µm, for each arc duration.

Tapered region (from 180µm to 1000um):

The sole tapered region, from z>180µm, behaves like described in paragraph 3.4.5.1, but just shifting the origin of the taper at z=180µm. Also in this case, for each arc duration, there is a l^*, $\Delta\vartheta^*$couple for the incoming field that will result in a null HOM excitation at the output. This l^*, $\Delta\vartheta^*$ couple, characterising the tapered region, must be matched by the l, $\Delta\vartheta$ couple, coming from the flat region, preceding the tapered region. We can calculate and tabulate the value of l^* and of $\Delta\vartheta^*$ needed at 180µm, to obtain minimum HOM excitation at the output.

Two regions combined, whole splice:

After having described the regions and the parameter of interest of both regions, we can understand the behaviour of the whole splice. The next chart shows the values of l^* and l versus arc durations.

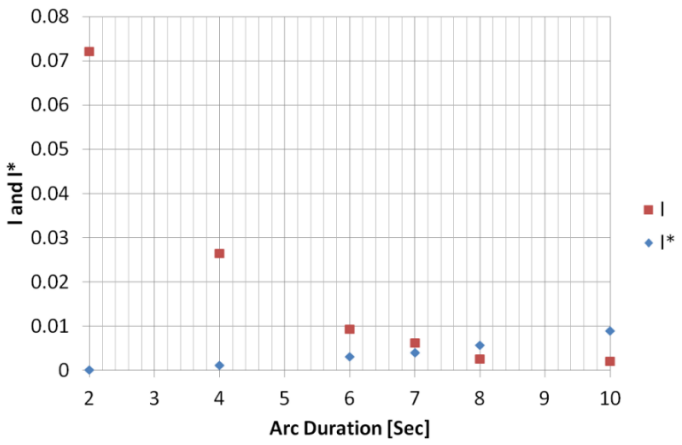

Figure 93. Values of l^* and l at various arc durations.

As shown by Figure 93, the arc duration resulting in equal values for l^* and l is close to 7 Seconds. An arc duration of 7.4 seconds would have better matched l^* and l, resulting in a better-optimised splice; from the point of view of the arc duration. Unfortunately, we do not dispose of a sample obtained with 7.4 seconds. Amongst the samples available, 7 seconds is the best arc duration found to empirically to optimise the splice. However, the theoretically lowest HOM excitation at the output of the splice is achieved when also the modal de phasing at the beginning of the taper is right. The phases $\Delta\vartheta$ and $\Delta\vartheta^*$, are plotted in the next chart.

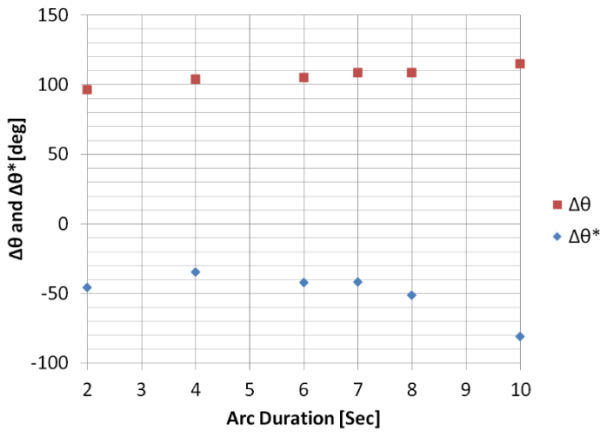

Figure 94. Values of $\Delta\vartheta$ and $\Delta\vartheta^*$ at various arc durations

From Figure 94 it can be seen that the distance between $\Delta\vartheta$ and $\Delta\vartheta^*$ is somehow constant up to 7 sec and then it starts increasing, worsening the desired matching. Again, 7 seconds is the arc duration fund to optimise the splice. However, $\Delta\vartheta$ and $\Delta\vartheta^*$ do not match at any arc duration. This justifies why the LP02 minimum found is just -25dB and not much less (S^2 noise floor is -45dB). To have also $\Delta\vartheta$ equalled to $\Delta\vartheta^*$, one could think of making a longer

flat region in order to tune $\Delta\vartheta$ at the beginning of the tapered area. Such kind of splice has not been attempted yet, even if the effect of having a progressively long transversal sweep has been highlighted in paragraph 3.3.3, in Figure 63 . However, the behaviour of the splice in the presence of a flat region of variable length can be simulated. To do so, after z = 180µm, we can insert an increasingly long replica of the IOR found at z=180µm, prolonging artificially the flat region. The result of this simulation, performed on the splice obtained with 7 seconds arc duration, is shown in the next two figures.

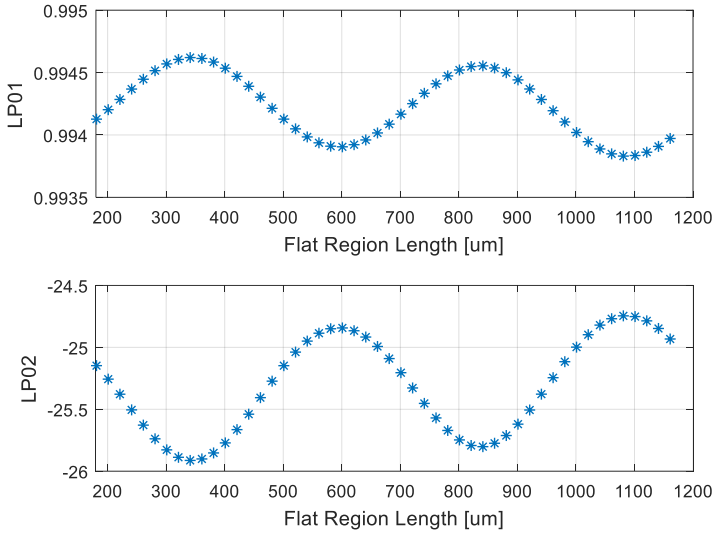

Figure 95. Effect of extending the flat region. Chart Plotted against Flat region length.

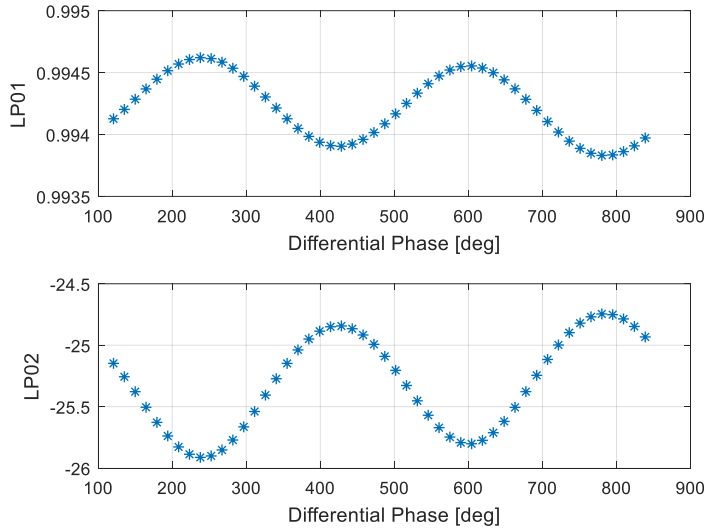

Figure 96. Effect of extending the flat region. Chart Plotted against the differential phase accumulated ($\Delta\vartheta$) when extending the flat region.

As verified empirically and showed in paragraph 3.3.3 by using transversal sweeps, an increasingly long flat region leads to a periodical modulation of the modal excitation. From Figure 96, we can notice that the period of the oscillation is 360 degree, highlighting how, a SM–MM splice has indeed the same features of an optical coupler (e.g. so called WDM coupler), from this point of view this work can certainly considered a novelty. From Figure 95, it is easy to notice that, if the flat region were 330µm long, the splice would have been even better (less LP02, more LP01). To a flat region, long 330µm corresponds an extra differential phase of about 150 degrees (Figure 96); this differential phase shift is exactly the distance between $\Delta\vartheta$ and $\Delta\vartheta^*$ in Figure 94, of 7 seconds. As a last remark, we notice that the ripple obtained for the LP02 with increasing flat region length is small, 1 dB circa; this is because the arc duration used is 7 second. If we had empirically used an optimum arc duration of 7.4 seconds, the ripple would have been much bigger.

3.5 Conclusions

In this chapter, we have illustrated the progress made in splice optimisation. We have introduced the type of fibres utilised through this dissertation, then the concept of dopants diffusion has been presented as mechanism exploited to match SM and MM fibre. The diffusion of the dopants was simulated by developing a model. The model, despite his simplicity, highlights the effect of the FS arc discharge in correspondence of the splice. The heat provided by the arc discharge provokes dopants migration and consequent altering of the guidance property of the AF. The S^2 has proven to be a very important in tool for the development of SM-MM splices. We have initially described some immediate applications of the S^2 such as the modal discrimination via selective bends and the evaluation of up tapered structure. Subsequently we have shown our golden applications of the S^2: the splice optimisation.

This optimisation is nowadays part of the SPI core technology. The splice optimisation part can be divided into two parts: the empirical part and the theoretical part. The details of these two parts were discovered in the same chronological order they are here exposed. The empirical and theoretical parts are quite interlaced since the samples obtained with different arc duration in the empirical part are later used as benchmark for the theoretical part. It was shown that there is an optimum arc duration that optimises the LP02 content. Cleaves and core concentricity dominate the outcome of the LP11 rather than the arc

property. From this point of view, the S^2 has been adopted also to qualify different splicing technologies, leading us to the current usage of the ROF technology. Already during the empirical characterisation, particularly in the sweep splice experiment, we saw features ascribable to couplers (periodical modal excitation). The empirical part of this work is certainly original as it has never been reported before. In the theoretical part, we recycled a theory developed for planar waveguides and adapted it for optical fibre. In the referenced papers, the theory calculates recursively the power coefficients for the modes making assumption about the index of refraction's evolution along the taper length. Here we actually measure the index of refraction along the splice and apply the modified theory; this approach to splices constitutes novelty. The developed theory has its limits as it does not account for coupling having different symmetries; however, it explains very well most of the observed phenomena in the experimental context we operated. The main result of this chapter is that, when trying to match a SM to MM fibre via diffusion splicing, aiming to minimise FM loss, one should not necessarily adopt "area matching" at the splicing point as criterion. Instead, we demonstrated what follows: Any reasonably long MM taper produces mode coupling, intrinsically. The mode coupling produced intrinsically can be pre compensate injecting the same amount of mode coupling at the entrance of the taper. The modal unbalancing injected at the splicing point will be annihilated by the mode coupling produced by the taper, resulting in pure SM excitation at the output. To be more precise, also the differential phase of the modes entering in the tapered area must be matched. This gives an idea on how to develop new splices and constitute the basis for future works.

4 Advanced laser characterisation techniques

In this chapter, a novel way of characterising HPFLs and MOPAs will be presented. The novel characterisation technique allows resolving, along the AF's length and at any power, quantities such as: pump absorption, inversion, signal power and non-linear effects. We have called this technique "vertical probing". We will initially describe the technique, subsequently we will recall a theoretical framework to explain the data and finally we will fit the empirical data.

4.1 Vertical probing

In our HPFLs and MOPAs, AF is laid on a metallic plate and it is kept attached to the plate by means of an adhesive film. Normally then the fibre is covered by a silicone composite that increases the thermal conductivity and allows long term, high power operation (Figure 115, left). In this case, we have not covered the AF with any silicone potting, keeping the optical fibres accessible from the top (Figure 97).

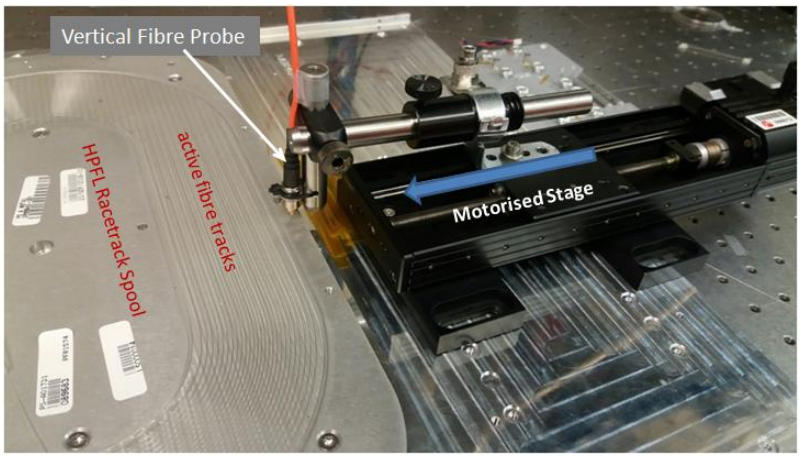

Figure 97. Vertical probing of the AF

A vertical fibre sweeps above the fibre coils probing the light scattered, sampling various points along the fibre length (one point per coil). The sweeping is accomplished by a motorised stage. On the other end, the vertical fibre is connected to an OSA (YOKOGAWA AQ6370), used as monochromator. The probed wavelengths are 950nm, 975nm and 1075nm. The reading of the monochromator in correspondence of these three wavelengths represent respectively the behaviour of the unabsorbed pump power, atomic inversion and signal power. These sweeps can be performed at any power, allowing us to track the three above mentioned laser properties at various powers. It is worth anticipating some fundamental limitations of the technique.

Limitation 1: Position of the two fibres composing the GTW with respect to the probing fibre. To improve thermal performance of the GTW, signal fibre is always positioned close to the metallic plate. As result, the AF core's light (1075nm and 975nm readings) must pass thought the pump fibre (located on top of the AF) before reaching the vertical probing fibre. In this sense, probing of the pump light, coming straight from the top fibre, is more direct than probing the light coming from the underneath signal fibre.

Limitation 2: Chirped winding of the GTW on the metallic plate. To improve thermal performance of the GTW, we usually lay the fibre sections exposed to higher pump power (close to the HR/OC) with looser coils than those where pump power is lower (in the centre of the spool). In the middle of the GTW length, fibre coils are very close to each other. The limited dynamic range of the OSA (-100dBm) creates a limit in the minimum NA usable for the vertical probing fibre. As result, the NA of the probing fibre must be sufficiently big to capture enough light. When fibres are too close to each other (centre of the oscillator), peaks readings are convolved by the presence of neighbouring fibres.

The two described limitations will be clearer once inspecting the data.

4.2 HPFLs modelling

The modelling of our devices is quite elementary and it is inspired by the work of Giles and Desurvire [133]. However, in this work, the vast majority of the parameters are effectively measured rather than assumed. Here, modelled and measured parameters used in this work he will be briefly recalled. For the total signal power P_s^{tot} along the oscillator length, we have:

$$P_s^{tot}(r_i, z) = |\psi^{s1}(r_i)|^2 P_{s1}^{+}(z) + |\psi^{s1}(r_i)|^2 P_{s1}^{-}(, z) + |\psi^{s2}(r_i)|^2 P_{s2}^{+}(z) + |\psi^{s2}(r_i)|^2 P_{s2}^{-}(z) \qquad (4.2.1)$$

Where $\psi_{s1,2}(r_i)$ are the normalised FM (1) and HOM (2) profiles calculated applying the Moroshita method[134] on the measured IOR measurement of the core. $P_{s1,2}^{+,-}$ Are the powers associated with the forward (+) and backward (-) propagating waves for modes (1, 2). At the steady state, inversion N_2 can be written as:

$$N_2(r_i,z) = \frac{N(r_i)\left(\sigma_{12}^{p}\left|\psi_p(r_i)\right|^2\frac{P_p(z)}{h\nu_p} + \sigma_{12}^{s}\frac{P_s^{tot}(z)}{h\nu_s}\right)}{\left(\sigma_{12}^{p}+\sigma_{21}^{p}\right)\left|\psi_p(r_i)\right|^2\frac{P_p(z)}{h\nu_p} + \left(\sigma_{12}^{s}+\sigma_{21}^{s}\right)\frac{P_s^{tot}(z)}{h\nu_s} + \frac{1}{T}} \quad (4.2.2)$$

Where $\mathrm{N(r_i)}$ is the radial distribution of the Yb [#/m3], measured with the SPI tomography system [140], $\mathrm{P_p}$ is the pump power, $\nu_{\mathrm{p,s}}$ are the signal and pump wavelength and $\sigma_{12,21}^{\mathrm{p,s}}$ are the emission and absorption cross sections of pump and signal. Both $\mathrm{N_2}$ and $\mathrm{P_p}$ will be subsequently fitted via vertical scanning along the fibre length z. The term ψ_{p} is modelled as follows:

$$\psi_p = \frac{o}{\sqrt{A_P + A_s}} \quad (4.2.3)$$

Where $\mathrm{A_{P,S}}$ represents the pump, signal fibre cladding areas. Here, the "o" quantity (smaller than 1), indicates the non ideal mode scrambling between pump fibre and signal fibre [10]. The rate equations for the forward and backward propagation waves for the pump ($P_p^{\pm}$) and signals $P_{s1,2}^{\pm}$ are:

$$\frac{\partial P_p^{\pm}(z)}{\partial z} = \pm P_p(z)\left[\sum_{i=1}^{n}\{(\sigma_{12}^{s}+\sigma_{21}^{s})N_2(r_i,z) - \sigma_{12}^{s}N(r_i)\}\left|\psi_p(r_i)\right|^2 2\pi L r_i \Delta r \mp \alpha_p\right] \quad (4.2.4)$$

$$\frac{\partial P_{s1}^{\pm}(z)}{\partial z} = \pm P_{s1}^{+}(z)\left[\sum_{i=1}^{n}\{(\sigma_{12}^{s}+\sigma_{21}^{s})N_2(r_i,z) - \sigma_{12}^{s}N(r_i)\}|\psi_{s1}(r_i)|^2 2\pi L r_i \Delta r \mp \alpha_s\right] \quad (4.2.5)$$

$$\frac{\partial P_{s2}^{\pm}(z)}{\partial z} = \pm P_{s2}^{+}(z)\left[\sum_{i=1}^{n}\{(\sigma_{12}^{s}+\sigma_{21}^{s})N_2(r_i,z) - \sigma_{12}^{s}N(r_i)\}|\psi_{s2}(r_i)|^2 2\pi L r_i \Delta r \mp \alpha_s\right] \quad (4.2.6)$$

Here $\alpha_{\mathrm{s,p}}$ represent respectively the signal, pump background loss. Background losses are measured in the fibre department area by mean of an Optical Fibre Analysis System (PK2600 by Photokinetics).

For the boundary conditions, at L =25m and L =0, we have:

$$P_p^+(0) = \ total\ pump\ power\ /\ 2 \qquad (4.2.7)$$
$$P_p^-(L) = \ total\ pump\ power\ /\ 2$$
$$P_{s1}^-(L) = \ P_{s1}^+(L) * OCR * S11$$
$$P_{s2}^-(L) = \ P_{s1}^+(L) * OCR * S12$$
$$P_{s1}^+(0) = \ P_{s1}^-(0) * HRR * S11$$
$$P_{s2}^+(0) = \ P_{s1}^-(0) * HRR * S12$$

The terms S11 and S12, measured via S^2, along with the steady state equation for the inversion (4.2.2), are the only terms responsible for mode coupling in our simple model. The gratings reflectivity OCR (output coupler) and HRR (High reflector) are those specified by the vendor or alternatively can be modified to account for spectral broadening. This model does not consider non-linear effects and does not treat the single wavelengths composing the spectrum singularly. However, in reality, due to non-linear effects (SRS, FWM and MAFWM), the laser spectrum broadens with part of the spectrum leaking out of the bandwidth of the gratings. It is therefore a mistake considering the same grating reflectivity (i.e. the nominal one provided by the grating's vendor) for each of the wavelengths composing the spectrum. In first approximation, we can consider all wavelengths of the spectrum to be subjected to an effective reflectivity.

The code for this modelling is written in Matlab by the author of this thesis. The numerical integration is performed with Runge Kutta, with a routine called BVP (boundary value problem). The benefit of BVP is that, on top of the rate equations, the boundary conditions can also be provided to the numerical solver. The BVP routine will take care of iterating between beginning and end of the oscillator to provide a converging solution.

4.3 HPFL measurement and data fitting.

To exemplify the vertical probing features and limitations, in Figure 98 we show the raw data acquired during a vertical sweep performed when output power was 2kW (Figure 98). LMA oscillator's details will be presented in due course of this chapter.

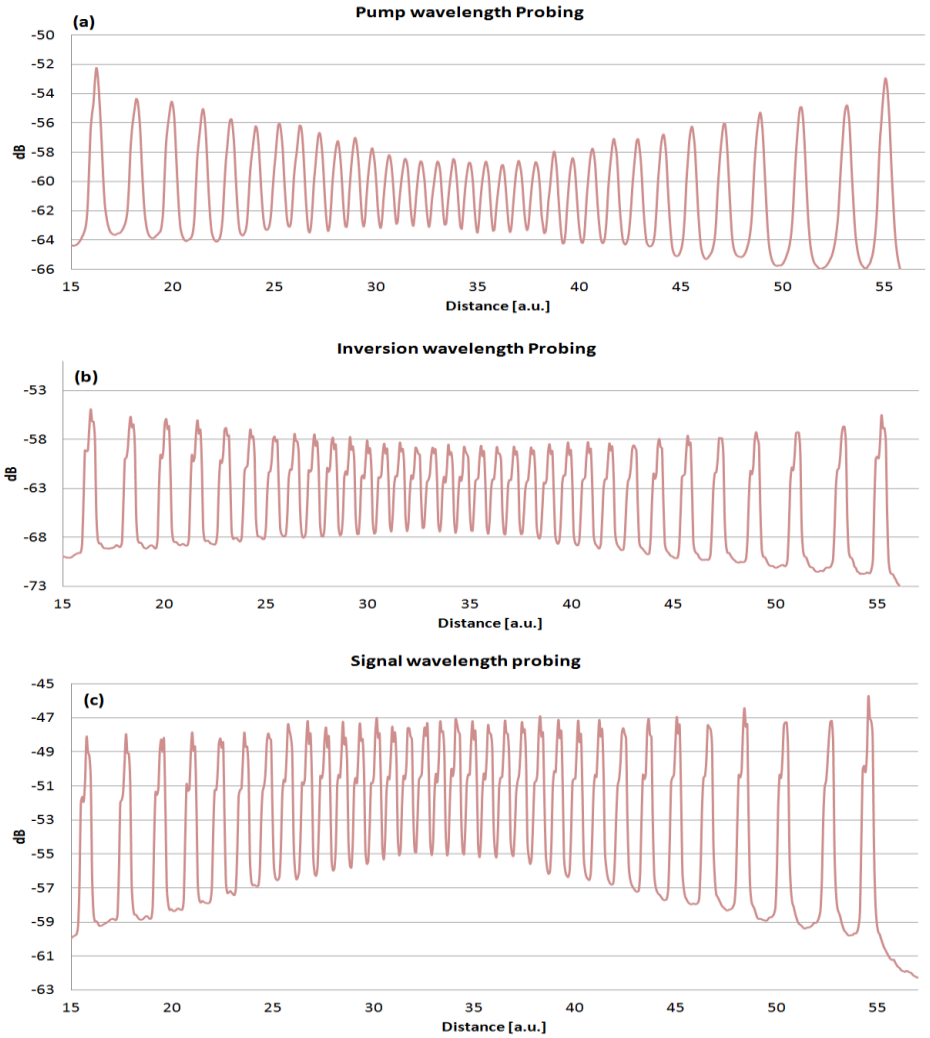

Figure 98. Vertical probing. Raw data acquired at 2kW. Readings obtained with monochromator aperture locked at (a) 942nm, (b) 1075nm and (c) at 1075nm

The device under test is a 25 meter long HPFL. In Figure 98, we recognise that the readings of peaks located in the centre of the oscillator are affected by the light coming from the neighbouring peaks. This is due to the chirped fibre winding mentioned in the previous chapter (Limitation 2). Secondly, only the readings of (a) are smooth (e.g. round). This is because in the reading of (a), related to the pump fibre, the light goes directly from the pump fibre (located on top) to the vertical probing fibre. Conversely, the peaks of charts (b) and (c) are not smooth and present three sub peaks. As explained before in "Limitation 1", the presence of these peaks is due to the fact that the signal light (coming from the bottom fibre) encounter the pump fibre before accessing the probing fibre. In the next figure, we will show the results obtained at eight different output powers, plotting the peak values of the ripples against the AF length.

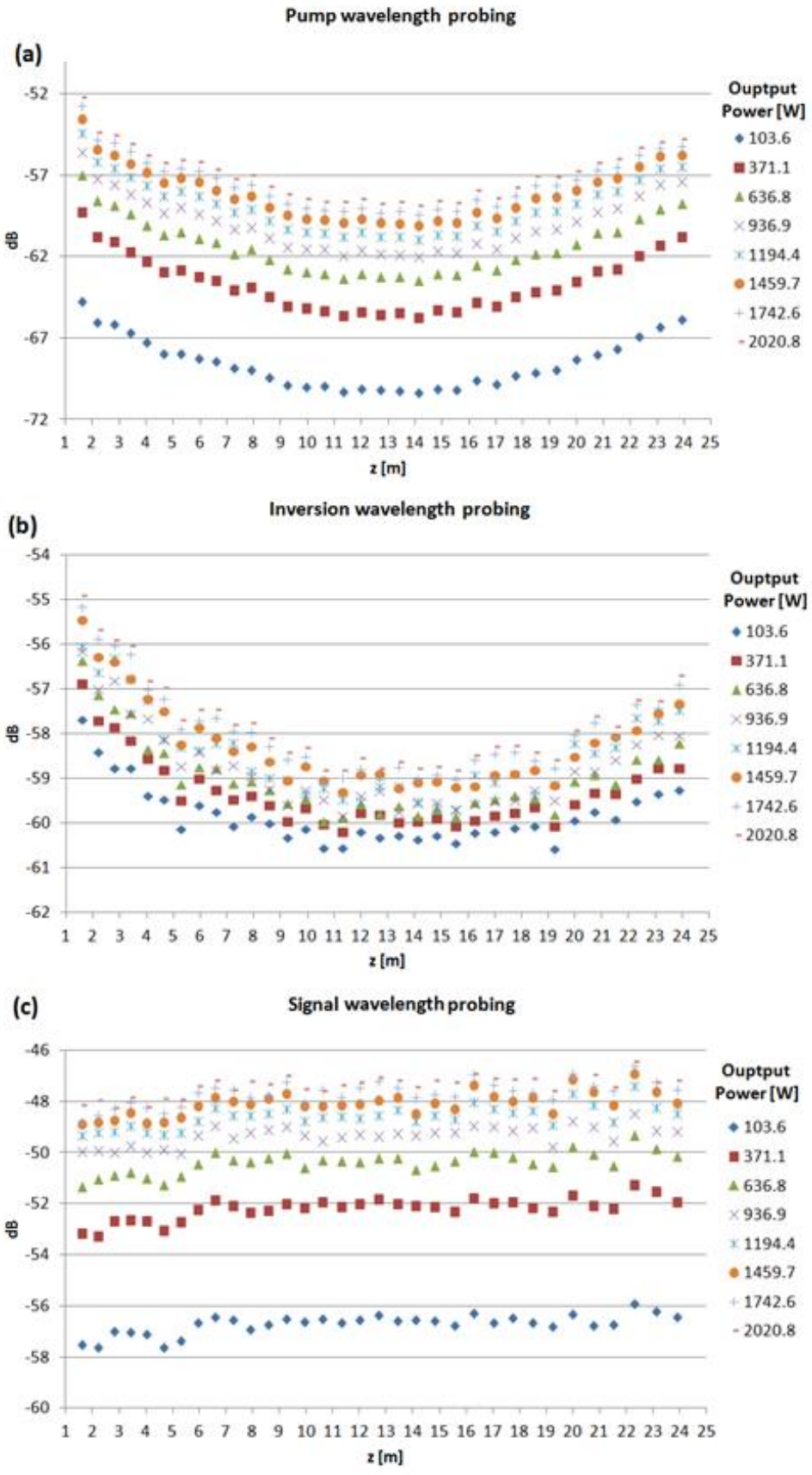

Figure 99. Vertical probing. Peaks value versus AF length. Peaks obtained at various output power (in the legend) with monochromator locked at (a) 942nm, (b) 1075nm and (c) at 1075nm.

In Figure 99, the z distance along the fibre has been quickly reconstructed by simple geometrical considerations and ignoring the chirping of the fibre's winding; in fact here we are more interested at the vertical part of these charts (y-axes). In Figure 99(a) we see that the scattering of the pump light has a symmetrical shape versus the fibre length. For each power, the difference in scattered power between the first point (on the left or right) and the central points (at about 13 meters) is of about 5dB. However, the readings at 13 meters, since affected by neighbouring fibres ("Limitation 2") are bigger than normal, probably even up to 2dB higher than they should be. Also, since at 13 meters we have equal contribution from pumps on both sides, we can assume that the pump light scattered due to a single pump is actually 3dB less than the read one. Keeping all this in mind, if one thinks at the laser as pumped only from one end, the residual pump power difference between the first and the central peaks can be estimated to be 10dB. If we then assume that pump abortion will continue to be attenuated exponentially, we have that the residual pump scattering difference between first and last peak will be about -20dB. In Figure 99(b), we recognise that the vertical points' location is noisier then in Figure 99(a); this is substantially due to Limitation 1. Vertical power jumps (or dip) located at particular z positions are common and repeat themselves similarly at any power; this testifies that the measurement is affected by fine details of the fibre winding (for instance the inclination of the GTW with respect to the metallic plate). Beside this, in Figure 99(b), we see that the light scattered is asymmetrical; this is substantially due to the different reflectivity of the OC (located at 25mt) and HR (located at 0mt). The difference of reflectivity unbalances the signal power along the AF length (signal is higher close to the OC and smaller close to the HR). This in turn makes the inversion unbalanced (inversion is higher at the HR side and smaller at the OC side). The nominal HR reflectivity is 99.99%, with central wavelength at 1075nm and BW of 10nm. The nominal OC reflectivity 14%, with central wavelength at 1075nm and with a BW of 2nm. It is worth noticing that the nominal reflectivity is quoted by the vendor and applies at low power regime. The worst measurement in terms of noise is certainly that of the signal light shown in Figure 99(c). Here, another fact that complicates even further the signal readings is that signal light coming from the core (at 1075nm) is very directional, resulting therefore in a scattered signal has high directionality as well. This makes the signal scattered at 1075nm more dependent on geometrical artefacts occurring during the fibre winding process. In Figure 99(c), for any output power, we recognise that signal power grows from zero to 25meters, gaining about 1dB of power. We can also notice that the signal's reading goes up rapidly in the first 7 meters, become

flat for about 12 meters and then, from 19 meters onward, starts growing again, but slowly than at the beginning of the laser. Before showing the usage of the model to fit the data of Figure 99, let us state other interesting high power test results. The optical/ optical efficiency measured for this laser is 75%, the mode stripper grid slope efficiency is 0.02[°C/W]. The grid mode stripper slope efficiency unit is °C/W, where °C is the temperature in Celsius measured by a thermal camera on the metallic grid surmounting the mode stripper (Figure 117, see next chapter) and W is the pump power in Watt. The end to end pump absorption is 18dB, the LP02 excitation measured by $S^2$is -36dB. To estimate the effective reflectivity of the OC it is useful to present the spectral output of this device up to 2.36kW. The output of this HPFL has been directed to the thermal head power meter, where spectrum was measured, with a 250um diameter, 1 meter long delivery fibre. Due to its large diameter, the delivery fibre contribution to SRS is entirely negligible. In Figure 100, the measured ouptut spectra is clearly wider than the OC bandwidth, therefore as power goes up, the effective reflectivity (i.e. fraction of light reflected back in the cavity) decreases.

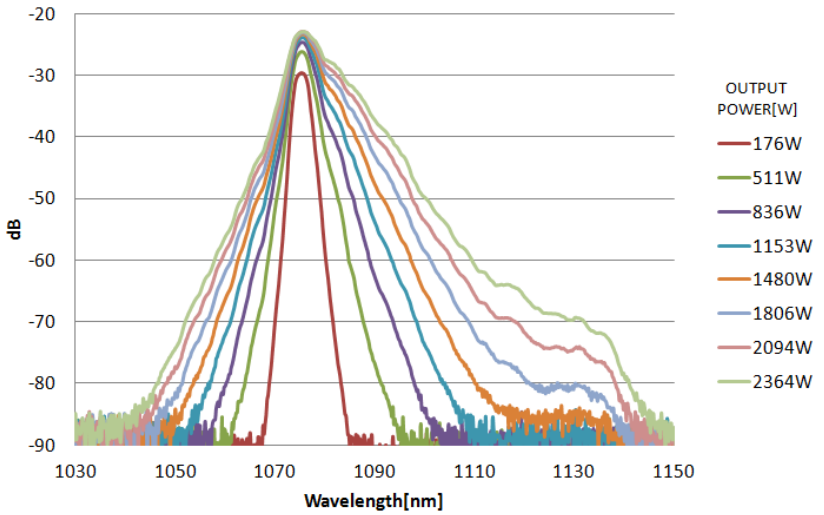

Figure 100. Spectral output of LMA laser under test.

The effective OCR in presence of such broad signal can be calculated considering the specs of the OC, normalising the spectra and utilising the measured output powers. In brief, to do so, we can set a 2nm wide region into which reflectivity is 14% and related the part reflected by that region to the total power inside the oscillator, just before the OC. The complete procedure for the calculation of the effective OCR is not discussed further here. The calculated effective OCR is presented in Figure 101.

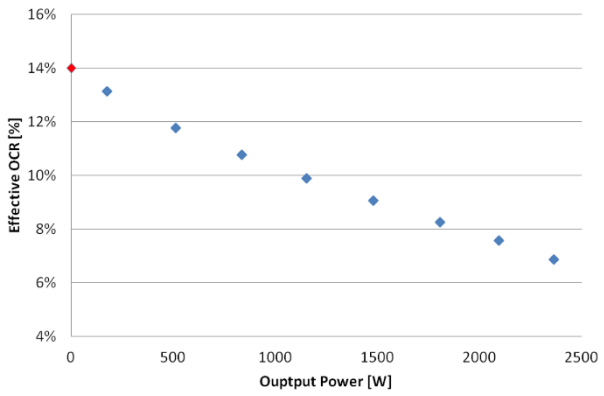

Figure 101. Effective OCR versus output power. In red the nominal reflectivity.

As it can be seen by Figure 101, the OCR effectively decreases with the output power. The effective HRR is assumed to be constant with power and equal to the nominal. This is due to the wide bandwidth of the HR, making any leakage outside this band negligible at any considered power. For the modelling we have used the measured IOR (to calculate the modal shapes) and the Yb distribution (Figure 102).

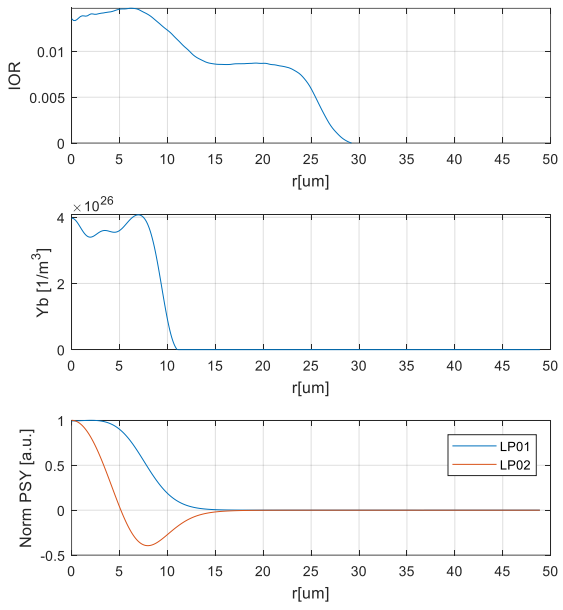

Figure 102. Laser model. From top to bottom: measure IOR(values relative to silica), measured Yb Concentration and calculated LP01 and LP02.

Comparing Figure 102(a) and (b) and referring to the fibre radius, we see that the Yb doping does not cover the core in its entireness. This technology is referred as selective doping. The details and advantages of the selective doping will be explained in a later session. For the cross sections we have used the values found in [135, 136].

We will now use the simple laser model to fit the data acquired with the vertical probing technique. The fittings have been performed at low power (103W) at medium power (936W) and high power (2020W) and presented respectively in Figure 103,Figure 104 and Figure 105.

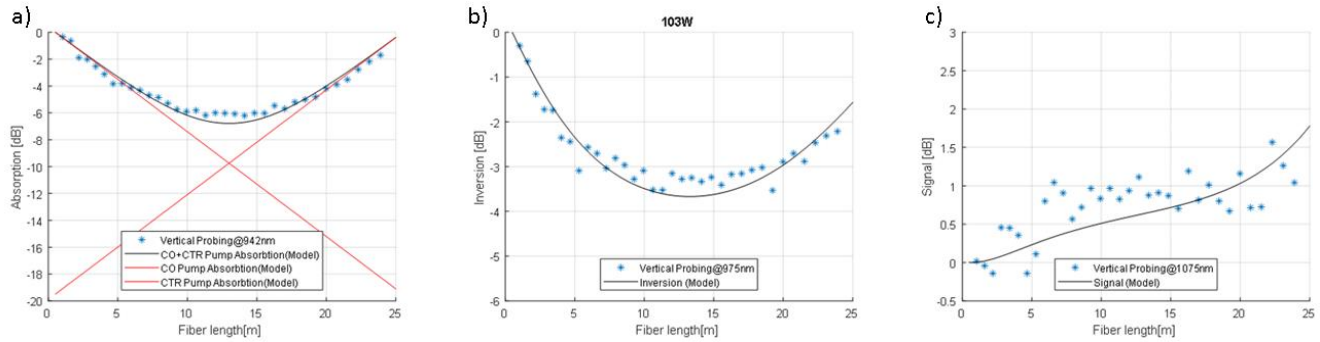

Figure 103. Vertical probing versus modelling at 103W. (a) Pump, (b) Inversion and (c) Signal.

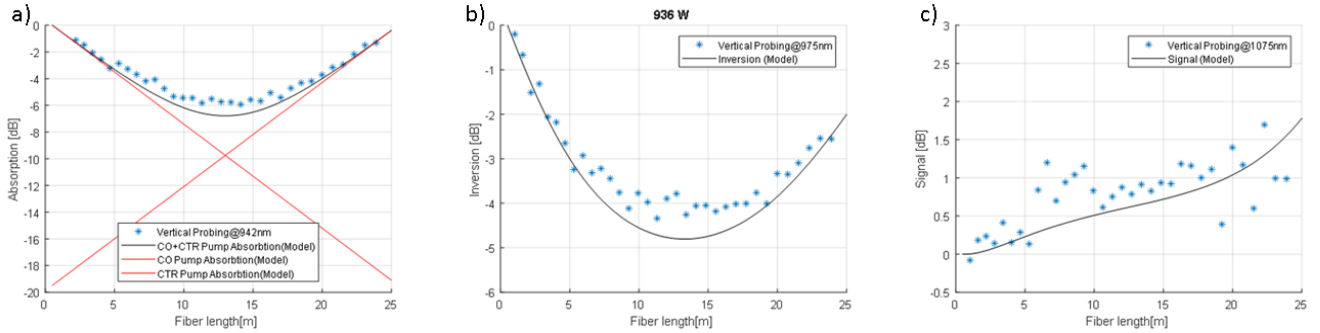

Figure 104. Vertical probing versus modelling at 936W. (a) Pump, (b) Inversion and (c) Signal.

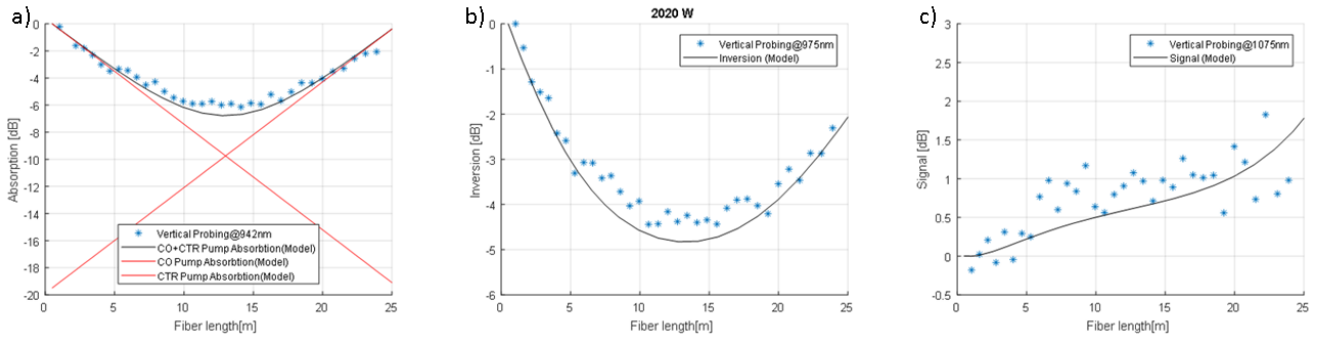

Figure 105. Vertical probing versus modelling at 2020W. (a) Pump, (b) Inversion and (c) Signal

For the three pump absorption fittings (three a) figures), the best value found for “o” in formula (4.2.3) is 0.46. With this value for “o”, the first and last sections of the fibre are well interpolated, resulting in total end-end absorption of about 20dB.

First, we notice that, in any of the nine charts here below, the empirical points in the centre are always higher than modelling; this is due to the previously explained Limitation 1. Second, there is discordance between the empirically measured end-end absorption (18dB) and the modelling (20dB). The discordance can be explained remembering that absorption in GTW saturates with length[10]. This saturation effect has not been embedded in our simple model, but it is in principle measurable. In fact, if the fibres were well spaced apart and the laser were pumped from one end only, this technique would certainly allow characterising the pump absorption saturation in GTW (future works).

To fit the inversion readings (three b) figures) at the three powers, we have had to adopt three different values for the effective OCR in (4.2.7) as with the single nominal value of OCR it was impossible to fit the three powers. The effective OCR used for 103W, 936W and 2020W are respectively 13%, 8.8% and 7.1%. These values closely resemble those calculated in Figure 101, or at the least have the same behaviour: they decrease with the power.

The model fails to fit the empirical data pertaining the signal readings. For the signal readings (three c figures) we see that both model and simulation forecast a growth at the beginning of the fibre, a plateau in the centre and a further grow toward the end. We also notice a vertical spread of the points. This vertical spread is little at the beginning of the cavity (L<5 meters) and big at the end of the laser (L>20meters). Figure 106 exemplify the concept of vertical spread of the signals point for the signal measured for 2020W case.

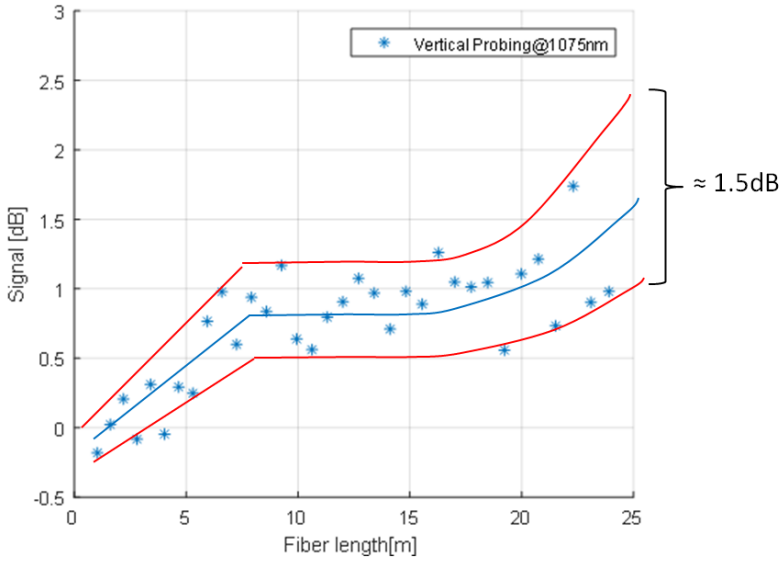

Figure 106. Spread of vertical points for signal readings at 2020W

The two red lines, pictorially surrounding the signal readings could effectively represent the envelope of a beating note between FM and HOM expressed like:

$$I^{\pm} = I_{FM} + I_{HOM} \pm 2\sqrt{I_{FM} * I_{HOM}} \qquad (4.2.8)$$

Manipulating formula (4.2.8), utilising the red/ blue lines and the output power, one can estimate $\mathrm{I_{HOM}(z)}$. For instance, at the end of the fibre, $\mathrm{I_{HOM}} \approx 30\mathrm{W}$.

So far, in our HPFLs model, the only contemplated mechanism for HOM coupling is via Yb competition and mode scattering at the splicing points. With an MPI of -30dB for the LP02, the simulated LP02 power at the end of the laser is only 1.1W and the laser efficiency is 77%. In reality, we measure an efficiency of 75% and we infer the presence of 30W of power in the HOMs in correspondence of the output. We need therefore to postulate some further mechanism of mode coupling accounting for the presence of HOM and lack of efficiency.

As frequently reported in the literature, TMI is believed to be caused by thermal or inversion related gratings formed by the beating between FM and HOM [28-35, 137-139]. The gratings formed by this beating, in turn, promote mode FM->HOM coupling and results in TMI. We can therefore speculate that, the bigger the fringe visibility of these so formed gratings, the bigger the vertical spread of the signal reading. Recalling the fringe visibility formula in the context of FM and HOM beating together, we have:

$$V = \frac{I_{max} - I_{min}}{I_{max} + I_{min}} = \frac{2\sqrt{I_{FM} I_{HOM}}}{I_{FM} + I_{HOM}} \qquad (4.2.9)$$

The so defined V can therefore be characterised empirically from the signal scattering measurement. For the measurement at 2020W, we obtain:

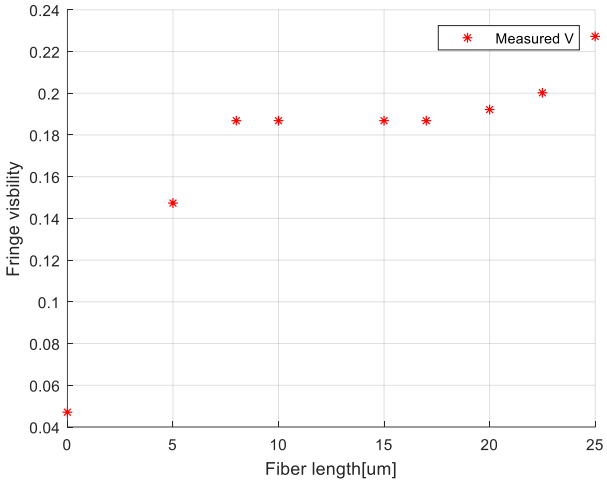

Figure 107. Fringe Visibility empirically measured from signal reading at 2020W.

In Figure 107, we notice that the measured FV is little at the beginning of the laser and big at the end of the laser. This behaviour follows the size of the vertical spread highlighted in Figure 106. Specifically, the FV seems to grow substantially from 0 to 7 meters, remains flat between 7 and 16 meters and then grows a bit further till the end of the laser. To provide some insight about the HOM coupling, we can alter the rate equation and add terms of scattering between modes. We need to model the FM->HOM scattering terms in order to obtain to the correct efficiency and modal excitation and therefore a good agreement between the calculated FV and the measured one. To model the mode coupling, we have altered the equations proposed in paragraph 4.2, in the following way:

$$\frac{\partial P_{s1}^{+}(z)}{\partial z} = P_{s1}^{+}(z)\left[\sum_{i=1}^{n}\{(\sigma_{12}^{s}+\sigma_{21}^{s})N_2(r_i,z)-\sigma_{12}^{s}N(r_i)\}|\psi_{s1}(r_i)|^2 2\pi L r_i \Delta r - \alpha_s - kf\right] \quad (4.2.10)$$

$$\frac{\partial P_{s2}^{+}(z)}{\partial z} = P_{s2}^{+}(z)\left[\sum_{i=1}^{n}\{(\sigma_{12}^{s}+\sigma_{21}^{s})N_2(r_i,z)-\sigma_{12}^{s}N(r_i)\}|\psi_{s2}(r_i)|^2 2\pi L r_i \Delta r - \alpha_s\right] + kf P_{s1}^{+} \quad (4.2.11)$$

$$\frac{\partial P_{s1}^{-}(z)}{\partial z} = -P_{s1}^{+}(z)\left[\sum_{i=1}^{n}\{(\sigma_{12}^{s}+\sigma_{21}^{s})N_2(r_i,z)-\sigma_{12}^{s}N(r_i)\}|\psi_{s1}(r_i)|^2 2\pi L r_i \Delta r + \alpha_s - kb\right] \quad (4.2.12)$$

$$\frac{\partial P_{s2}^{-}(z)}{\partial z} = -P_{s2}^{+}(z)\left[\sum_{i=1}^{n}\{(\sigma_{12}^{s}+\sigma_{21}^{s})N_2(r_i,z)-\sigma_{12}^{s}N(r_i)\}|\psi_{s2}(r_i)|^2 2\pi L r_i \Delta r + \alpha_s b\right] - kb P_{s1}^{-} \quad (4.2.13)$$

In the four rate equations above, the coefficient kf, kb account the coupling between LP01 (s1) toward LP02 (s2); particularly, kf is used for the forward waves (P_{s1}^{+} coupling to P_{s2}^{+}) and kb is used for the backward waves (P_{s1}^{-} coupling to P_{s2}^{-}). Furthermore, we can decide to utilise the coefficients in certain parts of the laser only; we can make kf, kb functions of z.

Five types of coupling configurations (CC) have been attempted. In Table 4, each column describes a CC, with its resulting efficiency, HOM excitation and a comment about the FV fit correctness. For each of the five CC, Figure 108 shows the calculated fringes of visibility.

CC number	1	2	3	4	5
Coupling Strength	0	0.00036	0.0004	0.0012	0.0012
Coupling Zone	NA	0-25mt	0-25mt	0-7.5mt	17.5-25mt
Coupling Verse	NA	FW-BW	FW	FW	FW
Laser efficiency [%]	77	75.2	75	75.4	76
HOM Power at z =25mt [W]	1.18	30.8	34	35	24
Fringe Visibility fitting	Too little	Bad at beginning of the laser	Bad in the middle of the laser	Best Fit	Bad fit

Table 4. Mode coupling scheme attempted.

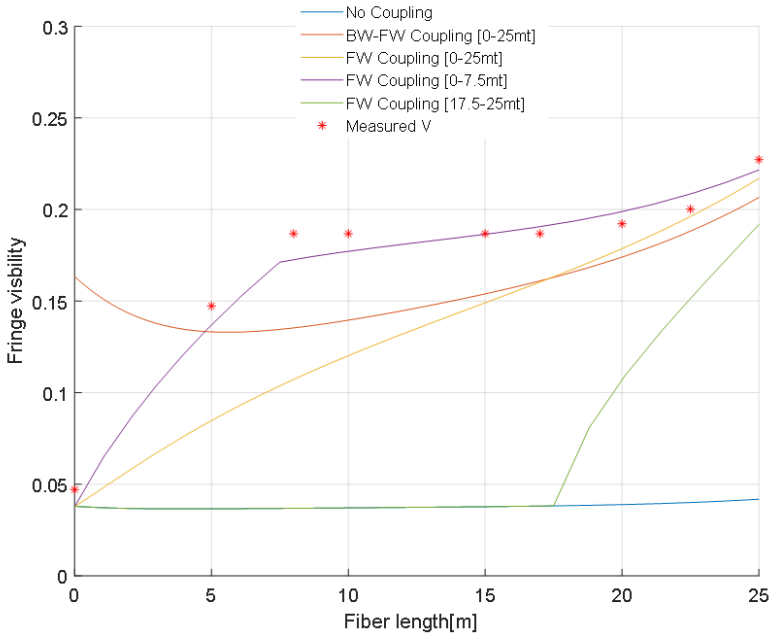

Figure 108. Fringe visibility in presence of different mode coupling mechanisms

In CC1, we have ignored any mechanism of modal coupling (other than at the splice). To obtain this we have set $kf = kb = 0$. As pointed out earlier on, this result in 77% of efficiency and very little HOM; this conflict both with measured efficiency (75%) and estimated HOM (35W), clearly the resulting FV in Figure 108 is too little compared to the measured one.

In CC2, we have used $kf = kb = 3.6x10^{-4}$ on the whole fibre length [0-25mt], in attempt to mimic a phenomenon of distributed scattering along the laser. With this configuration, we can fit the measured efficiency and HOM at the end of the fibre, however, calculated fringe visibility is too big at the beginning of the fibre.

In CC3, we have used $kf = 4x10^{-4}$, $kb = 0$ on the whole fibre length [0-25mt], in attempt to mimic a scattering only in the forward direction. With this configuration, we can fit the measured efficiency and HOM at the end of the fibre. Calculated FV is in agreement with the measured one both at the beginning and at the end of the fibre, but it fails anywhere else.

In CC4, we have used $kf = 1.2x10^{-3}\ (z \leq 7.5m),\ kf = 0\ (for > 7.5mt), kb = 0$. With this CC we attempted to mimic a scattering only in the forward direction, occurring only during the first 7.5 metres of the laser. We have attempted this scheme, because the coils close to the HR are tightly coiled and possibly responsible for LP01-> HOM coupling (Figure 109). With this configuration, we can fit well the measured efficiency, the HOM power at the end of the fibre. Furthermore, the calculated FV fits the measured FV all over the fibre length.

CC5 will be discussed later.

The results of CC4, fitting the empirical FV curve, efficiency and modal excitation, seems to suggest that the most likely mechanism of mode coupling is due to the tight bends located at the beginning of the laser; i.e. close to the, HR along the first 7.5 meters circa.

To verify the correctness of this assumption, the same spool has been tested as an amplifier twice: one time with the input close to the tight coils (output close to the loose coils) and the other time with the input close to the loose coils (output close to the tight coils).

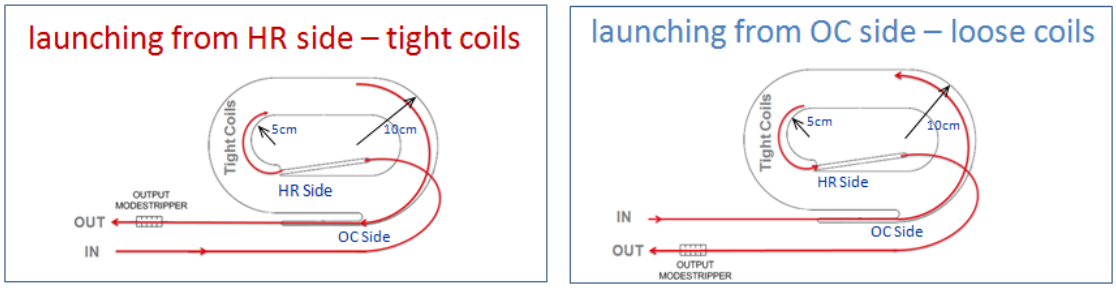

Figure 109. Spool used as an amplifier. Left: input close to tight coils. Tight: input close to loose coils

To obtain an amplifier out of the LMA oscillator, gratings have been cut out, keeping the SM-MM splice in place. To perform the MOPA test on this spool the, another LMA laser has been used as seed. The so built MOPA has been tested at high power, with output power and mode-stripper grid monitored. Starting from a "simmering" seed only power of 340W, seed and amplifier power has been ramped up until reaching 3.2kW of output power.

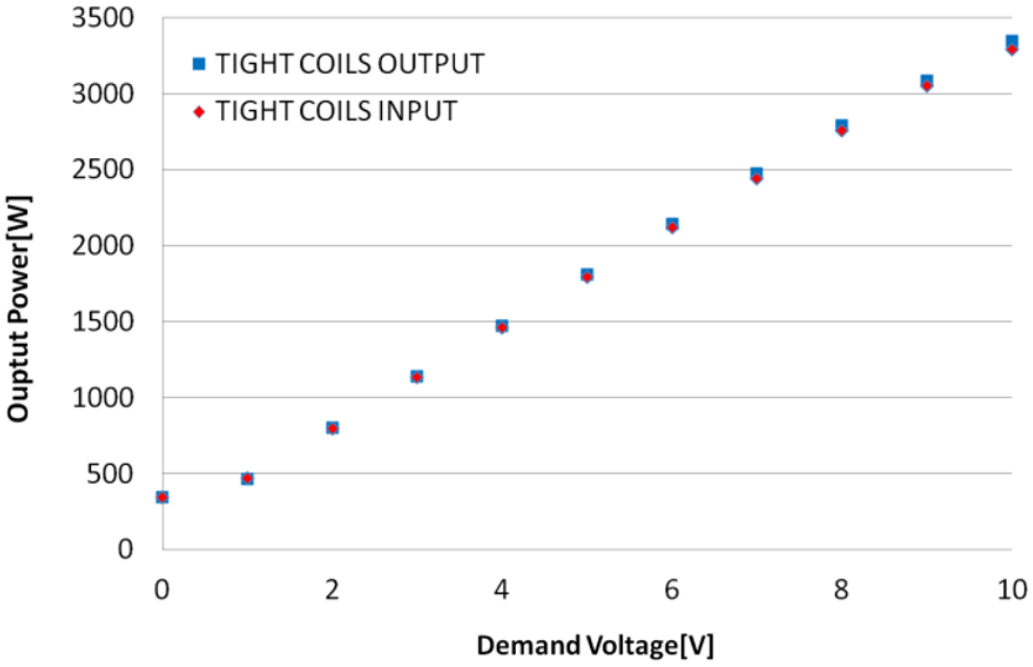

Figure 110. Output power MOPA tested in the two verses of propagation.

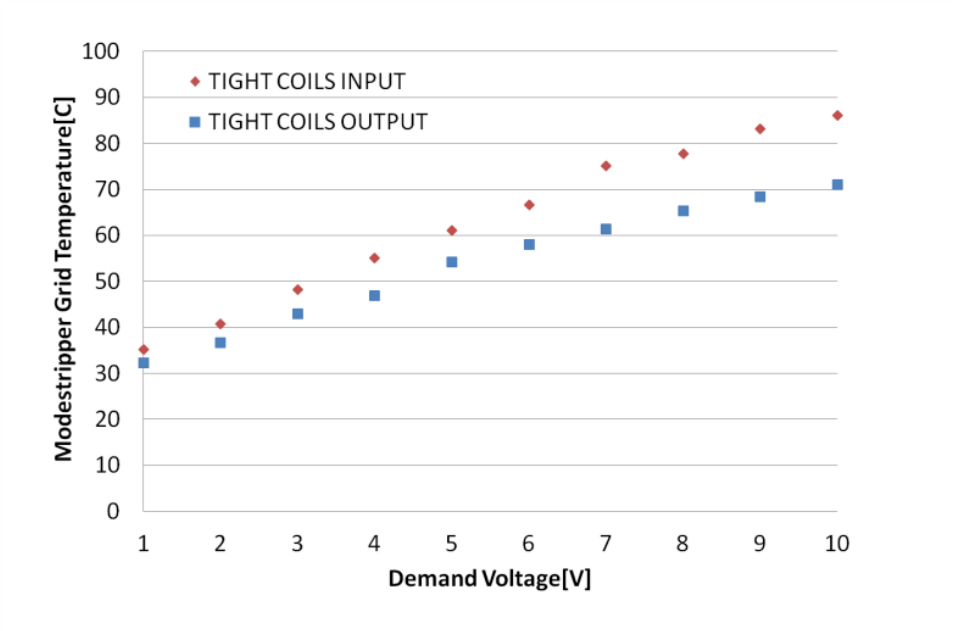

Figure 111. MOPA's Output mode stripper grid temperature in the two verses of propagation

Consulting Figure 110 and Figure 111 and comparing the performances of the two senses of propagation, it is possibly to spot how the tight coils at the input reduce the amplifier efficiency and increase the output mode-stripper grid temperature (and vice versa). If tight coils are at the input of the system, HOMs gets coupled at the beginning of the amplification process, then HOMs get amplified for a further 25meters, competing with the FM cavity and hence reducing the efficiency. The presence of more HOM in the case of tight coils at the input is also testified by a hotter mode-stripper grid at the output. In case of tight coils at the output, HOMs are equally coupled, but immediately dumped on the output mode-stripper without getting amplified. This is exactly the purpose of the simulation run with CC5 on the oscillator. In CC5 we have used $\mathrm{kf} = \ 1.2\mathrm{x}10^{-3}$, $\mathrm{kb} = 0$, with kf active only between 17.5 and 25meters and equal to zero everywhere else. With this simulation, we have a forward mode coupling only at the end of the amplification chain. CC5 is the swapped version of CC4, representing what we have empirically achieved done by swapping the verse of propagation in the spool. Comparing CC5 and CC4, we acknowledge that CC5 is 1% more efficient and has 11W less of HOM at the output, proving also theoretically that is better to have the tight coils at the output rather than at the input.

Another interesting and unique application of the vertical probing technique is the measurement of the whole spectral evolution along the fibre length. To implement this, for each fibre encountered during the transversal sweep of the stage, a whole spectral bandwidth of readings has been acquired [from 1065nm to 1105nm]. We have applied this

technique to measure the spectral broadening of the MOPA configuration briefly described above. The results obtained at 1500W, 2016W and 2800W will be presented respectively in Figure 112, Figure 113 and Figure 114. From the three figures, it is possible to notice that spectral broadening starts diverging from the centre of the fibre; regardless of the power. Given the limited dynamic range of the measurement (only 30dB circa) it was impossible to track SRS (located at 1130nm), however it is easy to notice the spectral broadening due to MAFWM immediately close to the main peak at 1075nm (seeding wavelength). Compatibly with the modelling of the HOM coupling mechanisms proposed earlier on, we also notice that no spectral broadening is present in the backward direction; making the idea of distributed scattering even more questionable.

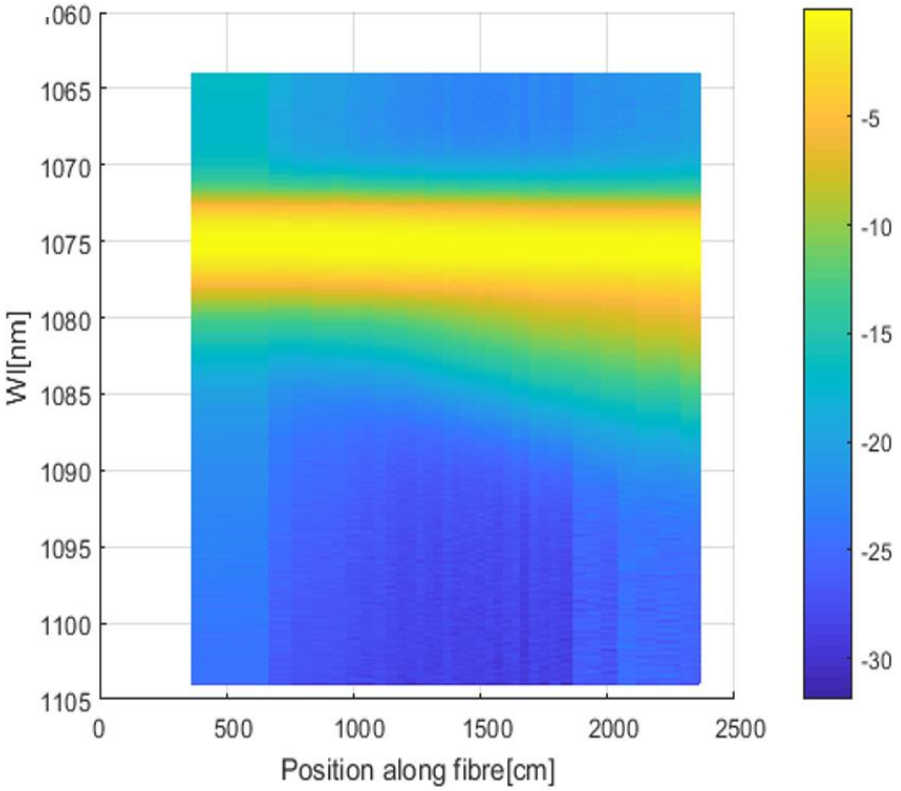

Figure 112. Spectrally resolved vertical probing at 1500W

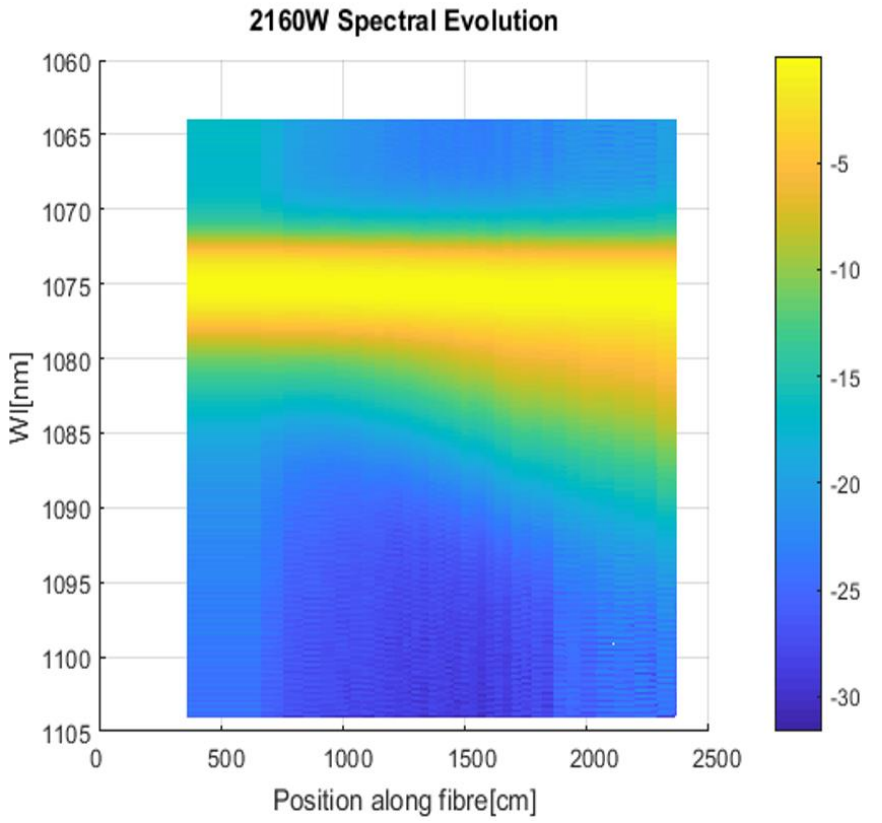

Figure 113.Spectrally resolved vertical probing at 2160W

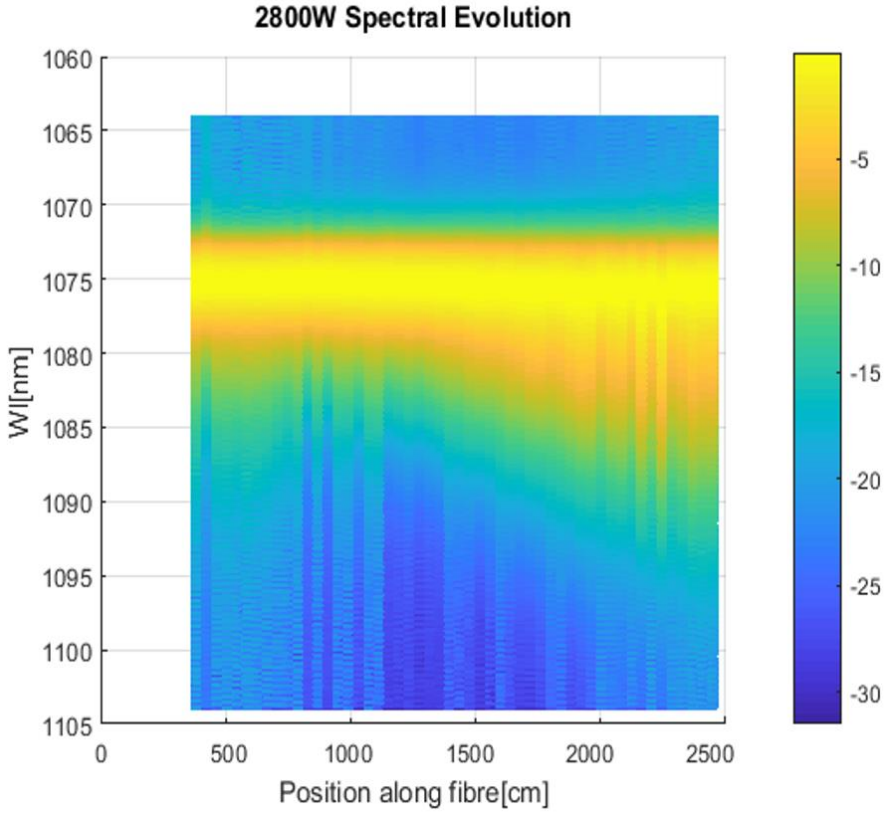

Figure 114. Spectrally resolved vertical probing at 2800W

4.4 Conclusions

In this chapter, we have demonstrated the limits and the potentials of an innovative measurement technique for HPFLs and MOPAs. For the first time, to the author knowledge, the pump absorption, the inversion and the signal of HPFLs have been tracked along the AF length. The limits of the technique are mostly related to the lack of dynamic range of the monochromator imposing a limit in the spatial resolution in between coils. The potentials of this technique are quite vast. For instance, it is known that absorption along the GTW fibre length is not exponential. A classic pump absorption measurement does not provide the designer with the real pump light distribution along the fibre length. Pump absorption distribution are usually achieved by tedious and destructive cutback measurement. This technique overcomes this problem providing directly details about the pump absorption distribution along the laser length. In HPFLs, to contain the SRS it is important to use the bare necessary fibre to guarantee sufficient pump absorption (e.g. 18dB). The technique can therefore used to optimise laser length according to pump wavelength, winding pattern, and the claddings' surface geometry to name a few. The novelty of the technique is that it allows fitting many parameters that resides in the rate equations: these are the most inner and before inaccessible parameter of the HPFLs and MOPAs. To the author's knowledge, for instance, no other technique has been adopted so far to track the inversion along the laser length and relate it to the effective reflectivity of the gratings. At the same time, we can track the signal along the fibre length. Retrospectively, the author is not surprised to have found a bad fitting for the signal measurement since HOM beating was nowhere to be seen in the simple rate equation proposed. Still, the technique sees what happens in real world systems and has been able to identify where HOM coupling takes place, providing very useful information to the laser design. More details connected with modal instability and mode coupling can be found in the work we presented in [75, 76] and recalled in the next chapter. To the author's knowledge, the spectral broadening along the fibre length has not been measurably reported before, so this technique also allows tracking of non-linear phenomena such as MAFWM. In the future this technique will be used to design lasers with new pump wavelengths (e.g. pump absorption optimisation). The method of the fringe visibility will be explored with more stable and unstable lasers, since the proposed one was not unstable at all. Measurement limits can be overcome by adopting un-chirped fibre windings and/or vertical fibres with collimators.

5 High Power fibre testing

Design of HPFLs involves the selection and optimisation of various parts such as: pump diodes (including wavelength and brightness), pump combiners, gratings strength and wavelength, active and passive fibre index of refraction, AF doping level and shape, to name a few. In this work, we will focus our attention on the optimisation of the fibres splicing and on the doping configuration of the AF. Initially, we will show the testing of a non-optimised HPFL, resulting in poor efficiency and severe TMI. Subsequently, we will show the performance of an optimised large mode area laser, performing stably. For the second laser, the splice optimisation has been controlled: it will be showed that the same laser with or without splice optimisation, results in a good or bad laser. This will prove the effectiveness of the discovered splice optimisation. We will also complement this work with a model and demonstrates that the right combination of selective doping and splice optimisation yields to lasers that are easier to splice, more stable and more efficient. The impact of the splicing technology and the effect of the core centrosimmetricity will be illustrated on several lasers built by the SPI Lasers production line. At the end of the chapter, we will present the performance of a laser obtained by putting together all the learning acquired during this PhD. This laser is so far the most efficient HPFLs built at SPI Lasers.

5.1 General laser description and high power testing configuration

In chapter 2, the pumping setup of the high power test-kit has been presented. In this paragraph we will focus on the probing of the HPFLs when powered up. The laser configuration is shown in Figure 115, Figure 116.

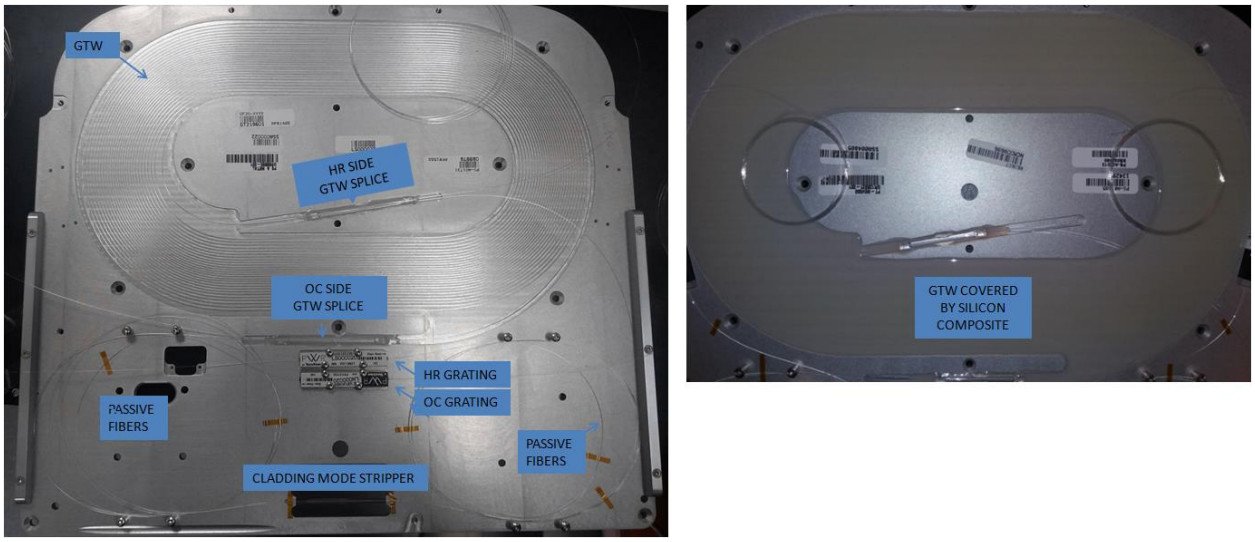

Figure 115. Top view of SPI Red Fox HPFL without (left) and with (right) silicon composite covering the GTW

By inspecting Figure 115(left), it is possible to notice how the GTW coils are tighter close to the HR (inner coils) and become progressively looser toward the OC (outer coils). The OC and HR side GTW splice are contained in a specially designed cylindrical structure that consents high power operations. The passive fibres are coiled on the plate at a specific radius; this as shown previously in paragraph 3.2.1, limits the modality in these sections of the system, especially in the case of DMF. To render the fibre resilient during long term testing and to improve the heat conduction of the fibre toward the metallic heat sink, the AF is covered by a UV curable silicone composite (Figure 115 right).

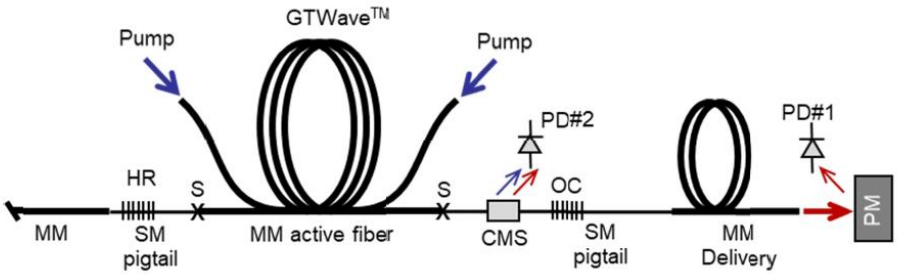

Figure 116. SPI HPFLs scheme and position of the probes during typical high power test. CMD stand for cladding mode stripper and PM stands for power meter.

The AF is a GTW, with a 250µm pump fibre and a 200µm signal fibre. The passive and active IORs have shapes very similar to those presented in Figure 36, Figure 37 (see later for more specific details). The gratings of this system are written on the passive fibres and

centred at 1075nm (HR reflectivity = 99.99%, OC reflectivity = 4%). The output passive fibre has a CMS. This mode stripper gets rid of both unabsorbed pump (very little), but most importantly this mode stripper gets rid of the residual signal light scattered by the SM-MM splice (due to suboptimal splicing). The system is pumped by 950nm diodes from both sides of the GTW in CW regime or with square pump pulses. The output power of the system is measured with a thermal head power meter. Two photodiodes PD#1 and PD#2, connected to an 8GHz oscilloscope, monitor the laser output, scattered off the thermal head power meter (PM), and the power stripped-off by the CMS, respectively. CMS are fabricated at SPILasers. The fabrication includes the removal of four centimetres of polymeric coating from around the passive fibers. The external part of the exposed glass is then made rough via laser processing. The rough part is then incorporated in a cylinder of glass (figure 117). In the test of the lasers, the CMS is surmounted by a metallic grid capturing the light scattered by the CMS. This metallic grid captures the light scattered from many angles with consequent increase of temperature of the grid. The temperature of the grid is then measured by a thermal camera.

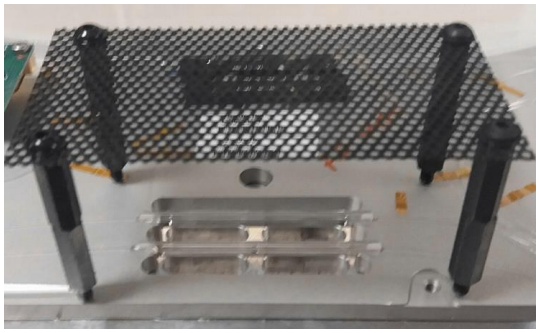

Figure 117. Cladding mode strippers surmounted by metallic grid.

Usage of a grid to quantify the light scattered by the CMS is much more reliable than using a photodiode. In fact, a minimum variation of the position of the photodiode results in a change of the readings.

As it will be clear later, using this grid allowed us to compare many lasers without bothering about photodiode position and light scattered directionality. Obviously, the photodiode has a much faster response than the grid. In HPFL oscillators and amplifiers, increasing the core's area of the AF mitigates nonlinear effects such as Stimulated Raman Scattering (SRS); especially since the AF is often the longest part. As a result, the majority of practical HPFL implementations make use of MM AFs, which renders them prone to TMI [25]. To ensure near-diffraction-limited laser output, the multimode AF is spliced to SM pigtails. However,

this spatial filtering is not ideal and small amounts of HOMs are likely to be excited. Conversely, in a reciprocal manner, HOMs can couple back to the FM of the SM fibres at the two SM-to-MM splices. Such modal cross-couplings at the SM/MM splices can potentially further complicate the HPFL performance. In anticipation of the experimental results presented in the following sections, we propose the following possible effective double-cavity configuration.

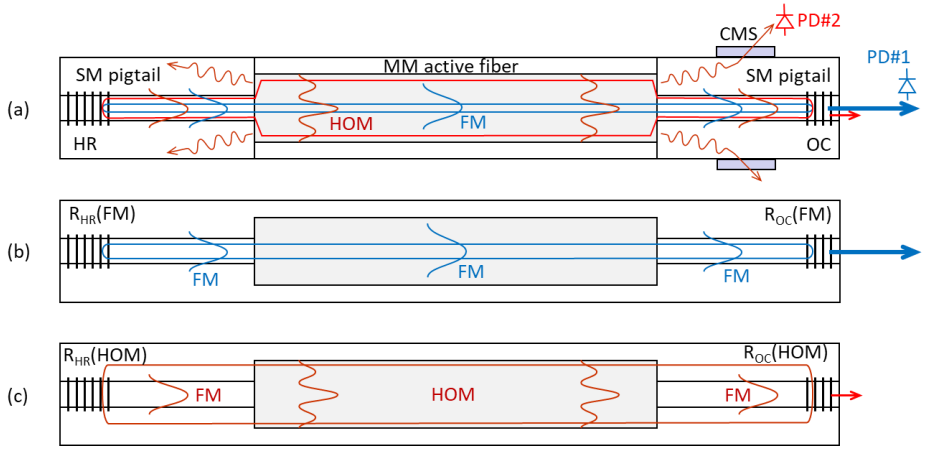

Figure 118. Effective double-cavity fibre laser configuration; (a) possible FM/FM/FM and FM/HOM/FM closed paths in the composite SM/MM/SM fibre cavity, (b) fundamental mode cavity (FMC), (c) effective higher-order-mode cavity (HOMC).

Figure 118 (a) shows a schematic of the SM/MM/SM fibre laser composite cavity, used in the experiments. The "in-coming" (with respect to the MM AF) FM of the SM pigtail, in addition to the well-matched FM, excites small amounts of HOM of the MM AF. In a reciprocal manner, "out-going" HOMs can couple back partially into the FM of the SM-pigtail. This way, after reflecting back from the OC and HR gratings, two distinct FM/FM/FM and FM/HOM/FM closed paths can potentially form. Figure 118(b) and (c) show the FM cavity (FMC) and HOM cavity (HOMC), formed by the FM/FM/FM and FM/HOM/FM closed paths, respectively.

It should be stressed that the effective reflectivities RHR(HOM) and ROC(HOM) of the HOMC are evidently much smaller than the corresponding values RHR(FM) and ROC(FM) of the FMC. As a result, a much higher roundtrip gain is required around the FM/HOM/FM closed path for the HOMC to lase or otherwise compete with the FMC lasing. It should be emphasized that the HOMC light scattered at the MM/SM splices will propagate into the cladding of the SM pigtail and it will eventually be stripped-off by CMS. Referring to the experimental setup of Figure 116 and the schematic of Figure 118(a), the readings of the

CMS photodiode (PD#2) will, therefore, be primarily associated with HOMs of the AF and the activity of the HOMC. The readings of the output photodiode (PD#1), on the other hand, are associated with the FM of the AF and the activity of the FMC. From this picture it is clear that splice optimisation plays a pivotal role in achieving efficient lasers, where only the FM/FM/FM cavity is active and the FM/HOM/FM is suppressed. To have a good performing laser, one should have no loss and all the gain in the FM/FM/FM cavity and infinite loss or/and zero gain for the FM/HOM/FM cavity.

5.2 Testing of a non-optimised laser

In this part, we will describe the testing of an unstable laser. This work has been published by our group in 2019[76] and presented to CLEO Europe back in the 2017 [75]. The charts of this section have been taken from [76]. The mentioned paper contains much more data than here presented; the reader is invited to read the full paper for further clarification. This particular laser was built in the year 2015, as a lucky attempt to scale the power with no effort, but just by increasing the available pump power. This laser has core radius of ~7μm and V number of ~5 and SM pigtails. From known measures on the AF perform, it was known that the Yb concentration was constant in the active core region (Yb ~ $5*10^{26}$ /m^3) and the optimised splice between SM-MM fibre criterion had not been discovered and adopted yet. The splicer used for the splicing of this laser is a two electrodes FUJIKURA FSM-100M (described in section 3.3.4).

5.2.1 CW Pump Mode of Operation

The output power of the laser was brought up to 1600W in eight steps; each step lasted 90 seconds to allow for thermal transients to equalize. PD#1, PD#2 and thermal head readings were recorded at 2Hz (180 samples per step). The response of the thermal head was ~1sec, and the photodiode voltages were acquired with high impedance. Once averaged on the scope, photodiode readings have an effective bandwidth of 10Hz.

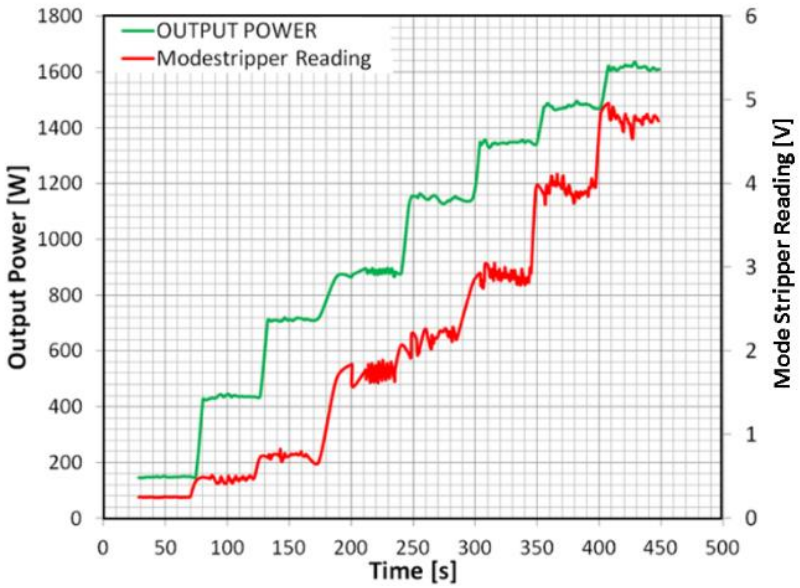

Figure 119 CW ramp logging; in green the output power and in red the CMS photodiode reading.

Figure 119 shows the thermal-head power meter and the associated CMS photodiode (PD#2) readings during the pump ramp up. It is shown that the signal output and the CMS reading are concurrently unstable at any power level. Figures 119 shows the time evolution of the normalized readings of PD#1 and PD#2, at average signal output powers of (a) 438W (step#2) , (b) 885W (step#4), (c) 1480W (step#7) and (d) 1620W (step#8), respectively. It is clearly shown that the two readings are in anti-phase. Since PD#1 and PD#2 readings monitor essentially the FMC and HOMC powers, it can be deduced that the two effective cavities are indeed competing and exchanging power. As discussed in Section 2.1, the two effective cavities overlap over the MM AF through the supported FM and HOM and, therefore, their power exchange is expected to be a result of transverse mode competition (TMC). In this case of quasi-CW operation, the observed power exchange time scales are very slow (~2-5s), implying that the output power instability is due to slow environmentally induced thermal effects. Further evidence of more complex anti-phase dynamics and different time-scale TMC are provided in Section 5.2.2,

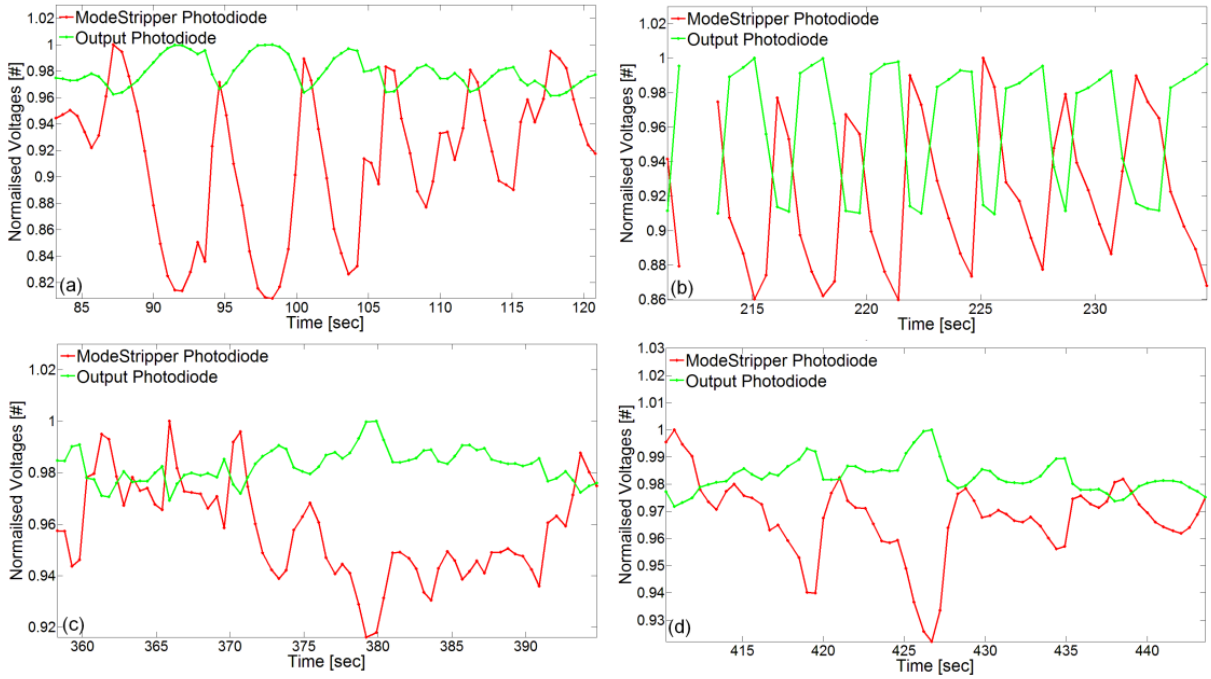

Figure 120. Normalised readings versus time of PD#1 and PD#2 at average signal output power of (a) 438W, (b) 885W, (c) 1480W, and (d) 1620W.

The average values (over 180 samples) of the signal output power and PD#2 readings, obtained during each step of the pump ramp, are plotted against the pump power in Figure 120. It is noticed that the slope efficiency of the laser decreases as the pump power is increased. Three distinct pump power ranges are identified, denoted as zone#1 (0-1.2kW), zone#2 (1.2-2.4kW) and zone#3 (2.4-3.5kW), where the slope efficiency changes from 62% to 51% and 38%, respectively. Conversely, PD#2 voltage slopes increase over the three zones. This clearly demonstrates that the drop-in laser efficiency with pump power is due to an increasingly larger power exchange between the FM and the HOMs in the AF, as a result of TMC.

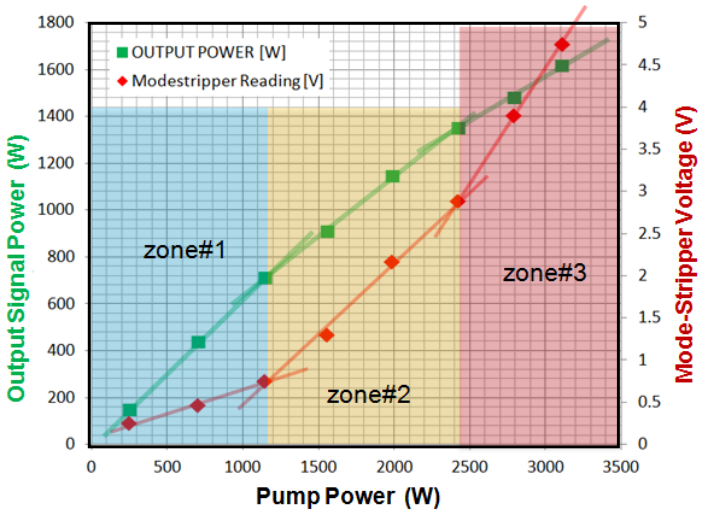

Figure 121. Average values of the output power and PD#2 voltage, obtained during the steps of the pump ramp, against pump power.

5.2.2 Pulsed Pump Mode of Operation

In this pumping mode of operation, the semiconductor laser pumps were turned periodically on-off with square pulses. The repetition rate and duty cycle were fixed at 1 kHz and 20%, respectively, whilst the pump power was step-wise increased to its maximum level. The output and CMS pulses were recorded at all power levels. The acquisition scheme was primarily limited in bandwidth by the photodiodes (~2 GHz). Pulses detected from the output (PD#1) and from the CMS (PD#2) photodiodes are shown in Figures 122-125 and 127, where part (a) zooms around the relaxation oscillation, part (b) shows the entire pulses normalized to their peaks, and part (c) is RF spectrum (obtained from the Fourier transform of the output pulses) calculated between 20 and 200μs only, thus excluding the relaxation oscillation. In part (c), the chart grid is aligned with the free spectral range (FSR) of the laser cavity. Peaks falling at multiples of 4.48 MHz are generated by the longitudinal mode beating (LMB). Zooming into the first relaxation oscillation peaks provides information about the relative state and inversion of the two effective cavities. Monitoring the "plateau" behaviour provides information about the transverse mode power exchange and competition, while the RF spectrum provides additional information about TMC, as well as, longitudinal mode competition (LMC).

5.2.2.1 Instability Zone#1

Figure 1212 illustrates the results obtained at a pump power of 486W. In Figure 1212 (a) and (b), the relaxation oscillation overshoots and "plateau" levels of both output

and CMS photodiode readings follow closely each other. This implies that, in this case, the CMS power is primarily due to residual scattering of the FM at the MM/SM fibre splice. At this point there is no evidence of strong secondary cavity activity. The noisy appearance of the CMS reading (red line) is due to low-level of optical signal, dominated by electrical noise. The RF spectrum in Figure 1212 (c) shows no discrete peaks or other pronounced spectral features.

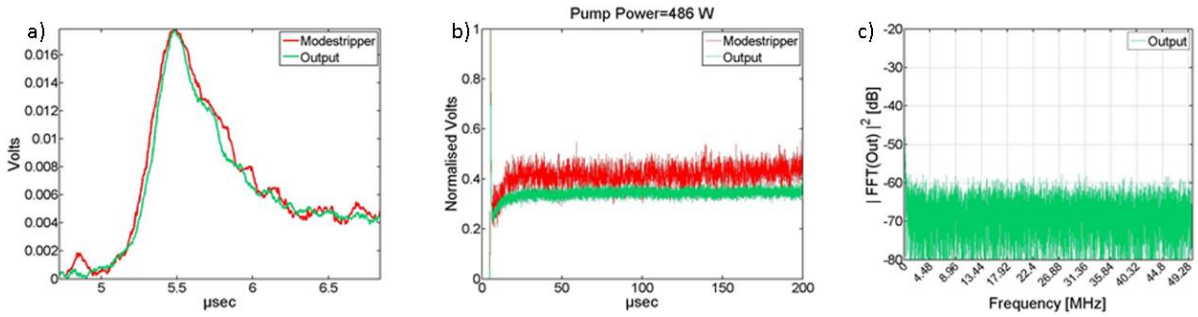

Figure 122. Output power (PD#1-green) and CMS (PD#2-red) readings over (a) relaxation oscillation (first 6.8µs), (b), entire pump pulse duration (0-200µs), and (c) FFT of output trace over 20-200µs period. The pump power is 486W.

After the initial adjustment, the electrical gain settings of PD#1 and PD#2 were left unchanged so that absolute changes in the FM and HOM power levels were monitored and recorded. Figure 123 illustrates the results obtained at a pump power of 778W (midway in zone#1). In Figure 123 (a), we observe that the relaxation oscillations recorded at the output (PD#1-green) and CMS (PD#2-red) differ significantly, with the CMS overshoot being ~x2 higher than the output one. At this power, the CMS overshoot is also delayed by about 10ns compared to the output peak. The temporal delay and higher overshoot recorded by PD#2 implies the presence of a HOMC, as shown schematically in Figure 118. The HOMC has lower Q factor and, therefore, requires higher inversion than the dominant FMC. As a result, HOMC has a longer turn-on delay and higher overshoot than FMC. Figure 123 (b) shows that, after ~80µsec, the two cavities start to compete, exchanging a substantial amount of power and indicating strong TMC. The two traces are in anti-phase and vary periodically with a period of ~ 20µs and a corresponding TMC frequency of ~ 50 kHz. As shown in Appendix A Fig. A2, these timescales are in good agreement with the thermal diffusion time associated with 7-8µm core radius. Such thermally-induced, low-frequency component does not appear in Figure 123 (c). It should be mentioned that similar temporal behavior and low frequency, thermally-induced spectral characteristics were observed with higher pump powers within zone#1.

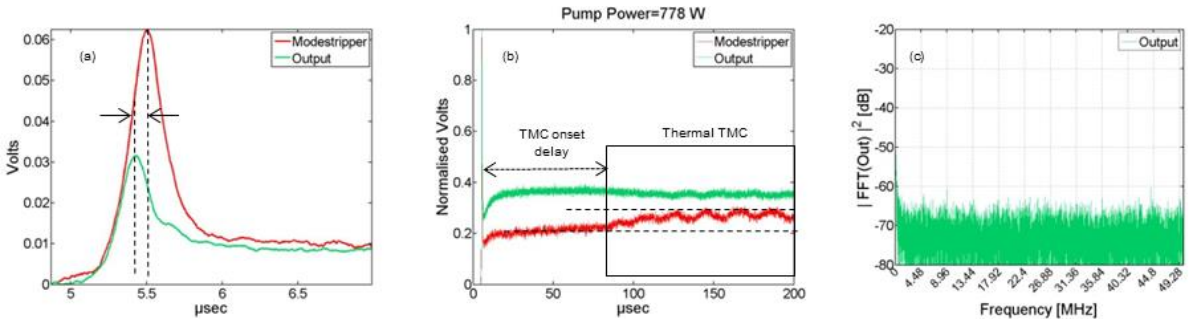

Figure 123. Output power (PD#1-green) and CMS (PD#2-red) readings over (a) relaxation oscillation (first 6.8μs), (b), entire pump pulse duration (0-200μs), and (c) FFT of output trace over 20-200μs period. The pump power is 778W.

5.2.2.2 Instability Zone#2

Instability zone#2 is characterized by a decrease in output power slope and an associated increase in the slope of HOM reading (PD#2), which indicates a stronger power exchange between FMC and HOMC. Figure 124 shows the results obtained with a pump power of 1497W. In Figure 124 (a), the HOMC overshoot has increased to ~x3 the FMC one. As before, Figure 124 (b) shows that after a delay of ~95μs pronounced TMC takes place with the same as before frequency of ~50kHz, characteristic of a thermally-induced perturbation. However, within zone#2, soon after the first relaxation oscillation, between ~10μs and ~90μs much faster dynamics were observed.

In Figure 124 (c), the FFT output trace, in addition to noticeable increased cavity FSR peaks, shows strong peaks at ~3.05MHz (with overtone at 6.1MHz), corresponding to the observed fast TMC dynamics. From Figure A5(b) in Appendix A, it is deduced that this range of characteristic frequencies corresponds to upper-state population (inversion) dynamics (denoted as i-TMC). The increased FSR peaks imply that TMC enhances the cavity LMB.

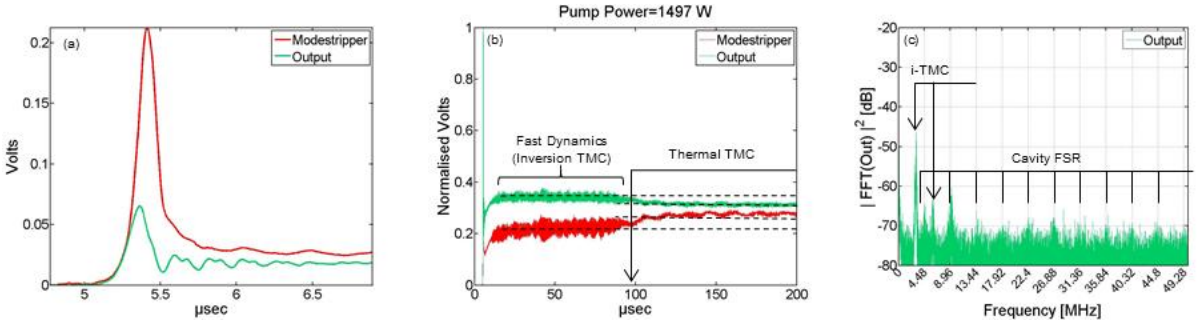

Figure 124. Output power (PD#1-green) and CMS (PD#2-red) readings over (a) relaxation oscillation (first 6.8µs), (b), entire pump pulse duration (0-200µs), and (c) FFT of output trace over 20-200µs period. The pump power is 1497W.

Figure 125(a) shows the output power (PD#1-green) and HOM (PD#2-red) traces at a pump power of 1730W. Figure 125 (b) is a zoom in the fast dynamics of Figure 125 (a) between 95-100µs. Clearly HOMC and FMC are in anti-phase, with oscillations in the microsecond regime, indicating fast TMC. As shown in Appendix A, the observed fast dynamics are again in good agreement with the expected population inversion relaxation time scales. The inversion-related fast dynamics are again interrupted and followed by much slower dynamics (period of ~20µs) of thermal origin. Figure 125 (c) shows the corresponding FFT.

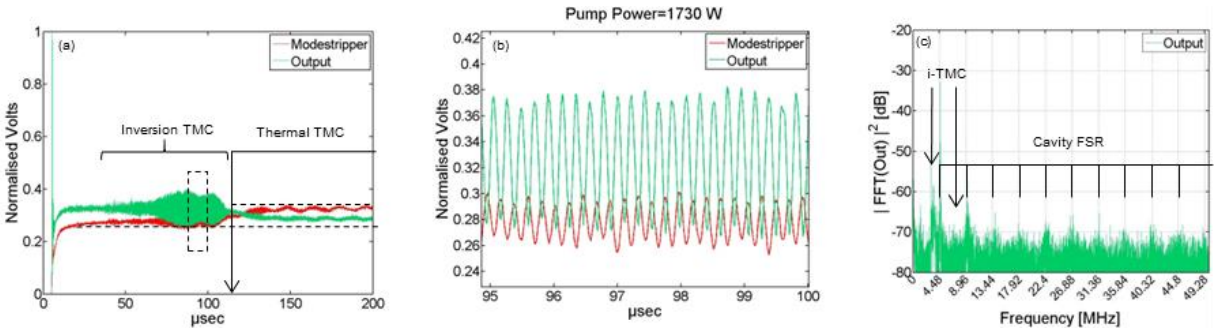

Figure 125: Output power (PD#1-green) and CMS (PD#2-red) readings over (a) entire pump pulse duration (0-200µs), and (b) zoomed in the 95-100µs region and (c) FFT of output trace over 20-200µs period. The pump power is 1730W.

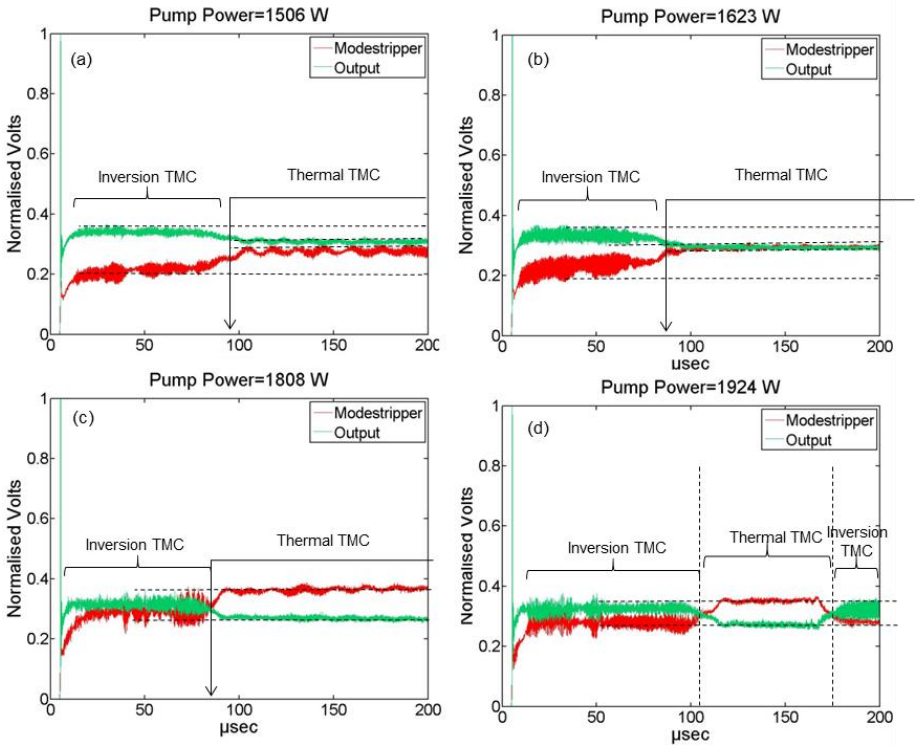

Figure 126: Output power (PD#1-green) and HOM (PD#2-red) traces at pump powers of (a) 1506W, (b) 1623W, (c) 1808W and (d) 1924W.

Similar responses were observed at all power levels within zone#2. Figure 126(a)-(d) show the output power (PD#1-green) and HOM (PD#2-red) traces at different pump powers. It is shown that, after the pumps are turned-on, the first relaxation oscillation is followed by fast, inversion-related TMC (i-TMC) over a period of 80-100µs. The i-TMC period is always characterized by fast (MHz range) inter-modal power exchange around constant average levels. This period is interrupted by sudden onset of much slower (~50kHz) dynamics, in line with thermal diffusion time scales. Over this thermal TMC (t-TMC) period there is a marked change of the PD#1 and PD#2 average readings, indicating that thermal effects result in a strong intermodal power exchange. As Fig. 126(d) shows, the thermal TMC period was sometimes interrupted and reverted to a fast i-TMC regime, with the average FM and HOM powers returning to their initial values.

5.2.2.3 Instability Zone#3

Instability zone#3 is characterized by a further decrease in output power slope and an associated larger slope of the HOM reading (PD#2), which indicates even stronger power exchange between FMC and HOMC. Figure 127 shows the results obtained with a pump power of 2303W (zone#2/zone#3 border) and 3000W. Figures 11(a), (d) show that the first

relaxation oscillations do not follow each other closely any more. Figure 127 (b), (e) are now characterized by much larger fast oscillations and stronger TMC due to inversion effects, throughout the pump pulse duration. The corresponding spectra in Figure 127 (c), (f) show that the main TMC frequency has shifted to 4.45MHz (close to the cavity FSR) and 5.4MHz (exceeding the cavity FSR), respectively. At these power levels, within zone#3, the strong TMC provokes strong LMB, as evidenced again by the much increased levels of cavity FSR peaks. This strong coupling between transverse and longitudinal modes in the FMC and HOMC results in full chaotic operation.

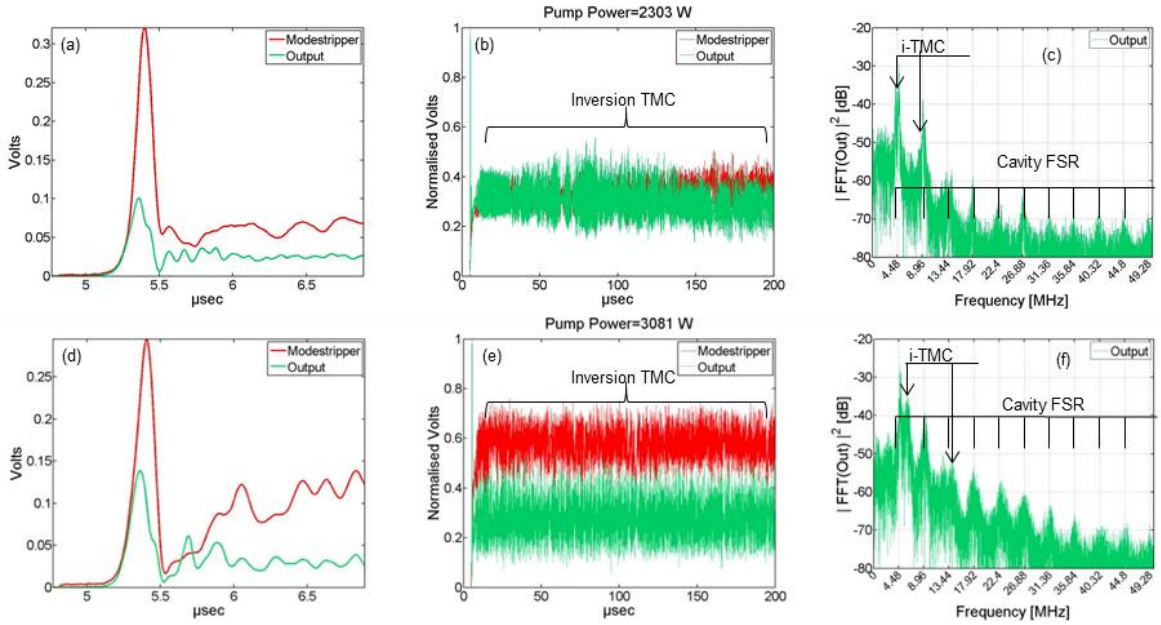

Figure 127. Output power (PD#1-green) and CMS (PD#2-red) readings over (a),(d) relaxation oscillation (first 6.8µs), (b), (e) entire pump pulse duration (0-200µs), and (c), (f) FFT of output trace over 20-200µs period. The pump power is (a)-(c) 2303W, and (d)-(f) 3000W.

5.2.3 Instability Map and Route to Chaos

Figure 128 shows the evolution of the fast TMC dynamics with pump power, in the frequency domain. Vertical lines on the frequency axis coincide with the fibre laser cavity FSR spacing due to LMB. Pump power axis incorporates 260 levels, ranging from 400W to 3000W in steps of 10W. The color scheme (z-axis - orthogonal to page) shows the absolute value of the FFT (in dB) of the output traces between 20-200µs. The three instability zones are also marked.

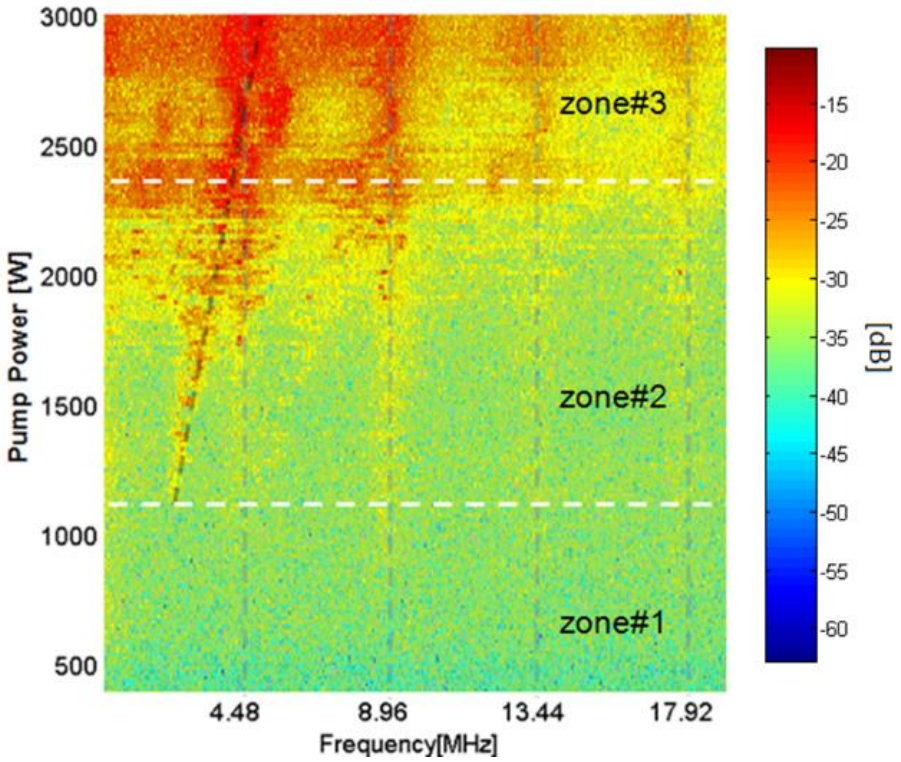

Figure 128. Pulsed measurement, synoptic. X Axis: frequency of the FFT, Y Axis: Pump Power, Z axis (orthogonal to page): modulus of the FFT in dB.

Up to 1.2kW of pump power (zone#1), nothing is noticeable in the MHz range. In this zone, only thermally-induced TMC of fixed low frequency (~50kHz) has been observed (see Figure 123). At a pump power of ~1.2kW (zone#2 bottom-end), a pronounced inversion-related TMC peak appears at ~2.5MHz. Further increase of pump power results in a quasi-linear increase of the dominant TMC frequency. At a pump power of ~ 2.4 kW (zone#2 top-end), the TMC frequency becomes resonant with the cavity FSR frequencies. Above this power level (zone#3) TMC provokes LMB and the laser acquires a chaotic output characteristic, which amounts to multiple strong FSR peaks and in-between spectral filling. At 2.4 kW, the chaotic behaviour is characterized by a broad RF spectrum, showing conspicuous excitation of frequencies up to ~13MHz. Within zone#3 above 2.4kW, the dominant TMC peak is larger than and no longer resonant with the first FSR peak. The sustained broad RF spectrum indicates persistent chaotic behaviour.

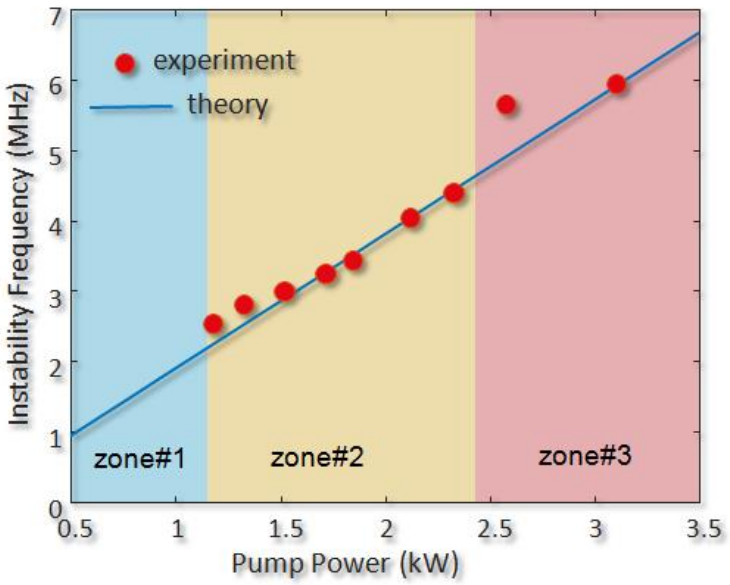

Figure 129. Inversion TMC's frequency dependence on pump power – comparison with theory.

In Figure 129, the variation of the dominant TMC frequency is compared with the population inversion related theoretical prediction (Eqn (9) in Appendix A). For the theoretical prediction, we have used parameters similar to the experimental values. The optical to optical conversion efficiency is ~55%, the pump wavelength is 950nm, the signal wavelength is 1070nm and the glass host was considered to be phosphosilicate. Theoretical and experimental results show a very good agreement. The quasi-linear dependence of the dominant TMC peak on the laser power further corroborates the dominant population inversion contribution to the observed TMC in zones#2 and #3.

5.3 Test of an optimised LMA laser.

In this section, we will present the splice optimisation and the test of a HPFLs. This laser was built in with bigger active (12μm core, V number equal to 7) and DM passive fibres. The radial Yb distribution for this laser occupies 2/3 of the core radius (Selective doping). This technology is internally referred as Large Mode Area (LMA). Yb distribution has been measured by a topographic system build in house in SPI. A similar topographic system has been developed by ORC and described in [140]. The SM-MM splice optimisation of this laser has been performed with the Ring Of Fire (ROF) - three electrodes FITEL-S184PM; we measured optimum arc duration at 6.1 seconds.

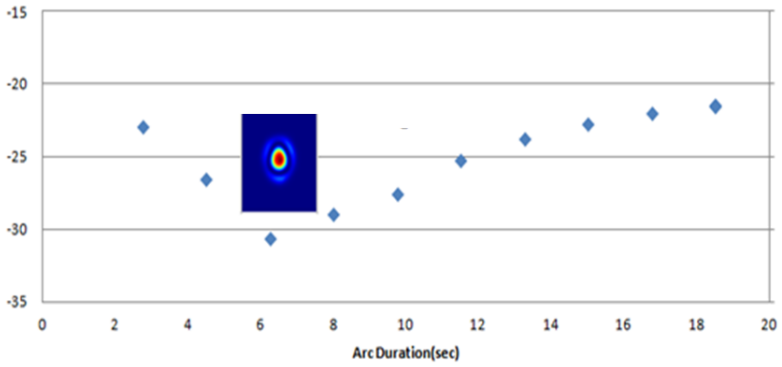

Figure 130. LP02 Optimisation

Subsequently, three high power tests have been performed on this laser building it with SM-MM splice arc durations equals to 2.2, 6.1 and 10 seconds. From Figure 131, the LP02 excitation for these arc durations is respectively -22.5dB, -30.5dB and -27.5dB. In the test described in Figure 131, the pump power has been ramped up in four steps; during each step, pump power has been kept constant for 100 seconds. During the test, output power and light scattered by the mode-stripper has been monitored, as described in the previous chapter. During this experiment, extreme care has been used to ensure that the relative position between photodiode and modestripper remained constant. From the test result in Figure 131, it is clear that, the lower the modal excitation, the better the efficiency and stability. The best performing laser is that obtained with the optimised arc duration (6.1 seconds, -30.5dB of LP02). The excursion of efficiency is estimated to be 16%, down to 59% from 77%, when LP02 goes from -30 to -22dB. In Figure 131 (a), the lower the LP02 excitation, the higher the output power. Conversely, in Figure 131 (b), the lower the LP02 excitation, the lower the reading of the CMS photodiode. This experiment proves that arc

optimisation is of pivotal importance when building HPFLs adopting SM filtering and diffusion splicing.

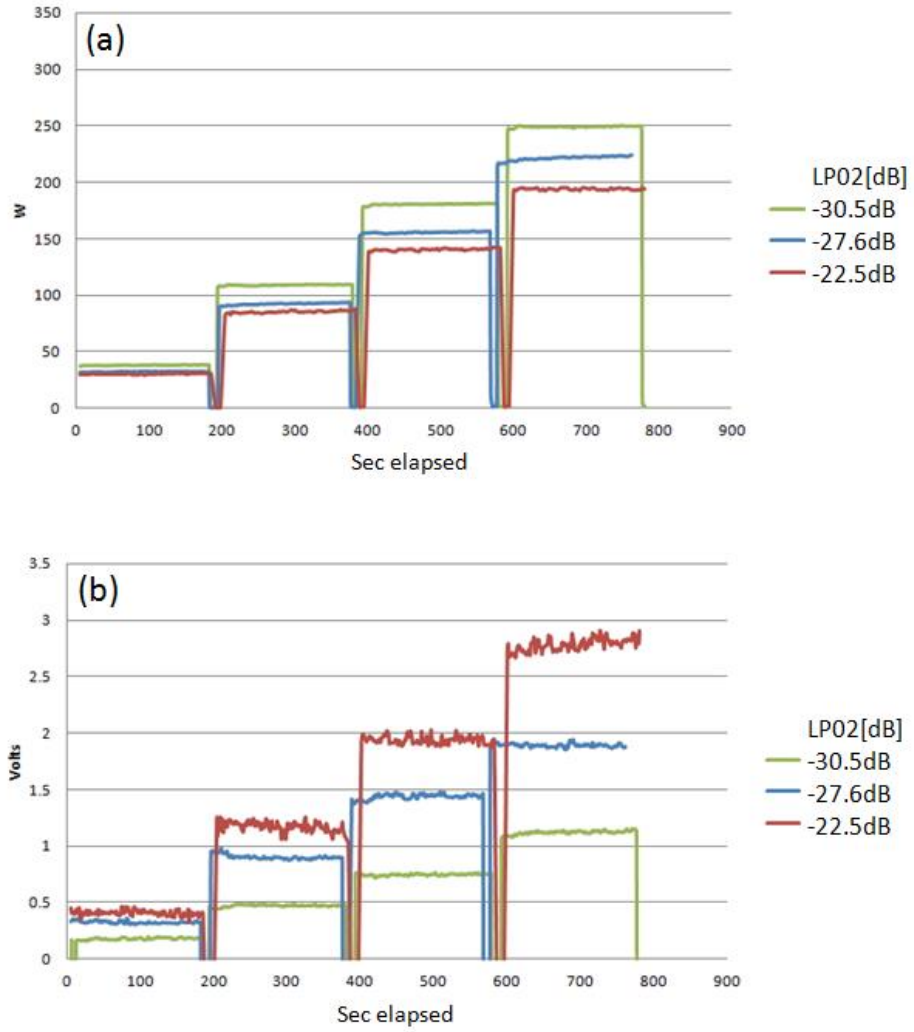

Figure 131. High power test of an optimised HPFL. (a) Output Power. (b) Mode-stripper photodiode. LP02 excitation is shown in the legend.

Once the splice was optimised, pulsed tests conducted on this laser, similar to that in section 5.2, did not show any of the complex features: Pulsed waveforms for CMS and output readings where similar at any power (up to the equivalent output power of 2500W, but with 10% duty cycle only). It was impossible to test this particular device at CW powers higher than 250 Watt. To test the various splices attempts quickly, in terms of laser efficiency result, the three ends of each of the two GTW splice where simply held on a piece of metal, with tape. As explained in paragraph 5.1, to achieve high power operation without GTW splice failure, GTW splice must be held in specifically designed cylindrical boats. However, putting in place these cylindrical boats, in between the different splice

optimisations and high power tests was time consuming and not available in the lab at the time. A complete set of high power CW measurements, on a LMA laser similar the one presented here, will be shown in paragraph 5.7.

5.4 Role of selective doping role in HPFLs design and manufacturing yield

In this paragraph, we will show the benefit of selective doping. To do so we will use the HPFL model presented (4.2) applied on the optimised LMA laser presented in paragraph 5.3. For such lasers, Figure 132 shows the IOR, the Yb concentration and the normalised intensity calculated for LP01 and LP02. The length of the described laser is 25 meters with pump-pump fibre absorption of 17dB circa.

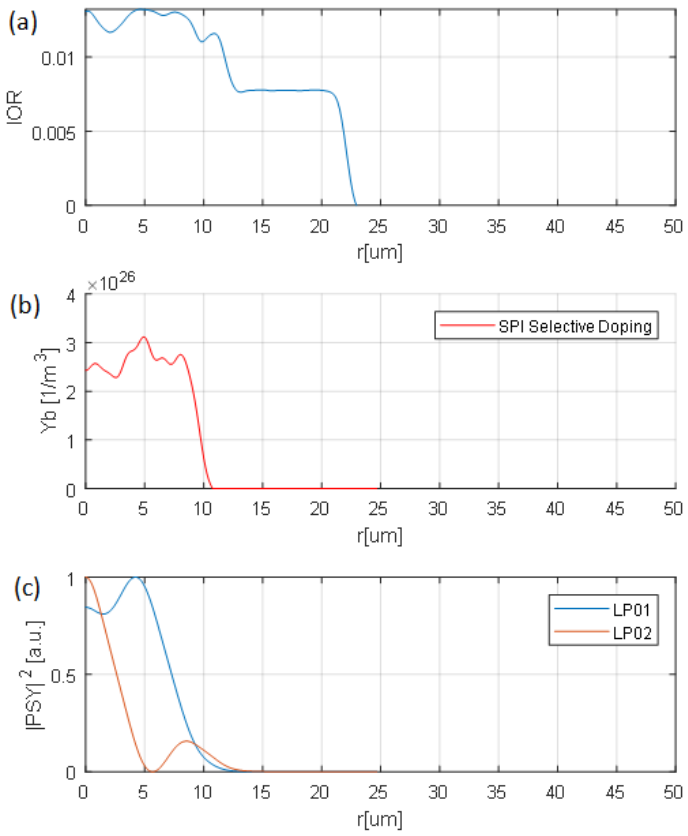

Figure 132. LMA AF.(a) IFA IOR, (b) Yb Concentration, (c) LP01 and LP02 Shape intensity

From Figure 132(a, b) we can see that the IOR extends up to 12.5µm circa whilst the Yb concentration extends up to 10µm. From Figure 132(c), consulting the modal intensities, we notice that LP01 intensity has a maximum close to where the LP02 has a minimum, at about 6µm of radius. We will show how selective doping increases laser efficiency and improves the First Pass Yield (FPY) in the manufacturing process. To demonstrate the effect of selective doping, the Yb distribution has been modelled as flat concentric regions of increasing radius (from 2µm to 12µm with step of 1µm). To preserve the pump absorption the number of ions of Yb has been kept constant; the smaller the radius of the flat zone, the higher the Yb concentration (Figure 133).

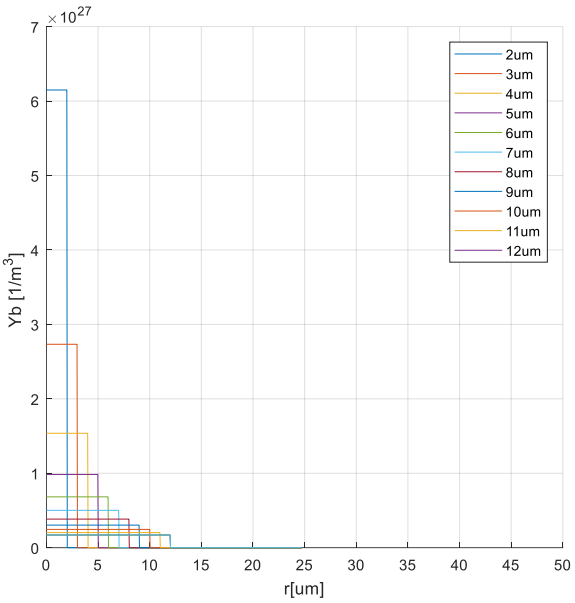

Figure 133. Flat round Yb concentrations modelled for LMA. To preserve absorption, the Yb level scales with the covered area.

Furthermore, for each doping distribution, different levels of excitation for the LP02 have been tested (from -30db to -15dB with steps of 5dB). The variation of LP02 excitation represent the possibility of having, on the production line, SM-MM splices whose arc duration is not perfectly optimised (i.e. wrong arc calibration, problems with the electrodes, etcetera). The effect of LP11 is thought to be constant (imagining reproducible LP11 excitation in case of good cleaves and good fibre centricity). The obtained results in terms of efficiency are plotted in Figure 134.

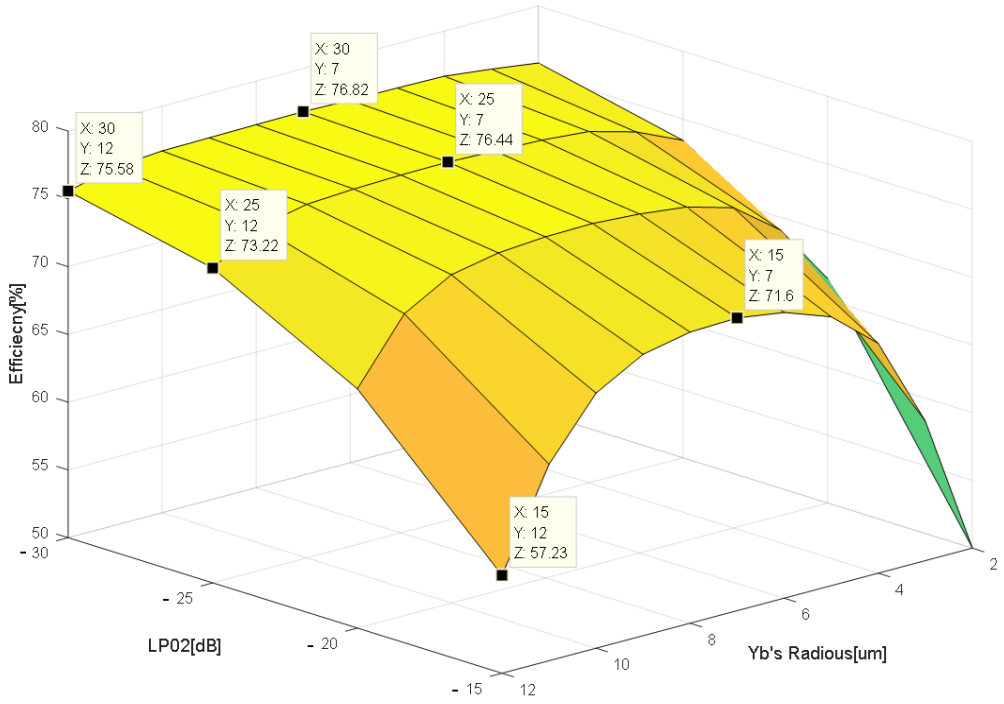

Figure 134. Role of selective doping in LMA design.

From Figure 134 it is possible to spot how, the lower the LP02 excitation the higher the efficiency; regardless of the Yb radial extension. For this reason, performing the LP02 optimisation maximises the efficiency of the laser and it is certainly worth doing it. However, if the doping has a radius equal to 7µm, the variation of efficiency resulting from an uncontrolled LP02 optimisation is minimal (at 7µm, efficiency varies of 5% when LP02 excitation goes from -30dB to -15dB). Vice versa in case the Yb covers the whole fibre, reaching 12µm of radius, the variation of efficiency resulting from an uncontrolled LP02 optimisation is quite big (at 12µm, efficiency varied of 20% when LP02 excitation goes from -30dB to -15dB). For this reason, selective doping helps in improving the repeatability in the process of laser manufacturing leading to improved FPY, with less attention on fine splice optimisation. The efficiency variation in presence of splice variation at 7µm is minimum because at about that radial distance there is a maximum for the LP01 and a minimum of the LP02 (Figure 132-c). In fact, by inspecting Figure 132(b,c) it is easy to recognise how, at 7µm the Yb overlap has maximum with the LP01 and a minimum with the LP02. Working with a radius of 7µm minimises the gain of the secondary cavity, in favour of the gain of the FM cavity. To kill even further the gain of the LP02 one could think of using an annular doping with a ring radius of 7µm (Figure 135).

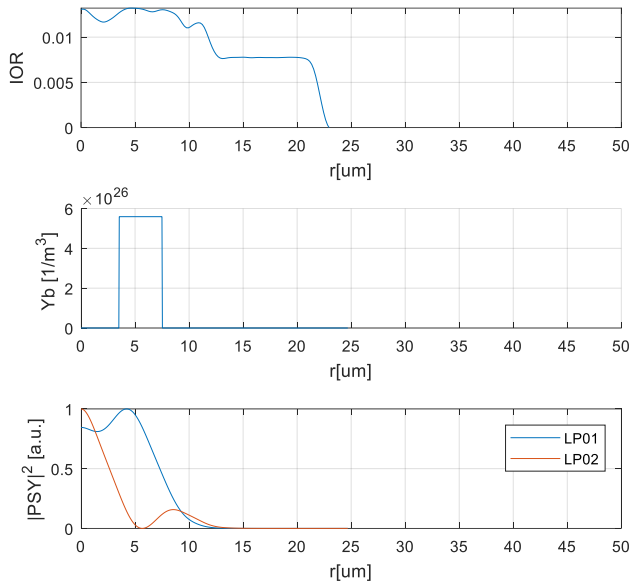

Figure 135. Ring Doped LMA Fibre.

In case of ring doping, an optimum can be found using a radius of 6µm and a radial width of 2µm. At the optimum, the efficiency variation is only 3.5% when LP02 varies from -30 to -15dB. In the case of this particular GTW, luckily, the Yb distribution is already ring shaped with the Yb distribution being endowed with a peak at around 5µm (Figure 132(b)). Finally, yet importantly, the simulated efficiency variation for this laser, with the real measured Yb GTW is about 8% when LP02 excitation goes from -30dB to -15dB. This drop in efficiency is slightly smaller than expected as, during the process of optimisation (paragraph 5.3), the observed drop was already 19% when LP02 optimisation was detuned by only 8dB. This might be due to the simplicity of this model that does not account for any other mechanism of mode coupling other than at the splice. As a final remark, we highlight the fact that Yb concentration cannot be increased arbitrarily without incurring in core deformation and fragmentation; this kind of anomaly in the core's structure will be shown in paragraph 5.6.

5.5 Splicing technology improvement in HPFLs

This section, shows the results obtained by splicing the laser of paragraph 5.3 with both FUJIKURA FSM-100M (two electrodes) and FITEL-S184PM (three electrodes ROF) splicers. As expected, with both splicers we find a minimum for the LP02. However, the LP02 minimum found with the FITEL splicer is consistently lower than that obtained with the FUJIKURA (Figure 136). This is substantially due to the fact that the heat profile provided by the two splicers lead to different taper shape, hence taper properties are different and optimisation outcome also differs.

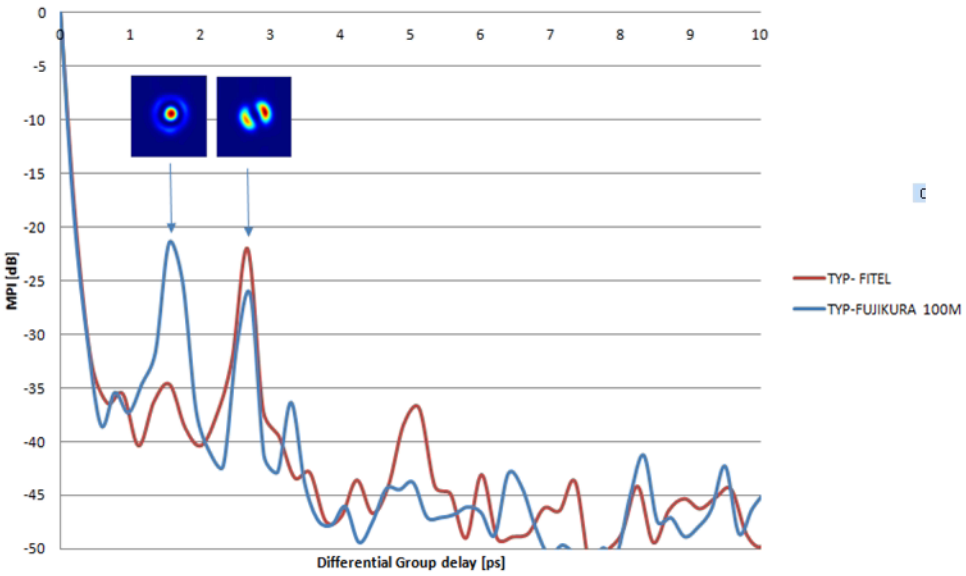

Figure 136. LP02 optimisation of FITEL splicer and with FUJIKURA splicer (typical values).

Contrarily to expectations, we did not see any appreciable improvement of LP11 excitation when using the ROF splicer over the two electrodes splicer. This is due to the LP11 excitation being most predominately dictated by fibre core-clad concentricity. During the test, the output power and light scattered by the mode stripper have been measured. This particular laser's absorption was 15dB. Given the high number of splicing attempt adopted, to quantify the light scattered by the mode-stripper, avoiding accidental movement of the mode-stripper photodiode, we have avoided the usage of the photodiode and used the metallic grid temperature (as described in the section 5.1). The laser has been spliced four times with the FUJUKURA and four times with the FITEL. The outcome of this

repeated measurement is presented in Figure 137, in terms of output slope efficiency (y axis) and grid temperature slope (x axis).

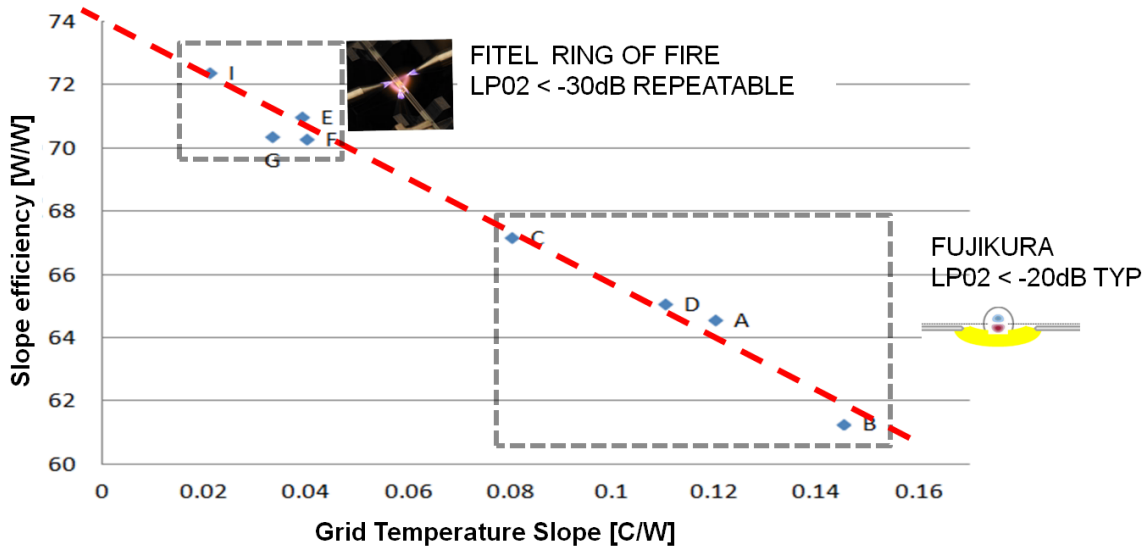

Figure 137. Efficiency and grid temperature slope adopting different splicers

As visible from Figure 137, points A,B , C and D, obtained with the FUJIKURA splicer have lower efficiency and higher grid temperatures that the points G E, F and I, obtained instead with the FITEL Splicer (these latter having higher efficiency and lower grid temperature). Splices obtained with the FUJIKURA, give less repeatable results (points contained in big grey dotted square) whilst splices obtained with FITEL are much more repeatable (points contained in the little grey dotted square). Compared to the three electrodes FITEL, the lack of repeatability of the two electrodes FUJIKURA can be explained due to intrinsic limits of the two electrodes technology when splicing large fibres. The higher average score for the FITEL is certainly due to the better LP02 suppression (Figure 136). On this aspect, we also notice that the eight points lay on a red dotted line, testifying that, the better the splice, the higher the efficiency and the less the HOM activity (less grid temperature). Looking at the top end of the red line, we can also infer that, if splices where infinitively good, the maximum efficiency for this particular laser would be about 74%. For this reason, since we started producing LMA lasers, we have always adopted the FITEL splicer and splice optimisation with arc characterisation.

5.6 Effect of core's circular symmetry

Despite having introduced the ROF technology and arc optimisation on all manufactured lasers, vast efficiency variations still occurred amongst the different fibres drawn. The following chart shows the slope efficiency (y-axis) and grid temperature slope (x-axis) for a broad range of oscillators build by the production line, during the alpha phase of LMA lasers. The targeted pump absorption of the devices is about 20dB.

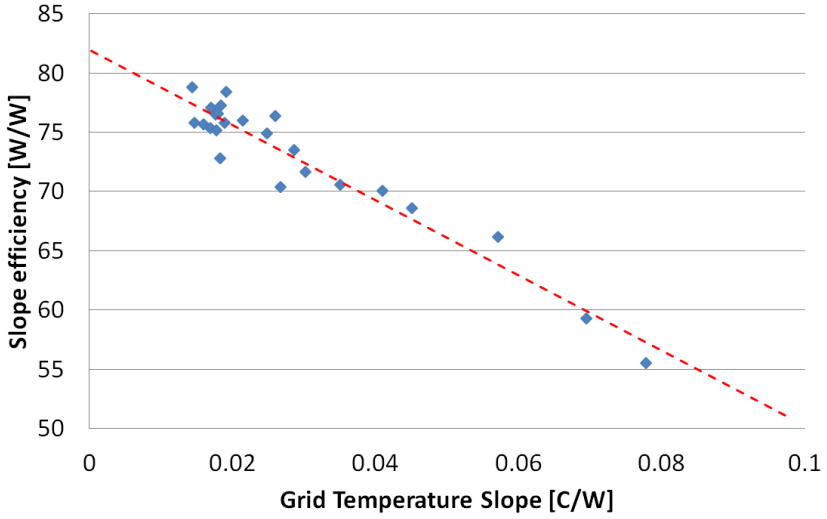

Figure 138. Grid slope vs slope efficiency on subset of mass produced HPFLs (20dB absorption, 945 nm pumping)

To produce the chart in Figure 138, several fibres were used. The grid adopted in the test of mass produced lasers is not exactly like that shown in Figure 117, however the inverse correlation between slope efficiency and grid's temperature slope is still in place. With 20dB of absorption and ideal splice (very cold grid= no HOM excitation), the maximum asymptotic achievable efficiency for these devices should is about 82%. Nonetheless, considering that the arc duration for all HPFLs was characterised and adopted for their construction, variability of the efficiencies was still not justified. Subsequently, a new correlation was found between LP01 shape and maximum performance of a drawn GTW.

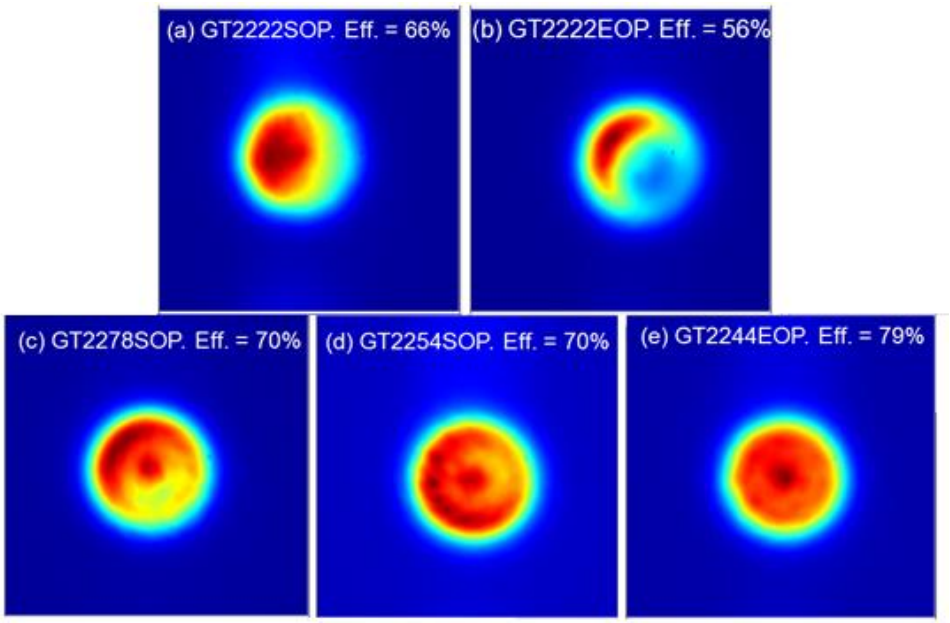

Figures 139. LP01 shape measured via S^2 versus maximum laser efficiency (in white fonts) achieved for different fibres drawing. LP01 images obtained in correspondence of optimised arc duration. For GT2222 there are two measurements (EOP: end of perform and SOP: Start of perform)

Figures 139 show the shape of the LP01 mode, measured at "0ps" delay image with the S^2 (refer to equation (2.2.2.7)), and the correspondent efficiency achieved on the line by four different GTWs. It is easy to spot how, LP01 centrosymmetry (intended as rotational symmetry) is directly correlated to laser efficiency: the higher the LP01's centrosymmetry, the higher the efficiency. This cannot be explained by the model of section 3.4, where perfect centrosymmetry was assumed. However, it is easy to realise that, the LP01 coupling (loss) between passive and AF will depend from their mutual shape. In fact, since the LP01 centrosymmetry of the passive fibre is almost perfect, the LP01 loss across the splice will only depend from the AF's LP01 centrosymmetry. It was subsequently proven by the fibre production department that centrosymmetric cores are easier to produce when using lower Yb concentration in the MCVD process. With the current fabrication technology there is therefore a trade off between core centrosymmetry (good for splicing) and high Yb level (good for absorption). Finally, we want to show how the "0ps" image obtained with the S^2 in correspondence of arc duration optimisation, closely resemble the LP01 calculated via beam propagation method* (BPM) over the 2D IOR measurement.

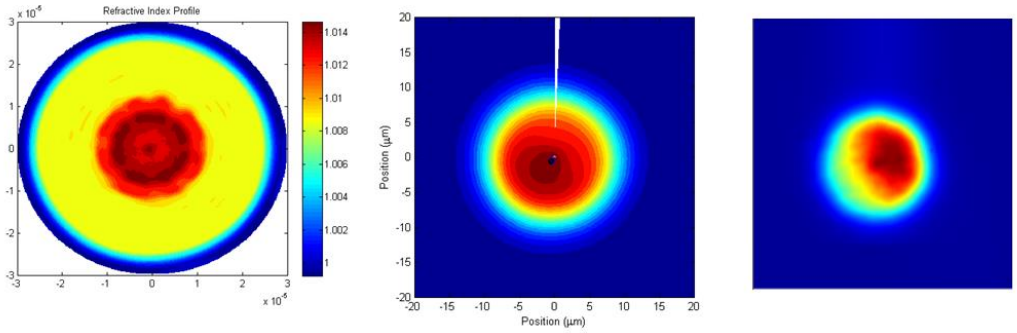

Figure 140. GT2222SOP. Left: 2D IOR meas. Centre: LP01 calculated via BPM. Right: S^2, "0ps" image as LP01 estimation

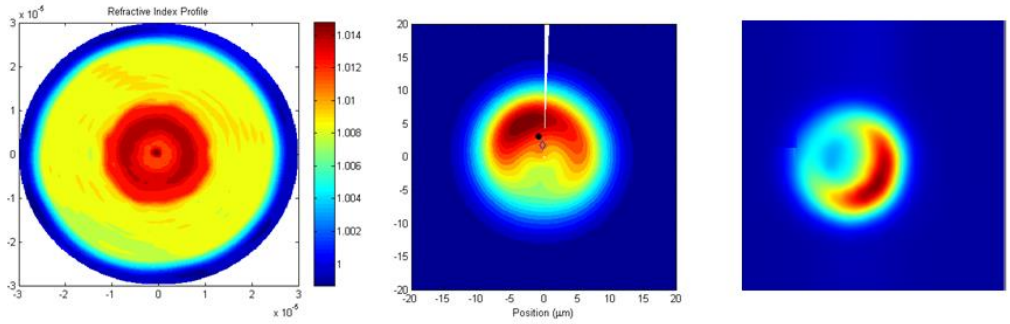

Figure 141. GT2222EOP. Left: 2D IOR meas. Centre: LP01 calculated via BPM. Right: S^2, "0ps" image as LP01 estimation

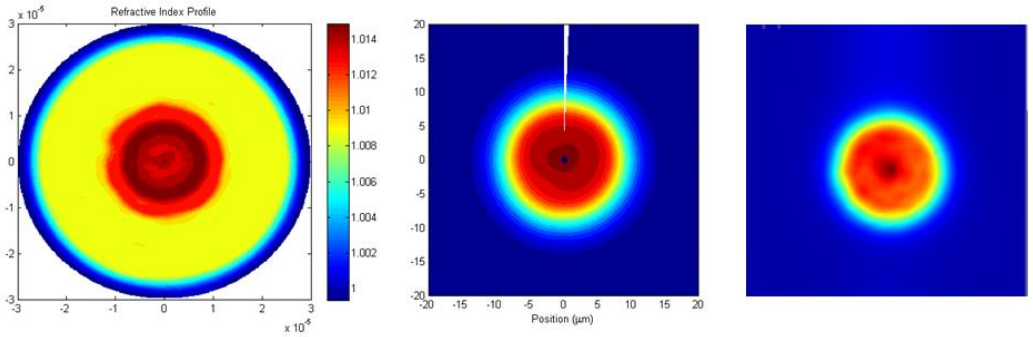

Figure 142. GT2244EOP. Left: 2D IOR meas. Centre: LP01 calculated via BPM. Right: S^2, "0ps" image as LP01 estimation

*BPM code developed by Dr. Andy Malinowsky at SPI Lasers.

*2D IFA measurements by Dr. Peristera Andreaku

5.7 Characterisation of a state-of-the-art commercial grade HPFL

In this section, we will present the data of the most efficient laser obtained at SPI to date. Obtainment of these results involved the implementation of all the expedients presented in this thesis, namely: SM-MM splice optimisation, Yb selective doping, selection of the AF core endowed with high centrosymmetry, selection of passive fibre with high core-clad concentricity. Furthermore, for this specific laser, we have also increased the quantum efficiency by using longer pump wavelengths (available to SPI from mid 2018) and shorter wavelength gratings. It will be shown that the maximum output power achievable by this laser is limited by SRS rather than by TMI.

5.7.1 Pump block characterisation

The pump diodes used are denominated 97xnm TUSP DM15, are produced by TRUMPF (USA), have the same foot print and brightness of those presented in paragraph 2.2.3, but longer wavelength.

Figure 143, TUSP DM15, multi emitter package

Pump block is made of 24 TUSP DM15, combined together with two 12X1 pump combiners. The two output fibres of the two combiners have a diameter of 250µm; these are matched with the GTW pump fibre diameter. The diodes are placed on a water-cooled cold plate similar to that shown in Figure 28. Temperature of the cold plate can be changed by changing the set point temperature of a pump block's reserved chiller (7500 W by Thermoflex). Since pump wavelength is not stabilised, actual wavelength depends on current and temperature of the pump block.

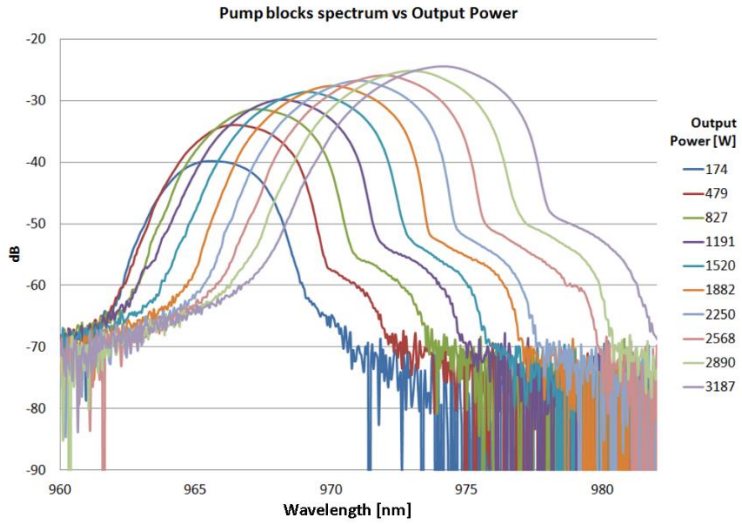

Figure 144. Combined pump diodes spectra at various pump powers. In this chart the chiller set point was 20 °C.

Figure 144 shows the spectrum recorded at the output of the combiners up to 3.2kW, with chiller set point equal to 20°C. It can be noticed that the peak wavelength shifts with power and that part of the spectrum exceeds 975nm (peak of the Yb absorption). In the next chart, the pump wavelength at the end output of a pump combiner has been measured against current and by using four different set points for the chiller (20°C, 25°C, 30°C and 35°C).

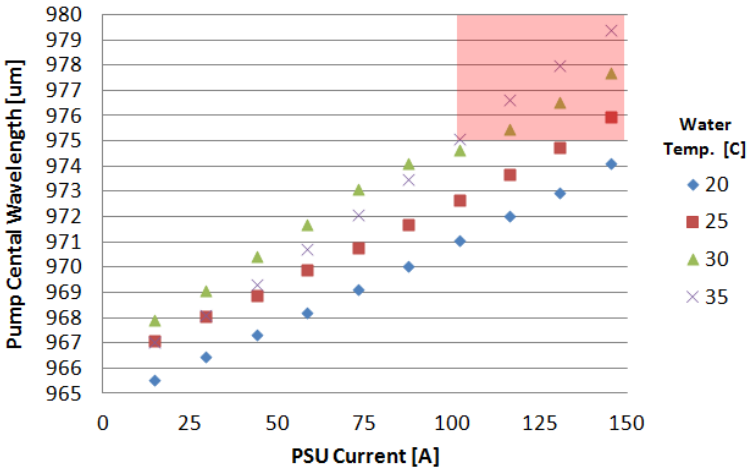

Figure 145. Pump wavelength characterisation as function of current and water temperature.

Figure 145 plots the peak wavelength at any current and with four different set point temperatures for the chiller. It can be noticed that, operating these pumps at currents bigger than 100 A and at temperatures higher than 30°C, will result in pump wavelength higher than 975nm. In the red square of Figure 145, the Yb absorption drops provoking two

undesirable consequences. First, if absorption drops, laser efficiency will drop, making the laser inefficient. Second, laser pump fibre will not absorb the pump light, there will be excessive residual pump light at each end of the GTW and pump block could mutually damage each other.

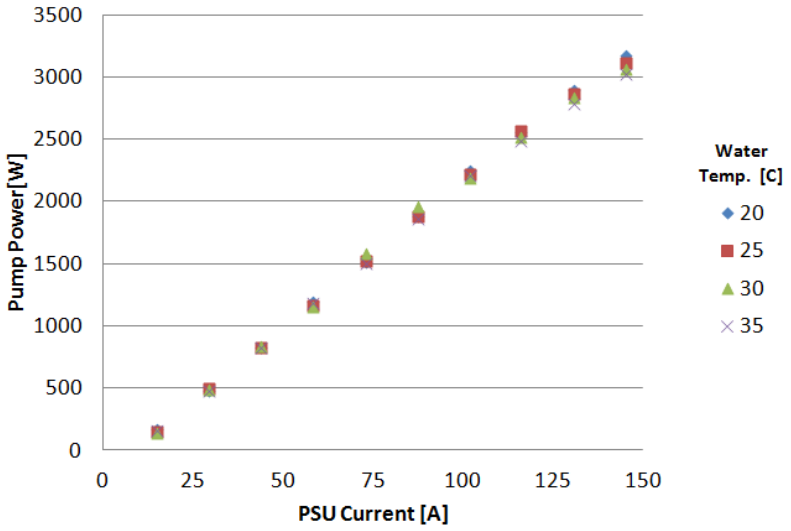

Figure 146.Pump block optical power as function of current and water temperature.

Figure 146shows the pump power deliverable by the pump block as function of the current and chiller set-point temperature. It can be noticed that, at any current, the power drops progressively with temperature.

5.7.2 Oscillator details

In order to reduce further the quantum defect, on top of being pumped with longer wavelengths, this oscillator adopts gratings with short wavelengths. Gratings central wavelength is 1069nm, with HR bandwidth of 10nm and reflectivity of 99.99%, OC bandwidth of 3nm and reflectivity of 14%. The DMF passive fibres (Figure 36) onto which FBG are inscribed have core clad concentricity of 0.1um; these are the highest concentricity currently achieved in SPI (typical concentricity is 0.2µm). DMF have been coiled on the laser plate with a coiling diameter of 8 cm, to reduce the LP11 content (for reference consult Figure 44 of paragraph 3.2.1). The AF core centrosimmetricity is also one of the best ever achieved with the current AF fabrication method (Figure 147).

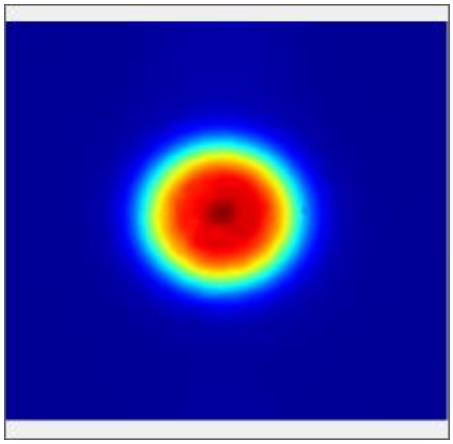

Figure 147. AF LP01 shaped measured by S^2 ("0ps" image).

The LP01 centrosimmetricity for the selected AF is spectacularly good (for reference the reader can consult the efficiency and LP01 shape presented in Figures 139). Without getting into the details of the fabrication process, according to the fibre department of SPI lasers, good core centrosimmetricity is easier to achieve when Yb contraction is about 50% less than normal (SPI LMA AF Yb concentrations are normally in the order of $4x10^{26}\,m^{-3}$). The Yb concentration for this AF is circa half of what normally used. Lowering the Yb concentration has not resulted in a drastic drop of absorption as we are now using longer wavelength for the pumps. AF length is 25 meters, oscillator fibre winding and appearance is like that shown in Figure 115. To avoid any uncertainly in the delivery of the correct arc power, the SM-MM splice optimisation has been conducted just before splicing the laser, resulting in an MPI of -40dB for the LP02 and -25dB for the LP11. These values for the MPIs are amongst the best ever achieved in SPI; this is anecdotally believed to be due to the effective area of this particular LMA ($260um^2$) that happened to be 5% lower than what we routinely produce ($280um^2$). By being slightly smaller, this LMA is thought to be inherently better matched with the DMF.

5.7.3 High power characterisation

The detection probes for this setup are located as in the measurement setup of Figure 116. The slope efficiency of laser has been measured at the four different chiller temperatures utilised for the pump characterisation.

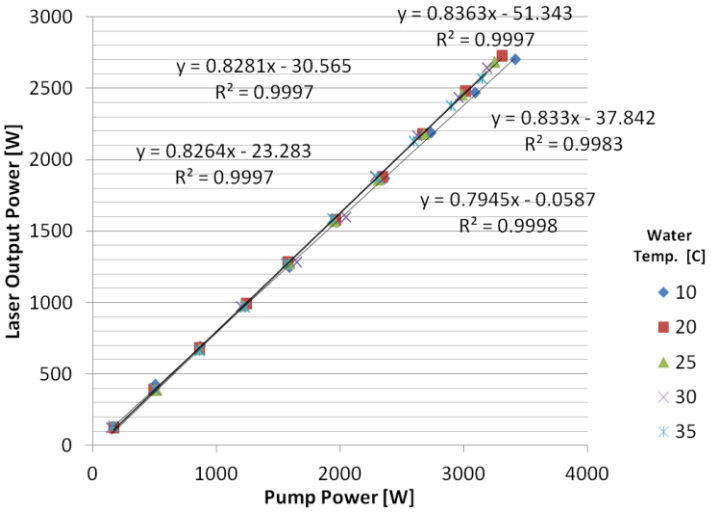

Figure 148. Slope efficiency versus chiller temperature.

Regardless of the set point temperature, slope efficiencies plots are linear up to full power, without any sign of roll off (Figure 148). The different slope efficiencies and maximum power dependence on wavelength is shown in Figure 149 and Figure 150.

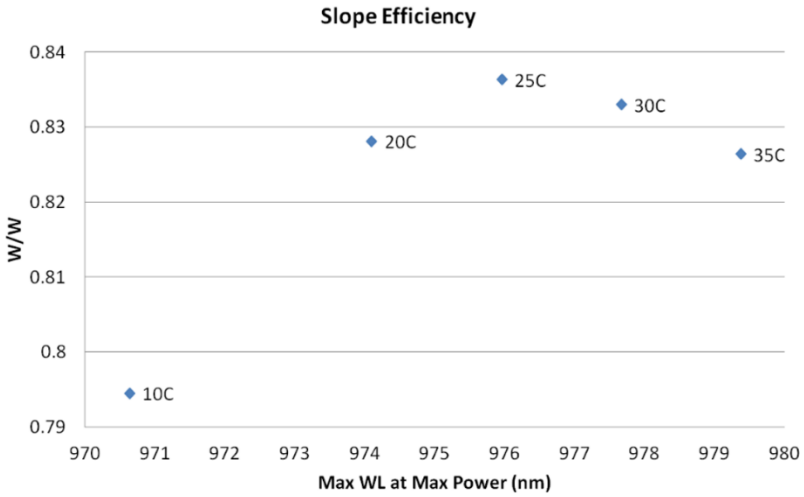

Figure 149. Slope efficiency versus wavelength. Wavelength quoted is the maximum achieved from the pump block at maximum pump power for each set-point chiller temperature (label of the points)

The maximum slope efficiency is reached at 976nm and it is 83.7%; presumably, maximum is at 976 nm due to optimum pump overlap between pump wavelength spectrum and Yb absorption spectrum.

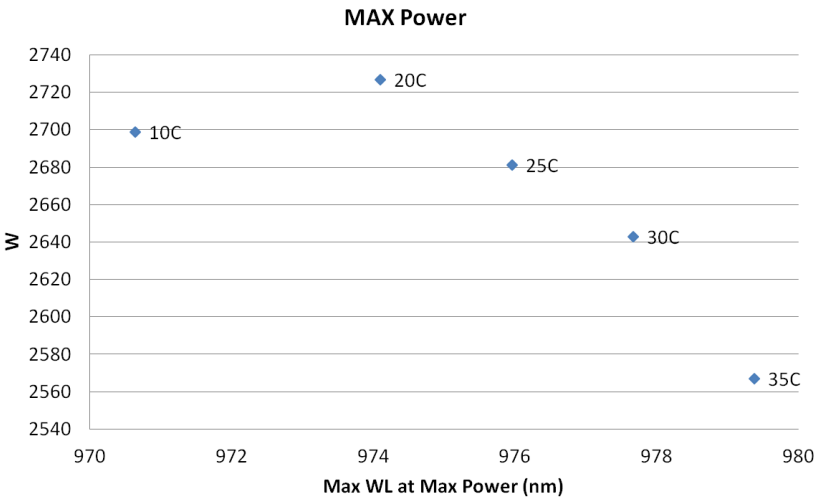

Figure 150. Maximum achieved power versus wavelength. Wavelength quoted is the maximum achieved from the pump block at maximum pump power for each set-point chiller temperature (label of the points)

Despite having the maximum efficiency, the point at 976 nm is not the one scoring the maximum output power; this is presumably due to the fact that the pump block starts to lose power when operated at increasingly higher temperatures. Maximum output power is reached at 974nm and is 2725W. The output spectrum of the lasers is shown in Figure 151. In this spectral measurement the BDF is an highly multimode fibre (250um diameter) not adding any significant SRS contribution.

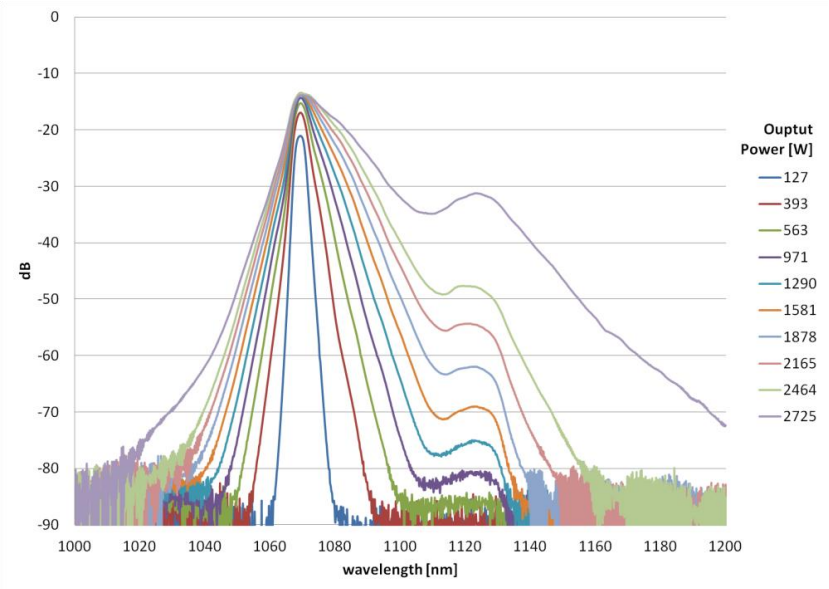

Figure 151. Output spectrum versus output power (with chiller set point at 20C).

From Figure 151, Figure 152 it can be seen that at about 2.5kW, SRS peak experiences a jump in power; this indicates that SRS is actually starting to “lase” due to unwanted spurious reflection in the cavity.

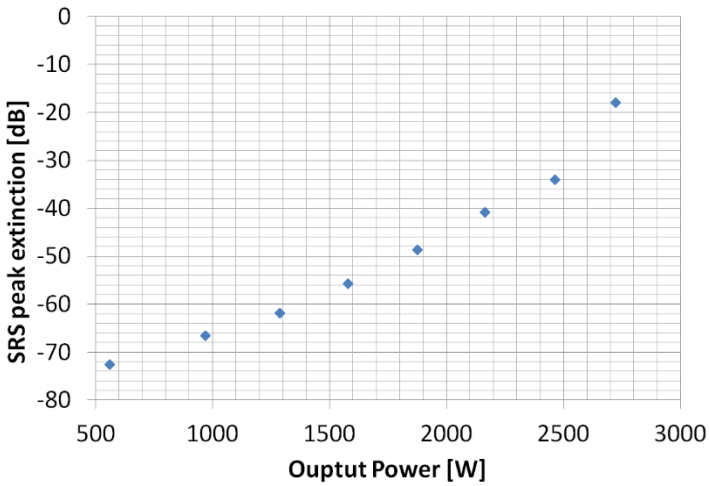

Figure 152. SRS peak extinction (distance from the main peak) versus laser’s output power.

Concurrently, at above 2.5kW, the laser becomes unstable (Figure 153).

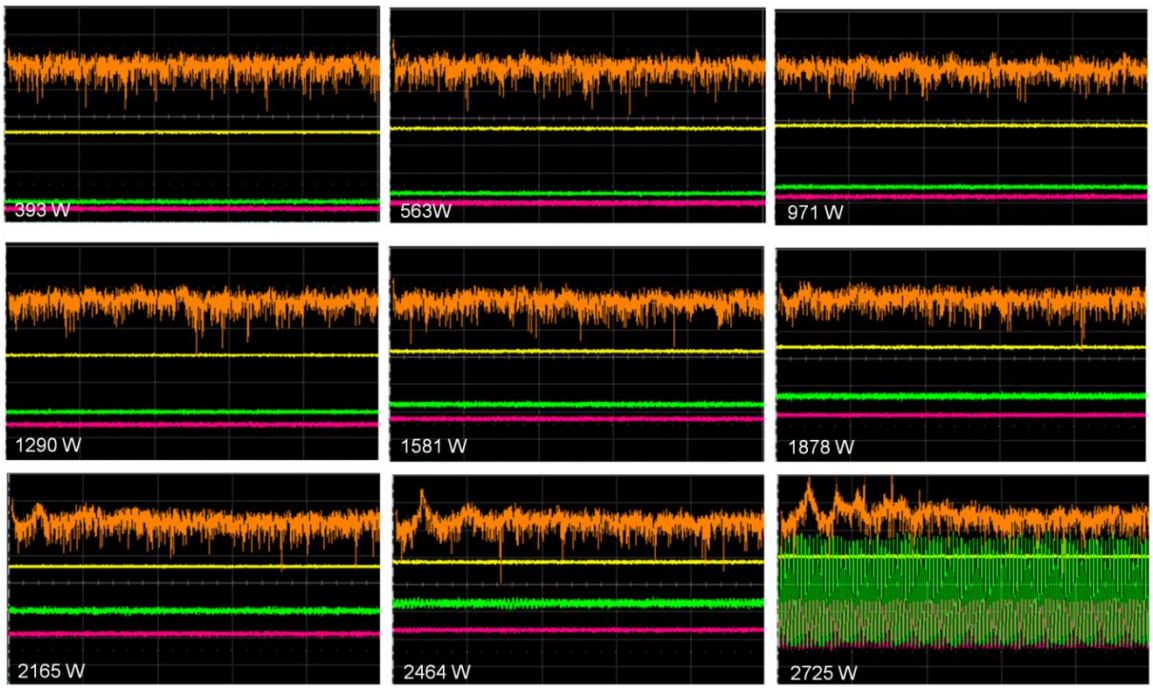

Figure 153. Oscilloscope screenshots at increasing output powers. Time division is 10us/div (total time 50us). Green waveform: output’s PD. Red waveform: CMS PD. Yellow waveform is the voltage driver (1-10 volts). Orange waveform: FFT of the output’s PD reading. In the FFT frequency division is 5MHz/division (25MHz in total) and vertical division is 20dB/div.

From Figure 153 it can be seen that at around 2.5kW, laser is unstable with output's spectral content at around 2MHz (+20dB above the noise). In the same fashion, also the signal coming from the CMS becomes unstable. Above 2.5kW, the laser becomes even more unstable, with temporal oscillation comparable with the CW part of signal and characterised by multiple overtones of 2MHz, resulting therefore in triangular waves (Figure 154).

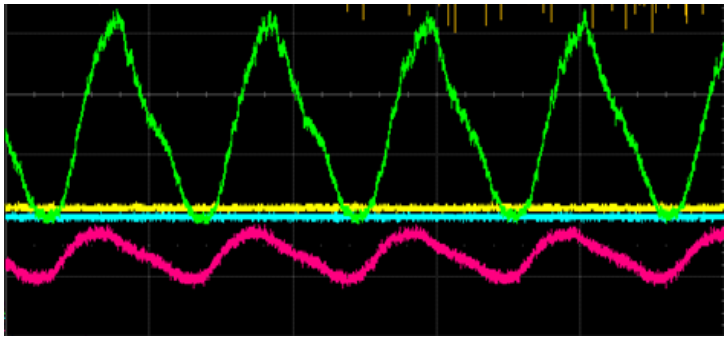

Figure 154. Oscilloscope screenshot at 2725 W. Time division is 500ns/div (total time 2.5us).

Reducing the time division of the oscilloscope (Figure 154), we realise that CMS and output readings are in phase. The fact that CMS and output are not in antiphase, excludes that this instability is of the same type reported in 5.2 and it has to be associated instead to the presence of SRS.

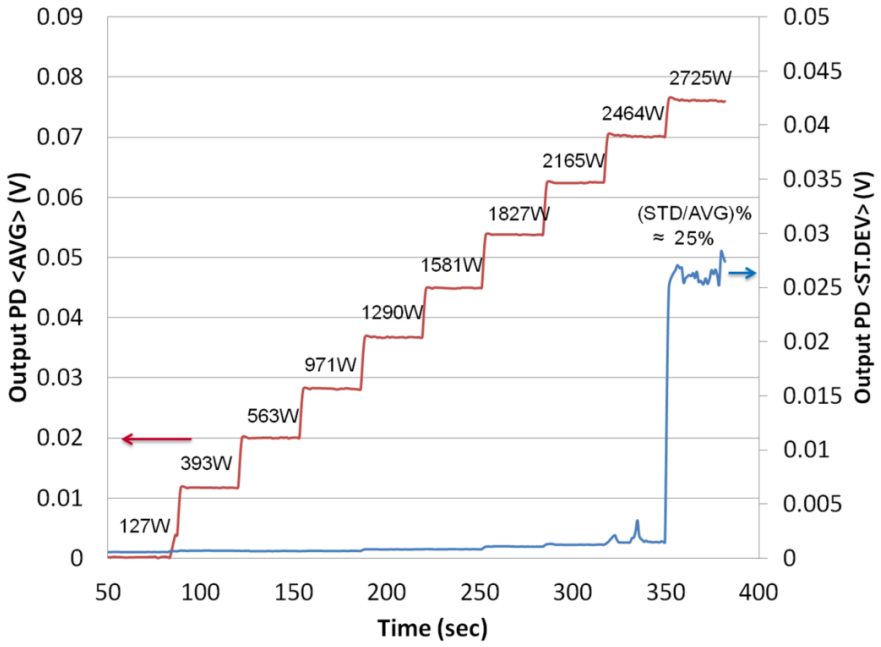

Figure 155. High power test kit output photodiode logging during power ramp.

During the power ramp (Figure 155), the test kit records at 1 hertz, the average and the standard deviation of the points on the screen of the oscilloscope (left axis for average and right axes for standard deviation). With the number of points refreshing on the oscilloscope's screen and the hardware available, the system measures without aliasing frequencies up to 100 MHz. In Figure 155, the average power measured during the various steps is used as a label (10 black labels, in Watts). Defining the RMS noise as the ratio between standard deviation and average, we can see than the RMS noise is less than 0.5% up to 2165 W, spikes up randomly at about 2464 W and diverges at 25% at 2725 W. Correlating the spectral results of Figure 151, and the noise results of Figure 155, we realise that both RMS noise and SRS, diverge at the same power level. From this correlation, we argue that the causes of instability for this laser is the excessive presence of SRS, known to destabilise HPFLs [141], rather than TMI. From the point of view of the stability, this laser would be a good candidate to operate efficiently, in single mode regime, up to 2kW.

However, to be sold as SM laser, this unit must have a Beam Delivery Fibre (BDF) that retains the modal purity and that is long enough to transport the light to the work piece. The ideal candidate as BDF is therefore an SMF. We will use here the SMF shown in Figure 35 as a BDF.

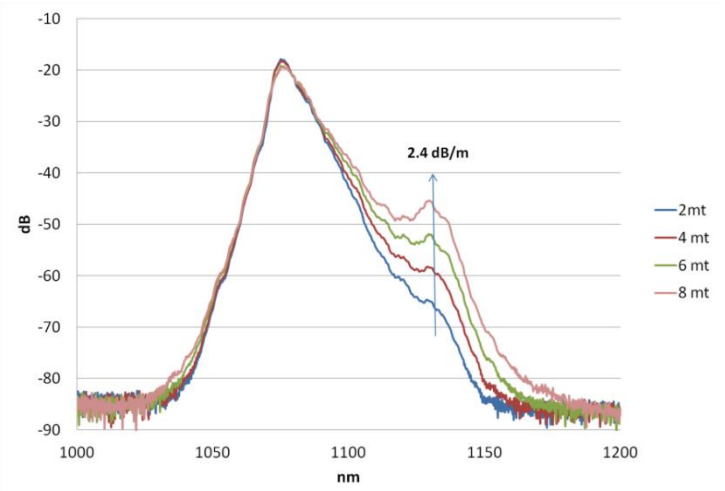

Figure 156. SRS cutback measurement at 2kW of output power.

The SRS contribution of such fibre to the spectral output of an LMA laser was measured via cutback (Figure 156). SRS cutback involved the measurement of the output spectrum with different fibre lengths and different oscillator's powers. For conciseness, in Figure 156, we report only the results obtained at 2kW. SMF contribution to SRS is 2.4dB/m at 2kW (1.2 dB/m/kW). From the applications laboratories of SPI lasers, it is known that back reflections can destabilise lasers and that having more than a certain critical amount of SRS can make lasers unsuitable for fine cutting (e.g. in SM regime). The maximum SRS extinction from the main peak is -30dB to cut low reflective materials (e.g. mild steel) and -40 dB to be able to cut highly reflective materials (e.g. copper). As a marketing exercise, by putting together the data of Figure 152 and the SMF contribution to SRS (1.2 dB/m/kW), we can build a map to assess the maximum BDF length usable for any power variant marketable for this oscillator.

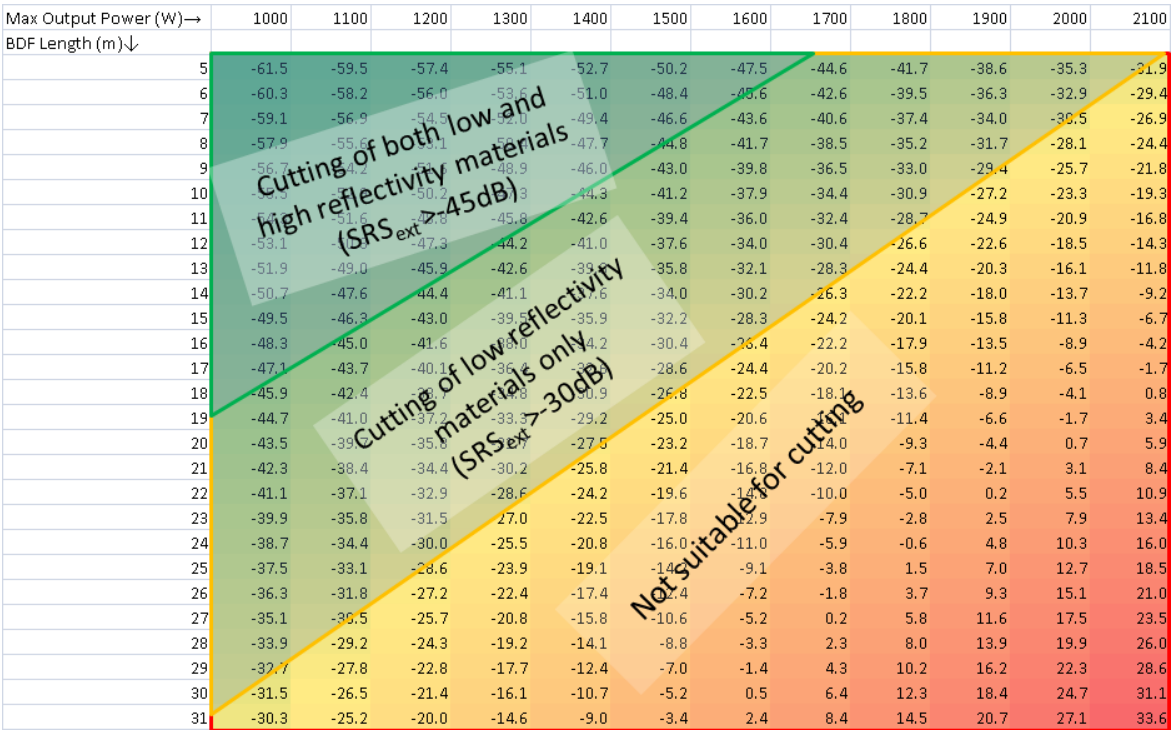

Max Output Power (W)→	1000	1100	1200	1300	1400	1500	1600	1700	1800	1900	2000	2100
BDF Length (m)↓												
5	-61.5	-59.5	-57.4	-55.1	-52.7	-50.2	-47.5	-44.6	-41.7	-38.6	-35.3	-31.9
6	-60.3	-58.2	-56.0	-53.6	-51.0	-48.4	-45.6	-42.6	-39.5	-36.3	-32.9	-29.4
7	-59.1	-56.9	-54.5	-52.0	-49.4	-46.6	-43.6	-40.6	-37.4	-34.0	-30.5	-26.9
8	-57.9	-55.6	-53.1	-50.5	-47.7	-44.8	-41.7	-38.5	-35.2	-31.7	-28.1	-24.4
9	-56.7	-54.2	-51.6	-48.9	-46.0	-43.0	-39.8	-36.5	-33.0	-29.4	-25.7	-21.8
10	-55.5	-52.9	-50.2	-47.3	-44.3	-41.2	-37.9	-34.4	-30.9	-27.2	-23.3	-19.3
11	-54.3	-51.6	-48.8	-45.8	-42.6	-39.4	-36.0	-32.4	-28.7	-24.9	-20.9	-16.8
12	-53.1	-50.3	-47.3	-44.2	-41.0	-37.6	-34.0	-30.4	-26.6	-22.6	-18.5	-14.3
13	-51.9	-49.0	-45.9	-42.6	-39.3	-35.8	-32.1	-28.3	-24.4	-20.3	-16.1	-11.8
14	-50.7	-47.6	-44.4	-41.1	-37.6	-34.0	-30.2	-26.3	-22.2	-18.0	-13.7	-9.2
15	-49.5	-46.3	-43.0	-39.7	-35.9	-32.2	-28.3	-24.2	-20.1	-15.8	-11.3	-6.7
16	-48.3	-45.0	-41.6	-38.0	-34.2	-30.4	-26.4	-22.2	-17.9	-13.5	-8.9	-4.2
17	-47.1	-43.7	-40.1	-36.4	-32.5	-28.6	-24.4	-20.2	-15.8	-11.2	-6.5	-1.7
18	-45.9	-42.4	-38.7	-34.8	-30.9	-26.8	-22.5	-18.1	-13.6	-8.9	-4.1	0.8
19	-44.7	-41.0	-37.2	-33.3	-29.2	-25.0	-20.6	-16.1	-11.4	-6.6	-1.7	3.4
20	-43.5	-39.7	-35.8	-31.7	-27.5	-23.2	-18.7	-14.0	-9.3	-4.4	0.7	5.9
21	-42.3	-38.4	-34.4	-30.2	-25.8	-21.4	-16.8	-12.0	-7.1	-2.1	3.1	8.4
22	-41.1	-37.1	-32.9	-28.6	-24.2	-19.6	-14.8	-10.0	-5.0	0.2	5.5	10.9
23	-39.9	-35.8	-31.5	-27.0	-22.5	-17.8	-12.9	-7.9	-2.8	2.5	7.9	13.4
24	-38.7	-34.4	-30.0	-25.5	-20.8	-16.0	-11.0	-5.9	-0.6	4.8	10.3	16.0
25	-37.5	-33.1	-28.6	-23.9	-19.1	-14.1	-9.1	-3.8	1.5	7.0	12.7	18.5
26	-36.3	-31.8	-27.2	-22.4	-17.4	-12.4	-7.2	-1.8	3.7	9.3	15.1	21.0
27	-35.1	-30.5	-25.7	-20.8	-15.8	-10.6	-5.2	0.2	5.8	11.6	17.5	23.5
28	-33.9	-29.2	-24.3	-19.2	-14.1	-8.8	-3.3	2.3	8.0	13.9	19.9	26.0
29	-32.7	-27.8	-22.8	-17.7	-12.4	-7.0	-1.4	4.3	10.2	16.2	22.3	28.6
30	-31.5	-26.5	-21.4	-16.1	-10.7	-5.2	0.5	6.4	12.3	18.4	24.7	31.1
31	-30.3	-25.2	-20.0	-14.6	-9.0	-3.4	2.4	8.4	14.5	20.7	27.1	33.6

Figure 157. Range of applicability of the presented HPFLs depending on power and BDF length.

5.8 Conclusions

In this chapter we have connected many of the learning of the previous chapters to explain the efforts made in order to scale the power of HPFLs at SPI Lasers. Also in this chapter, we have focussed our attention on the SM-MM splicing; here we explained how the splice actually affects the laser performance. We have therefore introduced the concept of the double cavity. On top of that, to characterise HOM excitation at high power we developed a measurement based on Calorimetry (metallic grid on the mode-stripper). This has allowed us to compare consistently the results of different splices across different lasers and AF. In this concluding chapter we showed the results obtained with three lasers, representing three classes of lasers.

The first laser showed constituted a bold attempt to scale the output power just by adding more pump power. A 250W rated lasers from SPI was pumped with a 2.4kW pump block. It must be stressed that yield for the production of these lasers, prior to 2016, was 56% and the cause of failure was the lack of stability and efficiency. Clearly, this scaling attempt did not work, but it gave us chance to study CW and transient TMC in HPFL. The FM and HOM power evolution effectively indicated the presence of two competing laser cavities, which resulted in rich output dynamics and full chaotic operation. The work shows

that the observed TMC phenomena are due to combined and interleaved inversion- and thermally-related effects, with distinctively different characteristic frequencies and power dependencies. The CW characterization obtained with slow detection shows the presence of TMC with envelopes on a slow seconds-timescale. Average values obtained from CW measurement are divided in three zones with progressively smaller output power efficiency. In low-power zone#1, only slow power variations are observed. At the top-end of zone#1, a pronounced thermally-induced TMC is measured with characteristic frequencies in the ~50kHz range. In zone#2, both thermal and inversion induced TMC coexist. The relative thermal and inversion related contributions to the observed TMC have been identified by monitoring the associated characteristic instability frequencies, under pulsed pumping. It is shown that in the transient regime, both inversion and thermal effects contribute successively to the observed power instabilities. In most of the cases, the output power initial relaxation overshoot is followed by fast (in the MHz range) inversion-related power competition between FM and HOMs with null average power exchange. Thermal effects overtake after ~80-100µs, showing much slower dynamics (in the 10s of kHz range) and characterized by marked FM/HOM power exchange. At the bottom-end of zone#2, inversion dominated TMC appears with characteristic frequencies ~2.5MHz (about half the cavity FSR). The instability characteristic frequency increases linearly with pump power until it matches the cavity FSR (first LMB) frequency at the top-end of zone#2. Further pump power increase into section#3 drives the HPFL into full chaotic behaviour. The co-existence and relative importance of the two effective cavities depends on the degree of HOM excitation at the SM-to-MM splices.

The second laser shown, denominated LMA laser, adopted a bigger core than the first. From the strong suggestion given by the test of the first laser, or more precisely from that class of lasers, we build the LMA laser by optimising routinely the SM-MM splices and by adopting selective doping. These mitigation remedies were effectively intended to kill the secondary spurious cavity verified in the past. Splicing the laser without arc optimisation, or as we showed with intentionally wrong arc duration, results in poor efficiency and stability. Furthermore, we demonstrated with modelling, that selective doping makes the efficiency of the laser less susceptible to splice optimisation preciseness. The so designed and build LMA lasers worked and went to production.

Since then, the production line of SPI lasers did not report instability and lack of efficiency as main cause of failure. Subsequently, by mean of S^2, we proved that also the LP01 lack of rotational symmetry has an impact on the laser efficiency. Despite the fact that the S^2 is not designed to infer about LP01, once found the LP02 minimum, the "0ps" image closely resemble the LP01 shape. This was confirmed by BPM method performed on the 2D measurement of the IORs. The fibre fabrication department at SPI Lasers has since started to find a way to build cores endowed with increased centrosymmetric cores. The current understanding is that it is easier to obtain "rounder" cores if the Yb concentration is less than $2.5x10^{26}$ m^{-3}. This clearly has an effect on the laser's pump absorption.

The third laser construction put together all the understandings acquired in the previous chapters and lasers so far presented; resulting in the most efficient KW series laser SPI lasers has ever built. This laser, classed as internally as ECO laser, also leverage on a reduced quantum defect as we narrowed the distance between pump and signal wavelength. This laser, whose pump work spectrally close to Yb absorption, needs extra care to ensure that pump temperature is somewhat stabilised. Above 2.5kW, this laser becomes unstable, but instability is not due to TMI, but to excessive SRS. As a last point, we have contextualised the applicability of this laser in the SM market evaluating which delivery fibre (max length) can be associated to any (max) power variant for this device.

6 Final conclusions and future works

This conclusive chapter reviews the work done during this PhD. On top of highlighting the novelty found in terms of photonics, we will also emphasise the valuable industrial know how produced for SPILasers. SPI began to introduce the LMA fibres for the construction of HPFLS in the year 2017. This triggered the need of improving the splicing technology. In order to understand better splicing, during the course of this PhD, we have developed the S^2 test-kit; both the hardware and software (Figure 22, Figure 25). The performance of the test-kit is acceptable: the full picture of the excited modes and modal contains can be measured in one minute circa. It was clear from first results of the S^2 that, to handle bigger fibres, the fusion splicer technology needed an update; therefore, we introduced the ROF technology. The so developed S^2 test-kit has proven to be a very versatile tool and it is currently used routinely by the R&D department of SPI Lasers. On top of that, S^2 has provided the R&D with compelling evidence that ultimately convinced the fibre department to achieve higher core-clad concentricity and higher core centrosymmetricity. To measure the HPFLs obtained with the new splicing technology, we also developed a high power test-kit; hardware and software (Figure 31,Figure 32 and Figure 34). With this test-kit, amongst many other things, we have been capable of testing the quality of the splices optimised via S^2, in terms of the outcome that matters (i.e. optical efficiency and stability). The high power test-kit is currently adopted by the R&D of SPI and it is certainly the most complete tool available to prototype and troubleshoots CW HPFLs. The test-kit also introduces a novel technique that resolves spatially and spectrally the radiation emitted by the active medium, therefore along its length (Figure 97). The advancement made in the splice technology has produced know how that is currently core technology of SPI Lasers. Virtually, every CW HPFLs produced by SPI is now optimised with the technique developed during this PhD. The adoption of the S^2 to optimise SM-MM splices is *per se* a novelty; having found a generic rule of optimisation is what makes this work unique. We originally found out that, in SM-MM splices leveraging on dopants diffusion, there is an optimum arc duration that allows LP02 minimisation (Figure 52). It was then empirically proven that LP02 minimised splices between SM passive fibres and MM AF, led to higher efficiencies in HPFLs (Figure 131). To have a better understanding of the splicing process, we measured with the IFA the index of refraction across the splice (Figure 71). We immediately noticed that the optimised splice samples created with the S^2 were not LP01 effective area matched (Figure 75). This looked counterintuitive, as it is

commonly believed that SM excitation in MM fibre can only be achieved by matching the MFD of the incoming beam (fibre) with the effective area of the LP01 mode of the MM fibre. For this reason, we recycled some old theory developed for tapers in planar waveguide, adapting them to function with fibres. The so developed model was then run on the IFA samples revealing that minimising the LP02 excitation contextually maximises the LP01 excitation (Figure 81,Figure 82). This explained why, HPFLSs spliced with the arc optimisation criteria were so efficient. Since the introduction of this technique, the production line of SPI did not report instability as main cause of failure. From its introduction, about 850 lasers have being spliced with the arc-optimised criteria. The fact that LP01 pure excitation in MM fibre can be achieved with a mismatched area splice is indeed one of the most important novelties of this work. This result has the potential to oppose and make vain the claims of a patent IMRA submitted in the 90s [131, 132]. The developed theory explains how the so developed splice optimisation, despite using a very short taper length, is effectively capable of selectively optimise only the FM of the MM fibre. Furthermore, theory gives a clear indication on how to develop a splice that can exceed the performance of that developed and currently used in SPI.

By using the high power test kit, we have been able to document the behaviour of three classes of lasers. The first described laser was a bold attempt made in the year 2017, resulted in a failure, to scale the output power of a 250W class laser up to kW level (paragraph 5.2). A rich analysis was made on the data acquired from this laser; the result of this analysis have been presented to CLEO 2017 [75] and subsequently published in the year 2019 [76]. This laser represents the class of lasers fabricated by SPI prior to 2017. The AF of these lasers had V = 5.5, with 0.13 NA and core radius equal to 7um. The passive fibre used for the gratings were purely SM. At the time, neither splice optimisation nor selective doping was adopted as criteria for the construction and fibre design of the AF. Prior to 2017, about 50% of the lasers resulted unstable at final test. With the development of the high power test-kit, we have been able to infer about the existence of a secondary parasitic cavity by measuring concurrently the readings of both MS and output (Figure 122-124). This gave a precise indication on how to solve the problem. To solve the problem we have put two remedies in place. First, we have increased the loss of this HOM cavity; we did this by optimising the splice and reducing therefore the LP02 launched in the cavity, at the splicing point. Second, we adopted selective doping reducing the gain competition between modes, favouring the FM overlap with the Yb over that of the HOMs.

The second class of lasers was conceived to reach the kW level by reducing the impact of SRS and therefore adopting LMA fibres. These classes of lasers are internally referred as LMA lasers. In these class of lasers, the AF has V = 8.6, with 0.13 NA and core radius equal to 12um. Furthermore, the passive fibre used for the gratings are dual moded, but coiled opportunely to filter the LP11. This second class of lasers adopted splice optimisation and selective doping. With these remedies in place, the secondary parasitic cavity was effectively suppressed and allowed operating up to 2 kW without instability. After the adoption of these two remedies, the FPY on production line went up to 90%, with the instability no longer figuring as the main cause of failure. A new measurement technique was developed to measure the power wasted by the CMS, by adopting a grid and a thermal camera. This "calorimetric" measurement proved to be extremely useful in increasing even further the performance of the lasers; both in the prototyping phase and in the subsequent alpha development. In the prototyping phase of the first LMA lasers we have been able to track the following parameters: output efficiency, mode stripper wasted energy and LP02 excitation. Given a specific AF, the higher the LP02 excitation, the higher the energy wasted by the MS, the lower the laser's efficiency. Vice versa, the lower the LP02 excitation, the lower the energy wasted by the MS, the higher the efficiency (section 5.3). As we demonstrated in chapter 3, minimising the LP02 corresponds to maximising the LP01. In the same period we verified that adoption of the ROF technology led to more repeatable splice and for this reason more repeatable laser efficiency (paragraph 5.5). In the alpha development, several different AFs reached the production the line. Notwithstanding splice optimisation, we still experienced variations of lasers' efficiency. With the help of the S^2, it was subsequently proven that efficiency depends also on the LP01 shape (paragraph 5.6). The S^2 is not designed to measure LP01 features and in principle, it could not. However, when the modal excitation is optimised, only the FM propagates in the MM fibre and image of the LP01 appears quite neat. We definitively proved that AFs with more centrosymmetric IORs result in rounder LP01 modes and higher laser efficiencies. This finding motivated the fibre department to find ways to optimise the centrosymmetricity of the newly developed LMA fibres. Finally, we have theoretically proven that the combination of splice optimisation and selective doping makes the process of splicing less sensitive to the precision of the splice. In this sense splice optimisation and selective doping made the process of fabrication easier, increasing the FPY.

The last laser presented belongs to the class of lasers referred internally as ECO. For the construction of this laser, all the understandings gathered in this work have been adopted, namely: splice optimisation, core having high centrosymmetricity and passive pigtails with high core clad concentricity. Furthermore this new laser operates at 97xnm, resulting in optical efficiency exceeding the 83% and by limited in power by SRS, rather than TMI (paragraph 5.7). Further development in the understanding of lasers can be achieved with the usage of the vertical probing technique. This approach is unique and never reported in the literature. With this technique, we have been able to measure the most inner parts of the laser, the quantities described by the rate equation, namely: pump, inversion and signal power (Figure 97). We measure these quantities, in a non-destructive way, along the fibre length at any power, live. The technique also allows tracking the whole spectral evolution along the active medium length, enabling therefore the tracking of non-linear effects.

For future work, the author would propose the following points.

- The author would like to make the S^2 measurement faster, especially in the acquisition data stage. S^2 technique could be made faster by the adoption of algorithms related to compressed interferometry. With this technique, the speed could become ten times shorter with little variation on the measurement accuracy [142, 143].

- The SM-MM splice could be further improved by developing a splice that optimises also the differential phase shifts of the modes, before they reach the up tapered zone (e.g. $\Delta\vartheta = \Delta\vartheta^*$ as per the nomenclature we defined in paragraph 3.4.5). To do so the author would initially characterise a bigger number of optimised splices. By analysing the data, the author would then establish if the characteristic $\Delta\vartheta^*$ of the splices is constant. If so, the new splice would be based on the creation of an initial flat zone (as referred in paragraph 3.4.5.2) of constant length, providing a differential phase shift $\Delta\vartheta$ that matches $\Delta\vartheta^*$. The flat section would then be followed by an optimised up tapered zone.

- As per the vertical probing, the author would initially improve the setup to resolve better the peaks and increasing simultaneously the dynamic range. This could be accomplished, for instance by using a vertical probing fibre endowed with a micro lens.

- An application of the vertical probing could be for instance the optimisation of the laser length. Since pump absorption along GTW fibres (in dB/m) is not constant and decreases after a certain length, there is the possibility that the AF length is not the strict necessary to guarantee enough absorption. In that case, the last meters of GTW would not account for increase of pump absorption but would certainly account for an increase of SRS. This sort of studies can be carried out in presence of multifaceted pump cladding, different winding patterns and pump wavelengths.

- If the dynamic range could be increased, then SRS could be also tracked along the length.

- The author would also be curious to prove more definitively if this technique is reliably able to locate the zones where mode coupling takes place (as shown only once in paragraph 4.3 - Figure 107). In this case, the technique would prove very even more effective in the design and verification of AF winding patterns.

Finally, we present the list of techniques, processes and devices developed during this PhD by the author and where they are currently used.

- S^2 test-kit for R&D
    - Software and hardware
    - C# software handover to ORC

- S^2 Arc duration characterising station for manufacturing (upload optimisation data on the server)
    - S^2 surrogate Software and hardware
    - 250 Samples of AFs samples characterised and uploaded to date

- HPFLs Splicing Stations (download optimisation data from the server to the splicer's hardware)
    - Software developed for multiple clients (NPI and manufacturing stations)
    - 850 between laser and amplifiers spliced with these stations to date

- Introduction of the ROF technology
    - Before only two electrodes splicers where used in the SPI site of Southampton

- V-Height calibration software for the calibration department
    - Calibrates the discharge symmetry for two electrodes splice (for legacy product)
    - Two electrodes FSs routinely calibrated

- Model to visualise dopants diffusion during fusion splicing (R&D)
    - Matlab code handed over to ORC for future works

- Algorithm to calculate mode coupling along the splices for R&D
    - Used by R&D when new LMAs models are introduced

- Usage of the S^2 / arc duration optimised beam to assess LP01 centrosimmetricity
    - Centrosimmetricity importance not appreciated enough in the past and calculated with complex and time consuming 2D IOR measurement followed by BPM algorithm

- High power test-kit for HPFLs and MOPAs (R&D, NPI)
    - Software and hardware
    - C# software handover to ORC
    - The most sophisticated tool for high power troubleshooting at disposal of SPILasers.

- Introduction of mode stripper Calorimetry grid (R&D and Production)
    - Allowed to correlate laser efficiency and wasted energy by mode-stripper.
    - Currently implemented also by the production line

- Invention of the vertical probe technique (R&D)
    - Allows the non-destructive, live measurement of pump, inversion and signal power along the fibre length. Allows the characterisation of non-linear effects along the fibre length and has the potential of measuring HOM coupling in the AF.

Appendix

Inversion and thermal timescales in high power fibre laser transients.

Transients in optical fibre lasers and amplifiers, due to pump and/or signal changes, are characterized by specific time scales defined by the dominant optical effects. Although population inversion and thermal effects are intimately interlinked, their characteristic time scales can differ substantially, depending on the operating and boundary conditions.

Thermal diffusion time scales

The temperature change distribution ΔT(r,ϕ,z;t) is given by the heat equation:

$$\frac{d\Delta T}{dt} - \alpha \nabla_T^2(\Delta T) = \frac{Q_T}{\rho_0 C_0} \qquad (1)$$

where $\alpha = \kappa_0/\rho_0 C_0$ is the glass thermal diffusivity, ρ_0, C_0, κ_0 are the glass density, specific heat capacity and thermal conductivity, respectively, and Q_T is the heat power density. Heat diffusion time scales are obtained by setting $Q_T = 0$ for t>0. Assuming a step-index fibre with R_1 and R_2 core and cladding radii, respectively, and simplified initial condition $\Delta T(r,\varphi,t) = \Delta T_0$ for $r<R_1$ and t=0, the temperature variation with time is then given by [144]

$$\Delta T(r,t) = \Delta T_0 \sum_{n=1}^{\infty} A_n J_0\left(\frac{\beta_n r}{\sqrt{\alpha}}\right) exp(-\beta_n^2 t), \ (t \geq 0) \qquad (2)$$

where β_n (n=1,2,3,…) are obtained from the boundary condition of the 3rd kind (BC#3):

$$J_0(z_n) - \left(\frac{z_n}{H}\right) J_1(z_n) = 0; \qquad H = \frac{R_2 h_2^*}{\kappa_2^*} \qquad (3)$$

where $\beta_n = \frac{z_n\sqrt{\alpha}}{R_2}$ and h_2^*, κ_2^* are the convection coefficient and thermal conductivity, respectively, of the surrounding cooling medium. The amplitude of the n^{th} thermal component is given by:

$$A_n = \frac{\int_0^{R_1} r' J_0\left(\frac{\beta_n r'}{\sqrt{\alpha}}\right) dr'}{\int_0^{R_2} r' J_0^2\left(\frac{\beta_n r'}{\sqrt{\alpha}}\right) dr'} \tag{4}$$

The diffusion time and the characteristic frequency of the n^{th} thermal component, on the other hand, are given by $\tau_n^{th} = \beta_n^{-2}$ and $f_n^{th} = \beta_n^2$, respectively. The case of large convection coefficient ($h_2^* \gg 1; H \to \infty$) corresponds to the boundary condition of the 1st kind (BC#1), namely, $J_0(z_n) = 0$.

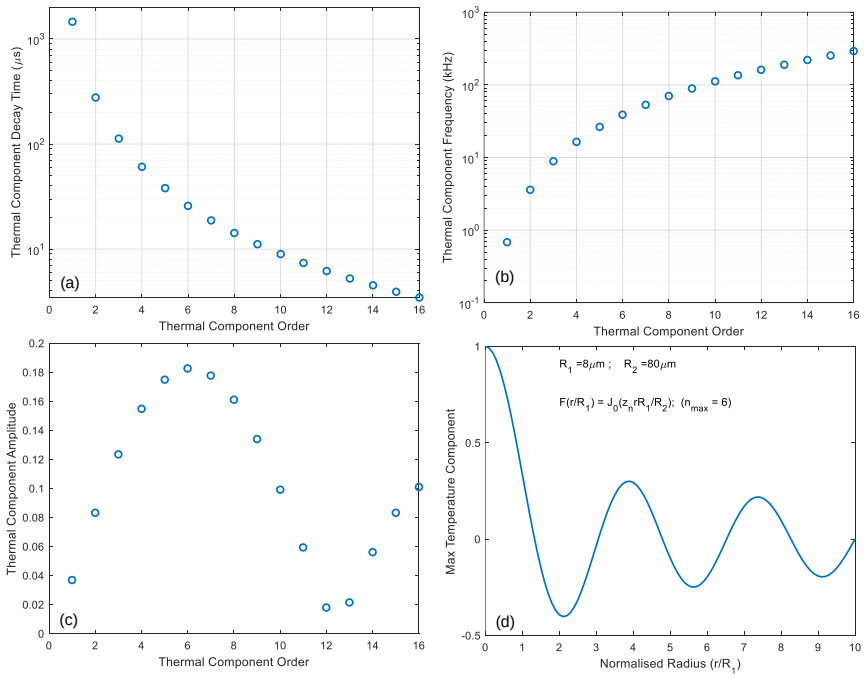

Fig. A1: (a) Diffusion time, (b) characteristic frequency and (c) amplitude of the n^{th} thermal component, for initial condition $\Delta T(r,\phi,t) = \Delta T_0$ for $r<R_1$ and t=0, and BC#1, (d) temperature variation of the maximum thermal component (n=6); R_1 = 8μm and R_2 = 80μm.

Figure A1 plots (a) the diffusion time (τ_n^{th}), (b) characteristic frequency (f_n^{th}) and (c) amplitude (A_n) of the n^{th} thermal component, for an initial condition $\Delta T(r,\varphi,t) = \Delta T_0$, for $r<R_1$ and t=0, and BC#1. It is shown that the diffusion time (characteristic frequency) decreases (increases) monotonically with the order of the thermal component. This is due to the fact

that thermal components of higher order show more and, therefore, sharper temperature variations along the fibre radius and, as a consequence, they diffuse faster. The amplitude of the thermal component, on the other hand, varies non-monotonically with order *n* and shows a maximum for the *n*=6. The corresponding diffusion time and characteristic frequency is ~25μs and 40kHz, respectively. Figure A1(d) plots the temperature variation along the normalized fibre radius for the maximum thermal component (*n*=6). For BC#1, the diffusion time of the n^{th} thermal component can be approximated by $\tau_n^{th} \approx \frac{R_2^2}{(\alpha\pi^2 n^2)}$.

Figure A2 plots (a) the diffusion time, and (b) the characteristic frequency of the maximum thermal component, as a function of the core radius. The initial condition is again $\Delta T(r,\phi,t) = \Delta T_0$, for $r<R_1$ and $t=0$, and BC#1 (blue line) and BC#3 (red line) are considered. The cladding/core ratio R_2/R_1 is 10. It is shown that the dominant diffusion time (frequency) increases (decreases) quasi-quadratically with the core radius.

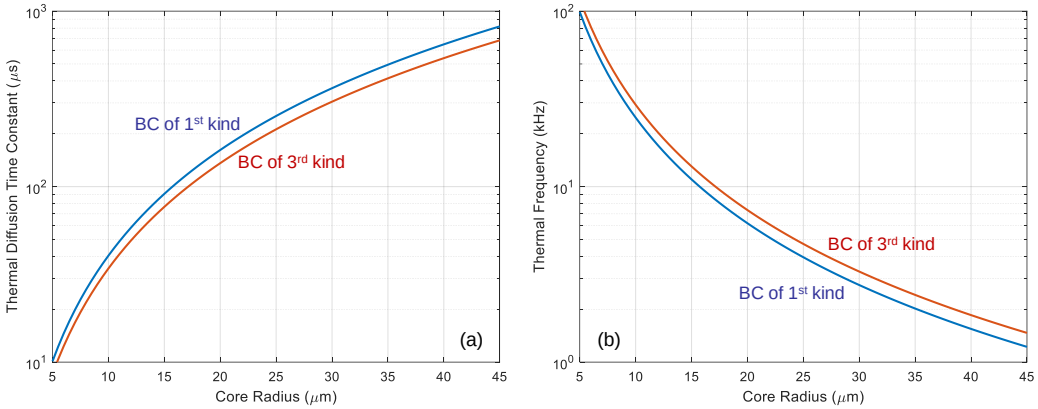

Fig. A2: (a) Diffusion time, (b) characteristic frequency of the maximum thermal component, as a function of the core radius. Initial condition $\Delta T(r,\phi,t) = \Delta T_0$, for $r<R_1$ and $t=0$, and BC#1 (blue line) and BC#3 (red line). Ratio $R_2 / R_1 = 10$.

Figure A2 also shows that the dominant thermal component diffusion time depends on the boundary conditions, with BC#3 having smaller diffusion times than BC#1. This is due to the fact that the dominant thermal components under BC#3 correspond to *n*=7 and, therefore, have sharper temperature features (see Fig. A3) and, consequently, smaller diffusion times.

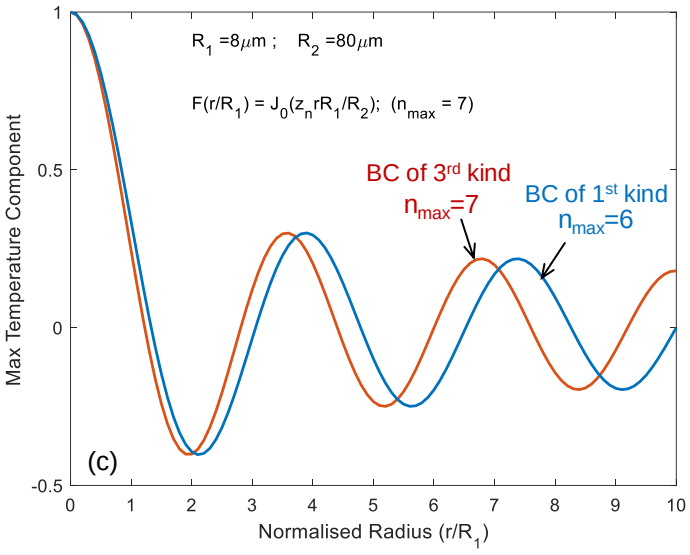

Fig. A3: Temperature variation of the maximum thermal component for BC1 (n=6) and BC3 (n=7). Initial condition $\Delta T(r,\phi,t) = \Delta T_0$, for $r<R_1$ and t=0, and BC#1 (blue line) and BC#3 (red line). R_1 = 8μm and R_2 = 80μm.

It can be shown that the variation of the dominant diffusion time with core radius for BC#1 can be approximated by $\tau_{th} \approx \frac{R_{1eff}^2}{(2.405^2\alpha)}$. It should be mentioned that the usually quoted approximation of the timescale associated with thermal effects $\tau_{th}^{'} \approx \frac{R_1^2}{\alpha}$ [31, 32] overestimates diffusion times by a factor of ~4.

Population inversion related time scales

Another mechanism that can induce index modulation and power exchange between modes is the inversion of the medium. The variation of the spatially averaged excited state population distribution N_2 is given by:

$$\frac{dN_2}{dt} + \frac{N_2}{\tau_{eff}^{inv}} = \frac{N_0}{\tau}\left[\frac{\sigma_{ap}}{\sigma_{ap}+\sigma_{ep}}\left(\frac{I_p}{I_p^{sat}}\right) + \frac{\sigma_{as}}{\sigma_{as}+\sigma_{es}}\left(\frac{I_s}{I_s^{sat}}\right)\right] \quad (5)$$

where $I_s^{sat} = \frac{h\nu_s}{[\tau(\sigma_{as}+\sigma_{es})]}$ and $I_p^{sat} = \frac{h\nu_p}{[\tau(\sigma_{ap}+\sigma_{ep})]}$ are the signal and pump saturation intensities, respectively, τ is the upper-state population lifetime and τ_{eff}^{inv} is the corresponding effective lifetime given by:

$$\tau_{eff}^{inv} = \frac{\tau}{1+\frac{I_p}{I_p^{sat}}+\frac{I_s}{I_s^{sat}}} \quad (6)$$

The signal and pump intensities are approximated by $I_s = \frac{P_s}{(\pi R_1^2)}$and $I_p = \frac{P_p}{(\pi R_2^2)}$, respectively. For a fixed pump intensity I_p and a change of signal intensity from I_{s1} to I_{s2} at t=0, the upper-lever population varies as:

$$N_2(t) = N_2^{ss}(I_{s2}; I_p) + \left[N_2^{ss}(I_{s1}; I_p) - N_2^{ss}(I_{s2}; I_p)\right] exp\left(-\frac{t}{t_{eff}^{inv}}\right); \quad (t \geq 0) \qquad (7)$$

where $N_2^{ss}(I_{s1}; I_p)$, $N_2^{ss}(I_{s2}; I_p)$ are the corresponding steady-state upper-state populations given by:

$$N_2^{ss}(I_s; I_p) = N_0 \left\{ \frac{\left[\frac{\sigma_{ap}}{\sigma_{ap}+\sigma_{ep}}\left(\frac{I_p}{I_p^{sat}}\right)+\frac{\sigma_{as}}{\sigma_{as}+\sigma_{es}}\left(\frac{I_s}{I_s^{sat}}\right)\right]}{\left(1+\frac{I_p}{I_p^{sat}}+\frac{I_s}{I_s^{sat}}\right)} \right\} \quad (8)$$

The associated characteristic frequencies are given by

$$f_{eff}^{inv} = \frac{1}{\tau_{eff}^{inv}} = \frac{1}{\tau}\left(1 + \frac{I_p}{I_p^{sat}} + \frac{I_s}{I_s^{sat}}\right) \quad (9)$$

From Equations (6) and (9), it is deduced that the characteristic time scales and frequencies depend on core/cladding radii, as well as, the pump and signal powers. Figures A4(a) and (b) plot the effective upper-level decay time, and corresponding effective frequency, respectively, as a function of signal power, for different core diameters. The optical-to-optical conversion efficiency is assumed 80%, and the cladding/core ratio R_2/R_1 = 10. The signal and pump wavelengths are λ_s = 1070nm and λ_p = 915nm, respectively, and the fibre core is considered to be of phosphosilicate composition.

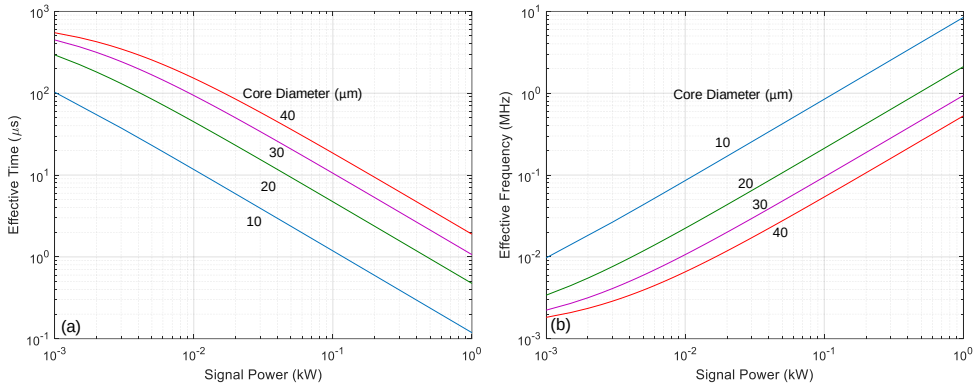

Fig. A4: (a) Effective upper-level decay time, and (b) corresponding effective frequency as a function signal power, for different core radii. Optical-to-optical conversion efficiency = 80%, ratio R_2/R_1 = 10, λ_s = 1070nm, λ_p = 915nm, phosphosilicate fibre.

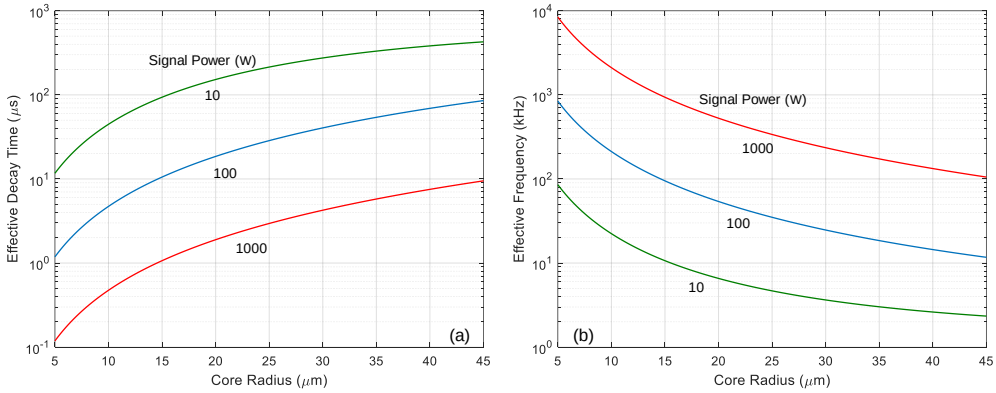

Fig. A5: (a) Effective upper-level decay time, and (b) corresponding effective frequency as a function core radius, for different signal powers. Optical-to-optical conversion efficiency = 80%, ratio R_2/R_1 = 10, λ_s = 1070nm, λ_p = 915nm, phosphosilicate fibre.

Figures A5(a) and (b) plot the effective upper-level decay time, and corresponding effective frequency, respectively, as a function of core radius, for different signal powers. The other parameters are as in Fig. A4.

In Fig A4(b) it is shown that, in inversion dominated dynamics for $I_s/I_s^{sat} > 1$ and fixed core/cladding radii, the effective frequency increases linearly with the signal power. Fig. A5(b), on the other hand, shows that for fixed power the effective frequency is inversely proportional to the core area, in a similar manner to thermally-induced effects (see Fig. A2(b)). Comparing Fig A5(b) and A2(b), however, it is becomes

apparent that thermally-induced transients show similar effective frequencies (~1-100kHz) only in the case of low signal power inversion-related dynamics (i.e. signal power ~10W). As the signal power is increased to kW level, the inversion-related frequencies increase to a 100kHz to 10s-of-MHz regime, while thermally-dominated transients are largely power independent.

At this point, it should be emphasized that the signal power dependence of the characteristic frequencies of the induced transients and their range of variation can be used as an indicator of the dominant (inversion or thermal) contributor to the observed power transients and instabilities in high power fibre lasers and amplifiers.

References

1. D. Tosi, and G. Perrone, "Fundamentals of Wave Optics and Optical Fibres," in *Fibre-Optic Sensors for Biomedical Applications*(Artech House, 2018), pp. 1-17.
2. R. T. Schermer, and J. H. Cole, "Improved bend loss formula verified for optical fibre by simulation and experiment," IEEE Journal of Quantum Electronics 43, 899-909 (2007).
3. K. Okamoto, *Fundamentals of Optical Waveguides* (Elsevier, 2006).
4. E. Snitzer, H. Po, F. Hakimi, R. Tumminelli, and B. C. McCollum, "Double clad, offset code Nd fibre laser," in *Optical Fibre Sensors*(Optical Society of America, New Orleans, Louisiana, 1988), p. PD5.
5. M. N. Zervas, and C. A. Codemard, "High Power Fibre Lasers: A Review," IEEE Journal of Selected Topics in Quantum Electronics 20, 23 (2014).
6. Grudinin, "Multi-fibre arrangements for high power fibre lasers and amplifiers," U. S. Patent, ed. (The University of Southampton, 2004).
7. Z. H. Huang, J. Q. Cao, S. F. Guo, J. Hou, and J. B. Chen, "The characteristics of pump light in side-coupled cladding-pumped fibres," Optical Fibre Technology 19, 293-297 (2013).
8. Z. H. Huang, J. Q. Cao, S. F. Guo, J. B. Chen, and X. J. Xu, "Comparison of fibre lasers based on distributed side-coupled cladding-pumped fibres and double-cladding fibres," Applied Optics 53, 2187-2195 (2014).
9. C. A. Codemard, A. Malinowski, and M. N. Zervas, "Numerical Optimisation of Pump Absorption in Doped Double-Clad Fibre with Transverse and Longitudinal Perturbation," in *Fibre Lasers Xiv: Technology and Systems*, C. A. Robin, and I. Hartl, eds. (Spie-Int Soc Optical Engineering, 2017).
10. M. N. Zervas, A. Marshall, and J. Kim, "Effective Absorption in Cladding-Pumped Fibres," in *Conference on Fibre Lasers VIII - Technology, Systems, and Applications*(Spie-Int Soc Optical Engineering, San Francisco, CA, 2011).
11. H. Zhan, Q. Y. Liu, Y. Y. Wang, W. W. Ke, L. Ni, X. L. Wang, K. Peng, C. Gao, Y. W. Li, H. H. Lin, J. J. Wang, F. Jing, and A. X. Lin, "5kW GTWave fibre amplifier directly pumped by commercial 976nm laser diodes," Optics Express 24, 27087-27095 (2016).
12. H. M. Pask, R. J. Carman, D. C. Hanna, A. C. Tropper, C. J. Mackechnie, P. R. Barber, and J. M. Dawes, "Ytterbium-doped silica fibre lasers - versatile sources for the 1-1.2 µm region," IEEE Journal of Selected Topics in Quantum Electronics 1, 2-13 (1995).
13. E. Desurvire, *Erbium-doped fibre amplifiers : principles and applications / Emmanuel Desurvire* (Wiley, 1994).

14. R. Paschotta, J. Nilsson, A. C. Tropper, and D. C. Hanna, "Ytterbium-doped fibre amplifiers," IEEE Journal of Quantum Electronics 33, 1049-1056 (1997).

15. C. A. Codemard, and M. N. Zervas, "UK industrial high-power fibre lasers," in *Technologies for Optical Countermeasures Xiii*, D. H. Titterton, R. J. Grasso, and M. A. Richardson, eds. (2016).

16. S. Jetschke, S. Unger, U. Ropke, and J. Kirchhof, "Photodarkening in Yb doped fibres: experimental evidence of equilibrium states depending on the pump power," Optics Express 15, 14838-14843 (2007).

17. J. Koponen, M. Soderlund, H. J. Hoffman, D. Kliner, and J. Koplow, "Photodarkening measurements in large-mode-area fibres," in *4th Conference on Fibre Laser - Technology, Systems, and Applications*(Spie-Int Soc Optical Engineering, San Jose, CA, 2007).

18. M. Hotoleanu, J. Koponen, T. Kokki, M. Laurila, and IEEE, "Experimental Verification of Spatial Distribution of Photodarkening in Large Mode Area Ytterbium Doped Fibres," 2008 Conference on Lasers and Electro-Optics & Quantum Electronics and Laser Science Conference, Vols 1-9, 234-235 (2008).

19. S. Jetschke, S. Unger, A. Schwuchow, M. Leich, and J. Kirchhof, "Efficient Yb laser fibres with low photodarkening by optimization of the core composition," Optics Express 16, 15540-15545 (2008).

20. S. Jetschke, S. Unger, M. Leich, and J. Kirchhof, "Photodarkening kinetics as a function of Yb concentration and the role of Al codoping," Applied Optics 51, 7758-7764 (2012).

21. B. Morasse, S. Chatigny, E. Gagnon, C. Hovington, J. P. Martin, and J. P. De Sandro, "Low photodarkening single cladding yttetbium fibre amplifier," in *4th Conference on Fibre Laser - Technology, Systems, and Applications*(Spie-Int Soc Optical Engineering, San Jose, CA, 2007).

22. M. Engholm, and L. Norin, "Preventing photodarkening in ytterbium-doped high power fibre lasers; correlation to the UV-transparency of the core glass," Optics Express 16, 1260-1268 (2008).

23. M. Engholm, P. Jelger, F. Laurell, and L. Norin, "Improved photodarkening resistivity in ytterbium-doped fibre lasers by cerium codoping," Optics Letters 34, 1285-1287 (2009).

24. G. P. Agrawal, "Applications of Nonlinear Fibre Optics, 2nd Edition," Applications of Nonlinear Fibre Optics, 2nd Edition, 1-508 (2008).

25. T. Eidam, C. Wirth, C. Jauregui, F. Stutzki, F. Jansen, H. J. Otto, O. Schmidt, T. Schreiber, J. Limpert, and A. Tunnermann, "Experimental observations of the threshold-like onset of mode instabilities in high power fibre amplifiers," Optics Express 19, 13218-13224 (2011).

26. M. N. Zervas, and IEEE, *Power Scalability in High Power Fibre Amplifiers* (2017).

27. M. N. Zervas, "Power Scaling Limits in High Power Fibre Amplifiers due to Transverse Mode Instability, Thermal Lensing and Fibre Mechanical Reliability," in *Conference on Fibre Lasers XV - Technology and Systems*(Spie-Int Soc Optical Engineering, San Francisco, CA, 2018).

28. C. Jauregui, T. Eidam, H. J. Otto, F. Stutzki, F. Jansen, J. Limpert, and A. Tunnermann, "Physical origin of mode instabilities in high-power fibre laser systems," Optics Express 20, 12912-12925 (2012).

29. K. R. Hansen, T. T. Alkeskjold, J. Broeng, and J. Laegsgaard, "Theoretical analysis of mode instability in high-power fibre amplifiers," Optics Express 21, 1944-1971 (2013).

30. L. Dong, "Stimulated thermal Rayleigh scattering in optical fibres," Optics Express 21, 2642-2656 (2013).

31. A. V. Smith, and J. J. Smith, "Mode instability in high power fibre amplifiers," Optics Express 19, 10180-10192 (2011).

32. H. J. Otto, F. Stutzki, F. Jansen, T. Eidam, C. Jauregui, J. Limpert, and A. Tunnermann, "Temporal dynamics of mode instabilities in high-power fibre lasers and amplifiers," Optics Express 20, 15710-15722 (2012).

33. B. Ward, C. Robin, and I. Dajani, "Origin of thermal modal instabilities in large mode area fibre amplifiers," Optics Express 20, 11407-11422 (2012).

34. S. Naderi, I. Dajani, T. Madden, and C. Robin, "Investigations of modal instabilities in fibre amplifiers through detailed numerical simulations," Optics Express 21, 16111-16129 (2013).

35. M. Karow, H. Tunnermann, J. Neumann, D. Kracht, and P. Wessels, "Beam quality degradation of a single-frequency Yb-doped photonic crystal fibre amplifier with low mode instability threshold power," Optics Letters 37, 4242-4244 (2012).

36. M. N. Zervas, "Transverse Mode Instability Analysis in Fibre Amplifiers," in *Fibre Lasers Xiv: Technology and Systems*, C. A. Robin, and I. Hartl, eds. (2017).

37. J. W. Dawson, M. J. Messerly, R. J. Beach, M. Y. Shverdin, E. A. Stappaerts, A. K. Sridharan, P. H. Pax, J. E. Heebner, C. W. Siders, and C. P. J. Barty, "Analysis of the scalability of diffraction-limited fibre lasers and amplifiers to high average power," Optics Express 16, 13240-13266 (2008).

38. M. N. Zervas, "Transverse Mode Instability Analysis in Fibre Amplifiers," in *Conference on Fibre Lasers XIV - Technology and Systems*(Spie-Int Soc Optical Engineering, San Francisco, CA, 2017).

39. M. N. Zervas, "Power Scaling Limits in High Power Fibre Amplifiers due to Transverse Mode Instability, Thermal Lensing and Fibre Mechanical Reliability," in *Fibre Lasers Xv: Technology and Systems*, I. Hartl, and A. L. Carter, eds. (2018).

40. Y. R. Gu, C. M. Lei, J. Liu, R. X. Li, L. Liu, H. Xiao, and Z. L. Chen, "Side-pumping combiner for high-power fibre laser based on tandem pumping," Optical Engineering 56, 5 (2017).

41. C. A. Codemard, J. K. Sahu, and J. Nilsson, "Tandem Cladding-Pumping for Control of Excess Gain in Ytterbium-Doped Fibre Amplifiers," IEEE Journal of Quantum Electronics 46, 1860-1869 (2010).

42. M. R. Albandakji, A. Safaai-Jazi, and R. H. Stolen, "Tapered photonic crystal fibres," in *Conference on Photonic Crystals and Photonic Crystal Fibres for Sensing Applications II*(Spie-Int Soc Optical Engineering, Boston, MA, 2006).

43. J. Limpert, S. Höfer, A. Liem, H. Zellmer, A. Tünnermann, S. Knoke, and H. Voelckel, "100-W average-power, high-energy nanosecond fibre amplifier," Applied Physics B 75, 477-479 (2002).

44. S. Stelzer, A. Mahrle, A. Wetzig, and E. Beyer, "Experimental investigations on fusion cutting stainless steel with fibre and CO2 laser beams," Lasers in Manufacturing (Lim 2013) 41, 392-397 (2013).

45. J. Nilsson, J. K. Sahu, Y. Jeong, W. A. Clarkson, R. Selvas, A. B. Grudinin, and S. U. Alam, "High power fibre lasers: New developments," in *Conference on Advances in Fibre Lasers*(Spie-Int Soc Optical Engineering, San Jose, Ca, 2003), pp. 50-59.

46. W. Shi, Q. Fang, X. S. Zhu, R. A. Norwood, and N. Peyghambarian, "Fibre lasers and their applications Invited," Applied Optics 53, 6554-6568 (2014).

47. J. F. Ready, "Industrial applications of lasers," IEEE Journal of Quantum Electronics QE 7, 278-& (1971).

48. J. F. Ready, "Industrial applications of high power lasers," Optical Engineering 17, 191-191 (1978).

49. A. Kratky, D. Schuocker, and G. Liedl, "Processing with kW fibre lasers - advantages and limits," in *17th International Symposium on Gas Flow, Chemical Lasers, and High-Power Lasers*(Spie-Int Soc Optical Engineering, Lisboa, PORTUGAL, 2008).

50. T. Kissinger, T. O. H. Charrett, and R. P. Tatam, "Range-resolved interferometric signal processing using sinusoidal optical frequency modulation," Optics Express 23, 9415-9431 (2015).

51. P. Kah, R. Suoranta, J. Martikainen, and C. Magnus, "Techniques for joining dissimilar materials: metals and polimers," Reviews on Advanced Materials Science 36, 152-164 (2014).

52. M. Kraetzsch, J. Standfuss, A. Klotzbach, J. Kaspar, B. Brenner, and E. Beyer, "Laser Beam Welding with High-Frequency Beam Oscillation: Welding of Dissimilar Materials with Brilliant Fibre Lasers," Lasers in Manufacturing 2011: Proceedings of the Sixth International Wlt Conference on Lasers in Manufacturing, Vol 12, Pt A 12, 142-149 (2011).

53. S. V. Kuryntsev, and A. K. Gilmutdinov, "The effect of laser beam wobbling mode in welding process for structural steels," International Journal of Advanced Manufacturing Technology 81, 1683-1691 (2015).

54. W. E. Frazier, "Metal Additive Manufacturing: A Review," Journal of Materials Engineering and Performance 23, 1917-1928 (2014).

55. G. Tapia, and A. Elwany, "A Review on Process Monitoring and Control in Metal-Based Additive Manufacturing," Journal of Manufacturing Science and Engineering-Transactions of the Asme 136 (2014).

56. N. Vukovic, P. Almeida, J. Chan, C. Codemard, and M. N. Zervas, "Fast and Controllable Beam Switching in a Pulsed Fibre Laser," IEEE Photonics Technology Letters 31, 927-930 (2019).

57. C. A, "Double-Clad Optical fibre for lasers and amplifiers," U. S. P. A. Publication, ed. (2004).

58. M. N. Zervas, "High power ytterbium-doped fibre lasers - fundamentals and applications," International Journal of Modern Physics B 28, 35 (2014).

59. R. M. Tao, P. F. Ma, X. L. Wang, P. Zhou, and Z. J. Liu, "Mitigating of modal instabilities in linearly-polarized fibre amplifiers by shifting pump wavelength," Journal of Optics 17, 7 (2015).

60. R. M. Tao, P. F. Ma, X. L. Wang, P. Zhou, and Z. J. Liu, "Study of Wavelength Dependence of Mode Instability Based on a Semi-Analytical Model," IEEE Journal of Quantum Electronics 51, 1-6 (2015).

61. P. Zhou, H. Xiao, J. Y. Leng, J. M. Xu, Z. L. Chen, H. W. Zhang, and Z. J. Liu, "High-power fibre lasers based on tandem pumping," Journal of the Optical Society of America B-Optical Physics 34, A29-A36 (2017).

62. "COHERENT Website: Fibre Laser Welding Cuts Costs and Improves Results," https://www.photonics.com/Articles/Fibre_Laser_Welding_Cuts_Costs_and_Improves

63. "FUJIKURA Website: What is fibre laser?," http://www.fibrelaser.fujikura.jp/eng/products/about-fibre-laser.html.

64. "NLIGHT Website: Semiconductor and Fibre Lasers."

65. D. Sliwinska, P. Kaczmarek, and K. M. Abramski, "Pump and signal power combiners for high-power fibre amplifier applications," Photonics Letters of Poland 7, 29-31 (2015).

66. D. Neugroschl, J. Park, M. Wlodawski, J. Singer, and V. I. Kopp, "High-efficiency (6+1)x1 combiner for high power fibre lasers and amplifiers," in *Conference on Fibre Lasers X - Technology, Systems, and Applications*(Spie-Int Soc Optical Engineering, San Francisco, CA, 2013).

67. D. Stachowiak, "High-Power Passive Fibre Components for All-Fibre Lasers and Amplifiers Application-Design and Fabrication," Photonics 5, 17 (2018).

68. "NUFERN Website. LMA-YDF Series.," https://www.nufern.com/.

69. R. M. Tao, R. T. Su, P. F. Ma, X. L. Wang, and P. Zhou, "Suppressing mode instabilities by optimizing the fibre coiling methods," Laser Physics Letters 14, 7 (2017).

70. R. M. Tao, P. F. Ma, X. L. Wang, P. Zhou, and Z. J. Liu, "1.3 kW monolithic linearly polarized single-mode master oscillator power amplifier and strategies for mitigating mode instabilities," Photonics Research 3, 86-93 (2015).

71. "IPG Technology, the laser revolution," https://www.ipgphotonics.com/en/whyIpg.

72. H. Zimer, M. Kozak, A. Liem, F. Flohrer, F. Doerfel, P. Riedel, S. Linke, R. Horley, F. Ghiringhelli, S. Demoulins, M. Zervas, J. Kirchhof, S. Unger, S. Jetschke, T. Peschel, and T. Schreiber, "Fibres and fibre-optic components for high power fibre lasers," in *Conference on Fibre Lasers VIII - Technology, Systems, and Applications*(Spie-Int Soc Optical Engineering, San Francisco, CA, 2011).

73. C. Schulze, A. Lorenz, D. Flamm, A. Hartung, S. Schroter, H. Bartelt, and M. Duparre, "Mode resolved bend loss in few-mode optical fibres," Optics Express 21, 3170-3181 (2013).

74. M. N. Zervas, "High power ytterbium-doped fibre lasers - fundamentals and applications (vol 28, 1442009, 2014)," International Journal of Modern Physics B 28, 1 (2014).

75. V. Scarnera, F. Ghiringhelli, M. K. Durkin, C. A. Codemard, M. N. Zervas, and IEEE, *Transient Modal Instabilities in High Power Fibre Lasers* (2017).

76. V. Scarnera, F. Ghiringhelli, A. Malinowski, C. A. Codemard, M. K. Durkin, and M. N. Zervas, "Modal instabilities in high power fibre laser oscillators," Optics Express 27, 4386-4403 (2019).

77. T. Y. Fan, "Laser beam combining for high-power, high-radiance sources," IEEE Journal of Selected Topics in Quantum Electronics 11, 567-577 (2005).

78. A. Klenke, M. Muller, H. Stark, F. Stutzki, C. Hupel, T. Schreiber, A. Tunnermann, and J. Limpert, "Coherently combined 16-channel multicore fibre laser system," Optics Letters 43, 1519-1522 (2018).

79. A. Avdokhin, V. Gapontsev, P. Kadwani, A. Vaupel, I. Samartsev, N. Platonov, A. Yusim, and D. Myasnikov, "High average power quasi-CW single-mode green and UV fibre lasers," in *Conference on Nonlinear Frequency Generation and Conversion - Materials, Devices, and Applications XIV*(Spie-Int Soc Optical Engineering, San Francisco, CA, 2015).

80. "Air force research laboratory, Stimulated Brillouin Scattering (SBS) Suppression Techniques," (2007).

81. T. J. Bronder, T. M. Shay, I. Dajani, A. Gavrielides, C. A. Robin, and C. A. Lu, "SBS mitigation with 'two-tone' amplification: a theoretical model," in *Fibre Lasers V: Technology, Systems, and Applications*, J. Broeng, and C. Headley, eds. (Spie-Int Soc Optical Engineering, 2008), pp. U352-U360.

82. I. Dajani, C. Zeringue, T. J. Bronder, T. Shay, A. Gavrielides, and C. Robin, "A theoretical treatment of two approaches to SBS mitigation with two-tone amplification," Optics Express 16, 14233-14247 (2008).

83. K. Shima, S. Ikoma, K. Uchiyama, Y. Takubo, M. Kashiwagi, and D. Tanaka, "5-kW single stage all-fibre Yb-doped single-mode fibre laser for materials processing," in *Conference on Fibre Lasers XV - Technology and Systems*(Spie-Int Soc Optical Engineering, San Francisco, CA, 2018).

84. B. Shiner, "The Impact of Fibre Laser Technology on the World Wide Material Processing Market," in *CLEO: 2013*(Optical Society of America, San Jose, California, 2013), p. AF2J.1.

85. E. A. Shcherbakov, V. V. Fomin, A. A. Abramov, A. A. Ferin, D. V. Mochalov, and V. P. E. D. H. G. a. M. P. Gapontsev, "Industrial grade 100 kW power CW fibre laser," in *Advanced Solid-State Lasers Congress*(Optical Society of America, Paris, 2013), p. ATh4A.2.

86. Kensuke, "History and vision of optical fibre fusion splicing technology," (2018).

87. 3SAE, "Homepage," https://www.3sae.com/test/index.php.

88. Yablon, *Optical Fibre Fusion Splicing* (Springer series in optical science, 2005).

89. B. S. Wang, and E. Mies, "Review of Fabrication Techniques for Fused Fibre Components for Fibre Lasers," in *Conference on Fibre Lasers VI - Technology, Systems, and Applications*(Spie-Int Soc Optical Engineering, San Jose, CA, 2009).

90. N. Bhatia, K. C. Rustagi, and J. John, "Single LP0,n mode excitation in multimode fibres," Optics Express 22, 16847-16862 (2014).

91. B. S. Wang, and E. W. Mies, "Advanced topics on fusion splicing of Specialty fibres and devices," in *Conference on Passive Components and Fibre-Based Devices IV*(Spie-Int Soc Optical Engineering, Wuhan, PEOPLES R CHINA, 2007).

92. W. K. Burns, and A. F. Milton, "Mode conversion in planar dielectric separating waveguides," IEEE Journal of Quantum Electronics QE11, 32-39 (1975).

93. A. F. Milton, and W. K. Burns, "Mode coupling in optical waveguide horns," IEEE Journal of Quantum Electronics 13, 828-835 (1977).

94. S. Lacroix, R. Bourbonnais, F. Gonthier, and J. Bures, "Tapered monomode optical fibres - understanding large power tarnsfer," Applied Optics 25, 4421-4425 (1986).

95. D. Marcuse, "Mode conversion in optical fibres with monotonically increasing core radius," Journal of Lightwave Technology 5, 125-133 (1987).

96. J. Luo, "Modeling dissimilar optical fibre splices with substantial diffusion," Journal of Lightwave Technology 25, 3575-3579 (2007).

97. A. J. Fielding, K. Edinger, and C. C. Davis, "Experimental observation of mode evolution in single-mode tapered optical fibres," Journal of Lightwave Technology 17, 1649-1656 (1999).

98. M. Skorobogatiy, C. Anastassiou, S. G. Johnson, O. Weisberg, T. D. Engeness, S. A. Jacobs, R. U. Ahmad, and Y. Fink, "Quantitative characterization of higher-order mode converters in weakly multimoded fibres," Optics Express 11, 2838-2847 (2003).

99. J. W. Nicholson, and A. D. Yablon, "Spatially and spectrally resolved imaging of higher-order-modes in large-mode-area fibres," in *Fibre Lasers V: Technology, Systems, and Applications*, J. Broeng, and C. Headley, eds. (Spie-Int Soc Optical Engineering, 2008), pp. XXXV-XXXVI.

100. J. W. Nicholson, A. D. Yablon, S. Ramachandran, and S. Ghalmi, "Spatially and spectrally resolved imaging of modal content in large-mode-area fibres," Optics Express 16, 7233-7243 (2008).

101. D. R. Gray, S. R. Sandoghchi, N. V. Wheeler, N. K. Baddela, G. T. Jasion, M. N. Petrovich, F. Poletti, and D. J. Richardson, "Accurate calibration of S2 and interferometry based multimode fibre characterization techniques," Optics Express 23, 10540-10552 (2015).

102. J. W. Nicholson, M. Mermelstein, A. D. Yablon, and IEEE, *Characterizing Discrete and Distributed Scattering of Higher-Order-Modes in Large-Mode-Area Fibres* (IEEE, 2008).

103. C. C. C. Carrero, G. Le Cocq, B. Sevigny, L. Bigot, A. Le Rouge, Y. Quiquempois, M. Bigot-Astruc, D. Molin, P. Sillard, and IEEE, "Using advanced S2 analysis to measure mode coupling in a 2-LP-Mode Fibre," 2016 Optical Fibre Communications Conference and Exhibition (Ofc), 3 (2016).

104. Y. An, J. Li, L. Huang, J. Leng, L. Yang, and P. Zhou, "Deep learning enabled superfast and accurate M2 evaluation for fibre beams," Optics Express 27, 18683-18694 (2019).

105. L. INTERFIBRE ANALYSIS, "Multi-Wavelength Optical Fibre Refractive Index Profiling Technology," http://www.interfibreanalysis.com/.

106. A. D. Yablon, "Multiwavelength optical fibre refractive index profiling," in *Fibre Lasers Vii: Technology, Systems, and Applications*, K. Tankala, and J. W. Dawson, eds. (Spie-Int Soc Optical Engineering, 2010).

107. A. D. Yablon, "New transverse techniques for characterizing high-power optical fibres," Optical Engineering 50, 6 (2011).

108. A. D. Yablon, "Optical-fibre refractive-index measurement takes a new direction," Laser Focus World 47, 57-60 (2011).

109. B. Sevigny, G. Le Cocq, C. C. C. Carrero, C. Valentin, P. Sillard, G. Bouwmans, L. Bigot, and Y. Quiquempois, "Advanced S-2 Imaging: Application of Multivariate Statistical Analysis to Spatially and Spectrally Resolved Datasets," Journal of Lightwave Technology 32, 4004-4010 (2014).

110. AForge.Net, "Open source C# framework designed for developers and researchers in the fields of Computer Vision.," http://www.aforgenet.com/framework/.

111. A. J, *C# 7.0 in a Nutshell: The Definitive Reference* (2018).

112. K. Lyytikainen, S. T. Huntington, A. L. G. Carter, P. McNamara, S. Fleming, J. Abramczyk, I. Kaplin, and G. Schotz, "Dopant diffusion during optical fibre drawing," Optics Express 12, 972-977 (2004).

113. J. Kobelke, K. Schuster, J. Bierlich, S. Unger, A. Schwuchow, T. Elsman, J. Dellith, C. Aichele, R. Fatobene Ando, and H. Bartelt, "Germania and alumina dopant

diffusion and viscous flow effects at preparation of doped optical fibres," Advances in Electrical and Electronic Engineering 15, 101-106 (2017).

114. J. Kirchhof, S. Unger, J. Dellith, and A. Scheffel, "Diffusion in binary TiO2- SiO2 glasses," Optical Materials Express 4, 672-680 (2014).

115. J. Kirchhof, S. Unger, K. F. Klein, and B. Knappe, "DIFFUSION BEHAVIOR OF FLUORINE IN SILICA GLASS," Journal of Non-Crystalline Solids 181, 266-273 (1995).

116. J. Kirchhof, S. Unger, and J. Dellith, "Diffusion of phosphorus doped silica for active optical fibres," Journal of Non-Crystalline Solids 345, 234-238 (2004).

117. J. Kirchhof, S. Unger, B. Knappe, and J. Dellith, "Diffusion in binary GeO2-SiO2 glasses," Physics and Chemistry of Glasses-European Journal of Glass Science and Technology Part B 48, 129-133 (2007).

118. S. Unger, J. Dellith, A. Scheffel, and J. Kirchhof, "Diffusion in Yb2O3-Al2O3-SiO2 glass," Physics and Chemistry of Glasses-European Journal of Glass Science and Technology Part B 52, 41-46 (2011).

119. S. Kuhn, F. Moller, C. Hupel, S. Hein, F. Beier, J. Nold, N. Haarlammert, T. Schreiber, R. Eberhardt, and A. Tunnermann, "Active materials for high-power fibre lasers prepared by All-Solution Doping technique," in *Conference on Optical Components and Materials XV*(Spie-Int Soc Optical Engineering, San Francisco, CA, 2018).

120. R. S, "Air force research laboratory. Appropriate measurement and consistent standard for high energy laser beam quality.," (2006).

121. Y. M. Jung, Y. C. Jeong, G. Brambilla, and D. J. Richardson, "Adiabatically tapered splice for selective excitation of the fundamental mode in a multimode fibre," Optics Letters 34, 2369-2371 (2009).

122. 3SAE, "Ring of Fire® Technology," http://www.3sae.com/ringoffiretechnology.php.

123. W. R, "Large Area Isothermic Plasma for Large Diameter and Specialty Fibre Splicing," (2007).

124. B. Samson, G. Frith, A. Carter, K. Tankala, and Osa, "High-power large-mode area optical fibres for fibre lasers and amplifiers," 2008 Conference on Optical Fibre Communication/National Fibre Optic Engineers Conference, Vols 1-8, 2412-2414 (2008).

125. W. J. Lai, V. J. J. Yeo, and IEEE, "Ytterbium Doped LMA-W-DCF for High Power Fibre Laser," in *15th International Conference on Optical Communications and Networks (ICOCN)*(IEEE, Hangzhou, PEOPLES R CHINA, 2016).

126. S. Ramachandran, J. M. Fini, M. Mermelstein, J. W. Nicholson, S. Ghalmi, and M. F. Yan, "Ultra-large effective-area, higher-order mode fibres: a new strategy for high-power lasers," Laser & Photonics Reviews 2, 429-448 (2008).

127. A. Carter, F. Corbin, D. Machewirth, B. Samson, K. Tankala, M. O'Connor, and IEEE, "High-power narrow-linewidth all-fibre amplifiers for power scaling applications," 2005 IEEE Leos Annual Meeting Conference Proceedings (Leos), 925-926 (2005).

128. J. J, "Corning whitepaper: An Overview of Macrobending and Microbending of Optical Fibres," (2010).

129. W. B. Gardner, "Microbending loss in optical fibre," Bell System Technical Journal 54, 457-465 (1975).

130. K. Morishita, "Numerical-analysis of pulse broadening in graded index optical fibres," IEEE Transactions on Microwave Theory and Techniques 29, 348-352 (1981).

131. M. E. Fermann, "Single mode amplifiers and compressors based on multimode fibre," U. s. patend, ed. (1998).

132. M. E. Fermann, "Single-mode excitation of multimode fibres with ultrashort pulses," Optics Letters 23, 52-54 (1998).

133. C. R. Giles, and E. Desurvire, "Modeling erbium-doped fibre amplifiers," Journal of Lightwave Technology 9, 271-283 (1991).

134. K. Morishita, "NUMERICAL-ANALYSIS OF PULSE BROADENING IN GRADED INDEX OPTICAL FIBRES," IEEE Transactions on Microwave Theory and Techniques 29, 348-352 (1981).

135. S. Suzuki, H. McKay, X. A. Peng, L. B. Fu, and L. A. Dong, "Efficient Highly Ytterbium-Doped Silica Fibres with Low Photo-darkening for High Power Fibre Lasers," in *Fibre Lasers Vi: Technology, Systems, and Applications*, D. V. Gapontsev, D. A. Kliner, J. W. Dawson, and K. Tankala, eds. (2009).

136. S. Suzuki, H. A. McKay, X. Peng, L. B. Fu, and L. Dong, "Highly ytterbium-doped silica fibres with low photo-darkening," Optics Express 17, 9924-9932 (2009).

137. D. Alekseev, V. Tyrtyshnyy, M. Kuznetsov, and O. Antipov, "Transverse-Mode Instability in High-Gain Few-Mode Yb3+-Doped Fibre Amplifiers With a 10-mu m Core Diameter With or Without Backward Reflection," IEEE Journal of Selected Topics in Quantum Electronics 24, 8 (2018).

138. D. Engin, J. Burton, I. Darab, F. Kimpel, and S. Gupta, "Yb-fibre-MOPA based high energy and average power uplink laser beacon for deep space communication operating under Nested PPM format," in *Conference on Laser Technology for Defense and Security XI*(Spie-Int Soc Optical Engineering, Baltimore, MD, 2015).

139. K. Brar, M. Savage-Leuchs, J. Henrie, S. Courtney, C. Dilley, R. Afzal, and E. Honea, "Threshold power and fibre degradation induced modal instabilities in high power fibre amplifiers based on large mode area fibres," in *Conference on Fibre Lasers XI - Technology, Systems, and Applications*(San Francisco, CA, 2014).

140. M. Vivona, J. Kim, and M. N. Zervas, "Non-destructive characterization of rare-earth-doped optical fibre preforms," Optics Letters 43, 4907-4910 (2018).

141. Y. Ye, X. Xi, C. Shi, H. Zhang, B. Yang, X. Wang, P. Zhou, and X. Xu, "Experimental Study of 5 kW High Stability Monolithic Fibre Laser Oscillator With or Without External Feedback," IEEE Photonics Journal, 1-1 (2019).

142. D. Mardani, H. E. Kondakci, L. Martin, A. F. Abouraddy, and G. K. Atia, "Modal analysis via compressive optical interferometry," in *2017 IEEE Photonics Conference (IPC)*(2017), pp. 621-622.

143. D. Mardani, A. F. Abouraddy, and G. K. Atia, "Efficient modal analysis using compressive optical interferometry," Optics Express 23, 28449-28458 (2015).

144. MN Ozisic, *Heat conduction* (1993).